THE UNIVERSITY *of* EDINBURGH

THE UNIVERSITY *of* EDINBURGH

3D printing of curved continuous carbon fibre reinforced polymer composites

Haoqi Zhang

A thesis submitted in accordance with the requirements for the degree of

Doctor of Philosophy

The University of Edinburgh

Institute for Materials and Processes, School of Engineering

August 2021

Declaration

I declare that the thesis has been composed by myself and that the work has not be submitted for any other degree or professional qualification. I confirm that the work submitted is my own, except where work which has formed part of jointly-authored publications has been included. My contribution and those of the other authors to this work have been explicitly indicated below. I confirm that appropriate credit has been given within this thesis where reference has been made to the work of others.

The work presented in Chapter 3 was previously published in *Composites Part B: Engineering* as *Performance-driven 3D printing of continuous curved carbon fibre reinforced polymer composites: A preliminary numerical study* by Zhang H (author of the declaration), Yang D (supervisor) and Sheng Y. This study was conceived by the author of the declaration and his supervisor. I carried out all the modelling, data analysis and writing in this work.

The work presented in Chapter 4 was previously published in *Composites Part B: Engineering* as *Failure analysis of 3D-printed woven composite plates with holes under tensile and shear loading* by Zhang H (author of the declaration), Dickson AN, Sheng Y, McGrail T, Dowling DP, Wang C, Neville A and Yang D (supervisor). This study was conceived by the author of the declaration and his supervisor. The printing experiment was conducted by Dickson AN through collaboration. I carried out all the modelling, characterisation, data analysis and writing in this work.

The work presented in Chapter 5 was previously published in *Additive Manufacturing* as *Fibre misalignment and breakage in 3D printing of continuous carbon fibre reinforced thermoplastic composites* by Zhang H (author of the declaration), Chen J and Yang D (supervisor). This study was conceived by the author of the declaration and his supervisor. Part of the modelling was

conducted by Chen J through collaboration. I carried out all the experiment, characterisation, data analysis and writing in this work.

Haoqi Zhang

Acknowledgements

First and foremost, I would like to give my most sincere thanks to my primary supervisor, Dr Dongmin Yang, who gives me the support and encouragement all the way through my PhD period. Additional thanks should be given to my co-supervisor, Prof. Conchúr Ó Brádaigh and Prof. Yong Sheng, for their suggestions for my PhD project.

My special thanks are given to Dr. Andrew Nigel Dickon and Prof. Denis P Dowling from UCD, who helped me with the 3D printing experiments in Chapter 4. Also thanks to Dr Jiayun Chen and Shuai Wang, who helped me with the simulation and optimisation method in Chapter 5 & 8, respectively. I would like to extend my thanks to all the colleagues: Xiaohong Zhu, Ka Zhang, Zhiyao Xu, Aonan Li and Jiang Wu for their company and all the valuable discussions. Finally, I wish to express my gratitude to my family and my girlfriend Jiayi Wu, who unconditionally support me throughout the entire time.

Abstract

Fused filament fabrication (FFF) 3D printing technology offers the opportunity to change the orientation of continuous fibres during the manufacturing process. This thesis investigates the fibre placement method, the printing quality of continuous filaments and the post-processing technique of the printed preforms, in order to manufacture the lightweight 3D-printed composites with curved continuous fibre reinforcements.

First, a new concept to place continuous curved fibres along principal stress trajectories is presented. Three cases under different loading conditions are studied numerically and compared with traditional composites reinforced with unidirectional fibres. The modelling results show that the stress concentration in both fibre and matrix are reduced significantly by the curved fibre placement and the stiffness of CFRP composites has been improved.

Secondly, a tailored fibre placement is achieved in the 3D printing experiment by altering the fibre orientation to leave a hole. The modelling and failure analysis are then conducted for 3D-printed woven composite plates with a hole under tensile and shear loading. Good agreement between numerical and experimental results is obtained, which exhibits a similar trend of strength improvement using the new placement technique.

After that, the mechanism of the void formation and manufacturing-induced defects during the printing process is investigated. Single printed stripe at various turning angles and curvatures are characterised using X-ray computed micro-tomography (μCT) scanning and optical microscopy. A finite element (FE) model of the printing process is also established to support the experimental measurement. It has been found that the void content and fibre misalignment result from the weak fibre/matrix interface and the uneven pressure executed by the nozzle. The increase of turning angle leads to more aggravated printing defects, including path inaccuracy, fibre twisting, folding and even fibre breakage.

Further, a hybrid technique is developed to manufacture composites with low porosity and customised curved fibre paths. Composite preforms are manufactured by FFF 3D printing and powder thermoset epoxy is added to the preforms to fill up the gaps, remove air voids and enhance the interfacial bonding through traditional vacuum bagging and oven curing process. In the standard UD 0° samples, the tensile stiffness and strength are increased by 29.3% and 22.1%, respectively. The hybrid manufacturing technique is also adopted to investigate the performance of the single-notched specimen under uniaxial tension. It is shown that the placement of continuous fibres along the principal stress trajectories significantly increased the failure strength as well as the fracture toughness of the composites.

Besides, the effect of fibre placement on the mechanical performance of open-hole composites under uniaxial tension is comprehensively studied. The concept of placing continuous fibres along the higher in-plane principal stress trajectories is found to improve the strength of the composites and postpone the crack initiation. Additional fibres, along the lower in-plane principal stress trajectories and around the hole, are found to alter the failure mode and mechanical performance of the samples. Together with the digital image correlation measurement, a FE model is also built based on the actual printing paths to understand the stress distributions due to different fibre placement methods.

Finally, a sequentially coupled optimisation for structural topology and fibre orientation is presented. Topology optimisation is first carried out to obtain the geometry of the structure and then the continuous carbon fibres are placed along the identified principal stress trajectories. Case study of Messerschmitt-Bolkow-Blohm (MBB) beam under three-point bending is performed. Compared with the state-of-the-art printing system, the strength and stiffness of the optimised sample are increased by 305% and 256%, respectively. With only 20% fibre usage, the optimised sample can achieve the same stiffness-to-weight ratio as the traditionally-manufactured composites.

Keywords:

3D printing; Fused filament fabrication (FFF); Curved continuous carbon fibre; Topology optimisation; Principal stress trajectories.

Lay summary

Fused filament fabrication (FFF) 3D printing technology offers the opportunity to change the direction of the continuous fibres during the manufacturing process. In this thesis, the placement method of continuous fibres, the printing quality of filaments and the post-processing technique of the 3D-printed samples are investigated. It aims to maximise the superior properties of continuous fibres and manufacture the lightweight 3D-printed composites with curved fibre paths.

First, a new concept of placing continuous curved fibres along the stress lines is proposed. It is achieved in the printing experiment by a modified desktop printer with the continuous paths. The powder epoxy is then used for post-treatment to reduce voids. Various cases with different loading conditions and complex geometries are performed via numerical simulations and experimental tests. Through them, the effect of fibre placement on the mechanical performance is comprehensively studied. In addition, the mechanism of printing process is investigated, to understand how the void and other defects format. Finally, the optimisation of fibre direction is combined with that of geometry to achieve the high stiffness-to-weight ratio structure.

Compared with the most advanced printing system, the strength and stiffness of the optimised sample are increased by 305% and 256%, respectively. Using only 20% fibre, the optimised sample can achieve the same stiffness-to-weight ratio as traditionally manufactured composite materials.

Table of Contents

List of Figures

List of Tables

Chapter 1 Introduction

1.1 Research motivation

The use of carbon fibre reinforced polymer (CFRP) composites has been increasing in recent years. Multiple industries such as aerospace, automotive, infrastructure and construction have developed new products and assemblies using CFRP composites due to their advantages including the high strength and stiffness, lightweight, low coefficient of thermal expansion and the excellent resistance of corrosion and fatigue. These superior properties are mainly attributed to the reinforcement with continuous carbon fibres. In traditional manufacturing, the hand lay-up process and vacuum-bagging/autoclave moulding are mostly used, in which continuous fibres are usually placed straight in each layer. Thus, additional machining processes, such as cutting and drilling, are required for products with complex geometries. This will inevitably cause waste of materials and a decrease in mechanical performance, since the continuous fibres are partially cut off and the manufacturing defects are introduced.

As an alternative, additive manufacturing, which is also known as 3D printing, has emerged for the fabrication of composites with highly complex geometries at a faster production time. Among them, Fused Filament Fabrication (FFF) 3D printing melts and deposits thermoplastic materials to produce three-dimensional parts and 1K/3K continuous carbon fibres (the fibre bundle consists of approximately 1000/3000 continuous carbon fibres.) can be integrated with thermoplastic to form the printing filaments. It offers the opportunity to customise the fibre paths during the manufacturing process and thus maximise the superior properties of continuous fibres for the higher strength/stiffness-to-weight ratio of the final products. Therefore, numerous researches are required for the FFF 3D printing of the curved continuous carbon fibre reinforced polymer composites, including the mechanism of the printing process,

the optimal placement methods of continuous fibres and even the optimisation method for both topology and localised fibre orientation. In addition, the modelling and failure analysis of 3D-printed CFRP composites should be performed to better understand the effectiveness of the curved fibre placement on the performance of final products.

1.2 Aims and Objectives

1.2.1 Aims

The main aim of this thesis is to 3D print CFRP composites with low-porosity and optimised curved fibre paths, in order to achieve a higher strength/stiffness-to-weight ratio. This is followed by the investigation of the mechanism of the printing process and the effectiveness of curved fibre placement to guide the future design for the FFF 3D printing of curved continuous carbon fibre reinforced composites.

1.2.2 Objectives

To achieve the above aims, the following four key objectives are defined:

(1) Developing fibre placement methods for CFRP composites with complex geometries, to release the stress concentration and improve the strength, stiffness and lightweight performance;

(2) Investigating the mechanism behind the printing of continuous carbon fibre filament, to reduce the defects and ensure the path accuracy during the printing process;

(3) Developing a hybrid manufacturing technique for the fabrication of 3D-printed composites with customised fibre paths and the low porosity;

(4) Carrying out the modelling and failure analysis of 3D-printed CFRP composites with curved fibres to evaluate the effectiveness of fibre placement methods.

1.3 Thesis outline

The thesis is divided into 9 chapters including Introduction, Literature review, six chapters of published or submitted journal papers on related objectives, and one chapter of summary. Since all the results in this thesis were published or submitted as journal papers, detailed abstract and introduction are presented at the beginning of each of the six chapters, according to the format requirement for including publication in thesis.

Chapter 2 presents an overall literature review related to this project, including fused filament fabrication 3D printing, the printing mechanism of continuous fibres, the placement methods of continuous curved fibres, post-processing techniques of 3D-printed composites and the modelling of 3D-printed composites.

Chapter 3 presents a new concept to place continuous curved fibres for CFRP composites, which can be achieved by FFF 3D printing technology. In this method, principal stress trajectories are generated based on the loading condition through finite element analysis (FEA) and used as the guidance of the placement paths for carbon fibres. A numerical study was performed and three cases (an open-hole single ply lamina under uniaxial tension and an open-hole cross-ply laminate under biaxial tension and normal pressure) were studied and compared with traditional reinforced composites with unidirectional fibres.

Chapter 4 presents the failure analysis of 3D-printed woven composite plates with a hole under tensile and shear loading. The tailored fibre placement is achieved by steering the fibre paths around a region to leave a hole. Also, the finite element (FE) modelling is performed to advance the understanding of the failure mechanisms, in which woven cells are built using stacking sequences and the fibre orientations around the hole are altered according to the 3D printing experiment. In order to compare this placement technique with that of a control group, the 'drilled' samples with the notch removed via mechanical machining are proposed. The

distribution of principal strain and displacement in the modelling are compared with the results obtained from Digital Image Correlation (DIC) and X-ray computed micro-tomography (μCT) scanning.

Chapter 5 investigates the formation of the void contents and manufacturing induced defects, such as fibre misalignment and breakage, during the printing process of 1K continuous carbon fibre filament. Single stripes at various turning angles and curvatures are printed by a desktop printer using a specific brass nozzle and then characterised using X-ray μCT scanning and optical microscopy. The FE models of the printing process is also built to support the experimental measurement.

Chapter 6 presents a hybrid technique to manufacture continuous curved carbon fibre reinforced composites with low porosity and customised fibre paths. Composite preforms are first manufactured by FFF 3D printing of continuous carbon fibre reinforced thermoplastic polyamide-6 (PA-6) filaments. Powder thermoset epoxy is added to the preforms to fill up the gaps, remove air voids and enhance the interfacial bonding through a traditional vacuum bagging and oven curing process. The hybrid manufacturing technique is also adopted to investigate the performance of 3D-printed curved continuous fibres in a notched specimen under uniaxial tension.

Chapter 7 employs the hybrid manufacturing technique to fabricate the open-hole composites with various fibre placement cases, in which the effect on the mechanical performance under uniaxial tension is comprehensively studied. The concept of placing continuous fibres along the higher in-plane principal stress trajectories is first adopted. The additional fibres, along the lower in-plane principal stress trajectories and around the hole, are then used to alter the failure mode of the samples. Together with the digital image correlation measurement, a FE model is

also built based on the actual printing paths to understand the stress distributions due to different fibre placement methods.

Chapter 8 presents a sequentially coupled optimisation of structural topology and fibre orientation for 3D printing of CFRP composites. Topology optimisation is first carried out to obtain the geometry of the structure under a specific load, and then the continuous carbon fibres are placed along the identified principal stress trajectories. Case study of Messerschmitt-Bolkow-Blohm (MBB) beam under three-point bending is performed. Also, different materials (polylactic acid and short fibre reinforced nylon-6) and printing systems (Markforged® with continuous fibres) are used to compare the mechanical performance of the optimised samples obtained from the hybrid manufacturing technique. Furthermore, the finite element analysis of the traditionally manufactured composite beams is carried out for the comparison and assessment of the lightweight performance of the optimised samples.

Chapter 9 summarises the main findings from Chapters 3-8 and suggests further considerations and recommendations.

Chapter 2 Literature review

2.1 FFF 3D printing

Additive manufacturing (AM), also known as 3D printing, is the fabrication of three-dimensional objects with materials added layer by layer [1]. For the additive manufacturing of polymer composites, three types of technologies are mainly used: resin photo-curing, powder sintering and filament extrusion. The detailed AM technologies, feedstock materials and working principle of them are shown in Table 2-1. Among them, the filament extrusion technology was first developed by Stratasys® in 1988 and named as fused deposition modelling (FDM) [2]. Another trademark fused filament fabrication (FFF) was also coined by RepRap® to give a phrase that would be legally unconstrained in its use. The FFF/FDM 3D printing uses the thermal print-head to liquefy the thermoplastic filament and then extrudes/deposits the melted materials via the heated nozzle on the heated platform [3, 4]. It offers a lot of benefits, including low cost, high speed, simplicity and simultaneous deposition of multi-materials [4]. Compared with the AM technologies using resin and powder, two advantages of the filament extrusion make FDM/FFF 3D printing become the most popular AM technology for composites: less materials waste and the convenience of being reinforced with discontinuous or continuous fibres.

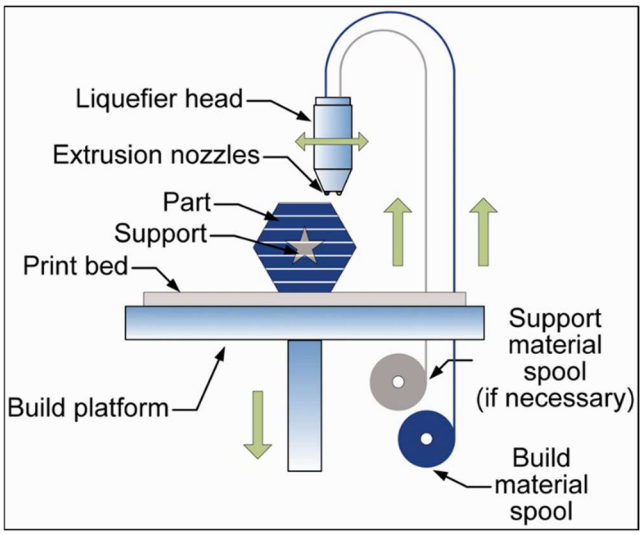

Figure 2-1 Working principle of FDM/FFF 3D printing [3, 5]

Table 2-1 Additive manufacturing technologies for polymer matrix composites [1]

Type	Additive manufacturing technology	Feedstock materials	Working principle
Resin photo-curing	SLA (Stereolithography) DLP (digital light processing)	Thermosetting resin	Laser scanning and UV induced curing
Powder sintering	SHS (Selective heat sintering) SLS (selective laser sintering)	Thermoplastic powder	Laser scanning and heat induced sintering
Filament extrusion	FFF (fused filament fabrication) FDM (fused deposition modeling)	Thermoplastic filament	Extrusion and deposition

Because of the way that the melted material is extruded, the printed material is confined to the thermoplastic which can be melted by the nozzle and then cooled and solidified on the print surface. A range of thermoplastic can be used as the structural material: polylactic acid (PLA), polycaprolactone (PCL), polycarbonate (PC), acrylonitrile butadiene styrene (ABS), polyethylene terephthalate (PETG), polyamide (PA), polyether ether ketone (PEEK) and so on, along with the support material: PVA (dissolvable) and the breakaway material (same with the

structural material but can be removed manually). The reinforcement materials can be short/chopped and continuous fibres: carbon, glass and kevlar, etc.

However, a common drawback that plagues thermoplastic material extrusion printing is the voids formed in the printed parts. Furthermore, with the inclusion of the discontinuous or continuous fibres, the void contents are increased due to the increased viscosity of the melted materials, the difference of the thermal expansion between fibre and matrix and the inadequate wetting of the fibre/matrix interface. For example, Figure 2-2 shows the void content in the continuous fibre filament and the 3D-printed FRP composites. In total, three types of voids are introduced in the printed parts: (i) void and pore in the single printed stripe/track. This type of voids rarely appears in the printing of pure thermoplastic, but it cannot be ignored when short and continuous fibres are impregnated with the filaments, which is mainly caused by the inadequate wetting between fibre/matrix and the high viscosity due to the mixed fibres, as shown in Figure 2-2; (ii) Gaps and inter-track voids between print paths (as shown in Figure 2-3). It is caused by the *in situ* consolidation of the FFF 3D printing and the improper geometry of the deposited bead; (iii) Voids and cracks between layers (as shown in Figure 2-4). They usually happen due to the temperature difference between the printed and printing layers and aggravate in the interface between layers with different materials, such as the pure thermoplastic layer and fibre reinforced layers.

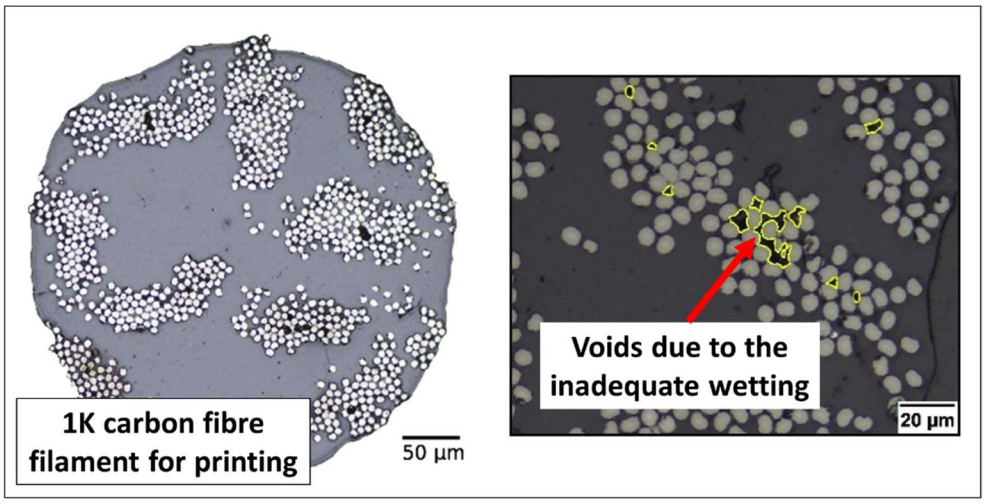

(a)

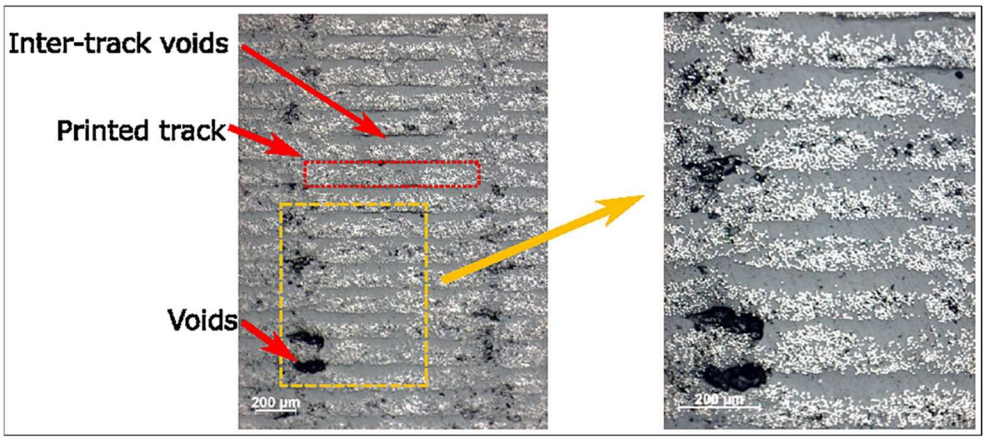

(b)

Figure 2-2 Void content in the (a) continuous fibre filament and (b) 3D-printed FRP composites [6, 7]

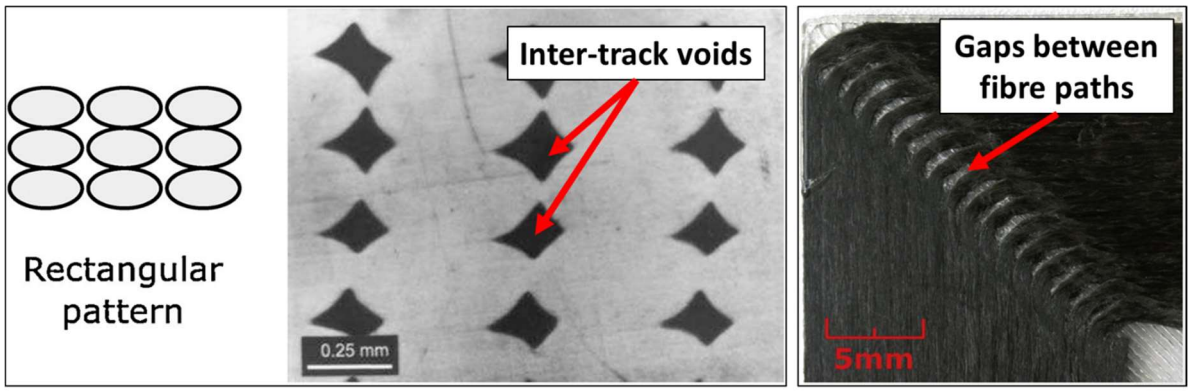

(a) (b)

Figure 2-3 (a) Inter-track voids and (b) gaps between print paths [6]

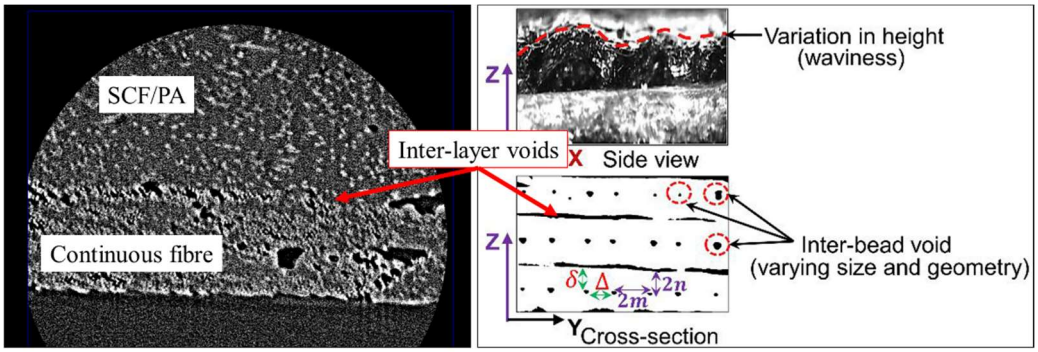

Figure 2-4 Void and cracks between layers [8]

In order to reduce the porosity, the effects of process parameters on void contents and mechanical properties were experimentally investigated by multiple researchers, including the nozzle/bed temperature [8, 9], print/feed speed [10] as well as the off-distance between nozzle and bed [11]. Also computational approaches for modelling the polymer melt flow and the associated effects of nozzle geometry were presented [12, 13]. The design of print paths was also optimised by using the skewed pattern to alter the structure formation on the meso-scale and then reduce the inter-track voids [14], as shown in Figure 2-5a. Apart from the research about void content, other issues such as the manufacturing efficiency, resolution and printing volume also limit the industrial application of FFF 3D printing. In previous researches, the microwave-assisted printing was used for the instantaneous heating to improve the printing speed and also decrease the porosity by reducing the temperature deviation [15, 16].

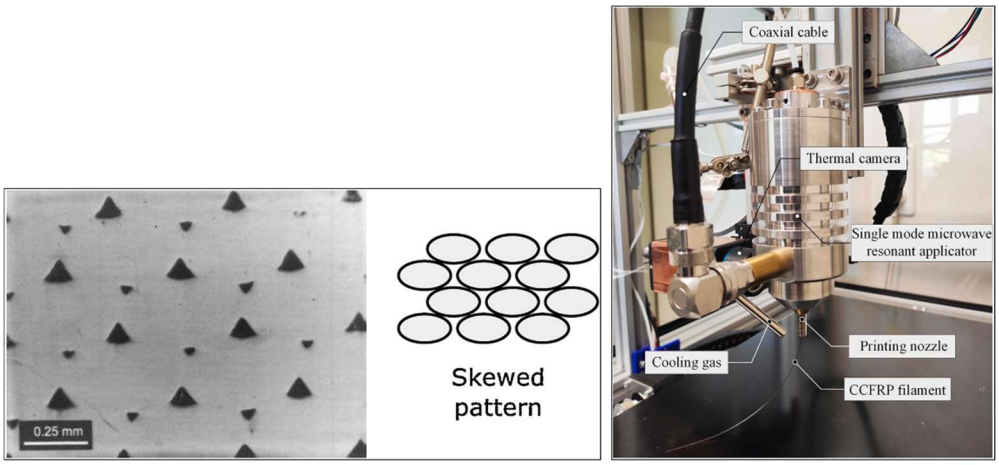

Figure 2-5 (a) Printing pure thermoplastic with skewed pattern to reduce the void formation [6] and (b) the illustration of the microwave-assisted printing head [16].

2.2 Printing of continuous carbon fibre filaments

As mentioned above, the inclusion of continuous fibre filaments is benificial for the FFF 3D printing of thermoplastic, enabling potential broader industrial and structural applications. In 2014, Markforged® released their first commercial printer for the fabrication of continuous carbon fibre reinforced polymer (cCFRP) composites. Multiple studies were performed to investigate the mechanical performance of cCFRP composites [17-20] and the Markforged® commercial 1K continuous fibre filaments were also widely-used as the material resource for researches on 3D printing of composites [21-24] (as shown in Figure 2-6b).

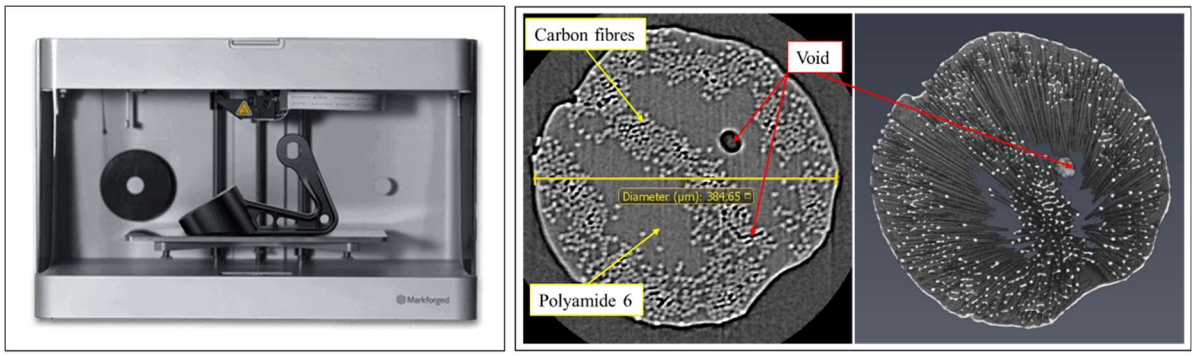

Figure 2-6 (a) Markforged® commercial printer and (b) its 1K continuous carbon fibre filament [25]

Researchers have also developed their in-house printer for the additive manufacturing of cCFRP composites. For example, dry continuous fibre bundles were impregnated with thermoplastic filament within the heated nozzle before being extruded [26-29], as shown in Figure 2-7a. Alternatively the fibre bundle could be fed directly to printer bed by a guide tube positioned after the nozzle [30, 31], as shown in Figure 2-7b. Compared with these in-nozzle and after-nozzle methods, the prior-to-nozzle impregnation method (beforehand fabrication of continuous filaments) offers more conveniences for the desktops printing and better path accuracy (compared with Figure 2-7c), since the volume fraction of fibre is consistent for the whole filament spool. Also, the fibre/matrix wetting of the prior-to-nozzle impregnation method is relatively good, because the high-temperature and high-pressure processes are more easily to be adopted in the separate step for the fabrication of continuous filaments.

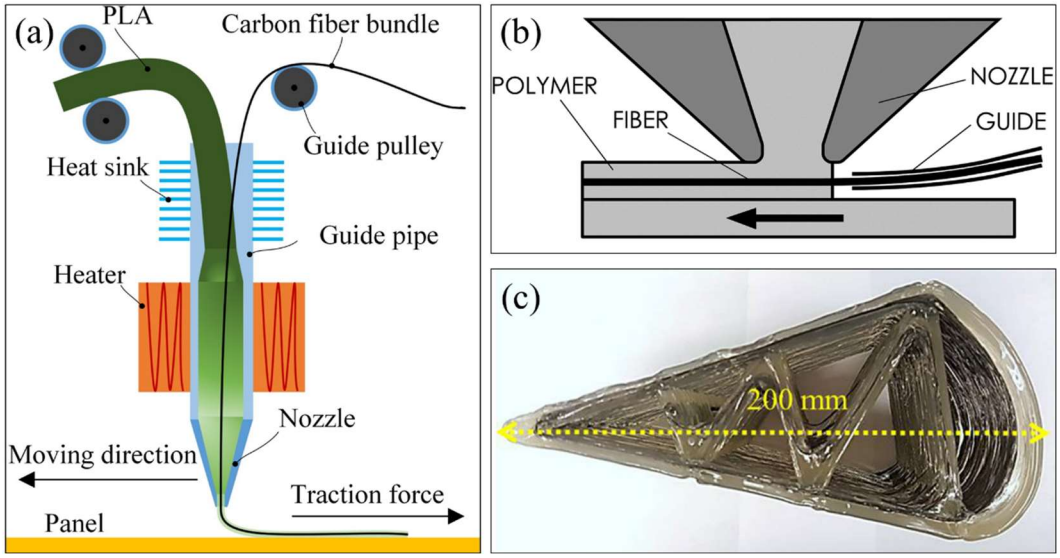

Figure 2-7 (a) In-nozzle impregnation [29] and (b) after nozzle implementation [31] methods for 3D printing of continuous fibres and (c) low-resolution samples from in-nozzle impregnation printing [32]

Besides the void formation mentioned in section 2.1, other manufacturing defects could also occur when printing the continuous fibres, including the misalignment, twisting, folding (more serve twisting with thickness change and reversal of inner/outer fibres) and fibre breakage (as shown in Figure 2-8). It was revealed in previous research [33, 34] that a fibre bundle was folded in a printing process of a curved section. Also, with a larger fibre bundle size or a smaller set radius, the printed radius would be lower than the set value [35, 36], as shown in Figure 2-9. These manufacturing defects occurs especially when printing with large curvatures and sharp corners. Since the printing of curved fibre paths is essential for the composites with complex geometries and customised performance, the mechanism behind them has to be further understood.

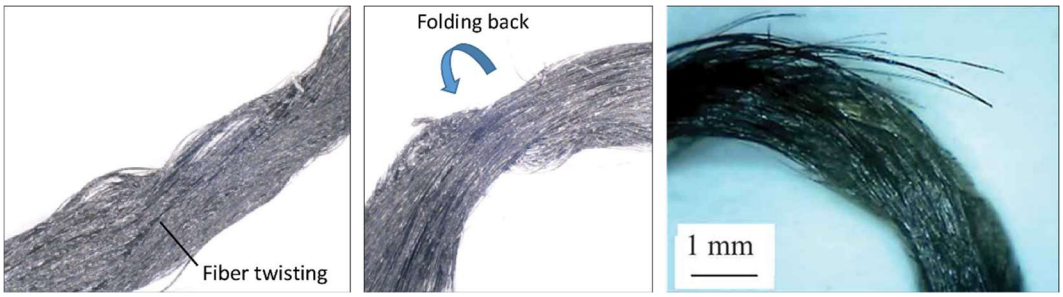

Figure 2-8 Manufacturing defects in the 3D-printed continuous carbon fibre filaments: (a) twisting (b) folding [35] (c) fibre breakage [33]

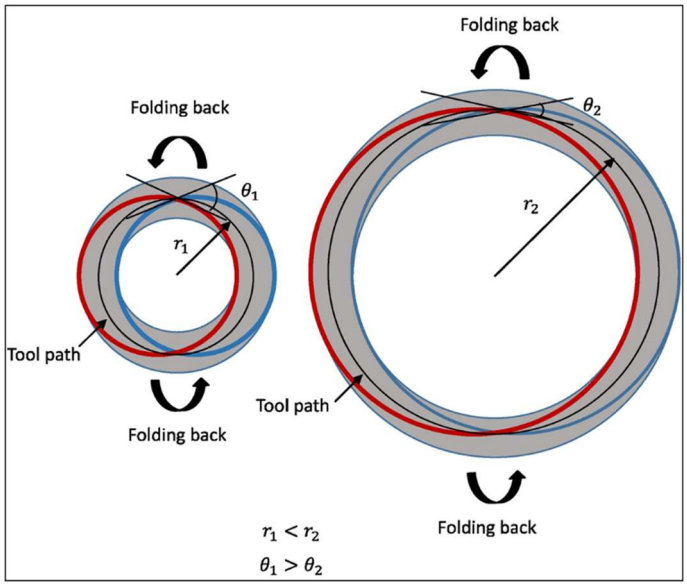

Figure 2-9 Manufacturing error between the set curvature and the printed radius [35]

2.3 Placement methods for continuous and curved fibres

The placement method for the continuous fibres is the key factor of the mechanical performance of the cCFRP composites. In the traditional manufacturing, although the stacking sequence was optimised [37, 38], continuous fibres are always placed straight in each layer. As mentioned in the Introduction chapter, placement methods for the curved fibres should be developed to avoid the machining processes and maximise the properties of the 3D-printed

cCFRP composites. Variable–stiffness design was first developed for proper placement of the fibres in the optimal orientations, in which the mechanical properties, such as stiffness [39] and buckling load [40], were improved in the computational simulations. However, the localised and discrete fibre orientation (as shown in Figure 2-10) can be very hard to achieve by either traditional or additive manufacturing. Thus, the streamline-generated methods are usually adopted to generate the actual printing paths of the continuous fibres. Among them, the streamlines of the fluid flow are employed for the avoidance of fibre cut-off in the composites with geometry singularity [41, 42], as shown in Figure 2-11. Another common approach is the stress-line method, in which the fibre orientation is maintained along the principal stress direction based on preliminary stress field calculations [43-46], as shown in Figure 2-12.

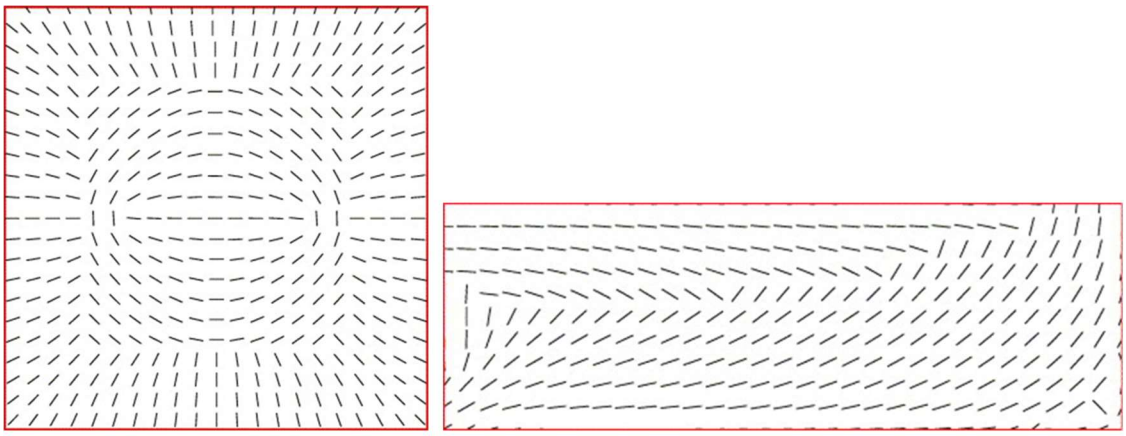

Figure 2-10 Variable–stiffness design of fibre orientation angles for (a) the clamped square plate under uniformly distributed loading and (b) the cantilever plate [39]

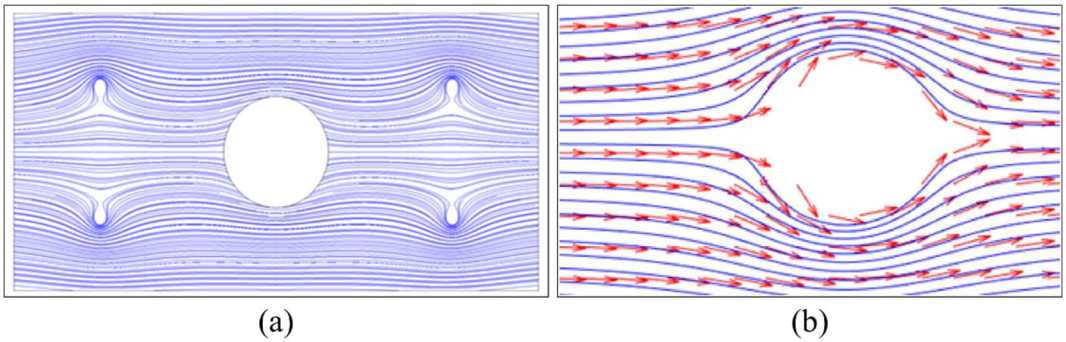

Figure 2-11 (a) Optimal result of the genetic algorithm based on perfect flow [42] and (b) trajectories taken from fluid flow around a cylinder [41]

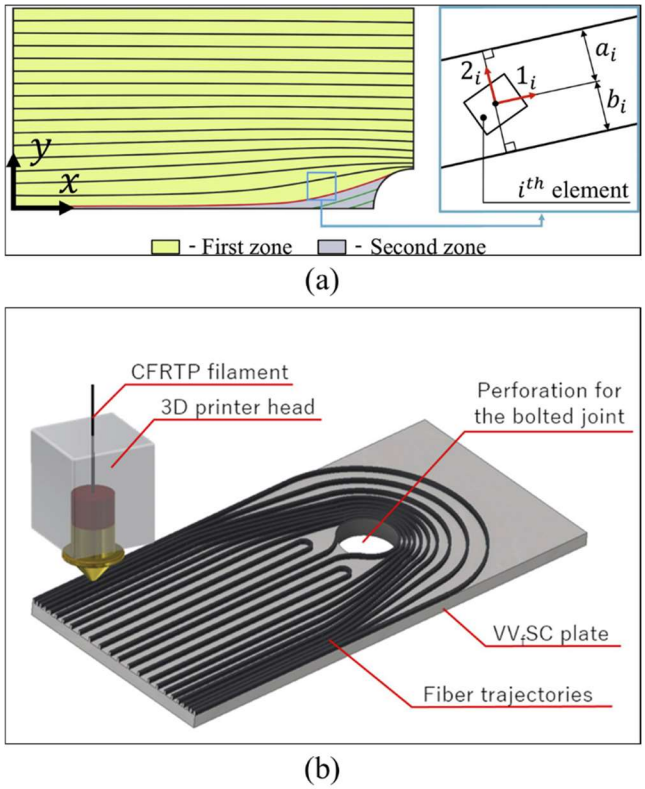

Figure 2-12 Stress trajectories for (a) open-hole tensile test [46] (b) bolt joint tensile test [44]

Furthermore, the topology optimisation can be integrated with the optimised fibre placement methods to achieve higher strength/stiffness-to-weight ratio [47], which further utilises the advantage of 3D printing for the manufacturing of highly complex geometries. For example, the continuous fibre angle optimisation (CFAO) method defined the elements with two variables, the density to determine the material existence and the angle for localised material orientation [48]. However, the local optimum usually occurred in this method. Thus, Discrete Material Optimisation (DMO) was adopted by using a set of discrete and manually given values for the orientation to address the local optimum issue [49]. Others methods were also developed, such as the load transmission path [50] and the adaptation of the tensor field design variables [51]. Although the average stiffness was increased (only compared with the pure/short-fibre-

reinforced composites in the experiment), the actual failure analysis of these topology-optimised composite structures with designed curved fibres has not been conducted. It is because of the difficulty to print customised fibre paths for such highly complex geometries, also the gaps and voids in the finished parts cause additional failures during the loading process. To manufacture such a complex geometry, short rather than continuous fibres were used as the reinforcement in the samples, as shown in Figure 2-13. For the printing of continuous fibre reinforced composites, the fibre paths had to be adjusted, also the delamination and discontinuous load-transfer occurred as shown in Figure 2-14 [52].

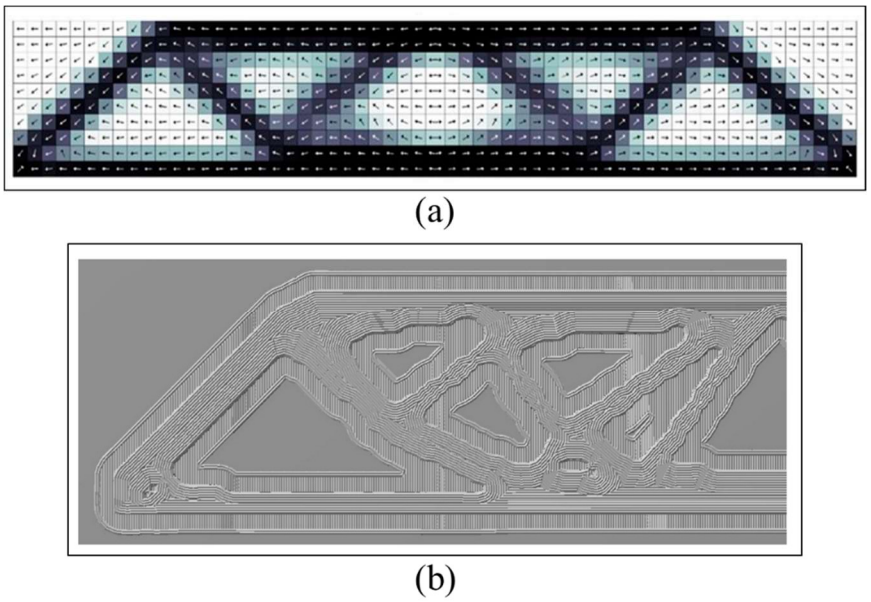

Figure 2-13 (a) CFAO density and fibre angle results for the MBB beam after 48 iterations (b) the printing experiment with short fibre reinforced composites [48]

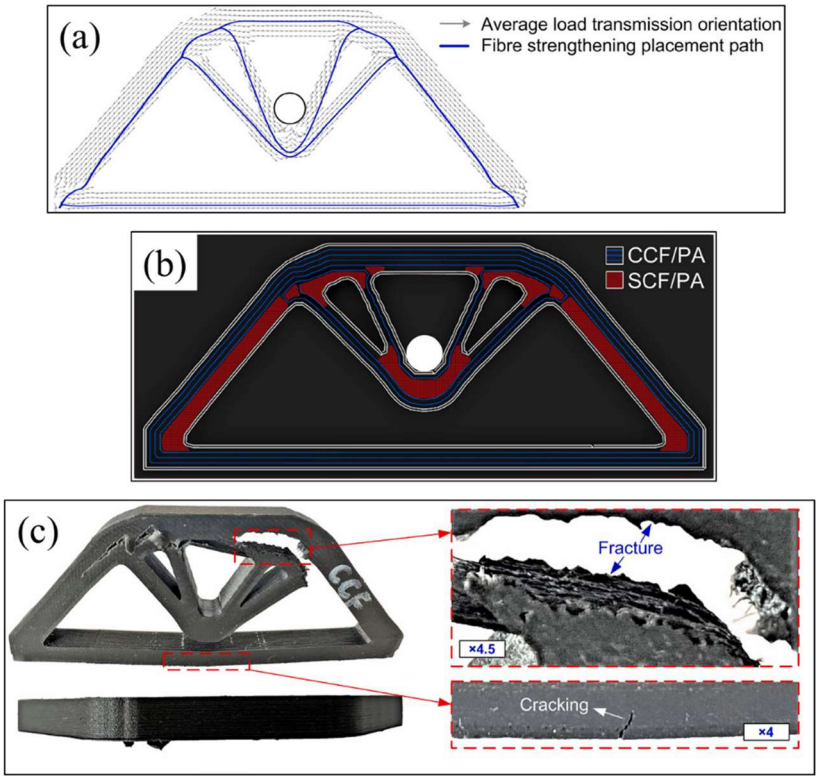

Figure 2-14 Topologically designed three-point-bending beam: (a) designed fibre paths (b) compromised materials placement in the printing experiment and (c) failure response with additional inter-laminar delamination [52]

2.4 Post-processing of 3D-printed composites

As mentioned above, the high porosity (about 3-10% depended on the printing parameters) of the 3D-printed cCFRP composites limits their use as the structural parts for load-carrying, compared with that of the traditionally-manufactured composites (low porosity < 1%). Thus, many studies were performed with the aims of void reduction, since 3D printing of continuous fibres was developed.

First of all, the *in situ* void reduction techniques were developed. Among them, a hot-compaction roller was equipped with a FFF-based 3D printer to press the filament against the printer bed immediately after the printing (Figure 2-15c) [53, 54]. Also the ultrasound-assisted

device (Figure 2-15a) and micro-screw extrusion process (Figure 2-15b) were utilised to obtain high pressure for good impregnation between fibre and matrix [55, 56]. Other researchers performed the 3D printing of continuous fibres in the low-pressure (1 Pa) processing conditions for the reduction in porosity [57]. Although the porosity was decreased to some extent, it could not be reduced to below 1% with the *in situ* techniques. For example, there was still a porosity of 5.7% for carbon fibre reinforcements under low-pressure printing [57]. Also, the compaction roller caused an irregular side surface due to the hatch spacing, and then increased voids in the vicinity of the side edges (with the porosity of 3%) [54]. Those processes for better impregnation between fibre and matrix could not eliminate the gaps between the print paths [53].

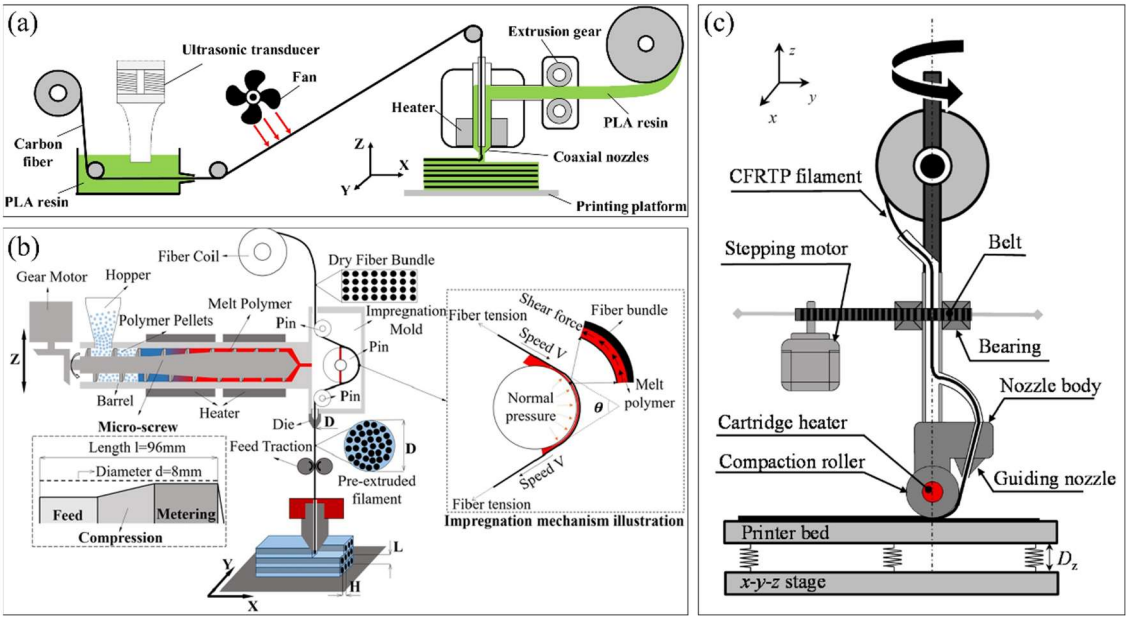

Figure 2-15 *In situ* technologies for void reduction in 3D printing of continuous carbon fibre: (a) ultrasound-assisted [55] (b) micro-screw extrusion process [56] and (c) equipped hot-compaction roller [53]

Therefore, post-processing treatment was adopted in some researches. As the most common one, hot-press treatment was widely used for strongest interface bonding by removing the air

gaps induced during printing between fibre and matrix. The influence of hot-press on the composites with mixed isotropic (unidirectional) fibre angles was investigated with varying temperature, pressure and time [58, 59], as shown in Figure 2-16a. It was found that the porosity decreases to approximately 0% with temperature up 250 °C. However, the working principle of the hot-press treatment is the softening (usually melting) of the matrix in 3D-printed composites under a relatively high temperature. Without the support of solid matrix, the misalignment of continuous curved fibres and even the failure of post-processing (as shown in Figure 2-16b) inevitably happened [60].

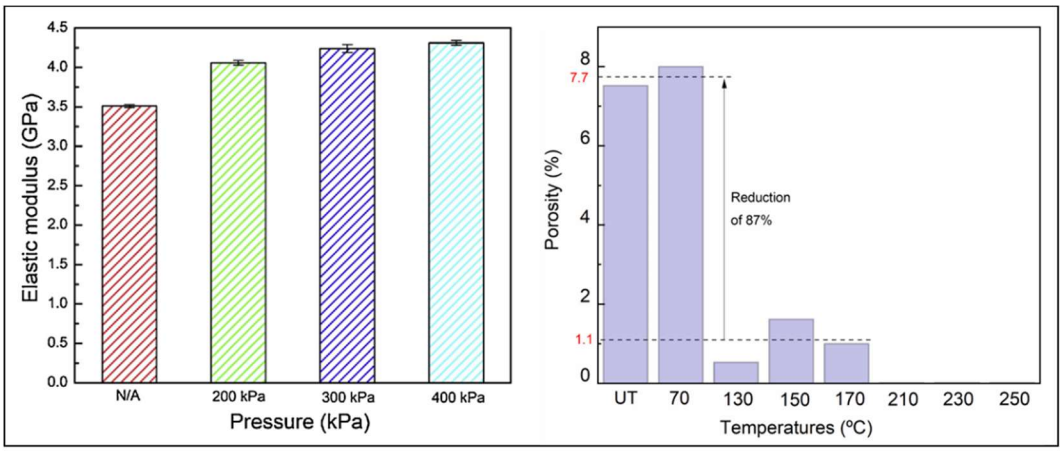

(a)

(b)

Figure 2-16 (a) Comparison of the elastic modulus and porosity with hot press and non-hot press [58] (b) Failure post-processing with fibre misalignment (Untreated sample also shown on the bottom) [60]

2.5 Modelling and failure analysis of 3D-printed curved fibre reinforced composites

As an anisotropic composite materials with reinforcement, the modelling and failure analysis of cCFRP composites are complicated. For the traditionally-manufactured composites, equivalent anisotropic properties are used based on the rule of mixture since continuous fibres are placed straight on each layer. However, when it comes to the modelling of 3D-printed composites with curved fibres, the equivalent properties and failure criteria cannot be directly adopted as usual. The localised fibre orientations and different mesoscale or microscale structures of the 3D-printed composites require a new modelling and failure analysis method.

In the recent research for the modelling, the constitutive model with different fibre contents was built based on 3D printing of continuous fibres, with the effect of void content also considered [61]. However, it only performed part of the modelling with unidirectional fibre placement in the 3D-printed samples [61], since the void content usually distributes unevenly in the composites with curved fibre paths. In order to simulate the localised fibre orientation, the coordinates of the material constitutive equation were rotated at the position with an angled fibre orientation (as shown in Figure 2-17), in which the consistent equivalent properties based on rule of mixture were used [62]. Furthermore, other researches simulated the fibre volume fraction and fibre orientation separately and then these two values were mapped onto the centroid of each element [63, 64]. However, in the real printing experiment, the printing paths of continuous fibres and pure thermoplastic are separate rather than being well mixed. Thus, the above equivalent and simplified methods could only partially simulate the performance of structures on a homogenised macroscale. The information at the meso-/micro-scale would be inevitably ignored, such as the failure as well as stress concentration in the matrix-rich areas

between the fibre paths. Also, the re-distribution of the stresses/strains in the whole domain (because of the curved fibre placement) would be missed.

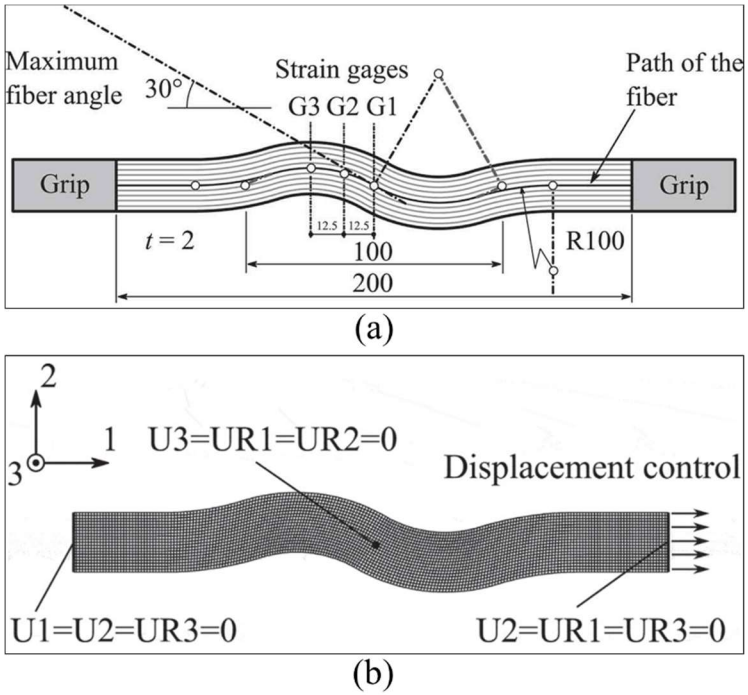

Figure 2-17 (a) A 3D-printed curvilinear specimen (b) the finite element model as the S-shaped one in the experiment [62]

For the 3D-printed composites with geometric singularities and curved fibre placement, only a few studies were conducted on the failure analysis due to the difficulty extract the customised fibre paths from the printing experiments. Most of the researchers had to rely on the commercial Markforged® printing system (with the Eiger software for fibre placement) to perform the slicing and path planning [65]. Due to the limited placement method (usually concentric) in Eiger software (as shown in Figure 2-18), the design flexibility was significantly constrained [66] and it is almost unlikely to achieve customised fibre paths [52]. Additionally, the high porosity in the samples printed by Markforged® system becomes another uncertainty when assessing the fibre placement, e.g. the sample may still fail at an early loading stage due to the large porosity even the fibre paths are customised and optimised. Therefore, the modelling

based on the real paths and the failure analysis for the low-porosity printed composites with customised fibre paths are required in order to better understand the FFF 3D printing of continuous curved fibre reinforced polymer composites.

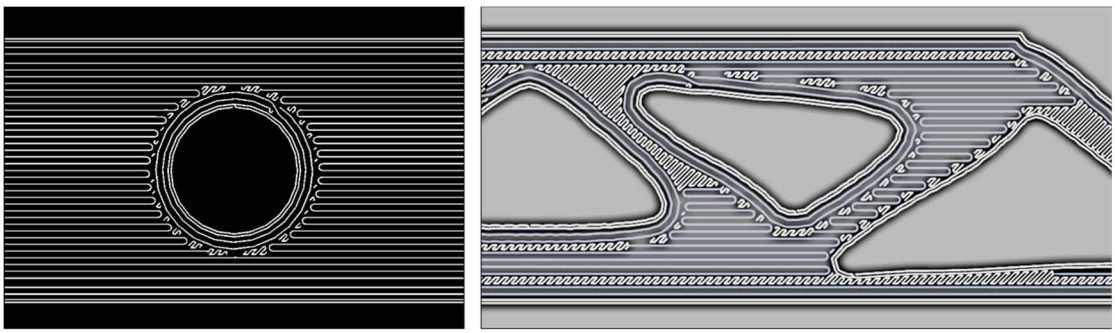

Figure 2-18 Limited fibre placement options for (a) open-hole tension (b) topology-optimised geometry in Markforged® Eiger software: concentric placement for geometric singularities with unidirectional fibres in other areas

2.6 Summary of literature review

The overall literature review presents the background and the state-of-the-art research for the FFF 3D printing of composite materials, especially for those with continuous carbon fibre reinforcement. It is found that the printing mechanism, the curved fibre placement method and the manufacturing technique for both low porosity and customised fibre paths need to be investigated or developed. Also, more studies about the modelling and failure analysis of 3D-printed cCFRP composites should be performed. Main knowledge gaps are summarised as below:

(1) The material extrusion AM technologies (FDM/FFF) are suitable for the 3D printing of composites with continuous fibre reinforcement. However, the void content in the

composites limited the structural application of the finished parts and the introduced short or continuous fibre reinforcement further leads to a higher porosity.

(2) The mechanism of the printing process of continuous fibre filaments has not been fully understood, especially for manufacturing-induced defects when printing with curvature and shape corner, such as misalignment, folding and fibre breakage.

(3) The *in situ* techniques for void reduction could not achieve a porosity lower than 1%. The common hot-press treatment had to melt the matrix of fibre filaments therefore inevitably caused the misalignment of fibre paths during the post-processing. Thus, the manufacturing technique needs to be improved for achieving low porosity and maintaining of the customised fibre alignment.

(4) AM technology offers the opportunity to customise the continuous curved fibre paths during printing, therefore the fibre placement methods for the cCFRP composites with complex geometries are in demand. Further optimisation for both topology and fibre orientation should be performed to achieve the high stiffness-to-weight ratio of 3D-printed composites structures.

(5) Only a few modelling and failure analysis were performed for the 3D-printed composites with continuous curved fibres in the previous studies. The effectiveness of different fibre placements and the mechanical response of 3D-printed composite structure have not been fully investigated, which should be further studied both numerically and experimentally.

Since the following six chapters are published or submitted as journal papers, more detailed background and literature review related to the individual topic will be presented at the beginning of these six chapters. Therefore, chapter 2 only provides a summarised review of related researches as well as the background for the whole project, and some reduplicated

references are inevitable between the chapter of literature review and the individual introduction of the papers.

Chapter 3 Performance-driven 3D printing of continuous curved carbon fibre reinforced polymer composites: A preliminary numerical study [*]

Abstract

This chapter presents a new concept to place continuous curved fibres for CFRP composites, which can be fulfilled by potential additive or hybrid manufacturing technology. Based on the loading condition, principal stress trajectories are generated through finite element analysis (FEA) and used as the guidance of the placement paths for carbon fibres. Three numerical cases, an open-hole single ply lamina under uniaxial tension and an open-hole cross-ply laminate under biaxial tension and normal pressure, are studied and compared with traditional reinforced composites with unidirectional fibres. The modelling results show that the stress concentration in both fibre and matrix are reduced significantly by the curved fibre placement and the stiffness of CFRP composites have been improved. This concept of performance-driven optimisation method could lead to a useful tool for the design of future 3D printing process for fibre reinforced composites.

Keywords

Continuous curved fibre; Performance-driven manufacturing; 3D printing; Finite element analysis (FEA)

3.1 Introduction

Carbon fibre reinforced polymer (CFRP) composites are widely used in aerospace, automobile

[*] This chapter was published in Composites Part B in June 2018.

and infrastructure industry because of its high strength and high stiffness-to-weight ratio. In the 1960s, the Automated Fibre Placement (AFP) technology was developed for the manufacturing of large structures by placing multiple layers of composite lamina to form a laminate. Input materials for the placement process are mainly unidirectional fibres, which are pre-impregnated (Prepreg) with the matrix material [67]. Compared with AFP, 3D printing (also known as additive manufacturing) is a process that enables the efficient manufacturing of parts with complex shapes. Instead of using Prepreg as in AFP, 3D printing uses filament or bundle of fibres and produces small size of printing beads to form a part [1] without the need of moulds. Thus, it is able to manufacture composites at low labour and production costs with an immense range of complexities [68].

Recently, a few new 3D printing technologies for CFRP composites have been developed. Among them, fused deposition modelling (FDM®) [69] developed by Stratasys Ltd. is able to print continuous aligned carbon fibres as shown in Figure 3-1 [29]. The mechanical performance of these composites under different loading condition have been evaluated [17, 20, 26, 30, 70-72]. On the other hand, new design principles and methods in printing progress are being developed, such as hot-press treatment to reduce porosity and improve the strength and stiffness of the printed composites [5, 28, 59, 73, 74].

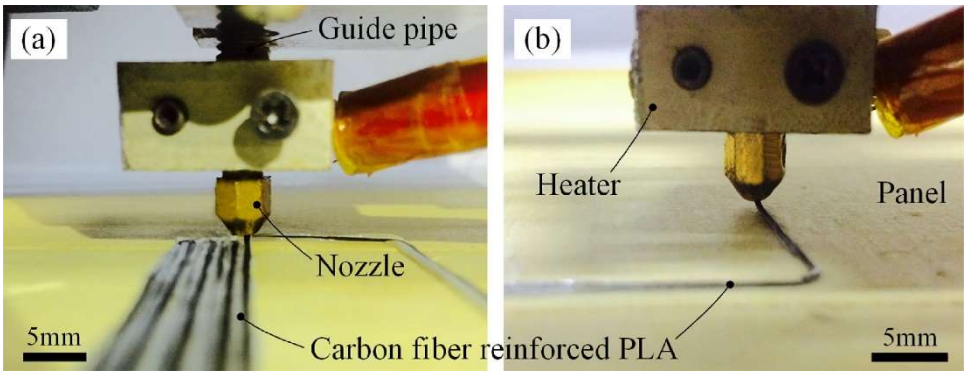

Figure 3-1 3D printing process of the continuous carbon fibre reinforced composite. (a) Printing the straight area of composite sample (b) Printing the corner of composite sample.

For composite laminate, the stacking sequence of each ply with different angles must be optimised to achieve the designed stiffness on each direction [37, 38, 75-77]. However, the fibres are placed straight in each ply of the laminate and drilling machines are used to manufacture the notched composite specimens in the traditional manufacturing process [78-81]. Thus, the outstanding properties of fibres may be underutilized and most of fibres near the hole are cut off, which provokes severe stress concentration and reduces stiffness and strength of constructions with geometric discontinuities.

The new additive manufacturing technology offers the opportunity to change the orientation of fibres during the manufacturing process, therefore, an optimisation method of continuous fibre placement is required for the 3D-printed CFRP composites. To fully utilize the properties of fibre, a few algorithms have been developed to adjust the placement of fibres [40, 42]. These methods usually require multiple variables and some assumptions, which complicates the process of optimisation. In addition, the orientation of CFRP material has to be optimised in each element when carrying out finite element analysis, without considering whether the real manufacturing process is possible to achieve it or not [40, 46, 82]. It also brings discrete fibre angles in the mesh and large discrepancy of fibre angles between the adjacent elements. Also, the stress distribution is inaccurate since CFRP lamina is treated as an equivalent homogeneous material in these numerical simulation [42].

To maximise the potential of 3D printing for lightweight CFRP composite structure, a feasible method for continuous fibre placement is essentially required. For composites, material with excellent tensile property and slender shape is usually placed along principal stress trajectories to improve the mechanical performance, such as steel bars in the concrete. Also, some researchers tried to make cellular materials with cell walls that align with the stress trajectories in order to improve load distribution [83]. In this chapter, we present a new concept of printing

long carbon fibre along the trajectories of maximum or middle principal stress. Finite element analysis of specimens with only matrix material is first used to generate the trajectories of principal stress. We carry out numerical studies on three cases including single ply lamina under uniaxial tension and cross-ply laminates under biaxial tension and normal pressure, where fibres and matrix are defined as different isotropic materials. The change of stress distribution and stiffness of models are discussed and compared to traditional composite lamina or laminate.

3.2 Methodology

Since the tensile properties of carbon fibres are superior in the fibre direction, we aim to place fibres along the direction of maximum tensile stresses. In other words, the optimised path of fibres should align with stress trajectories which are lines whose direction at each point gives the orientation of the maximum or middle principal stress. For the optimisation problem, we first simulate the specimen printed using only matrix material under uniaxial tension. With the data of in-plane stresses of each node from finite element analysis, we calculate the orientations and values of maximum principal stresses by Eqs. 1-2.

$$\tan\varphi = -\frac{\sigma_x-\sigma_y}{2\tau_{xy}} \pm \sqrt{1+\left(\frac{\sigma_x-\sigma_y}{2\tau_{xy}}\right)^2} \tag{1}$$

$$\sigma_1/\sigma_2 = \frac{\sigma_x+\sigma_y}{2} \pm \sqrt{\left(\frac{\sigma_x-\sigma_y}{2}\right)^2+{\tau_{xy}}^2} \tag{2}$$

where σ_x is stress in x-axis direction, σ_y is stress in y-axis direction, τ_{xy} is shearing stress, φ is the angle between the stress normal to the stress trajectories at a point and the x-axis, σ_1 is the value of maximum principal stress, σ_2 is the value of middle principal stress (Two values of angle φ are calculated for maximum and middle principal stress). Then the coordinates and angles for maximum/middle principal stress of each node are imported into Tecplot 360 software. Stress trajectories as streamlines are created by entering start position, gap and

number of streamlines. We can also change the number of the streamlines in a ply in order to obtain models with different volume fraction of fibres. For case studies in this chapter, these streamlines are extracted and imported into a FEM software (ABAQUS) with a specific width as a part, therefore, optimised models with curved fibres can be studied.

As shown in Figure 3-2, Case One focuses on modelling an open-hole single ply lamina, where its length is 100 mm and its width is 50 mm. The radius of the hole is 20 mm and the thickness of the plate is 1mm. The tensile stress of 400 MPa is applied to the right side of the plate. The left side of the plate has a constrained degree of freedom in horizontal displacement along the x-axis. The stress distribution is obtained by FEA with 5748 quadrilateral element and 5844 nodes. Mechanical properties of carbon fibres and matrix used in present study are listed in Table 3-1. As shown in Figure 3-3, eight maximum principal stress trajectories are generated for the printing path of fibres ($V_f = 3.4\%$, all the V_f mentioned in this chapter are the average values of the included fibre, since the fibre fraction of 3D-printed composites with continuous fibre reinforcement is no longer constant in different local areas).

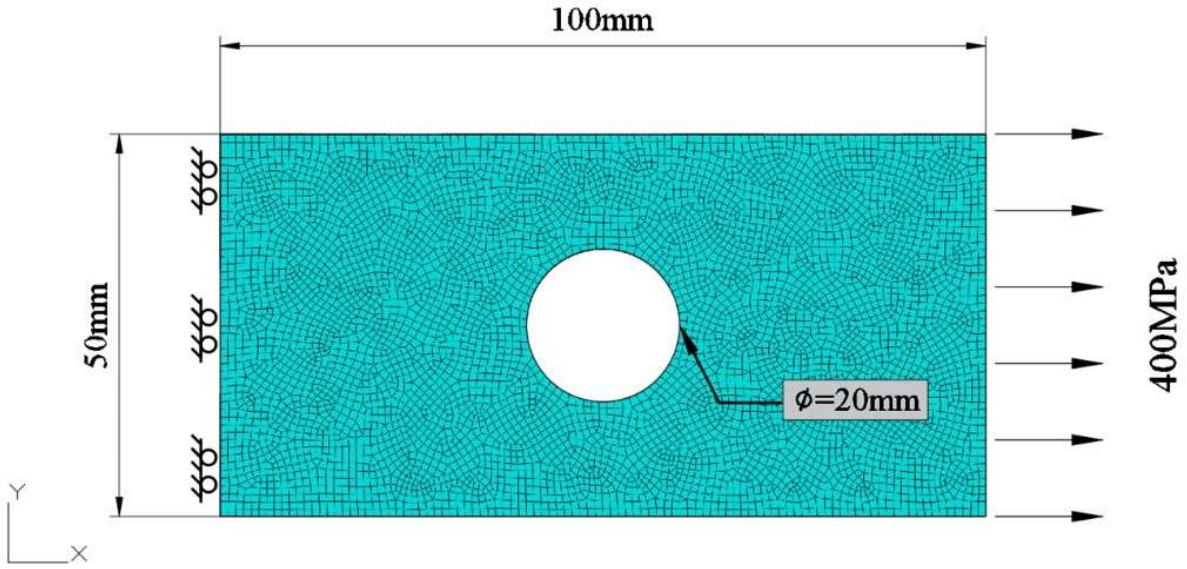

Figure 3-2 Configuration of the CFRP plate with a hole under uniaxial tension (Case One).

Table 3-1 Mechanical properties of carbon fibres and epoxy [84].

Material	Modulus of elasticity	Poisson's ratio
IM7 Carbon fibres	276 GPa	0.28
Hexcel HexPly 8552 Epoxy matrix	4.76 GPa	0.37

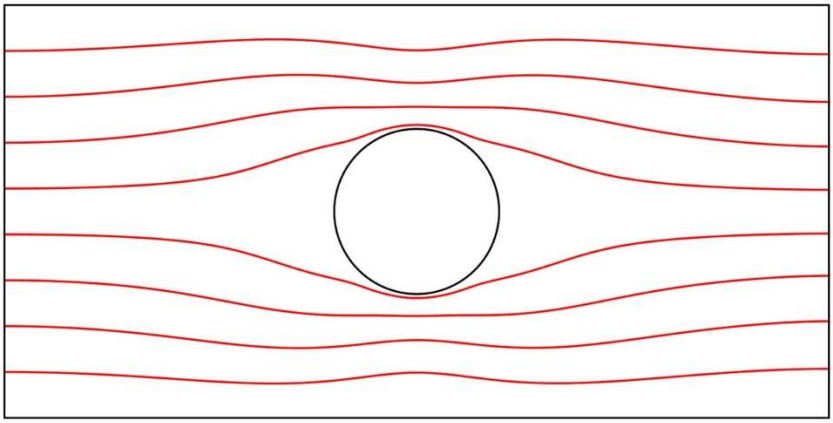

Figure 3-3 Generated maximum principal stress trajectories (red lines) at $V_f = 3.4\%$.

In this optimisation method, fibres are simulated as a bundle with the width of 0.2 mm (The print resolution of present commercial 3D printers can be 100 microns, such as Mark Two Printer supplied by MarkForged®, Somerville, MA) along the generated stress trajectories as shown in Figure 3-4. In this specific case, an equivalent volume fraction of fibres V_f between 1.7% and 27.2% without any overlap of fibres can be achieved. For the conventional optimised composites, fibres are placed the along x-axis direction straightly as shown in Figure 3-5.

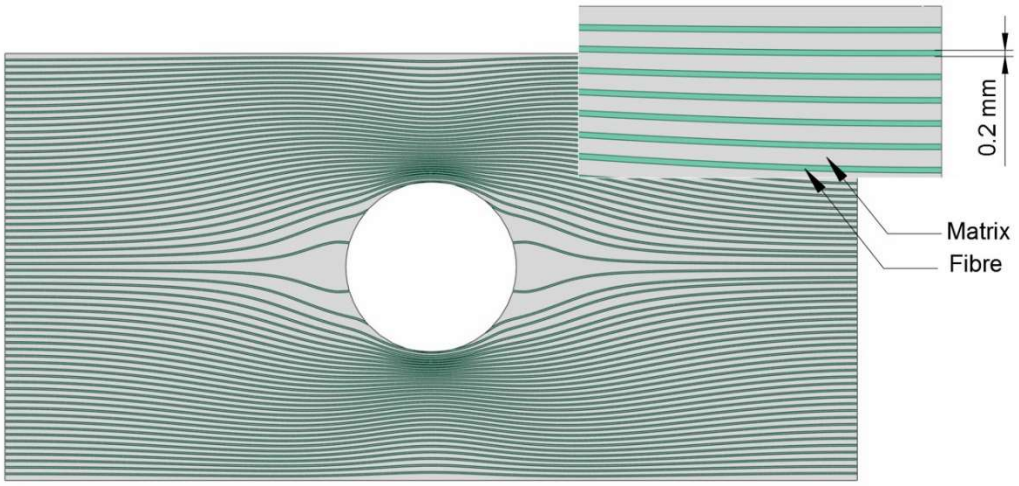

Figure 3-4 Optimised CFRP plate with an equivalent volume fraction of fibres $V_f = 27.2\%$.

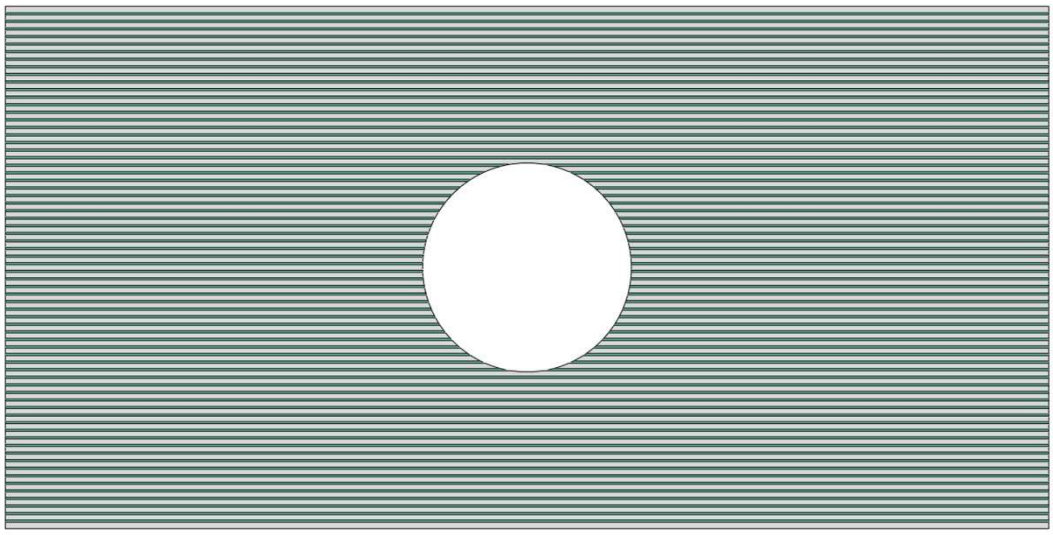

Figure 3-5 FEM model of a conventionally optimised CFRP plate with an equivalent volume fraction of fibre $V_f = 27.2\%$.

3.3 Numerical case studies

Three cases are investigated in this chapter. Besides Case One shown above, Case two is an open-hole laminate under biaxial tension with the same length, width and radius of the hole.

As shown in Figure 3-6(a), the tensile stress of 400 MPa is applied to the right and bottom sides of the laminate. The left side of the laminate has a constrained degree of freedom in horizontal displacement along the x-axis while top side has a constrained degree of freedom in vertical displacement along the y-axis. The optimised model consists of 4 piles and the thickness of each layer is 0.2 mm. The biaxial tension is considered as the combination of two perpendicular uniaxial tension. We optimize the fibre alignment in each ply, therefore, the stress trajectories in each layer can be obtained from the simulation under uniaxial tension as shown in Figure 3-6(b) and Figure 3-6(c). With the same stacking sequence and thickness, conventionally optimised CFRP plate with a hole consists of 4 plies where fibres are placed along 0 and 90 degrees symmetrically, i.e. (0/90)s.

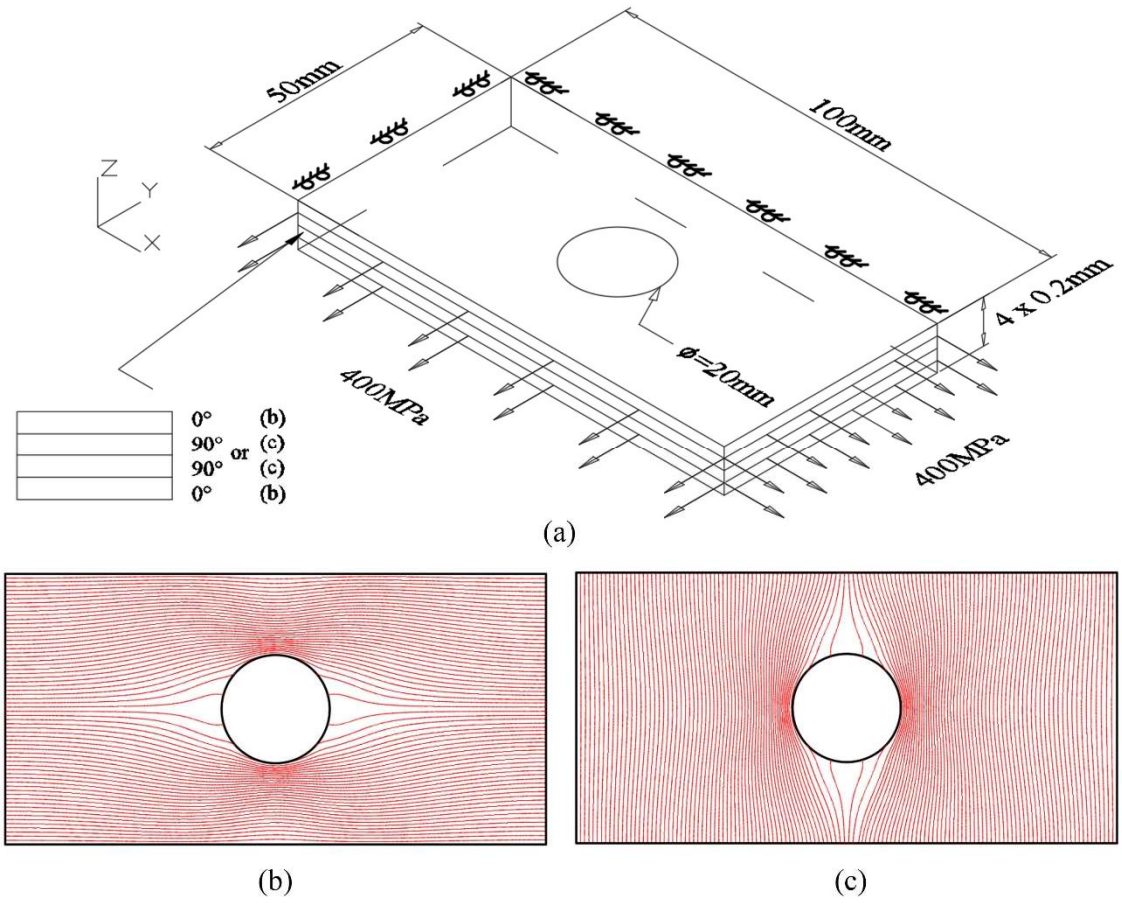

Figure 3-6 Optimised CFEP plate under biaxial tensile loading (Case Two, $V_f = 27.2\%$): (a)

Configuration and stacking sequence (b) Stress trajectories generated under uniaxial tension along x-axis direction (c) Stress trajectories generated under uniaxial tension along y-axis direction

Case Three is an open-hole laminate under normal pressure. The size of laminate as well as the number and thickness of plies are the same as in Case Two. As shown in Figure 3-7(a), the normal pressure of 400 MPa is applied to the top face of laminate and its four sides are fixed. For optimised fibres placement in plies, two kinds of optimisation paths are applied, where fibres are placed along maximum and middle principal stress trajectories as shown in Figure 3-7(b) and Figure 3-7(c). The stacking sequence is shown in Figure 3-8, where plies are set symmetrically, i.e. (Maximum/Middle)s. In order to compare the improvement of mechanical performance, two different traditionally optimised models with unidirectional fibres are simulated, i.e. (-45°/45°)s and (90°/0°)s. Because of the symmetrical geometry, material and boundary conditions of Case Three, we only simulate a quarter of the plate in the following numerical study for this case.

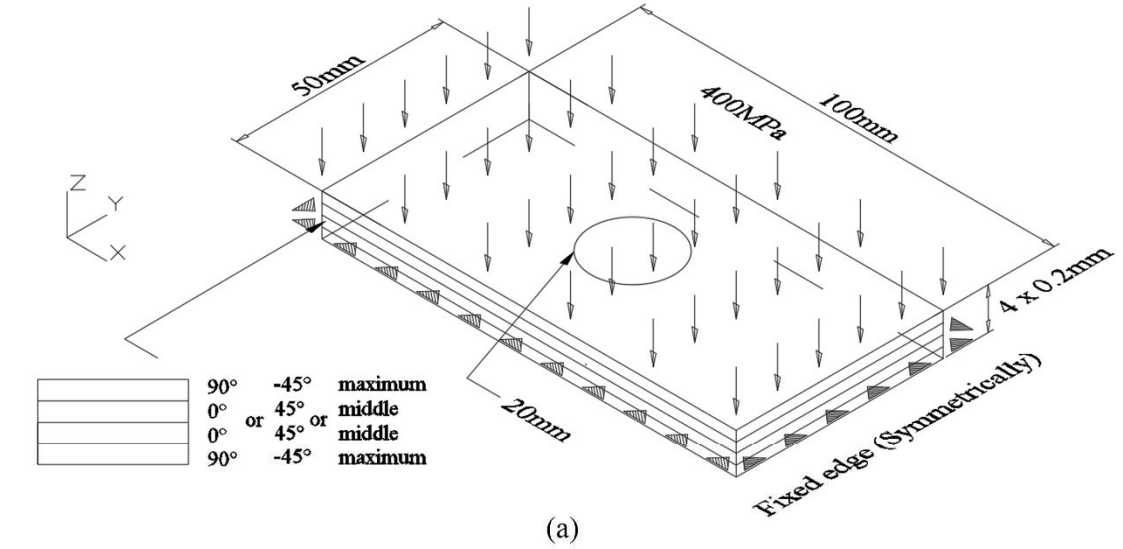

(a)

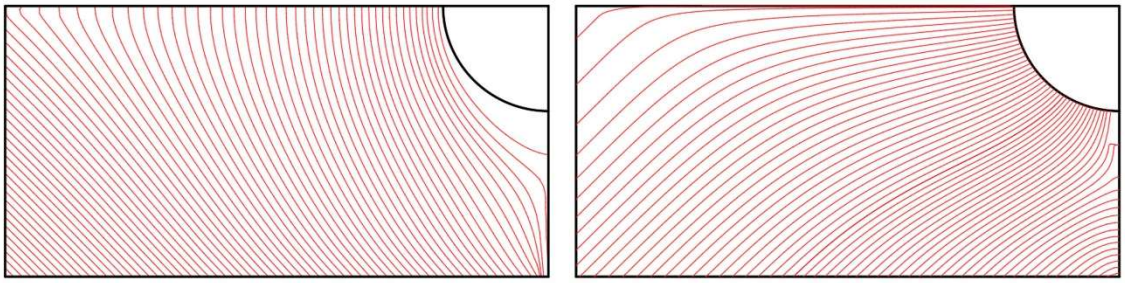

(b) (c)

Figure 3-7 Optimised CFEP plate under normal pressure (Case Three, V_f =27.1%): (a) Configuration and stacking sequence (b) Maximum principal stress trajectories (c) Middle principal stress trajectories

3.4 Results and discussion

FEM models for all above mentioned cases were developed and numerical results were compared with those from models of composites with unidirectional fibre placements.

With Eqs. 3-5, the maximum von Mises stress in the regions of fibre and matrix, respectively, the stiffness and the maximum stress concentration factor are calculated.

$$\sigma_s = \sqrt{\frac{(\sigma_1-\sigma_2)^2+(\sigma_2-\sigma_3)^2+(\sigma_1-\sigma_3)^2}{2}} \quad (3)$$

$$K_{tmax} = \frac{\sigma_{s-m}}{\sigma_0} \quad (4)$$

$$k = \frac{P}{\delta_{max}} \quad (5)$$

where σ_1 is the value of maximum principal stress, σ_2 is the value of median principal stress, σ_3 is the value of minimum principal stress, σ_s is the von Mises stress, σ_{s-max} is the maximum von Mises stress, σ_0 is the nominal stress, K_{tmax} is the maximum stress concentration factor, P is the resultant force of the edge, δ_{max} is the maximum displacement, and k is the stiffness of the composites. We discuss the stiffness of all these models and the maximum stress concentration factor in fibre and matrix of the first two series of models, since CFRP lamina is treated as an equivalent homogeneous material in FEA and the distribution of stress is not comparable with the first two heterogeneous models.

To evaluate whether stresses distribute evenly adjacent to the hole or not, the average values of Von Mises stress in the matrix within 2mm of the edge of the hole are calculated and plotted. As shown in Figure 3-8(d), the values are represented by the distance between the points in the curve and the origin of the coordinate plane. Therefore, if the curve is similar to a circle with a small radius, stresses are small and also distribute evenly adjacent to the hole in this specific model.

For Case One, results from models without any overlap of fibres are represented by solid lines (the volume fraction of fibre between 1.7% and 27.2%) as shown in Figure 3-8. The maximum stress concentration factor and stiffness have little differences between new and traditional optimisation method with the volume fraction of fibre 1.7%. As the fibre volume fraction increases, models with curved fibre show increasingly better performance. With the fibre volume fraction 27.2% (which is highest fibre volume fraction without any overlap of fibres), the maximum stress concentration factors in both fibre and matrix reduce by almost 60% (60.3% and 59.8%, respectively). The stiffness in x-axis direction of the plate with curved fibres

increases by 39.7% in comparison with the traditionally optimised models with unidirectional fibres. In terms of comparison between models with unidirectional fibres and model using lamina material, the stiffness of composites has a marginal error of 6.9%, which is acceptable and also indicates that the method modelling fibre and matrix separately is applicable.

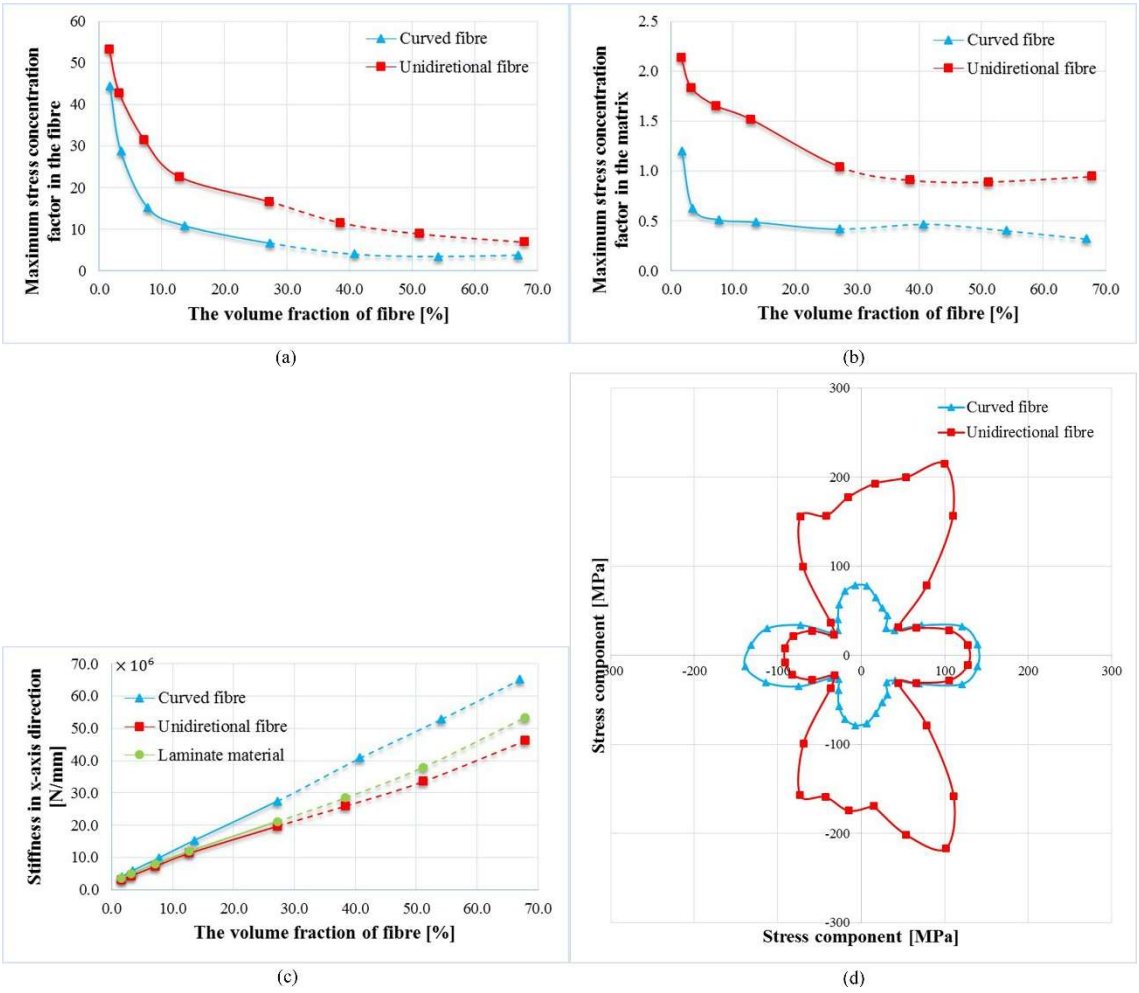

Figure 3-8 Comparisons of mechanical performance in Case One: (a) maximum stress concentration factor in the fibre (b) maximum stress concentration factor in the matrix (c) stiffness in x-axis direction (d) Von Mises stress distribution in the matrix at the circumference of hole ($V_f = 27.2\%$)

Considering the improvement of printing technology in the future, we also simulate new optimised models with higher volume fraction of fibre, where the widths of carbon fibre

bundles are 0.3, 0.4 and 0.5 mm and the number of carbon fibre bundle is the same as in the model with a fibre volume fraction of 27.2%. Fibres are assumed to be printed without matrix material in the area near to the hole and the results are plotted out by dotted lines, as shown in Figure 3-8. The maximum stress concentration factor in the fibres decreases continuously and factor in the matrix fluctuates slightly when the volume fraction of fibre increases from 27.2% to 67.9%. Also, the stiffness increases continuously. In terms of the comparison between models with curved and unidirectional fibres, new optimised models with fraction between 30% and 40% present better performance. Except for slightly fluctuating concentration factor in the matrix, factor in the fibre reduces by 60% and stiffness of composites increases by 57% approximately.

In Table 3-2, the distribution field of Mises stress for Case One with the fibre volume fraction 27.2% are shown. For models with unidirectional fibres, the maximum Mises stresses, no matter in the fibres or matrix, concentrate in a very small area near to the top and bottom edge of the hole. It can also be observed that the Mises stresses are distributed more evenly in the models with curved fibres. The maximum stresses in the fibre distribute on a larger area adjacent to the hole, because of that, the maximum Mises stresses in the matrix do not concentrate on the top and bottom edge of the hole. As shown in Figure 3-8(d), in the region adjacent to the hole, although the stresses reduce significantly, they do not distribute evenly since only carbon fibres in x-axis direction are optimised in this case with single ply.

Table 3-2 Von Mises stress distribution in Case One with a fibre volume fraction 27.2%

	The whole plate	Region of matrix
Curved fibre	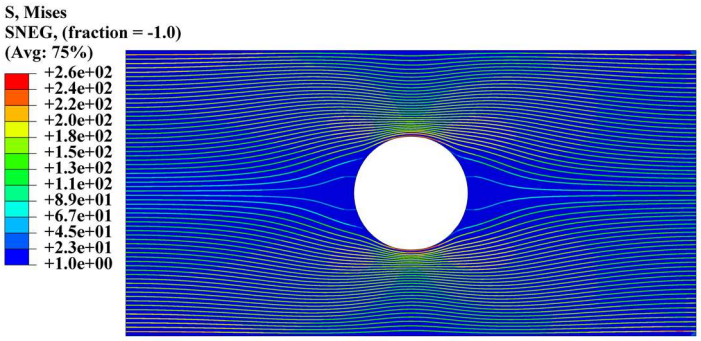	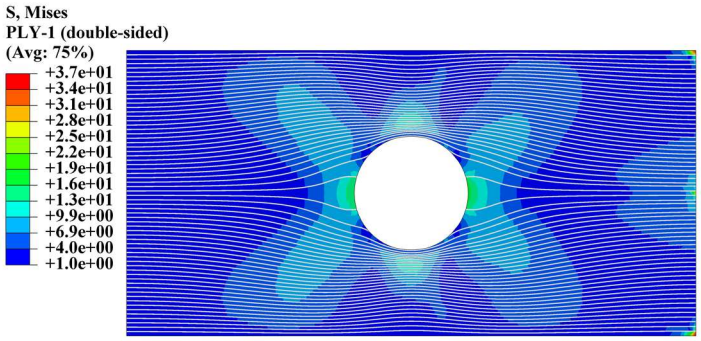
Unidirectional fibre	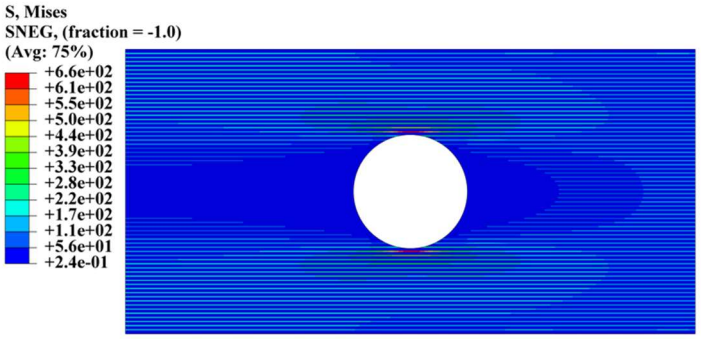	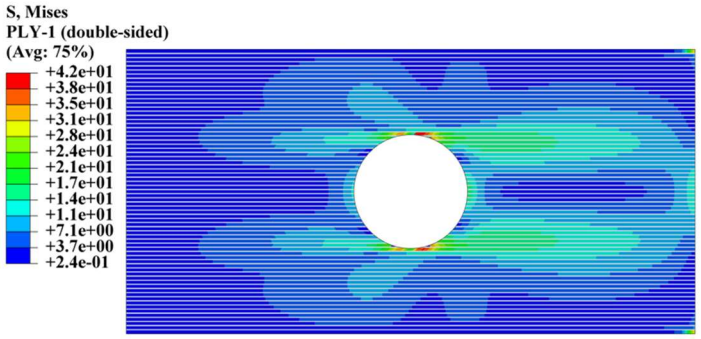

For Case Two, as shown in Figure 3-9, models with fibre volume fractions from 6.4% to 27.2% are simulated, which is a representative fraction range according to the result from Case One. Compared with traditional optimisation method, models with curved fibres show better mechanical performance as the fraction increases. For the model with fraction 27.2%, the maximum stress concentration factor in the fibre and matrix reduces by 33.0% and 62.5%, respectively. Since Case Two is an open-hole laminate under biaxial tension, the stiffness of the composites in both x-axis and y-axis direction is analysed, which increases by 24.6% and 49.3%.

Distribution field of Mises stress for Case Two is shown in Table 3-3. We consider two different types of fibre placement in a ply, x-axis direction layer and y-direction layer, which are compared with 0° and 90° plies in the traditional optimisation method with unidirectional fibres. As can be seen in the comparison of stress distribution for the whole plate, the maximum stresses in the fibre distribute in a larger area around the hole and also have a smaller value. For the region of matrix, the Mises stresses distribute quite evenly and stress concentration is not obvious in the model with curved fibres while the Mises stress much concentrate near to the hole in the model with unidirectional fibres. Similarly, as shown in Figure 3-9(e) and Figure 3-9(f), Von Mises stresses with smaller values distribute evenly in the region adjacent to the hole, which proves that the new optimisation method can reduce the stress concentration significantly in this case.

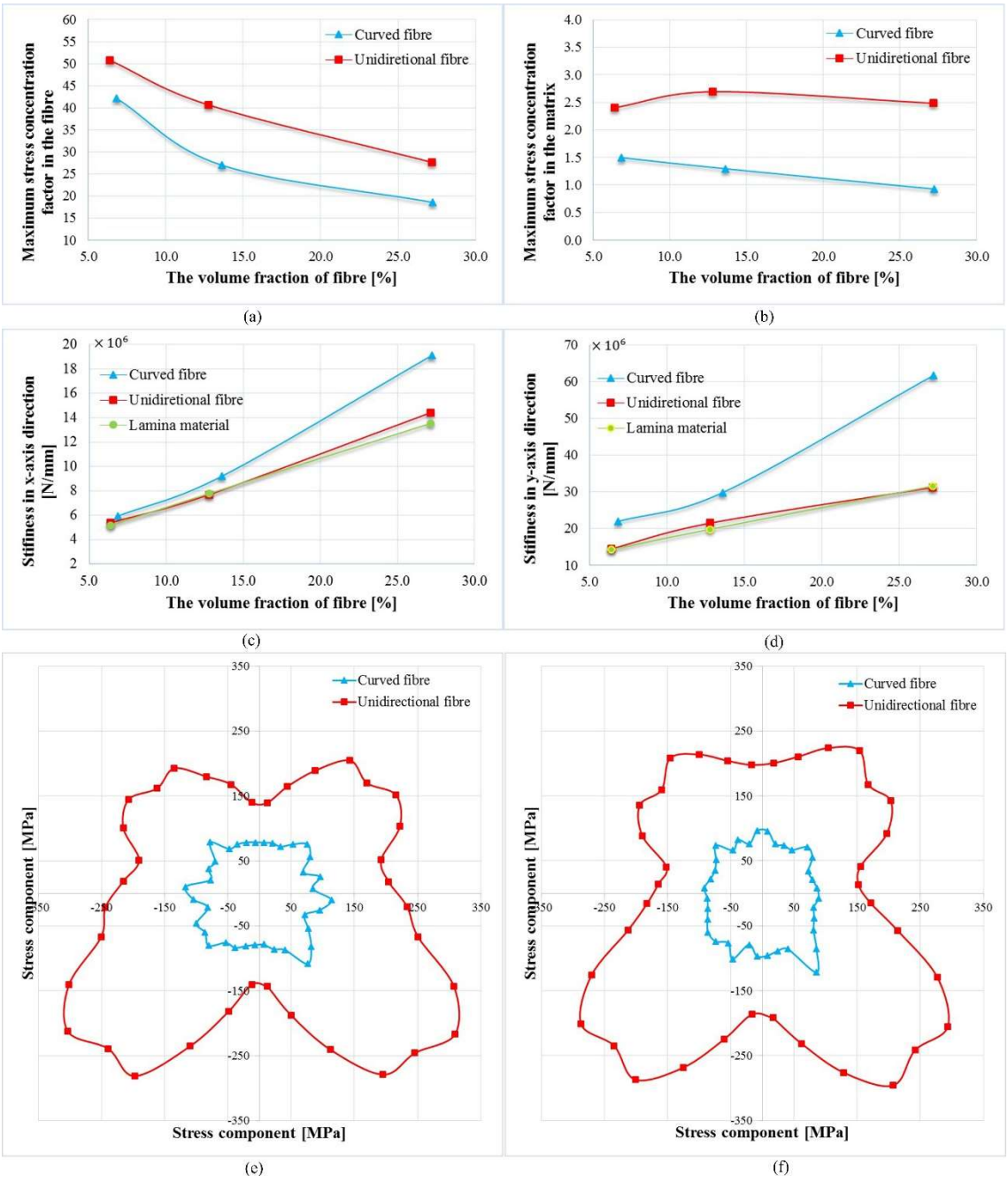

Figure 3-9 Comparisons of mechanical performance in Case Two: (a) maximum stress concentration factor in the fibre (b) maximum stress concentration factor in the matrix (c) stiffness in x-axis direction (d) stiffness in y-axis direction (e) Von Mises stress distribution at the circumference of hole in x-axis direction ($V_f = 27.2\%$) (f) Von Mises stress distribution at the circumference of hole in y-axis direction ($V_f = 27.2\%$)

Table 3-3 Von Mises stress distribution in Case Two with a fibre volume fraction 27.2%

		The whole plate	**Region of matrix**
X-axis direction ply	Curved fibre	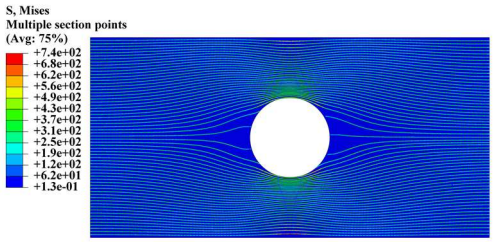	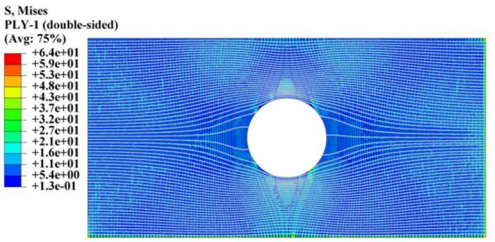
	Unidirectional fibre	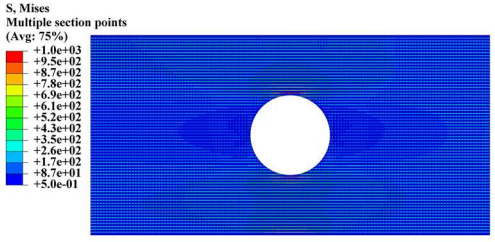	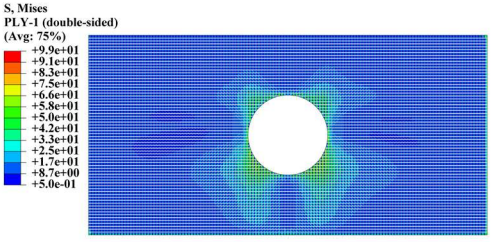
Y-axis direction ply	Curved fibre	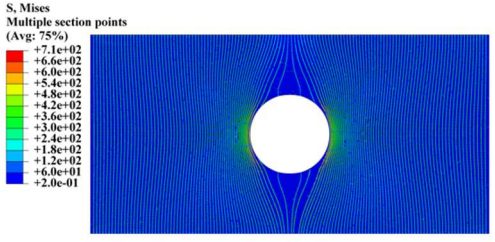	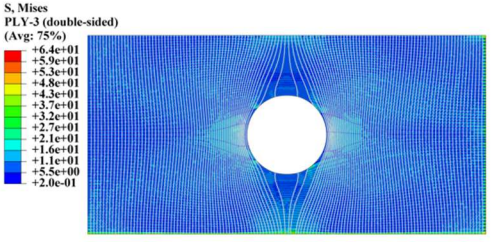
	Unidirectional fibre	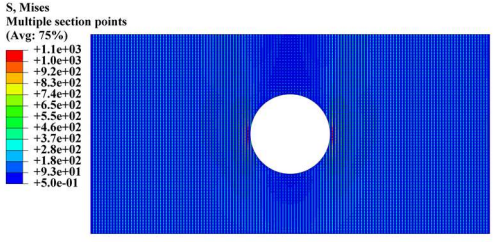	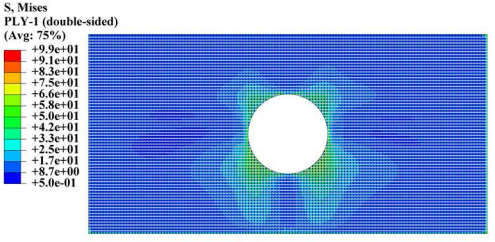

For Case Three, as shown in Figure 3-10, models with stacking sequence (-45°/45°)s show better performance than models with stacking sequence (90°/0°)s both in maximum stress factor and stiffness. Therefore, we compare models with optimised curved fibres with the unidirectional models with fibre volume fraction from 16% to 36%. As in Case One and Two, the effect of optimisation gradually diminishes when the overlap of fibres appears. Mechanical performances are improved significantly with a fibre volume fraction around 27.1%. The maximum stress concentration factor reduces by 28.9% and 36.1% in the fibre and matrix. Also, the stiffness in z-axis direction increases by 32.4%.

As shown in Table 3-4, Von Mises stresses in the optimised model are well-distributed both in the fibre and matrix compared with the other two models. In the fibre, stresses with maximum values are distributed in a wider region that is no longer near the hole. For the matrix, as shown in Figure 3-10(d) and Figure 3-10(e), the curves of Von Mises stress adjacent to the hole are more similar to a circle and the values are reduced significantly, which shows the new optimisation method has a great impact on the improvement of mechanical performance of laminate under normal pressure.

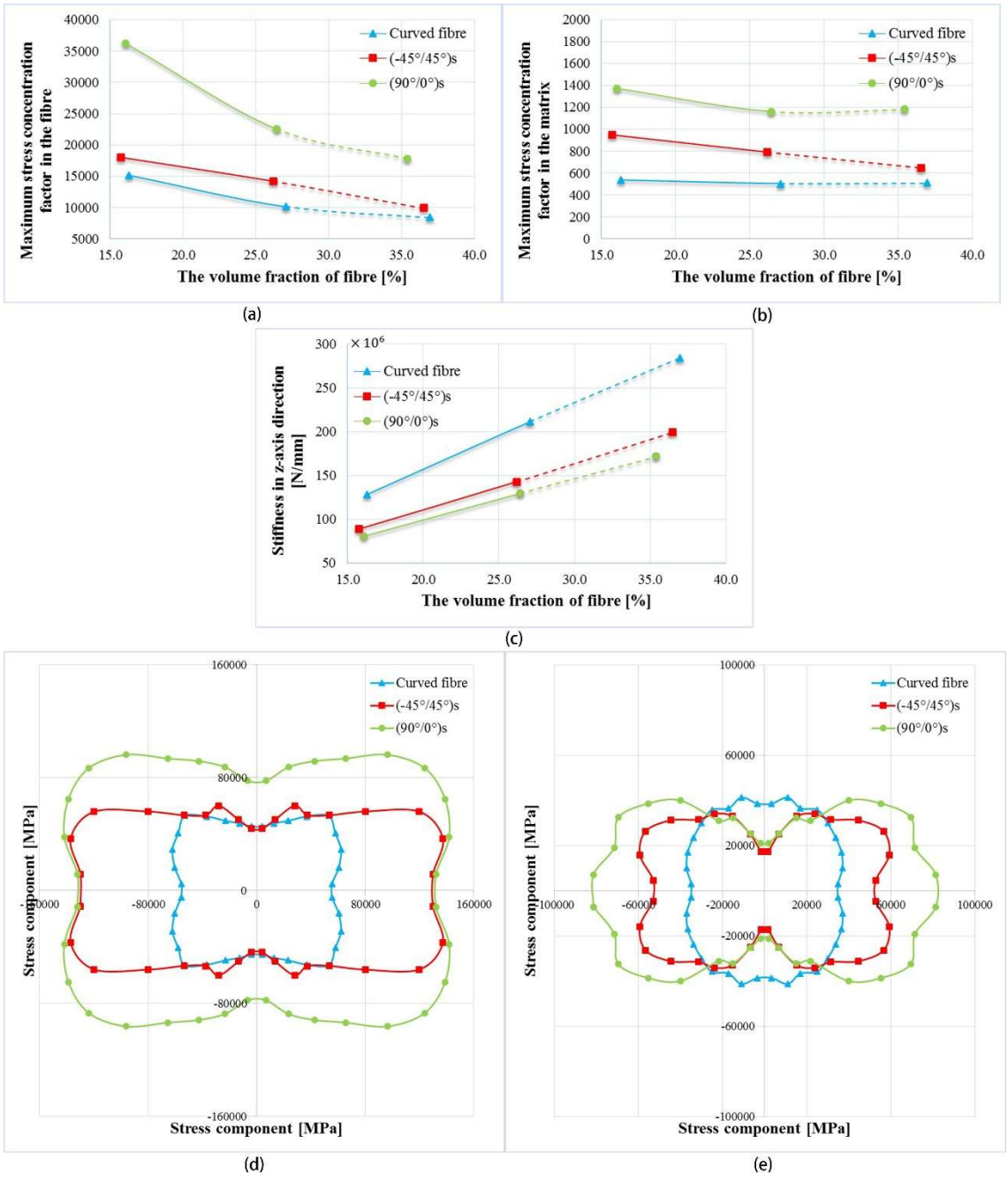

Figure 3-10 Comparisons of mechanical performance in Case Three: (a) maximum stress concentration factor in the fibre (b) maximum stress concentration factor in the matrix (c) stiffness in z-axis direction (d) Von Mises stress distribution in the matrix at the circumference of hole in the top/bottom plies ($V_f = 27.1\%$) (e) Von Mises stress distribution at the circumference of hole in the middle two plies ($V_f = 27.1\%$)

Table 3-4 Von Mises stress distribution in Case Three with a fibre volume fraction 27.2%

	Curved fibre	(-45°/45°)s	(90°/0°)s
The whole plate	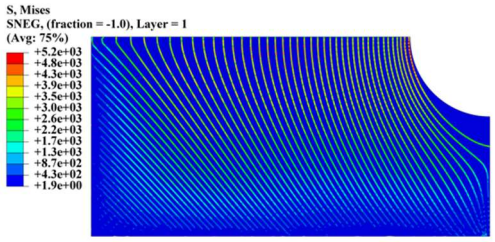	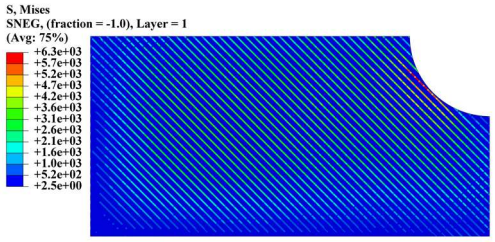	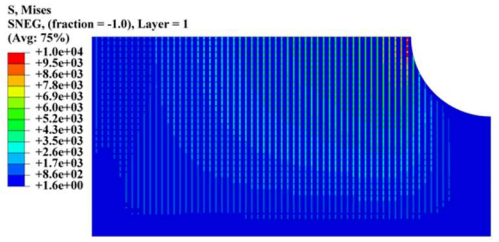
Top/bottom plies (in the matrix)	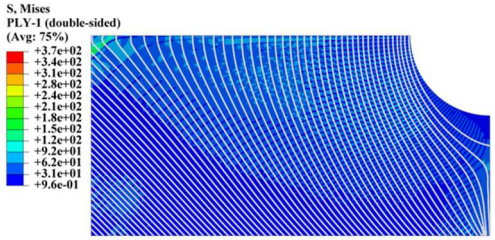	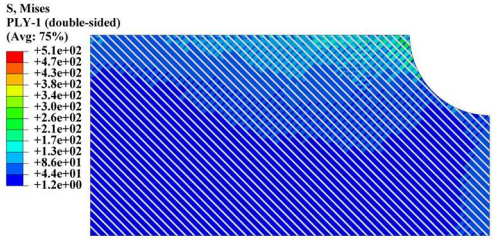	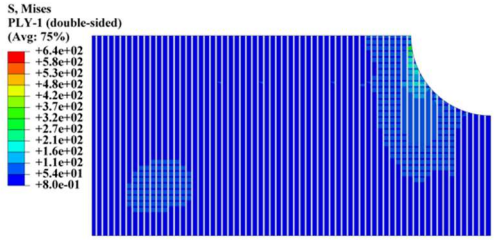
The middle two plies (in the matrix)	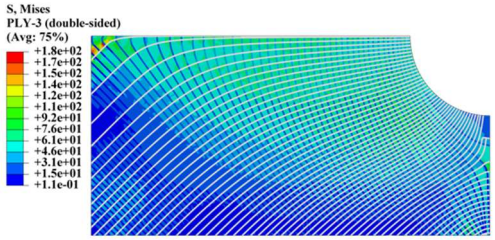	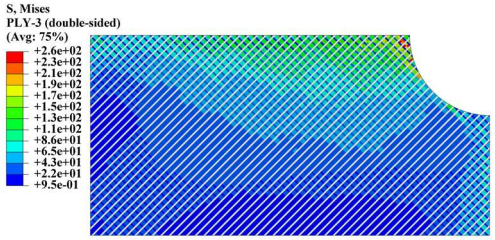	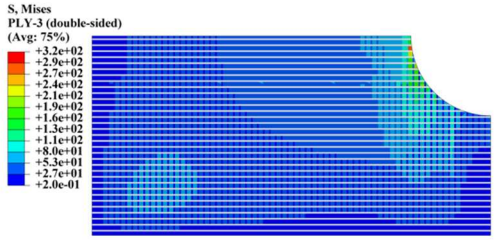

3.5 Conclusions

This chapter presents a new optimisation method to place continuous curved fibres without inter-section specifically for future application to 3D printing of CFRP composites. The method adopts maximum or middle principal stress trajectories as the placement path of carbon fibres, which aims to fully utilise the mechanical properties of fibres. By altering the number of placement path, the volume fraction of fibres in 3D-printed composites can be controlled. The mechanical performance of optimised-printing CFRP composites are discussed in comparison with traditional optimisation method with unidirectional fibres. Three representative cases, i.e. an open-hole single ply lamina under uniaxial tension and an open-hole laminate under biaxial tension and normal pressure were used to assess the newly proposed fibre placement method. In all case studies, it is confirmed that the curved fibre placement follows the principal stress trajectories will significantly improve the mechanical performance of the composite specimens in terms of stiffness and strength comparing to the traditional unidirectional fibre placement.

This new concept of performance-driven optimisation method could offer a very useful and powerful tool for the design of future 3D printing process for fibre reinforced composites with complex and discontinuous geometry. It is worth to mention that although stress distributions near the hole are improved by curved fibre placement, there are still some stress concentrations. Also, when the overlap of fibres appear, the effect of optimisation starts to decrease. Future researches are required to address these issues and also the implications to the challenges of the 3D printing technology need to be discussed with the manufacturing industry.

3.6 Corrections

This chapter was written and published in 2018, but a few minor mistakes were made because of the inadequate understanding of 3D printing, modelling method and their mechanism during the first year of the author's PhD project. According to the policy of the university, the

published work cannot be subject to revision. Thus, this Corrections section is presented especially in the thesis to discuss those mistakes and avoid misleading future readers.

(1) The definition of two principal stresses

In this chapter, the definitions of ‘maximum’ and ‘middle’ are used for two principal stresses. However, for the plane stress state, the principal stress toward out-of-plane direction is always equal to 0, and the other two could be both positive/negative, or one positive and one negative. Therefore, these two stresses in the text should be the higher and the lower values of the in-plane principal stress.

(2) More accurate boundary condition for the symmetry

The boundary condition and the way of load application in this chapter are incorrect. The best way of load application should be a concentrated load at a reference node coupled with the loading side so that it will generate a constant horizontal displacement along the side. As for the constrained side, besides the degree of freedom in horizontal displacement is constrained, a corner point of this side should be fixed for stable convergence. Although this chapter is a preliminary numerical study, the boundary condition and the load application should be achievable for the symmetry and future experiments.

(3) The setting and material properties of carbon fibre

In this chapter, the carbon fibre is defined with homogeneous material properties and the deposited area of it are assumed to be without matrix. In the actual printing, the printing filaments of continuous carbon fibre have to be mixed/impregnated with thermoplastic or thermosetting polymer. The highest fibre volume fraction of the state-of-art technology is 50% approximately. Thus, the setting of material properties and the assumption are not precise enough. An updated FE modelling method is presented in Chapter 7, with reasonable setting of material properties as well as separate definitions

of infilled matrix and deposited continuous fibre filament.

Chapter 4 Failure analysis of 3D-printed woven composite plates with holes under tensile and shear loading [*]

Abstract

This chapter presents the modelling and failure analysis of 3D-printed woven composite plates with a hole under tensile and shear loading. In the finite element (FE) software, woven cells are built using stacking sequences, which are then linked together to form the FE model of the woven laminate. According to the 3D printing experiments, tailored fibre placement is achieved in the simulation by altering the fibre orientation around a region to leave a hole. In order to compare this placement technique with that of a control group, 'drilled' samples with the notch removed via mechanical machining was proposed. Three cases, open-hole laminates under tensile loading and double-shear and single-shear bearing, are studied to advance the understanding of the failure mechanisms. Good agreement between numerical and experimental results has been obtained, which exhibits a similar trend of strength improvement using new placement technique. The distribution of principal strain and displacement in the modelling are consistent with the results obtained from Digital Image Correlation (DIC) and X-ray computed micro-tomography (μCT) scanning. It suggests that the avoidance of fibre breakage and the overlap of printed materials around the hole can significantly increase the failure strength and prevent the propagation of cracks.

Keyword

Carbon fibre reinforced plastic (CFRP), 3D printing, Woven composites, Finite element analysis (FEA), Digital Image Correlation (DIC), X-ray computed micro-tomography (μCT).

[*] This chapter was published in Composites Part B in January 2020.

4.1 Introduction

Additive manufacturing technology, commonly known as 3D printing, is a process that enables the efficient manufacturing of parts with complex shapes [85, 86]. At present, the most widely used 3D printing process is fused filament fabrication (FFF). From prototypes to final parts, automotive [87], aerospace [88], medical [89] industries have already adopted FFF as an alternative manufacturing process. FFF 3D printers use a thermoplastic filament, which is heated to its melting point and then extruded, layer by layer, to create a three dimensional object [69]. An emerging material for 3D printing is fibre-reinforced plastic (FRP), a composite material made of a polymer matrix reinforced with fibres, which is widely used for automotive and aerospace structures because of its high strength and high stiffness-to-weight ratio [90].

Recently, a few new 3D printing technologies for FRP composites have been developed. For example, Markforged released the first commercial system that could 3D print continuous fibre filament in 2014. The mechanical performance of composites with continuous fibre reinforcements including carbon, Kevlar and glass fibres has been evaluated by researchers [6, 20, 91-93]. The tensile strength value of printed composites reinforced by continuous carbon fibres is up to 6.3 times higher than that obtained with the non-reinforced nylon polymer [17]. Even the continuous aligned fibres can be printed along designed path, which offers more flexibility to overcome the major obstacle, the creation of assemblies from multiple components, in the area of composite manufacturing.

In traditional manufacturing, mechanical fastening (currently used for composite joining) is required and notches have to be present in the structure before fastening, which creates major stress risers and weakens the composite material. For composite structures with geometric discontinuities, reinforced fibres are usually placed straight in each layer and the notch punching process would cut off those fibre, which underutilises the outstanding properties of

them. Some optimal designs of continuous fibre placement have been made for the 3D-printed FRP composites to fully utilise the properties of the fibre [40, 42, 43, 46], typically follow a path for fibre determined by finite element models [94-96].

Tailored fibre placement or fibre steering is a technique for placing fibres by using a sewing or tape placement system, which has been used to increase the mechanical performance of composite materials. Some researchers applied this idea to 3D printing to solve the joining problem. They introduced a new fibre placement technique, which allows for the printing of woven multi-laminate composite structures with complex internal geometries [21, 97]. The results were then compared with that of similar composites processed through current state-of-art machining processes, which showed it has the potential as a replacement technology for joining or repairing composites. However, there was limited experimental data available from the fracture processes so further analysis especially for internal material information and crack propagation needs to be conducted to evaluate the failure mechanism of these woven multi-laminate composite structures.

In this chapter, 3D-printed woven carbon fibre reinforced plastic (CFRP) composites were investigated by finite element analysis (FEA) to explore the failure mechanisms of 3D-printed woven composites. Firstly, the new fibre deposition technique and the numerical simulation method are presented. Then open hole tensile and shear bearing response tests are carried out by the finite element method. The numerical results are discussed and compared with the experimental results, in order to identify the reasons why 3D-printed woven multi-laminate composite structures have better performance. Also the Digital Image Correlation (DIC) and X-ray computed micro-tomography (μCT) scanning were used to characterize the specimens to obtain more analytical information about failure. From the correlation between FEA, DIC and μCT data, damage evolution processes under tensile and shear loading conditions were revealed.

4.2 3D printing of woven composites

4.2.1 3D Printing System & Materials

The carbon fibre feedstock filament was sourced from Markforged CA. These filaments (0.35mm diameter) consist of two materials, a fibre bundle (reinforcement) and an impregnated polymer (matrix). The fibre bundle consists of approximately 1000 continuous 7μm diameter carbon fibres. The matrix material is a Nylon blend developed by Markforged. The filament is provided on 150cm^3 or 50cm^3 spools and is stored in a dry box to reduce moisture uptake, this is due to Nylons hygroscopic nature. The thermal properties of the "Prepreg" carbon fibre filaments are evaluated using differential scanning calorimetry (DSC). The glass transition temperatures T_g= 68 °C but the melting peak was found to be absent even the filaments was exposed to 250°C for 30 hours [57]. Previous authors have highlighted that the shape and size of the melting peaks observed in DSC are dependent on the thermal history of the nylon polymer [98]. This indicates that the filament may have been exposed to relatively high temperature during the fabrication process.

Printing was carried out utilising a Prusa i3 printer chassis with a modified fibre printing head. A 1.3mm Markforged fibre nozzle was installed. For the specimen produced in this study a print temperature of 245°C, and a speed of 10mm/s was used. Samples were printed onto an unheated Garolite print plate which was coated in a layer of PVA, to ensure adequate adhesion during printing.

4.2.2 Fibre pathing

The filaments used in this study contains continuous fibres, and as such toolpaths cannot stop and start as they would during polymer printing. It was therefore necessary to generate a continuous toolpath (G-code), as described previously [97]. Continuous toolpaths were generated through a parametric Python script, with output commands compiled in a spreadsheet

software package before transfer to the printer. Sample plates could be customised by the altering input parameters (such as sample size, weave spacing, feature locations, print speed, etc.). Examples of rectangular woven laminates are shown in Figure 4-1. Note that carbon fibre stiffness precludes the use of tight cornering whilst printing. It was therefore necessary to take larger sweeping corners to avoid fibre breakages, which caused 'selvedge' (excess) material in the preparation of specimens. It can also be seen in Figure 4-1 how different numbers of filaments within each unit cell affect the woven structure. This can also drastically reduce the 'selvedge' material, as seen when comparing that of the tensile and the bearing response specimen patterns. The path used in the bearing response specimen was more efficient with less wastage.

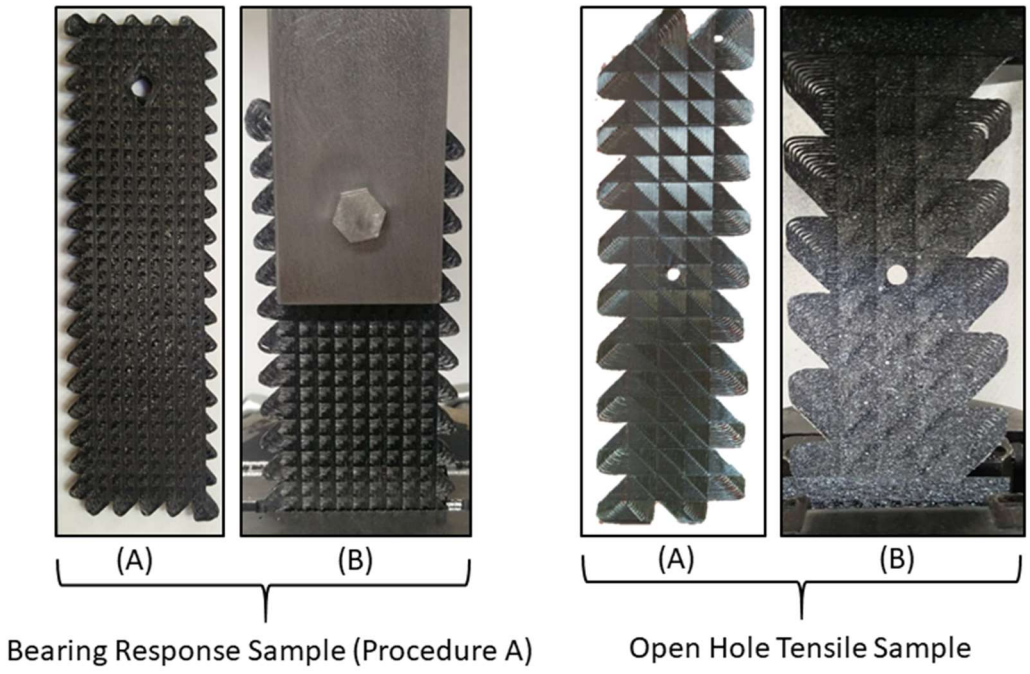

Figure 4-1 Finished composite sample (A) and sample mounted (B) for both open hole tensile and bearing response tests. A smaller woven unit cell was used to minimize waste material in bearing response samples [97].

4.2.3 Tailor woven and drilled samples

In order to compare this tailored placement technique with that of a baseline/control group, a second group of samples was proposed. These ‘drilled’ samples had a 6mm notch removed from the required locations via mechanical machining. In the case of open-hole tensile samples this was achieved through die punching the samples, which was possible due to their low thickness of just 0.35mm. As bearing samples were approximately 3.1mm thick it was necessary to drill the notches using a diamond coated bit. An example of both a ‘tailor woven’ and a ‘drilled’ 6mm notch are shown in Figure 4-2.

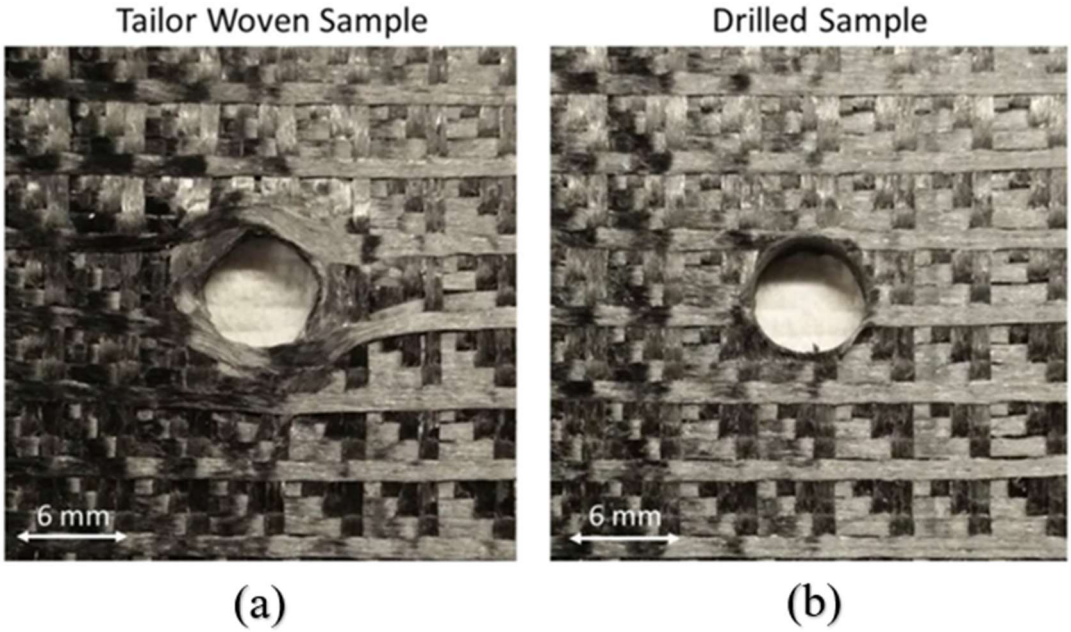

Figure 4-2 The ‘tailor woven’ (a) and ‘drilled’ (b) samples for bearing response testing. Note the fibres remain unbroken in the ‘tailor woven’ samples versus the discontinued fibres in the ‘drilled’ sample [97]

4.2.4 Mechanical testing

This section introduces the specimen setup in the experiment. Detailed geometric information

and schematic diagram will be shown in next section. Both open hole tensile and bearing response tests were performed on an Instron 100kN 8501 hydraulic tester (50kN in Tensile). Hydraulic grips ensure equal gripping pressure on each tab (500Psi). A preload of 5N was applied to specimen prior to test start to take up slack from gripping apparatus.

As per ASTM D5766 (open hole tensile) the specimens were tested at a crosshead speed of 1mm/min. They were adhesively bonded onto carbon epoxy tabs, this acts to minimise strain concentrations at the gripping points, and was particularly important for un-notched samples which contained no hole for strain concentration.

As per the ASTM D5961 (bearing response) standard the specimens were tested at a crosshead speed of 2mm/minute. Double shear specimens were held in a steel support structure using a steel M6 nut and bolt, tightened to a torque of 3Nm (using a Torqueleader ADS 4, 0.8-4Nm, torque wrench). This structure evenly applies shear from either side of the specimen. In the case of single shear specimen, carbon epoxy doublers were bonded to the ends of each specimen using a toughened cyanoacrylate to reduce stress concentrations from the grips. A steel M6 nut and bolt were then used to fasten the two specimens together with an applied torque of 3Nm. Two M6 washers were also used as pressure distributors on either side.

4.2.5 Digital Image Correlation (DIC) and X-ray µCT scanning

Digital image correlation system was used as a video extensometer to obtain extension measurement. Since the bolts in the shear bearing tests covered the hole, this system was only used for the specimens in open-hole tensile test. A crosshead speed of 1mm/min was used so as to acquire accurate DIC readings. For this detection system to function, a random speckle pattern was applied to the surface of the specimens. A white elastic spray paint was used to speckle this pattern.

The specimens after failure in shear bearing tests were examined by a Zeiss Xradia Versa 410 µCT system. The same µCT parameters were used for specimens in double and single shear

bearing tests and produced a voxel size of 1.9397μm. An accelerating voltage of 80keV and a power of 7W were used in this system. The specimens were rotated 360° and 1600 projections at one second exposure time were collected on a charge-coupled device detector. To obtain clear images, results from μCT system were reconstructed using Zeiss built-in reconstruction software and the threshold value was determined by analysing experience.

4.3 Failure characterization and finite element analysis

4.3.1 Finite element model

In this chapter, a FEM software ABAQUS is used to simulate the failure of 3D-printed woven composites plates. The plates are set as 3D shell models and the 'composites layup' module is applied to define the stacking sequence and properties of the elements. The elastic properties and damage properties of CFRP used in the present study are shown in Table 4-1 and Table 4-2, respectively. The damage initiation and evolution of fibre reinforced composites are judged by using Hashin failure criteria in ABAQUS, which is based on the works of Hashin and Rotem [99].

Four different damage initiation mechanisms are taken into consideration in the Hashin damage initiation criterion: fibre tension (F_f^t), fibre compression (F_f^c), matrix tension (F_m^t), and matrix compression (F_m^c). According to the failure modes, the following four equations Eqs (6) - (9) are applied.

$$F_f^t = \left(\frac{\sigma_{11}}{X^T}\right)^2 + \alpha\left(\frac{\tau_{12}}{S^L}\right)^2 \tag{6}$$

$$F_f^c = \left(\frac{\sigma_{11}}{X^C}\right)^2 \tag{7}$$

$$F_m^t = \left(\frac{\sigma_{22}}{Y^T}\right)^2 + \left(\frac{\tau_{12}}{S^L}\right)^2 \tag{8}$$

$$F_m^c = \left(\frac{\sigma_{22}}{2S^T}\right)^2 + \left[\left(\frac{Y^C}{2S^T}\right)^2 - 1\right]\frac{\sigma_{22}}{Y^C} + \left(\frac{\tau_{12}}{S^L}\right)^2 \tag{9}$$

where σ_{11}, σ_{22} and τ_{12}, are the applied stresses and α is a coefficient ($0.0 \leq \alpha \leq 1.0$) that

determines the contribution of the shear stress to the fibre tensile initiation criterion. In this work, the value α =1.0 is used as in the model proposed by Hashin in 1980 [100].

In ABAQUS software, the Hashin criterion is parallel to the evolution of damage. It is based on four fracture energies which correspond to four different material failure modes. The fracture energy values presented in Table 4-2 was used for each mode previously explained. However, it is a challenge that using damage energy to determine the combination of Hashin criterion and damage evolution. Other standard tests on fracture energies of FRP composite are still to be developed [101-103].

When one of the parameters (F_f^t, F_f^c, F_m^t and F_m^c) exceeds the unit value, the damage criterion of the corresponding failure mode is met, and the stress at this point is calculated as follows:

$$\sigma = C_d \varepsilon \tag{10}$$

where ε reflects the strain and C_d reflects the matrix of damaged elasticity:

$$C_d = \frac{1}{D}\begin{bmatrix} (1-d_f)E_1 & (1-d_f)(1-d_m)v_{21}E_1 & 0 \\ (1-d_f)(1-d_m)v_{12}E_2 & (1-d_m)E_2 & 0 \\ 0 & 0 & (1-d_s)GD \end{bmatrix} \tag{11}$$

$$D = 1-(1-d_f)(1-d_m)v_{12}v_{21} \tag{12}$$

where E_1, E_2, G, v_{12} and v_{21} are shown as Table 4-1. d_f, d_m and d_s reflect the current state of fibre, matrix and shear damage, respectively, which derived from damage variables d_f^t, d_f^c, d_m^t and d_m^c as follows:

$$d_f = \begin{cases} d_f^t & \text{if } \sigma_{11} \geq 0 \\ d_f^c & \text{if } \sigma_{11} < 0 \end{cases} \tag{13}$$

$$d_m = \begin{cases} d_m^t & \text{if } \sigma_{22} \geq 0 \\ d_m^c & \text{if } \sigma_{22} < 0 \end{cases} \tag{14}$$

$$d_s = 1-(1-d_f^t)(1-d_f^c)(1-d_m^t)(1-d_m^c) \tag{15}$$

After the damage initiates, the damage variable of each mode is calculated by means of

$$d = \frac{\delta_{eq}^{f}(\delta_{eq}-\delta_{eq}^{0})}{\delta_{eq}(\delta_{eq}^{f}-\delta_{eq}^{0})} \quad (16)$$

where δ_{eq}^{0} is the equivalent displacement when the damage criterion of material was met initially and δ_{eq}^{f} is the equivalent displacement when the material was damaged completely. Figure 4-3 shows their relation graphically. The values of δ_{eq}^{0} for the various modes depend on the elastic stiffness and the strength parameters specified as part of the damage initiation definition. The values of δ_{eq}^{f} for the various modes depend on the respective energy dissipated during damage G^{c}.

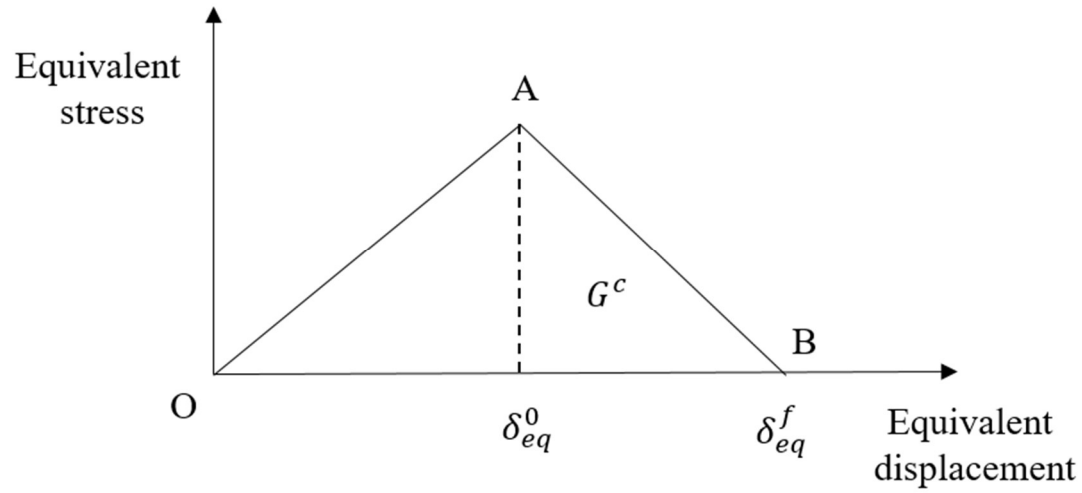

Figure 4-3 Linear damage evolution of Hashin failure criteria.

Table 4-1 Elastic properties of 3D-printed CFRP by Mark One/Two [93, 104].

Modulus of elasticity in fibre direction ($\mathbf{E_1}$)	54 GPa
Modulus of elasticity in transverse to fibre direction ($\mathbf{E_2}$)	26 GPa
In plane Poisson's ratio ($\mathbf{v_{12}}$ & $\mathbf{v_{21}}$)	0.30
Share modulus ($\mathbf{G}$)	5000 MPa

Table 4-2 Damage properties of 3D-printed CFRP by Mark One/Two [93, 105, 106].

Tensile strength in carbon fibre direction ($\mathbf{X^T}$)	700 MPa
Compressive strength in carbon fibre direction ($\mathbf{X^C}$)	320 MPa

Tensile strength in transverse to carbon fibre direction ($\mathbf{Y^T}$)	33 MPa
Compressive strength in transverse to carbon fibre direction ($\mathbf{Y^C}$)	131 MPa
Longitudinal shearing strength ($\mathbf{S^L}$)	29 MPa
Transverse shearing strength ($\mathbf{S^T}$)	29MPa
Tensile fracture energy in carbon fibre direction ($\mathbf{G_{ft}^c}$)	91.6 N/mm
Compressive fracture energy in carbon fibre direction ($\mathbf{G_{fc}^c}$)	79.9 N/mm
Tensile fracture energy in transverse to carbon fibre direction ($\mathbf{G_{mt}^c}$)	0.22 N/mm
Compressive fracture energy in transverse to carbon fibre direction ($\mathbf{G_{mc}^c}$)	1.1 N/mm
Viscosity coefficient	0.005

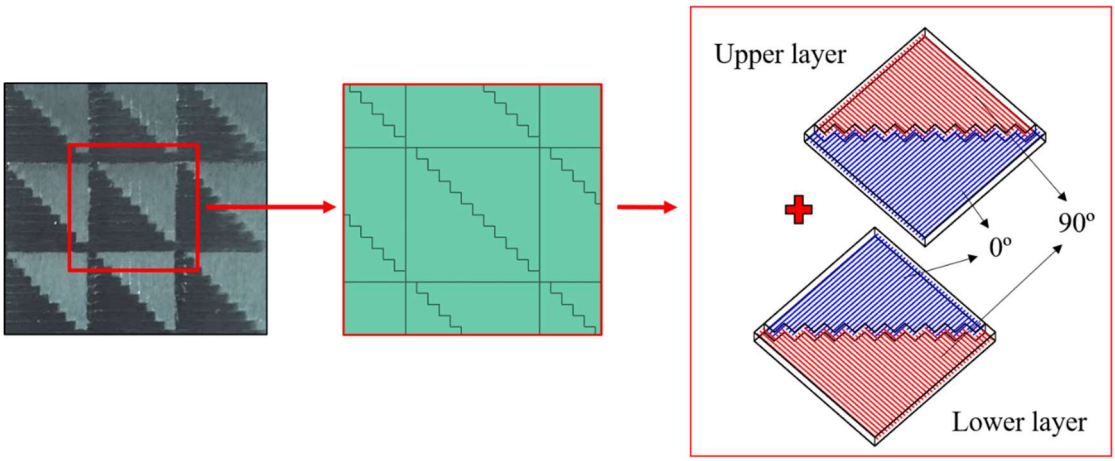

Figure 4-4 Modelling of woven composites structure: detailed image of finished woven laminate (left), 'cell' structure in FEA (middle) and schematic representation of a two-layers woven cell (right).

The woven structure produced in this study can be broken down into unit cells (Figure 4-4 highlights nine of these 'cells'). The modelling of woven laminate begins with the simulation of these square cells, as shown in Figure 4-4. Each cell consists of two parts which are separated by polylines from topleft to downright. For a two-layer woven laminate, the stacking sequences of fibres are exactly the opposite in these two parts, $(0/90)_s$ and $(90/0)_s$, respectively. This modelling method makes the material properties of the woven composites in the numerical simulation similar to the experimental ones.

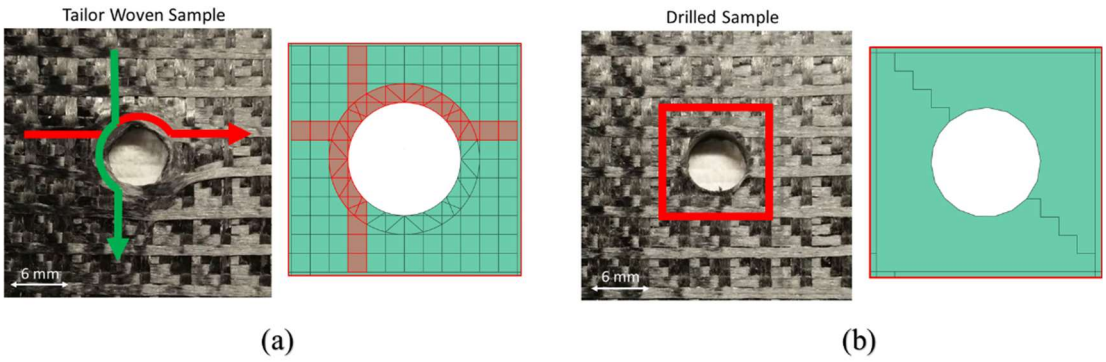

Figure 4-5 Modelling of the hole for (a) 'Tailor-woven' and (b) 'drilled' specimens

As shown in Figure 4-5(a), fibres from the X and Y axis were diverted around a region to leave a hole in the 'tailor woven' specimen. In the real printed samples, the overlap of the filaments would cause the ring area to swell slightly and form a densified buffer zone. In the FE model, a ring with the same width as printing width (1mm) is set around the hole. The first material orientation (fibre direction) of CFRP is set along this ring when the printing paths of the filament get into this ring region. Since the diameter of the hole is 6 mm, six printed filaments were diverted in the X and Y axis directions, in which the overlap of materials is formed as the overlap of red and green lines shown in Figure 4-5(a). It causes different height in the ring and other regions and also improves the stiffness in the region around the hole, which is consistent with the case of real printed samples.

For the 'drilled' specimen, specimens are notched using a die punch after printing. In numerical simulations, a model of intact woven composites without holes is made firstly and a hole is cut off from the centre of the intact model to form the drilled case, as shown in Figure 4-5(b).

4.3.2 Tensile loading test

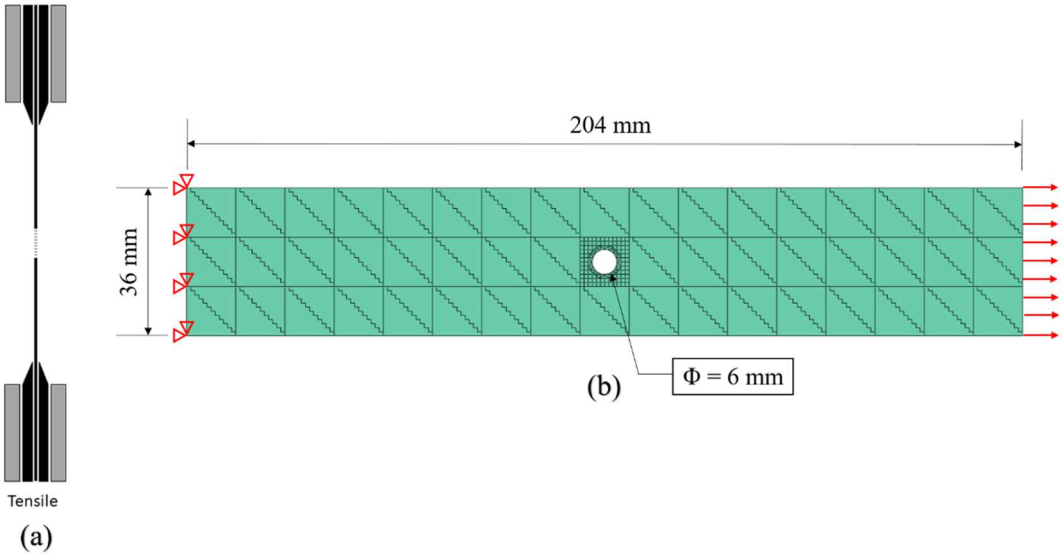

Figure 4-6 (a) Specimen setup for tensile test (b) the schematic diagram in the FE model

As shown in Figure 4-6, the first case is an open-hole laminate under uniaxial tensile loading according to ASTM-D5766 standard test method, where its length is 204 mm and its width is 36 mm. As mentioned above, a hole with 6mm diameter is placed in the centre and the plate consists of 2 plies of 0.17 mm thick. Each two plies make up a woven layer. The left side of the plate is fixed and the displacement along longitudinal direction is applied to the right side of the plate. The plate has a constrained degree of freedom in vertical displacement along the z-axis to eliminate the effect of warpage on the results. 'Tailor woven', 'drilled' and 'intact' specimens are studied in this case.

4.3.3 Shear bearing test

Numerical simulations of shear bearing tests were carried out according to ASTM-D5961 standard test method. These two cases are the laminates under double and single shear bearing, where their length is 172 mm and their width is 36 mm. The plates consist of 18 plies of 0.175

mm thick (9 woven layers) and the dimeter of the holes is 6mm. According to standard test method for shearing response, the centre of the hole is 20 mm from the right side and 18 mm from the top side. For double shear bearing test, the left side of the plate is fixed and a rigid pin is placed in the hole with the same diameter and the displacement along longitudinal direction, as shown in Figure 4-7. For single shear bearing test, the rigid pin is bound to a bolt of 2 mm thick and 6.5 mm in diameter. As shown in Figure 4-8, displacement of pin is loaded in the position 1.575 mm (half of the plate thickness) from the plate, which ensures the woven laminates are under the same loading condition as in the experiment. In the simulation of shearing tests, the plates have a constrained degree of freedom in vertical displacement along the z-axis in order to eliminate the effect of warpage caused by the unsymmetrical stacking sequence of real samples. The default set of contact is used in the interaction between the pin and the woven composites, which is 'frictionless' and 'hard contact' (only allow the transfer of compressive stress) for tangential and normal behaviour. Only 'tailor woven' and 'drilled' specimens are studied in shear bearing tests.

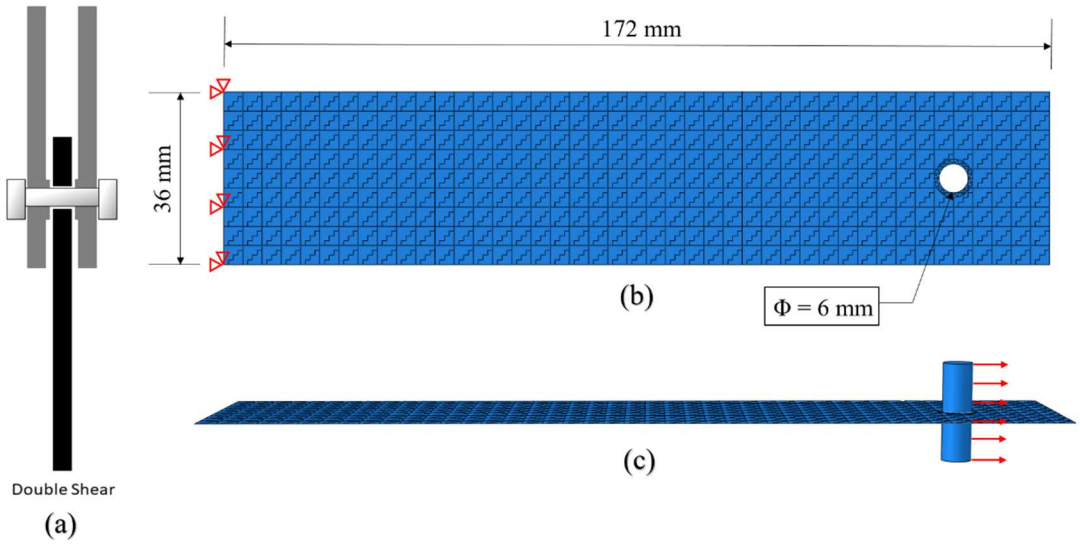

Figure 4-7 Specimen setup (a) for double shear bearing test and the schematic diagram from top view (b) and front view (c) in the FE model

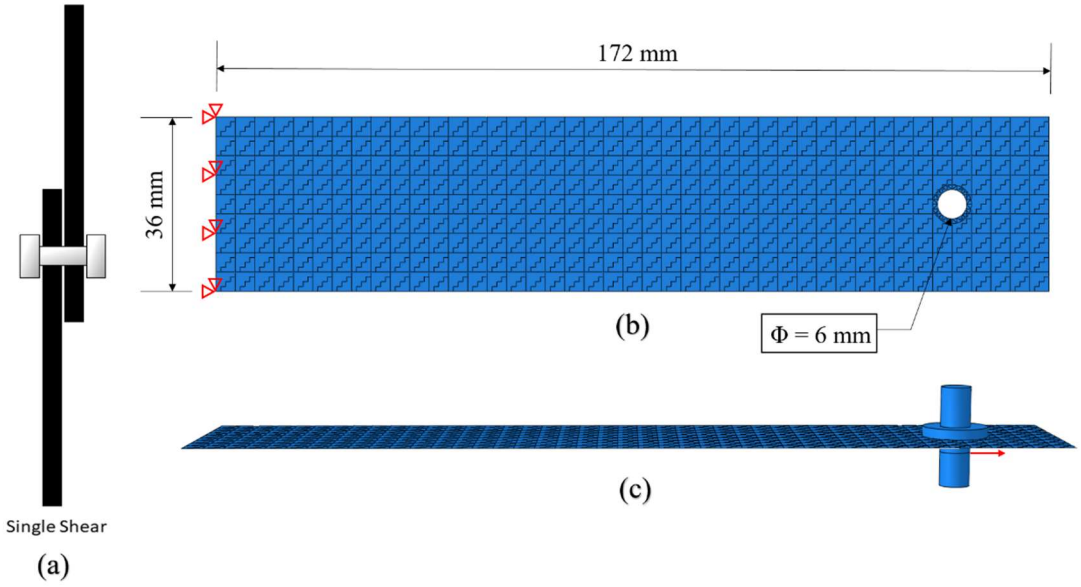

Figure 4-8 Specimen setup (a) for single shear bearing test and the schematic diagram from top view (b) and front view (c) in the FE model

4.4 Results and discussion

In this section, the results of the numerical simulations are compared with that obtained from the experimental data which were reported previously [97]. Just to note that there is limited experimental data available from the fracture processes. For example, bolts had to be placed above the hole and used for fastening during the shear bearing experiments. Thus, the displacement around the hole cannot be obtained from the DIC measurement. Therefore, the results captured from the numerical simulations, such as strain distribution and the evolution of damage, would be helpful for the further understanding of the failure mechanism.

4.4.1 Open hole tensile

In the tensile loading case, examples of the average tensile strengths and strains for each

specimen are shown in Figure 4-9 and stress-strain graphs compiled in Figure 4-10. For ‘tailor woven’ and ‘intact’ specimens, the tensile strength from numerical simulations are 10-15% higher than those obtained experimentally. A possible explanation for this behaviour is that the presence of air voids caused by 3D printing process would reduce the material properties of CFRP and make the strength values a little lower than the materials data provided by Markforged company [104] while approximately 60% higher for ‘drilled’ specimen resulted in a considerable number of defects in the region around the hole such as fibre breakage, which could not be directly simulated in the present FE model. Comparing the experimental and modelling data given in Figure 4-9 & Figure 4-10, it is clear that both exhibit a similar trend of strength improvement obtained for the hole obtained using the ‘tailor woven’, compared with that for the drilling technique. In the presented FEA results, the strength of ‘drilled’ specimen reach 76% that of intact specimen, while ‘tailor woven’ specimens exhibited strengths which were 11% higher, and 13% lower than that of ‘intact’ specimens. Figure 4-9 also shows the comparison of tensile strains for ‘tailor woven’, ‘drilled’ and ‘intact’ specimens (1.4%, 1.3% and 1.7%, respectively, in the simulation). The tensile strains of ‘tailor woven’ and ‘intact’ specimens show good agreement between the experiment and simulation while the value of ‘drilled’ specimen in the experiment is lower than that in simulation. As mentioned before, this is because in reality the drilling process of CFRP composites cuts off the carbon fibres and also generates serious defects including burrs, tearing, delamination, matrix thermal damage and so on [107]. These defects reduced the properties of the material around the hole and lowered the experimental strength of the ‘drilled’ sample.

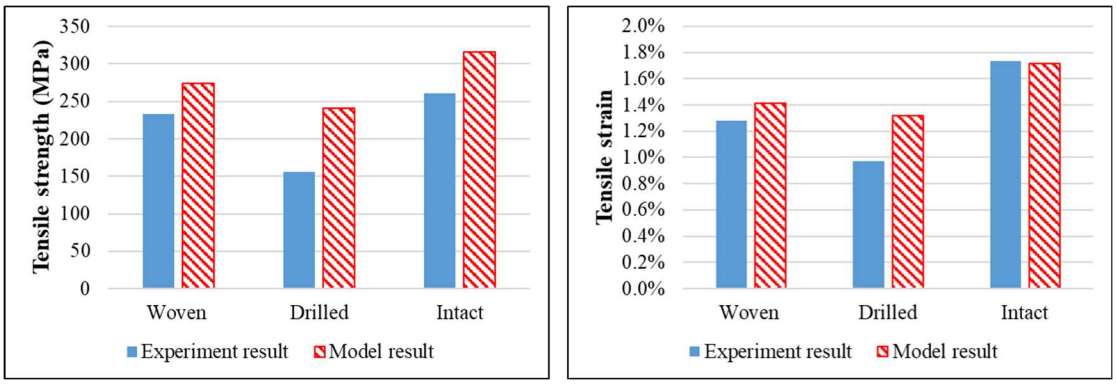

Figure 4-9 Tensile strength (left) and tensile strain (right) for each type of specimen

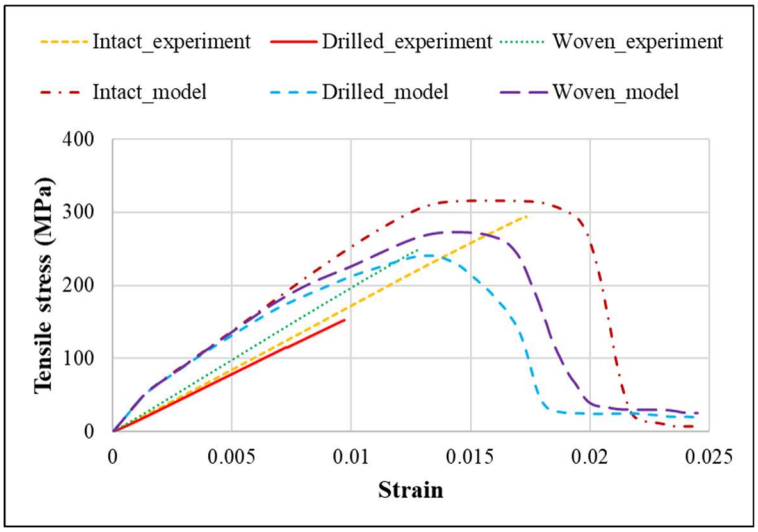

Figure 4-10 Stress-strain curve for each type of specimen in tensile loading tests

As shown in Figure 4-11, the maximum principal strain distribution from the FEA is similar to that in DIC images, which illustrates the reliability of the FE models. For the 'drilled' specimen, the immediate left and right regions of the hole bear most of the load due to the discontinuity of the fibres caused by the die punching process. As shown in Figure 4-11(b) & (c), the strains with higher values (in red colour) concentrate in very small regions in the vicinity of the hole and the cracks propagate straight along the left and right directions. The failure mode was

consistent with the type LGM (lateral, gage and middle) failure in ASTM D5766, wherein the laminate failed in tension laterally across the centre of the hole and exhibited faster crack propagation. For the 'tailor woven' specimen, maximum principal strains still concentrate around the hole but not in the immediate left and right regions since more materials are placed in this area during the 3D printing woven process. These continuous and uncut fibres transferred and distributed the loads from the hole to the surrounding area, which makes it like a variable-stiffness design [39] where the material orientations are allowed to vary in a continuous manner over the domain. As similar optimisation of fibre orientations near a hole [43, 82], tailor woven technique did reduce the localised strains and increase load-carrying capacity. Instead, strains are concentrated on the corners of the region around the hole, which can be seen in the FEA contours as well for the level of strain given in the DIC images. It was observed that cracks initiated from the corners and then propagated outwards in a more irregular pattern compared with that obtained for the drilled composite, as shown in Figure 4-11. The failure mode is the type MGM (multi-mode, gage and middle), in which laminate failed in tension at the hole and exhibited multiple modes including laterally and angularly in various sub-laminates. Also crack arrest was observed at weft-warp intersections, shifting the crack onto a different layer, as shown in Figure 4-11(a).

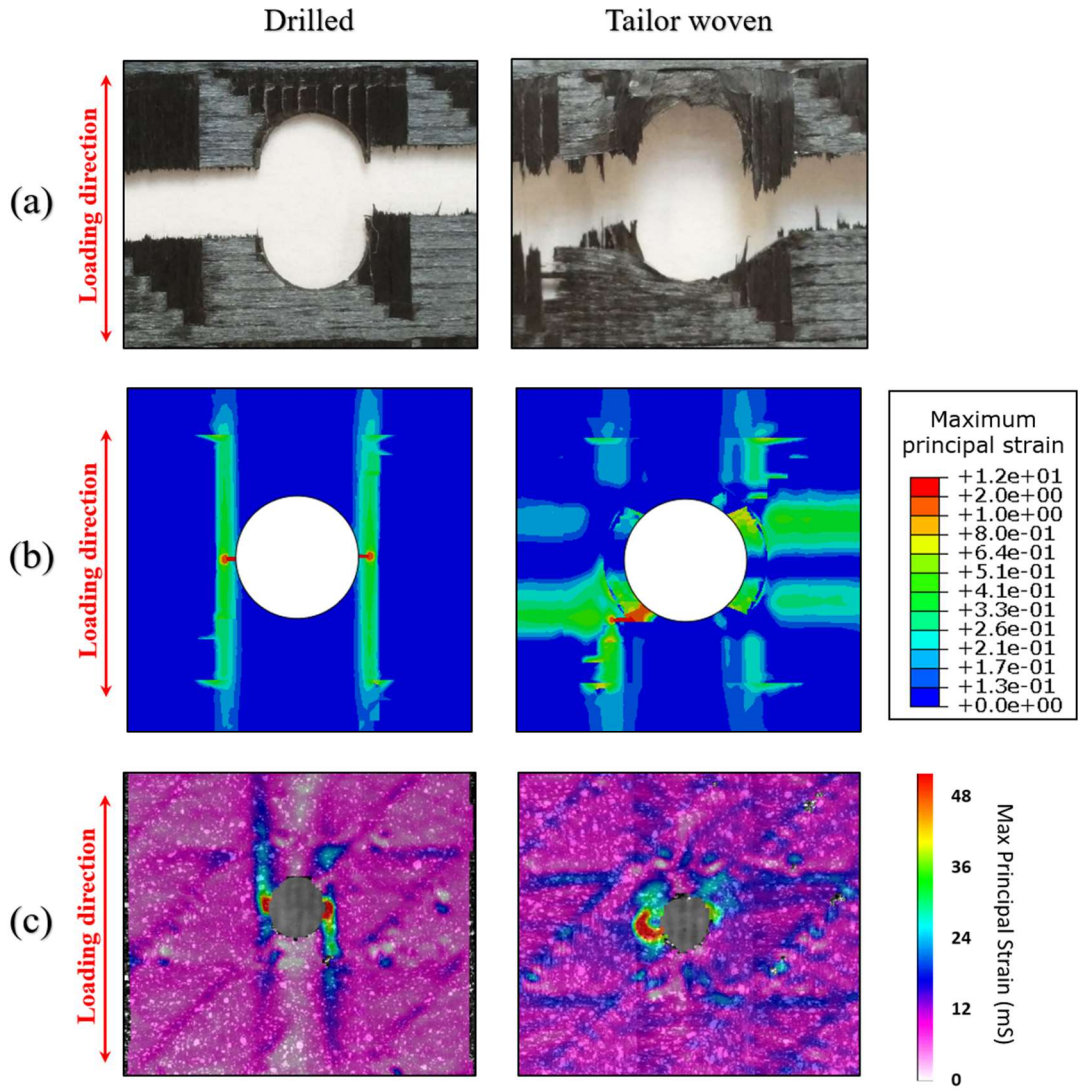

Figure 4-11 Fracture pattern of 'drilled' (left) and 'tailor woven' (right) specimens: (a) fracture zone around the hole in experiment, (b) the distribution of maximum principal strain from FEA prior to failure and (c) DIC images immediately prior to failure.

4.4.2 Double Shear Bearing Response

The average shear strengths and strains for 'tailor woven' and 'drilled' specimens in double shear bearing test are compiled in Figure 4-12. Good agreement between numerical and experimental results has been obtained, where the shear strength increases from about 150 MPa

to 250 MPa for the holes obtained using the tailor woven placement, compared with the drilled composites. The shear strains of 'tailor woven' specimen are similar but there are some differences of the shear strains of 'drilled' specimen. As the stress-strain graphs shown in Figure 4-13, when the strain reached to 22%, the curves of 'drilled' specimens come to the inflection point, which means the damage starts to develop in the laminate. However, in the experimental result, bearing stress continues to increase by about 20% as the stiffness declines. Since the actual printed materials contain multiple voids, the material around the hole shifted as it was squeezed by the steel pin, which can be observed in the Mirco-CT images below. For FEA results, the failure progress evolved more quickly because the material is assumed to be ideal and homogeneous in the simulation.

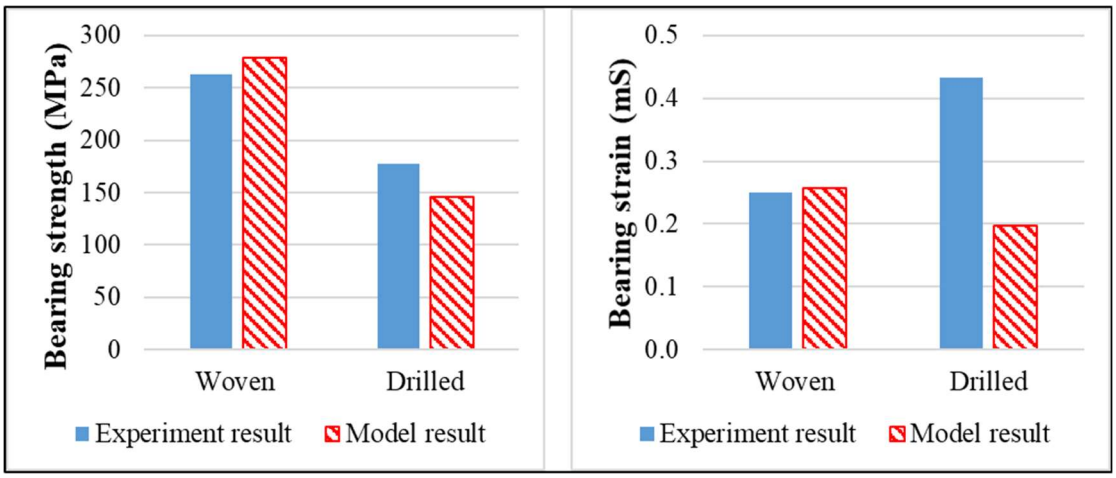

Figure 4-12 Bearing strength (left) and strain (right) for 'tailor woven' and 'drilled' specimens in double shear bearing test

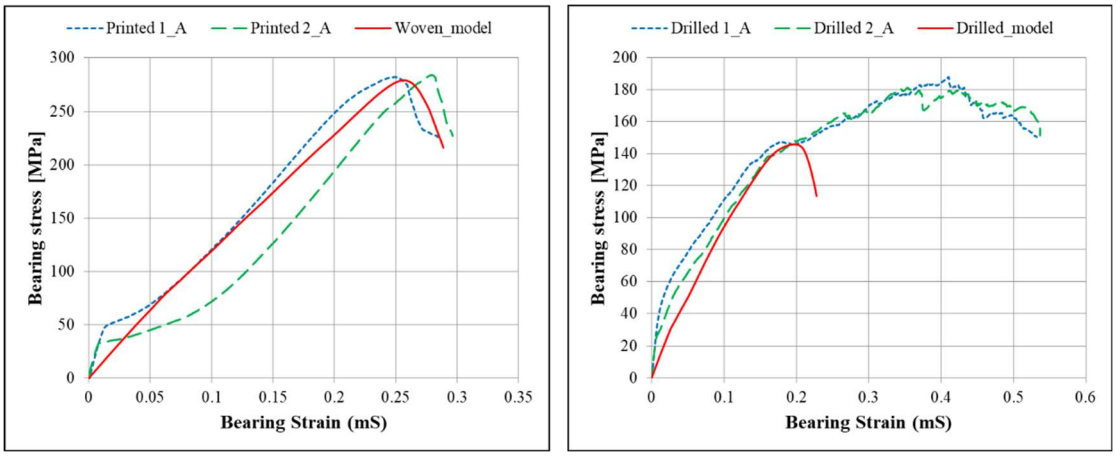

Figure 4-13 Stress-Strain Curves for 'tailor woven' (left) and 'drilled' (right) specimens in double shear bearing test

The progressive distributions of maximum principal strain are shown in Figure 4-14, which indicate how the damage initiates and propagates in the plate. For the 'drilled' specimen, the cracks initiate on the flanking sides of the hole and then propagate along the longitudinal direction, which is consistent with the 'shearout' failure mode. Instead the damage of 'tailor woven' specimen only occurs at the edge extruded by the steel pin and do not propagate to other areas of the plate. It is the B1I (bearing, first hole and inapplicable) failure mode in ASTM D5961. CT scan images shown in the Figure 4-15(a) confirm the FEA results discussed above. The cracks are marked by the red circles, which show the damage actually occur at the flanking sides in the 'drilled' specimen and at the edge extruded by the steel pin in the 'tailor woven' specimen. Also, the deformed shapes of the hole are similar between the experimental and numerical results in Figure 4-15(a) & (b), where the hole has undergone a huge deformation in the 'drilled' specimen because of the extrusion of the pin. Some fibre displacement is also visible at the hole of 'tailor woven' specimen, but this elongation is minor compared to that observed in the case of the drilled specimen. Figure 4-15(c) shows that the improvement of shearing strength and difference of failure process are caused by the overlap of continuous

materials around the hole in the ‘tailor woven’ specimen. The diversion of the filament around the hole makes the material dense in this region, which protects the specimen from the damage and crack propagation. In contrast, major buckling and delamination are seen in drilled specimens, as a result of compression of the discontinued fibres.

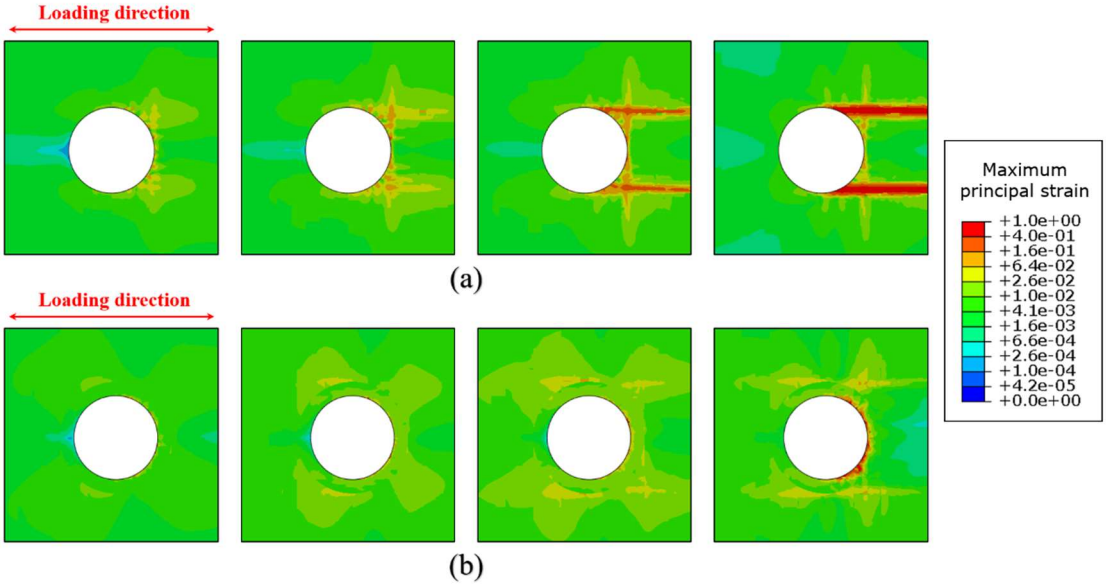

Figure 4-14 The progressive distributions of maximum principal strain in double shear bearing test: (a) ‘drilled’ and (b) ‘tailor woven’ specimens.

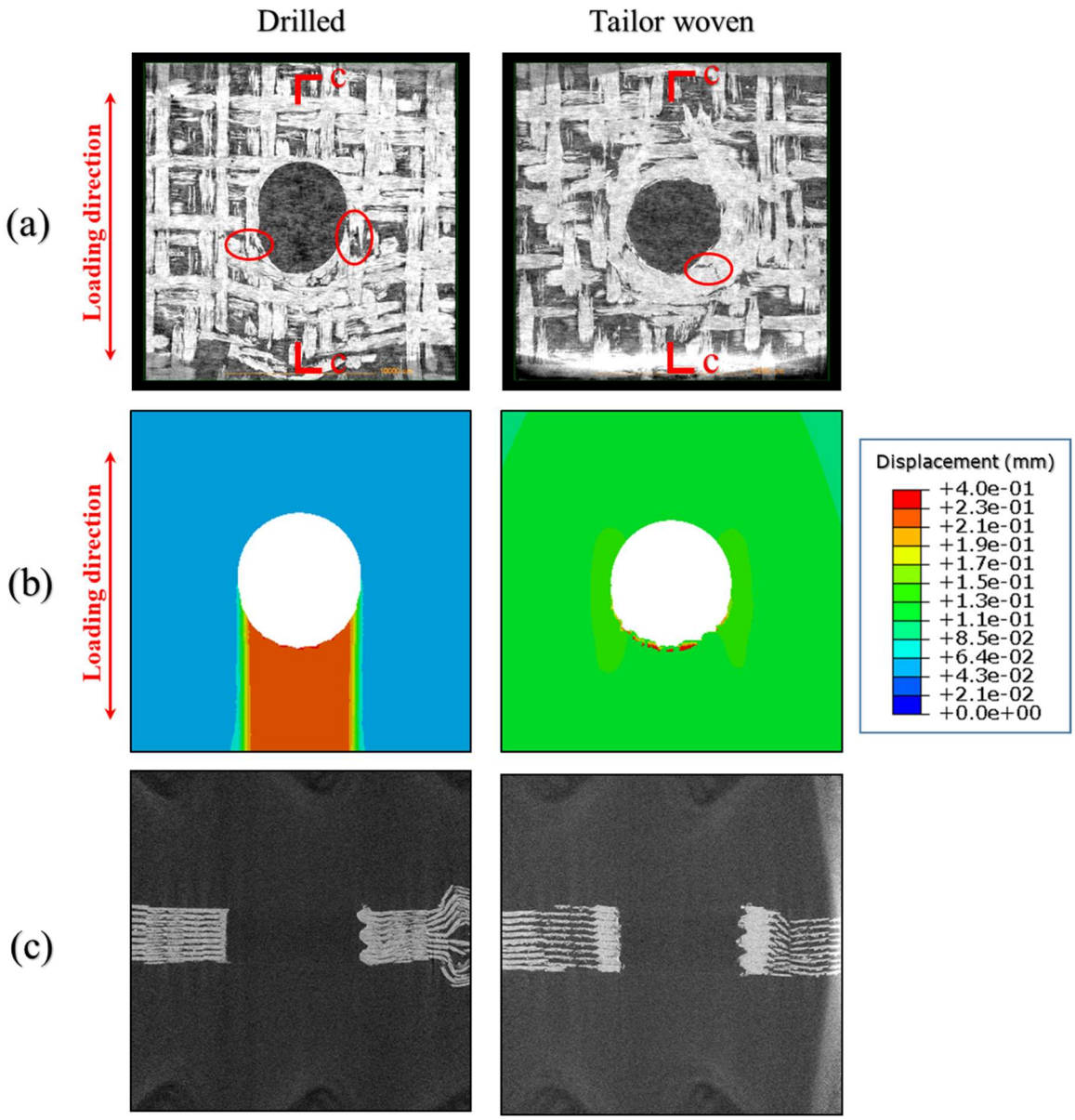

Figure 4-15 Integrity of the hole after double shear bearing test, 'drilled' specimen (left) and 'tailor woven' specimen (right): (a) Cross section images after failure from μCT scanning, (b) Distribution of displacement after failure from FEA and (c) Section view after failure from μCT scanning.

4.4.3 Single shear bearing response

The average shear strengths and strains for 'tailor woven' and 'drilled' specimens in single

shear bearing test also show good agreement, as shown in Figure 4-16. Shear strength increases from about 150 MPa to 200 MPa and the comparison of stress-strain graphs shown in Figure 4-17 is similar to those graphs in double shear bearing test. In general, except for the different shear strength due to loading conditions, the damage processes of these two shear bearing tests are similar and the mechanisms behind them are the same. Another difference is the compression caused by bolt rotation in single shear bearing. In term of it, tailor woven specimen exhibited better resistance and reduced the movement of the bolt. In contract, buckling due to the compression from the bolt is observed in the drilled specimen, and therefore delamination occurs above the hole. The distributions of maximum principal strain in Figure 4-18 indicate the cracks initiate at the flanking sides of the hole in the 'drilled' specimen. On the contrary the damage in 'tailor woven' specimen only concentrate on the edge extruded by the steel pin, which also can be seen from the μCT images in Figure 4-19(a). The failure mode of 'drilled' sample is 'shearout' while 'tailor woven' sample exhibits bearing (B1I) failure mode. The deformation of the hole in these two samples show good agreement as well.

The 3D-view videos (4 videos for 'drilled' and 'tailor woven' specimens in double and single shear tests) obtained from μCT system have been uploaded as supplemental documents to provide more detailed and intuitively clear information about the specimens after failure. It proves the reliability of the FEA model and the improvement of mechanical performance due

to the tailor woven printing technique.

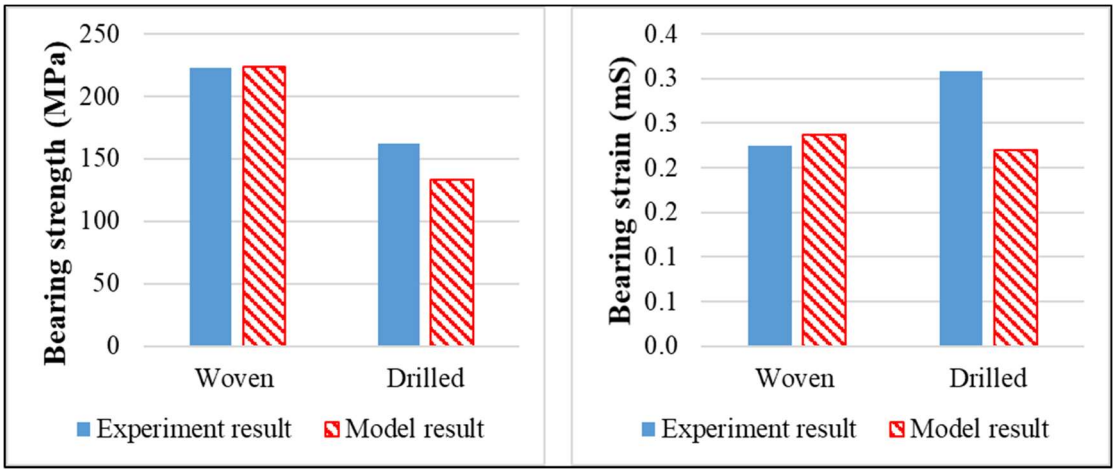

Figure 4-16 Bearing strength (left) and strain (right) for 'tailor woven' and 'drilled' specimens in single shear bearing test

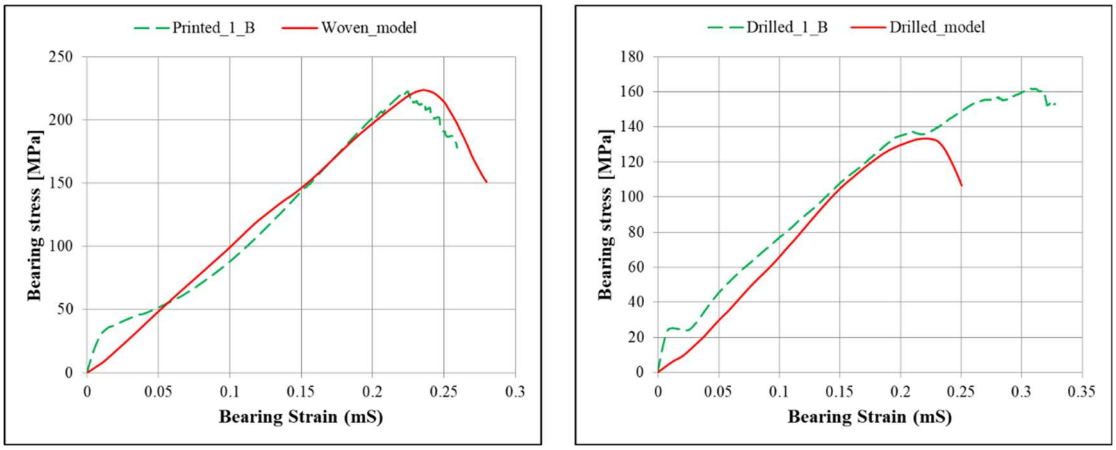

Figure 4-17 Stress-strain curves for 'tailor woven' (left) and 'drilled' (right) specimens in single shear bearing test

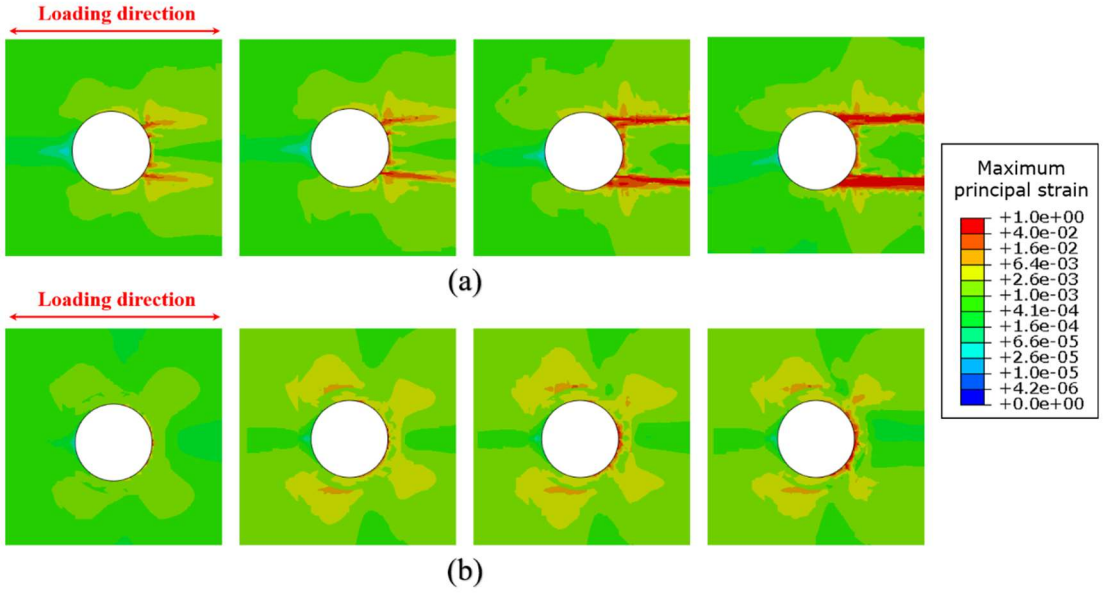

Figure 4-18 Progressive distribution of maximum principal strains in single shear bearing test: (a) ‘drilled’ and (b) ‘tailor woven’ specimens

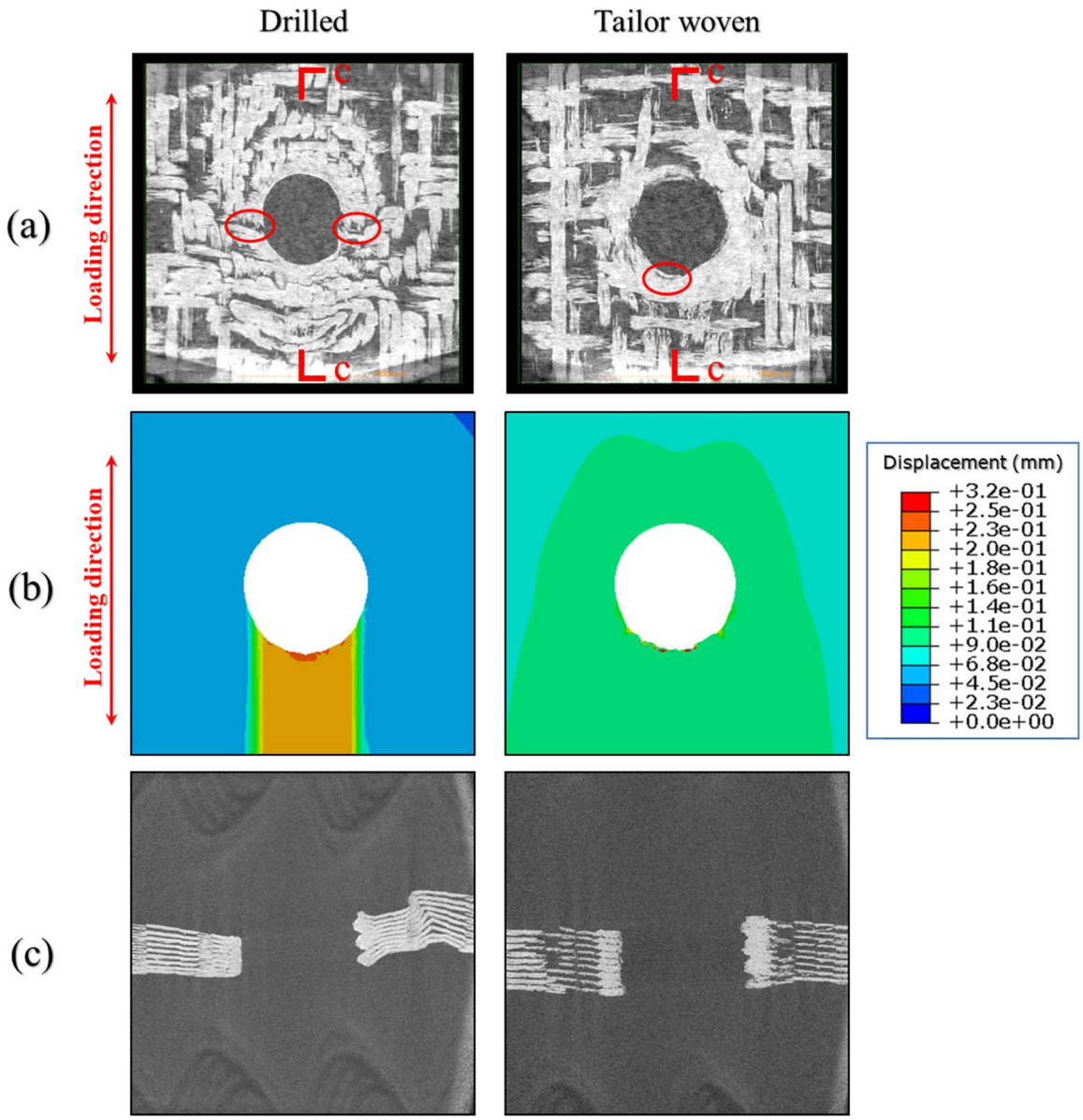

Figure 4-19 (a) Cross section images after failure from μCT scanning (b) The distribution of displacement after failure (c) Section view after failure from μCT scanning: 'drilled' (left) and 'tailor woven' (right) specimen in single shear bearing test

4.5 Conclusions

This chapter presents the FE modelling and failure analysis of 3D-printed woven composite plates into which 6 mm holes were placed. The specimens were obtained using the 'tailor

woven' and 'drilled' techniques by diverting the filament to make the hole during printing and by drilling the hole, respectively. The models of each specimen are established by FEM and Hashin failure criteria is used to predict the damage initiation and evolution of 3D-printed woven carbon fibre reinforced polymer composites. Three mechanical tests, tension and double-and single-shear bearing, are studied. Also Digital Image Correlation (DIC) and X-ray computed micro-tomography (μCT) scanning were used to characterise the failure process. The numerical and experimental results show good correlation. Using tailor woven printing technique, the avoidance of fibre breakage and the overlap of printed materials around the hole have increased the strength of the woven laminates by more than 40%. This also improved the damage process in these three loading cases in terms of the migration of the damage initiation and prevention of cracks propagation.

The FE model itself could offer a useful tool for analysing the mechanical performance of 3D-printed composites with designed fibre placement. The failure analysis in this chapter clarify the mechanism behind the improvement of performance achieved by tailor woven fibre placement, which can be used for the design of future 3D printing process for FRP composites. It is important to highlight that while the mechanical properties are improved, the relationship between performance and fibre placement has not been quantified. Also the performance of 3D-printed woven composites under complex loading and geometry have not been tested. Future research is required to address these issues.

4.6 Corrections

The failure criteria used in this chapter is a built-in module in Abaqus software, which is based on the works of Hashin and Rotem in 1973 and 1980 [99, 108]. Hashin managed to separate failure modes of the fibre reinforced composites into two mutually exclusive groups, fibre failure and matrix failure. Subsequent development of it involved subdividing them into tensile

and compressive modes [109].

As the development of failure criteria for fibre reinforced composites, the irrationality of Hashin failure criteria has been critically reviewed. For example, one of the assumptions of Hashin failure criteria is the Mohr criterion. However, the stresses in composites are not principal stresses in the same sense as those employed in the Mohr criterion or Mohr's circle [109]. Also, previous research demonstrated that the changes in elastic constants induced by damage depend on certain damage related material constants [110]. In continuum damage mechanics (CDM) formulation, eight damage related material constants for UD FRP composite have been identified. If seven of these constants have been solved, the remaining one can be determined by a numerical virtual test using a FE model, which means the principle of Hashin failure criteria, four damage variables are defined independently for each mode, is contradictive and irrational [110].

The lack of rationality in the formulation of composite failure criteria can be seen as an acute symptom to be addressed in order to progress in this front of scientific endeavour before any further sophistications to be added to the derivative ends and existing theories.

Chapter 5 Fibre misalignment and breakage in 3D printing of continuous carbon fibre reinforced thermoplastic composites *

Abstract

This chapter investigates the formation of manufacturing induced fibre misalignment and breakage during fused filament fabrication (FFF) 3D printing of 1K continuous carbon fibre filament. Single stripes at various turning angles and curvatures are printed by a desktop printer Prusa i3 using a specific brass nozzle and characterised using X-ray computed micro-tomography (μCT) scanning and optical microscopy. A finite element (FE) model of the printing process is also established to support the experimental measurement. It has been found that high porosity and fibre misalignment in the printed straight stripe result from the weak fibre/matrix interface and the uneven pressure executed by the nozzle. Increase of turning angle and/or reducing of curvature radius leads to more aggravated printing defects, including shape inaccuracy, fibre twisting, folding and misalignment, due to the excessive force from the nozzle, de-bonding with the print bed and the unmatched geometry of nozzle outlet and fibre filament. Severe fibre breakage and significant change of thickness can be seen in the samples with turning angles larger than 120° or curvature radius smaller than 5 mm, while the wrinkles of the stripe in the inner periphery appear more frequently as the curvature radius decreases.

Keyword

3D printing; continuous carbon fibres; X-ray computed micro-tomography; fibre breakage; fibre misalignment; Finite element analysis

* This chapter was published in Additive Manufacturing in December 2020.

5.1 Introduction

Continuous carbon fibre-reinforced polymer (CCFRP) composites have been increasingly used in airframes and other high-end industrial products [87, 88] due to their superior mechanical properties such as high strength-weight and stiffness-weight ratios [43]. Traditional manufacturing methods of CCFRP, such as autoclave and resin transfer moulding, have difficulties to fabricate composites with complex geometry [111], since continuous fibres in the fabric preforms are usually aligned in specific directions. Notches and holes normally need to be created by subtractive machining processes such as drilling and cutting when mechanical fastening is needed. These machining processes could induce residual damages including delamination and fibre breakage which may compromise the structural integrity of the composites [107, 112].

To mitigate the defects caused by subtractive machining processes, alternative manufacturing methods have been explored to place continuous fibre tows and fabricate composites with complex geometries. Among them, Automated Fibre Placement (AFP) uses small fibre tows (typically 8 mm wide or less) to form composites, which leads to better precision and increased deposition rates when compared with experienced laminators for hand lay-up. For composite parts with complex geometries, fibre tows can be steered along the desired fibre paths. However, the diameter of the compaction roller and the head geometry limits female mould radius that can be used for parts built with this technology [113]. Also, several defects may appear during tow steering, which includes out-of-plane wrinkling, blistering, tow pull-ups and shearing effects. A continuous tow shearing (CTS) technique has been proposed to shear dry tows to mitigate these defects with success [114], but it has only been applied to composite plates with relatively large curvatures.

Another recently developed technology, additive manufacturing (also known as 3D printing) has shown potential to fabricate continuous fibre-reinforced composites with highly complex

shapes in both 2D and 3D. Among them, Fused Filament Fabrication (FFF) 3D printing melts and deposits small thermoplastic filament (usually with 1k fibre tows) layer by layer to create the composite parts [43]. In 2014, Markforged® released a series of 3D printers, e.g., Mark One/Two, which can manufacture composites with continuous fibre reinforcement [2]. Supported by its dedicated software Eiger, Mark Two printer places the fibres around the geometry singularity using a concentric approach. Other researchers also developed in-house printers for CCFRP composites [26, 28, 29], which were generally achieved by impregnating the fibres with a matrix material before extruding or within the nozzle [30]. Compared with AFP, 3D printing of CCFRP offers better surface finishing and more design freedom but less efficient [115], due to a higher resolution of the printing system and a smaller width of the printed fibre tows (1-2 mm) [116].

The mechanical performance of 3D-printed composites with continuous fibre reinforcements has been evaluated by researchers [92, 117, 118]. Some of them developed numerical simulations to predict the progressive damage of 3D-printed curvilinear CCFRP composites [62]. It has been revealed that the productivity of the 3D printing process and the quality of final parts depend on a large number of factors, including the geometric complexity of the part as well as the process parameters such as printing speed and fibre orientation [29, 119]. Despite the advantages and capabilities, 3D printing also comes with its own limitations. For instance, the significant voids content results in much lower stiffness and strength than expected [20, 70, 120], compared with traditionally manufactured FRP composites. Also, the fibre bundle could be twisted, folded or even broken when printing a curved section [33]. In addition, the printed radius turned out to be lower than the designed value with a larger fibre bundle size or a smaller set radius [35]. In previous studies, the effect of these defects on mechanical performance has yet been investigated and there is still a lack of established relationship between printing parameters and the formation of those defects. This is large because the fundamental

mechanisms for the FFF 3D printing of CCFRP composites have not been fully understood. Therefore, a comprehensive study is needed for the 3D printing process of CCFRP, especially for the curvilinear paths. Furthermore, a more detailed simulation of the printing process will be helpful for the further understanding of the mechanisms.

In this chapter, the printing induced defects including fibre misalignment (wrinkling, twisting and folding) and breakage are investigated during the FFF 3D printing of CCFRP composites using 1K carbon fibre filament and a specific brass nozzle. First, void formation and fibre misalignment in the printed straight stripe are studied. Then a set of single stripes are printed out at various turning angles and curvatures to represent the complex geometries of notches and holes, which are characterised using X-ray μCT scanning and optical microscopy. A finite element (FE) model of the printing process is also established to aid the understanding of the mechanisms of continuous fibre printing in terms of local stress distributions.

5.2 3D printing of CCFRP

5.2.1 Printing filaments and nozzle

The printing material 0.375 mm carbon fibre (CF) filament is sourced from Markforged®. The previous study had evidenced that polyamide 6-I (PA6-I) is the polymer matrix for CF filaments and the polymer coating is a polyamide 6 (PA6) [7]. A μCT scan of its internal structure is shown in Figure 5-1(a) & 1(b). It can be seen that the cross-section of the filaments is relatively irregular circular with the diameter 0.35 to 0.40 mm and carbon fibres are arranged well straight along the longitudinal direction of the filament. The volume fraction of carbon fibres V_f is measured as 21.34% ($V_f = v_f/v_c$, v_f is the volume of fibres and v_c is the volume of the composite). However, as shown in the cross-section, the fibres are not evenly distributed in the filament, instead, they are concentrated into 3 parallel zones. This leads to two regions

mainly composed of PA6-I in the filament, in which noticeable air bubbles are observed. Some small voids are trapped around the carbon fibres, indicating a weak interface adhesion between the fibre and matrix. The average porosity of the CF filament is measured as 0.7%. All these pores formed in the fabrication process of CF filament may affect the mechanical properties of 3D-printed finished parts.

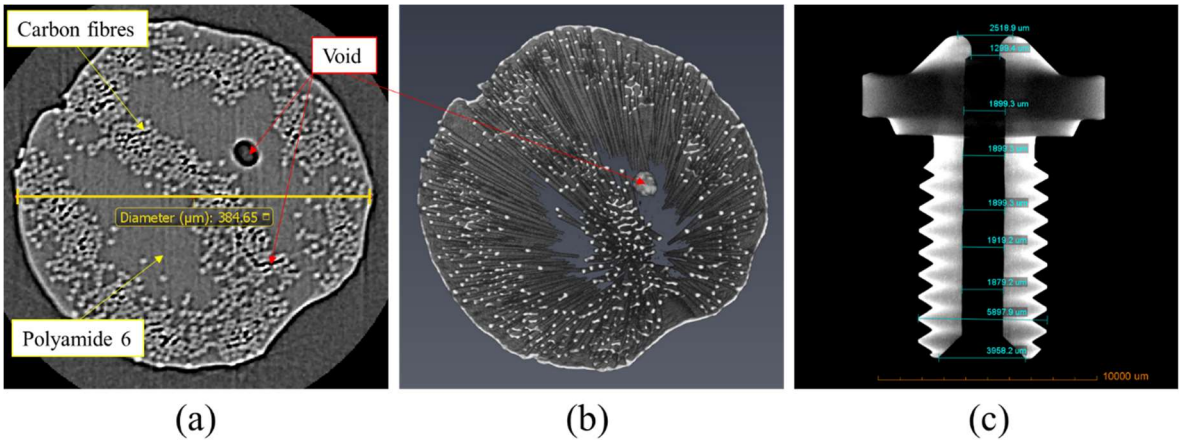

Figure 5-1 µCT scans of filament and nozzle: (a) cross section and (b) 3D view of continuous carbon fibre filament; (c) brass nozzle

The brass nozzle used for the CF filament printing is also sourced from Markforged. Dimensions of the nozzle are measured from its µCT scan, which is illustrated in Figure 5-1(c). The nozzle has a standard M6 screw thread and an outlet diameter of 1.3 mm. There is a thermostable plastic (Polytetrafluoroethylene, PTFE) tube inside the nozzle but for the benefit of measuring the dimensions of the nozzle, it is not shown in the CT image due to its low density compared with the brass. The PTFE plastic tube is used as a guide of CF filaments while maintaining a more uniform temperature distribution for the CF filament and avoiding sticking and friction with the inner wall of the brass nozzle. The large difference between the diameters of the nozzle outlet and CF filament (1.3 mm and 0.375 mm, respectively) is one of the main reasons causing the inaccuracy of fibre paths. Unlike other nozzles for the printing of

pure thermoplastic (such as ABS and PLA) as well as short fibre-reinforced thermoplastic, it has rounded corners at the tip which presses the heated continuous fibre filament on the printer bed. The continuous carbon fibres are passively pulled out from the nozzle as it moves. This is the unique mechanism of the continuous fibre printing process and will be represented in later numerical modelling. Moreover, the friction between the nozzle and melted CF filament could wear the tip of nozzles, which consequently causes inaccuracy of the fibre paths in the printing process.

5.2.2 Desktop 3D printing

The Prusa i3 MK3s printer is used in this study and a schematic diagram of 3D printing CCFRP is shown in Figure 5-2. The printer is open-source and G-code acceptable, which is friendly to the modification of continuous fibre printing and the design of customised fibre paths. Also, its precise 'Live Z Adjust' option can set the off-distance with the increment of 5 μm during the printing, in order to provide better adhesion and proper pressure for the printed CF filament. The filament is heated to a temperature of 245°C and the off-distance between nozzle tip and printer bed is set to 0.1 mm approximately. As mentioned before, the heated continuous fibre filament was pressed on bed by the tip of nozzle, and the followed material was pulled out passively. Therefore, the step motor of filament feeding can be switched off during the continuous fibre printing, and the speed of nozzle movement is equivalent to a passive feed rate of 5 mm/s, which means the free end of the CF filament is slightly under tension due to the twine of the spool, but the passive feeding of filament would not be affected. Samples are printed onto an unheated Garolite printer plate which was coated with a layer of PVA, to ensure adequate adhesion at the start of the printing.

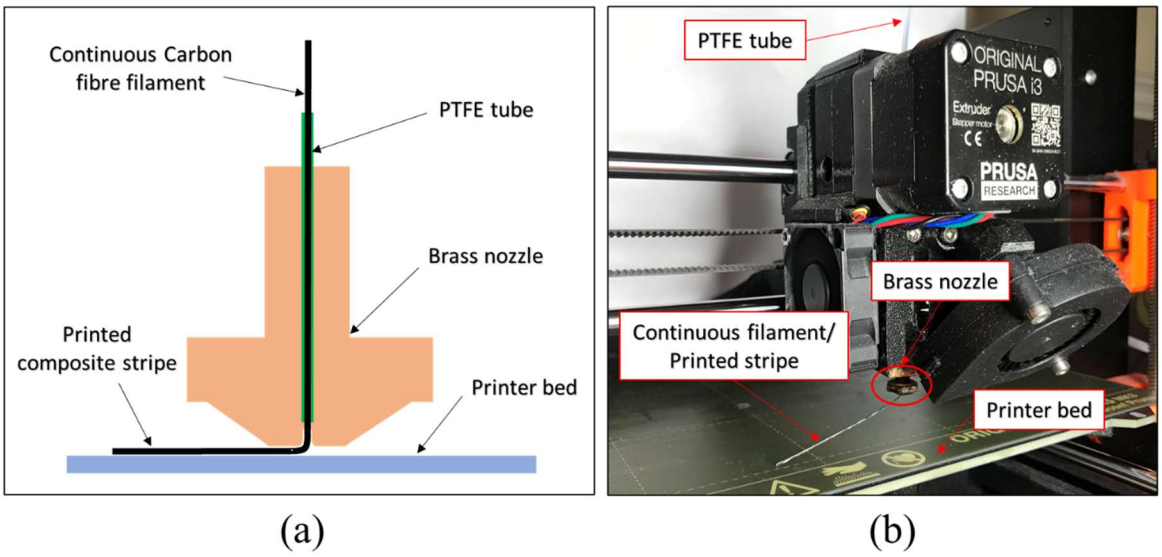

Figure 5-2 (a) Schematic diagram of 3D printing of continuous carbon fibre filament (b) modified print head with the nozzle

A straight stripe of continuous CF is printed first, as a base unit of the finished part. The internal microstructures are characterised by X-ray μCT scans to explore the printing quality of continuous CF filaments. Then a set of single stripes of the composites are printed with different turning angles ranging from 30° to 180° at an increment of 30°, as well as various curvature radius ranging from 2.5mm to 20mm. The study of turning angles reveals the manufacturing of composites with complex geometry and singularity, like sharp corners and notches, while curvature radius more represents circular holes in the composite structures. Since the filament used in this study contains continuous fibres, and the toolpaths cannot be the same as those in traditional thermoplastic printing. Therefore, continuous toolpaths (G-code) are generated through a MATLAB script and then transferred to the printer. The case studies with different turning angles and curvature radius aim to investigate the mechanisms of fibre wrinkling and breakage during the 3D printing process.

5.3 X-ray μCT scans and optical microscopy

X-ray μCT scans of original filament and printed stripes with various turning angles are carried out on a Zeiss Xradia Versa 410 μCT system. For other samples printed at various curvature radius, optical microscope characterisation was carried out on a Zeiss Stemi 2000 Stereo Zoom Microscope. The reason for using optical microscopy instead of X-ray μCT for those samples is that optical microscopy gives a much larger view of the printed samples than X-ray μCT so as to provide more useful information of the fibre wrinkling along the whole printed curve.

The X-ray source with an accelerating voltage of 80 kV and a power of 7 W is used for all scans. The exposure time and effective pixel size vary for each sample to achieve the possible best intensity and contrast of the images, as listed in Table 5-1. Each sample is fully rotated by 360° during the scan, resulting in thousands of projections collected on a 1k x 1k pixel, noise suppressed charge-coupled detector. The raw data are reconstructed using a Zeiss built-in reconstruction software to obtain clear images and the threshold value is determined by analysing experience.

Table 5-1 Exposure time and effective pixel size for the samples in X-ray μCT scans

	Raw filament	Straight single stripe	Single stripes with different turning angles					
			30°	60°	90°	120°	150°	180°
Exposure time (s)	5	2	2	2	8	2	2	2
Effective pixel size (μm)	1.023	2.638	3.293	3.293	3.123	2.826	2.384	3.293

For this chapter, the voids percentage and fibre volume fraction are quantified following the image processing steps in Avizo software (commercial software for data visualisation and analysis), as shown in Figure 5-3. Because the images obtained from μCT scanning are usually not good enough for later processing such as edge detection, filtering technique is necessary to

remove the noise [121]. The median filtering used in this chapter is considered to be a technique for linear smooth processing, often used to preserve edges while removing noise, in which the main idea is to run through the signal entry by entry, replacing each entry with the median of neighbouring entries [122]. As shown in Figure 5-3, compared with raw images, the noise in the matrix material is reduced effectively and the boundaries between different materials are easier to detect in images after median filtering.

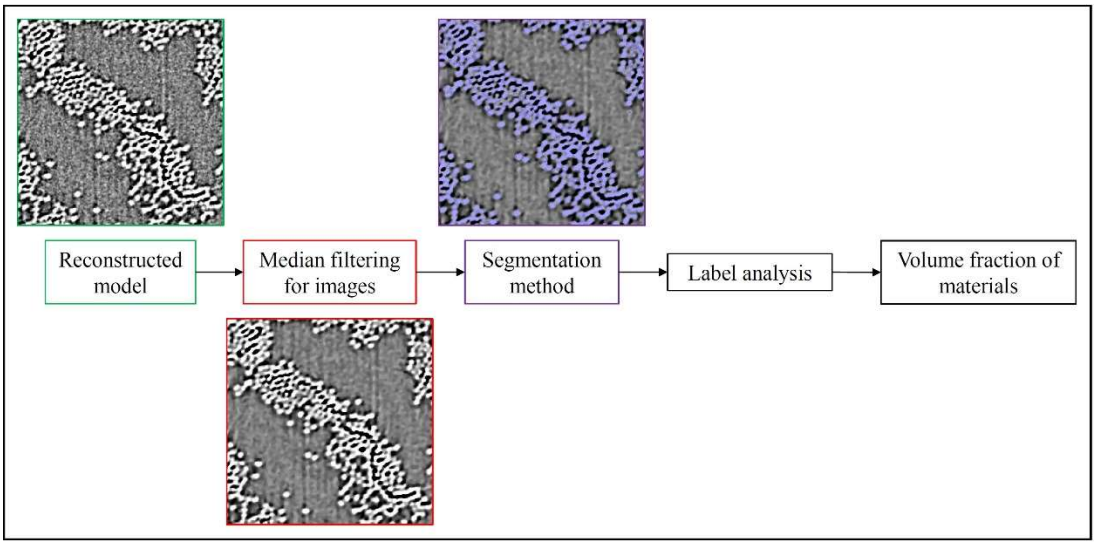

Figure 5-3 Steps of images processing and quantitative analysis

Then the segmentation method is used to separate void, fibres and matrix. The grey values are sorted from low to high, and the different materials can be segmented by changing the intensity range. In this study, the lowest grey value threshold is the void, the middle is the polyamide 6 and the highest is the fibres (in colour black, grey and purple, respectively), as shown in Figure 5-3. The application Label Analysis is used to label all the constituents detected from segmentation method and volume of them can be calculated, therefore volume fraction of different materials can be obtained.

5.4 Finite element modelling

A finite element (FE) model is established in ABAQUS/Explicit to further investigate the influence of turning angle and curvature radius on the printing quality of a single printed stripe. Also, the parametric studies about filament/tape width and fibre volume fraction are carried out to inform the design of 3D printing filament.

In real printing experiments, the original filament with a cylindrical shape (as shown in Figure 5-1a) is heated up in the heating chamber and passively pulled out as a result of the movement of the printer head. The printer nozzle exerts a contact pressure on the heated filament, changing the shape of the filament from cylindrical to roughly rectangular. As shown in Figure 5-4 (a), this process is reasonably simplified in the FE model by using a tape with a rectangular cross-section passing through a guide in the printer nozzle. The geometry and dimensions of the printer nozzle are informed from the measurement in μCT image as in Figure 5-1 (c), while the printing tape is assumed to have a width of 1 mm and a thickness of 0.1 mm according to the μCT image in Figure 5-5. The size of approximate global seeds is 0.05 mm so 20 elements per millimetre mesh in the longitudinal direction. The shell thickness is set to 0.1 mm in the thickness direction. In our modelling, the printer nozzle and the guide are both considered as rigid bodies. A total of 4000 S4R shell elements are adopted for the printing tape, with predefined cohesive properties for the printer bed to represent the bonding behaviour.

The printing tape is considered as transversely isotropic and assumed elastic, wherein the modulus of elasticity in fibre direction (E1) is calculated and determined in light of weighted average modulus of T300 carbon fibre and polyamide 6. A more sophisticated elastoplastic constitutive law for thermoplastic composites could be considered in the FE model but the challenges to determine the model parameters at elevated temperature make the model validation extremely difficult. Therefore, qualitative elastic analysis is mainly focused on the

modelling results at this stage. The modulus in transverse to fibre direction (E2) is four orders of magnitude smaller than E1, allowing relatively free deformations of fibre tape in the transverse direction, corresponding to the real printing process at a high temperature. Also, the default set of contact is used in the interaction between the tape, the nozzle, print bed and the guide, which is 'friction factor = 0.01' and 'hard contact' (only allow the transfer of compressive stress) for tangential and normal behaviour. In order to simulate the bonding condition between printing tape and printer bed, a cohesive contact is predefined between the contact surfaces. Previous research of AFP manufacturing process [111] is used as a source of reference and the material properties of the printing tape and interfacial parameters under 245-degree temperature are listed in Tables 5-2 & 5-3. Since the time-temperature superposition along with viscoelastic material properties is complicated and hard to decide, only properties measured at appropriate rates and temperatures for both fibre tape and interface are considered. Among them, interface parameters are increased by two orders of magnitudes considering the higher viscosity of thermoplastic PA-6 (approximately 120 Pa·s at 240°C [123]).

The simulation process is divided into 3 steps (Figure 5-4b & c) and the printer bed is always fixed in all steps. In step 1, the rigid nozzle moves downwards and presses the filament onto the printer bed. Only two translational degrees of freedoms (DOFs) are released for the nozzle, and an upward force (1 N) acts at end of filament above the nozzle to straighten the filament in the PTFE guide. After that, the gap between nozzle and printing bed reduces to 0.1 mm, and it is maintained for the rest of the simulation. In step 2, the nozzle moves 2 mm horizontally along the longitudinal direction of the composite printed on the bed. In step 3, the nozzle moves in another direction translationally with a specific turning angle or a curvature from those selected in the printing experiments in Section 2.

The FE model with those selected parameters is first qualitatively validated against the experimental measurements in terms of tape deformation and stress concentration, as will be

discussed in Section 5. Furthermore, the datasheet provided by TORAY company shows that the tensile strength of single T300 carbon fibre is 3530 MPa and strain at failure is 1.5%. According to typical elastic assumptions, the axial strain ε can be expressed as $|\varepsilon| = {}^{d}/_{2\rho}$ when a fibre with a diameter of d (7 μm) is bent to a curvature radius of ρ [36]. Supposing that fibres in the fused filament bend independently, the minimum curvature radius of T300 carbon fibre can be calculated as 233 μm. These data will also be compared with the modelling result, which acts as the supplement of the elastic model.

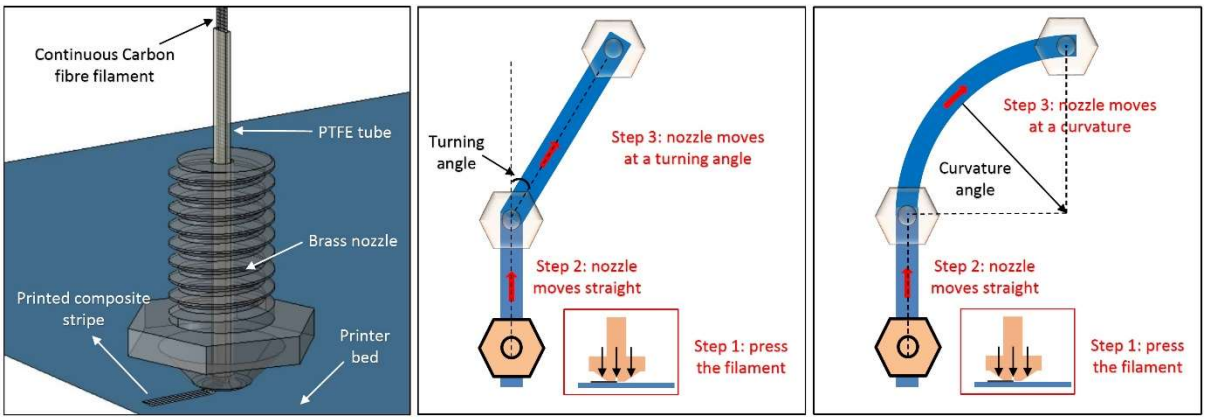

Figure 5-4 FE model of the printing process of CCFRP: (a) The assembled model, and (b) & (c) the simulation processes

Table 5-2 Mechanical properties of printed carbon fibre filament [111, 124]

Density	E_1	E_2	v_{12}	G_{12} & G_{23} & G_{13}
1.4 g/cm^3	31 GPa	4.6 MPa	0.2	30.25 MPa

Table 5-3 Interface parameters [125]

Cohesive stiffness K_{nn}, K_{tt}, K_{ss}	Maximum Stress	Fracture Energy
329.23 N/mm^3	38.52 MPa	0.868 N/mm

5.5. Results and discussion

5.5.1 Experimental observations

The shape of the printed straight stripe is like a flat ribbon because the filament is pressed on the bed by the tip of the nozzle during the printing process. The shape is also affected by the printing speed and the off-distance between the nozzle and the bed. With the printing parameters used in our study, the printed straight stripe is about 1.3 mm in width and 0.10 mm in thickness. The porosity at the central region of the stripe is measured as 1.39% in Avizo and the fibre volume fraction is approximately 20% (since the edge area of the printed stripe is too irregular to be measured).

As shown in Figure 5-5 (b), voids mainly appear between the fibres, which indicates the low adhesion between fibres and matrix in the printed CCFRP composites. In addition, more pores are found at the edges of the stripe in Figure 5-5 (b) & (c), which are likely due to the uneven pressure acting on the filament by the tip of the nozzle. Large gaps occasionally appear on the bottom surface of printed stripe, indicating a weak inter-laminar strength, which could be caused by the cooling within a very short time [126], too fast nozzle speed and/or insufficient compaction from the nozzle. The results reveal a lot of voids of the 3D-printed CCFRP composites and indicate the expected mechanical performance is hard to be achieved by the present 3D printing technique, compared with that obtained from traditional manufacturing with porosity <1% at a fibre volume fraction >50% [127, 128]. For instance, in hot compression moulding, the creation of the interfaces and the diffusion of the material is ensured since the material is kept under high-pressure levels at temperatures above T_g for a long period of time (280 °C for 3.5 min under a compression pressure of 4 kg/cm^2 for CF/polyamide 6 pre-impregnated sheets [128]). In addition to high porosity, misalignment of continuous fibres is also a serious issue, even when printing along a straight path, as shown in Figure 5-5 (a). All

these manufacturing induced defects would significantly reduce the stiffness (and strength) of the finished part, and in particular, the fibre misalignment would easily trigger the buckling failure of composites under compression loading [129, 130].

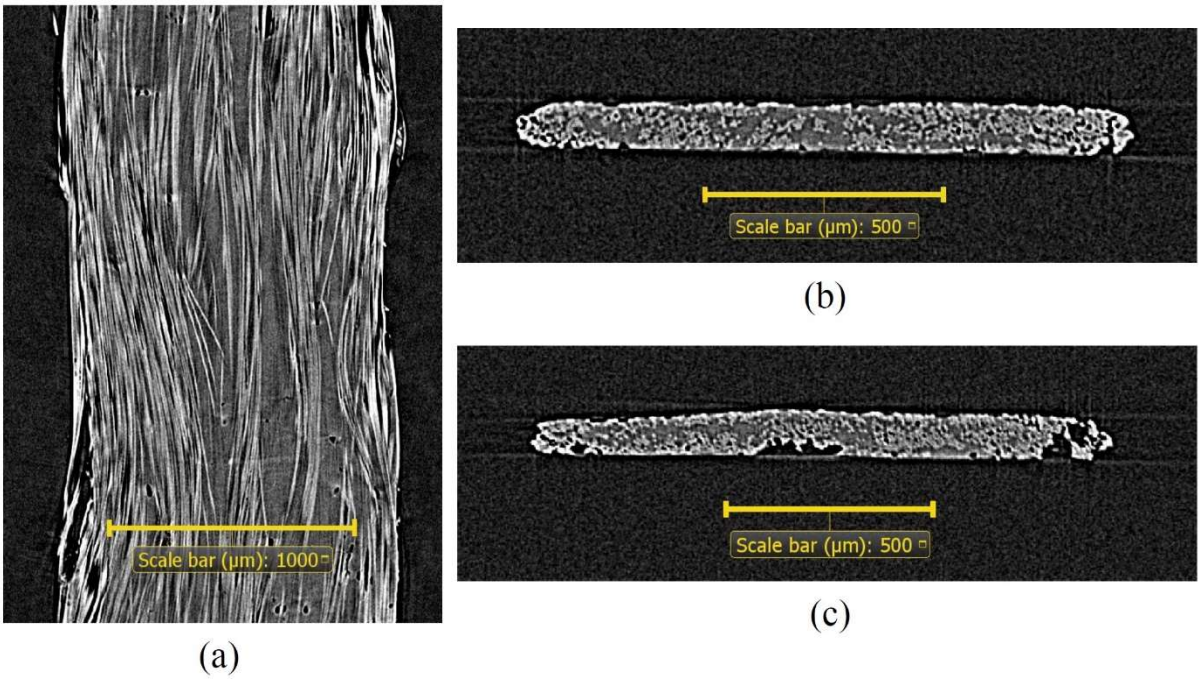

Figure 5-5 μCT images of a printed straight stripe: (a) overview and (b) & (c) cross sections

The μCT images of a single stripe at different turning angle (30°, 60° and 90°) are shown in Figure 5-6, wherein the dashed lines show some of the representative fibres in the bundle of each case and the black points indicate the location where the nozzle was turned. With a turning angle 30°, the filament is flattened on the bed as a tape, in which the actual turning angles of most continuous fibres are consistent but slightly smaller than 30°. The inaccuracy of the printing path is likely caused by the unmatched diameters between the nozzle and the filament (1.3 mm and 0.375 mm, respectively), which also makes a curved section rather than a turning point with a specific angle in this case. It can be seen that no folded section is formed when printing at such a small turning angle, but different deformation between the continuous fibres

at outer and inner edges of the bundle is observed, *i.e.*, fibres in the inner periphery are slightly twisted and wrinkled while fibres in the outer periphery are stretched in tension because of the force received from the print nozzle.

As the turning angle increases, the inaccuracy of the printing path becomes more apparent. As shown in Figure 5-6 (b) & (c) for the turning angles of 60° and 90°, paramount and complex deformation of fibre bundles is observed. Folding of fibre bundles starts to occur when the turning angle increases to 60°, in which some continuous fibres at the outer periphery are misaligned and then flipped over to the inner periphery. The folding scenario is assumed to be caused by the twisting torque due to the adhesive force from the printer bed and tensile force from the printer nozzle [33]. However, no noticeable fibre breakage is found in the printed stripes with a turning angle up to 90°, in which the folding of curved fibres may play a protective role.

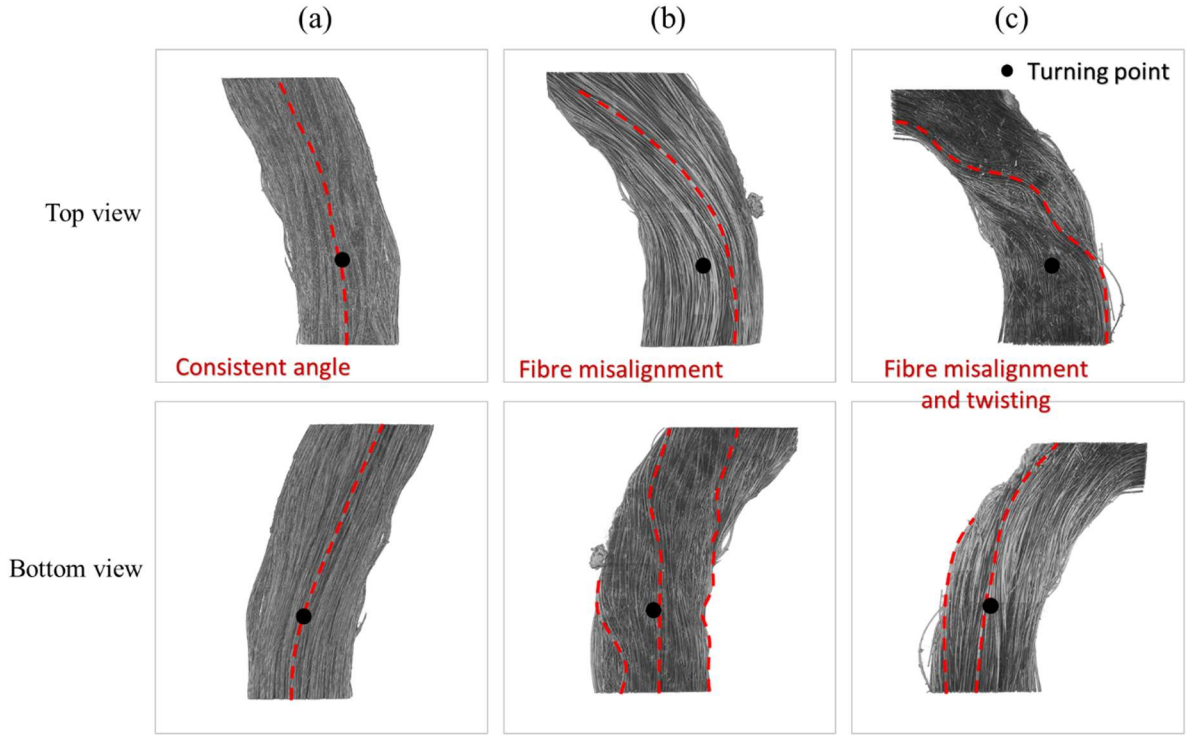

Figure 5-6 3D-printed carbon fibre filament a turning angle of (a) 30° (b) 60° and(c) 90°

As the turning angle further increases to 120°, noticeable folding can be seen at the turning point of the printed filament, which is accompanied with a complete switch of the inner and outer circumferences before and after the curved section. Also, the average width of the printed filament is reduced due to the folding at the turning point, as shown in Figure 5-7 (a). This could enlarge the gaps between the printing stripes and cause large fibreless areas, thus leading to a local weakness in the parts with complex geometries [6]. At the turning angles of 150° and 180°, the fibres are severely twisted and misaligned, and more importantly, the fibre breakages are observed. As shown in Figure 5-7 (b), a matrix rich area is created and the excessive overlap of continuous fibres causes the upheaval of printed filament at the turning point. The printing process could be terminated due to the fibre breakage and upheaval of printed filament. These results also indicate that even if the filament can be printed out at such turning angles the mechanical properties would have much deteriorated at the curved section.

In summary, the μCT scans show the error of the printing path increases as the turning angle alters from 30° to 120°. Also, the printing induced defects such as fibre wrinkling, twisting and folding become more severe. However, in the printing cases with a turning angle no more than 120°, no noticeable fibre breakages are seen for the specific printing parameters and filaments used therein, which may benefit from the folding of the fibres at the curved section. In the samples with turning angles of 150° and 180°, fibre breakage and significant change of thickness can be seen at the turning section, which means such large turning angles should be avoided in the path design of continuous fibre printing.

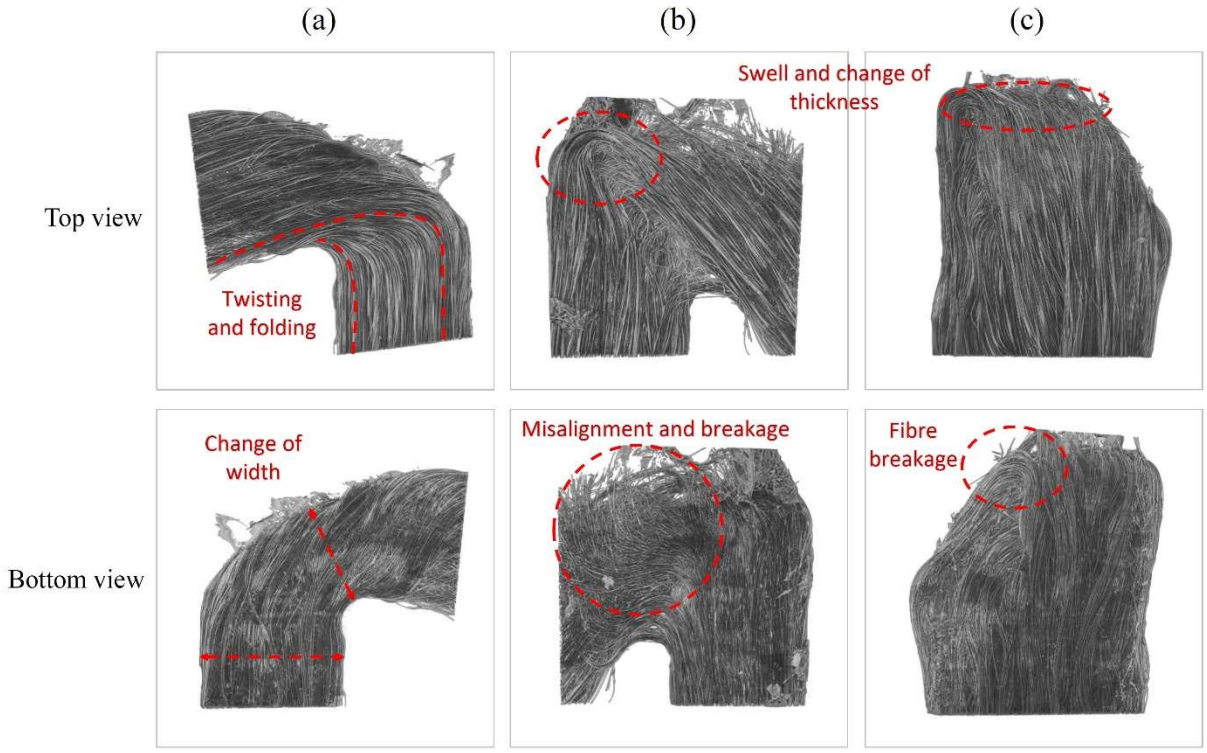

Figure 5-7 3D-printed carbon fibre filament a turning angle of (a) 120° (b) 150° and (c) 180°

For the printed stripes with various curvatures, optical microscopy was used to give a larger view and more information about manufacturing induced defects. Same printing parameters are used as in the cases with turning angles. The results with curvature radii of 2.5, 5, 10 and 20 mm are shown in Figure 5-8. For the single stripe with a curvature radius of 20 mm, no obvious surface defects can be observed and the width of the single stripe is roughly consistent along the printing direction. In the case with 10 mm, fibres in the inner periphery are twisted and wrinkled. When it comes to 5 mm, these two defects appear more frequently. For the case with a curvature radius of 2.5 mm, the single stripe can hardly be printed properly on the bed as designed paths and the folding phenomenon with a complete switch of the inner and outer circumferences is observed. Also, a small number of fibres are broken in the cases with a curvature radius of 5 and 2.5 mm, although the printing curvatures are smaller than the minimum curvature (233 μm) obtained from the calculation with typical elastic assumptions.

Therefore, the fibre breakage is more likely to be caused by the shear stress in the printing process, which will be further investigated in the modelling section.

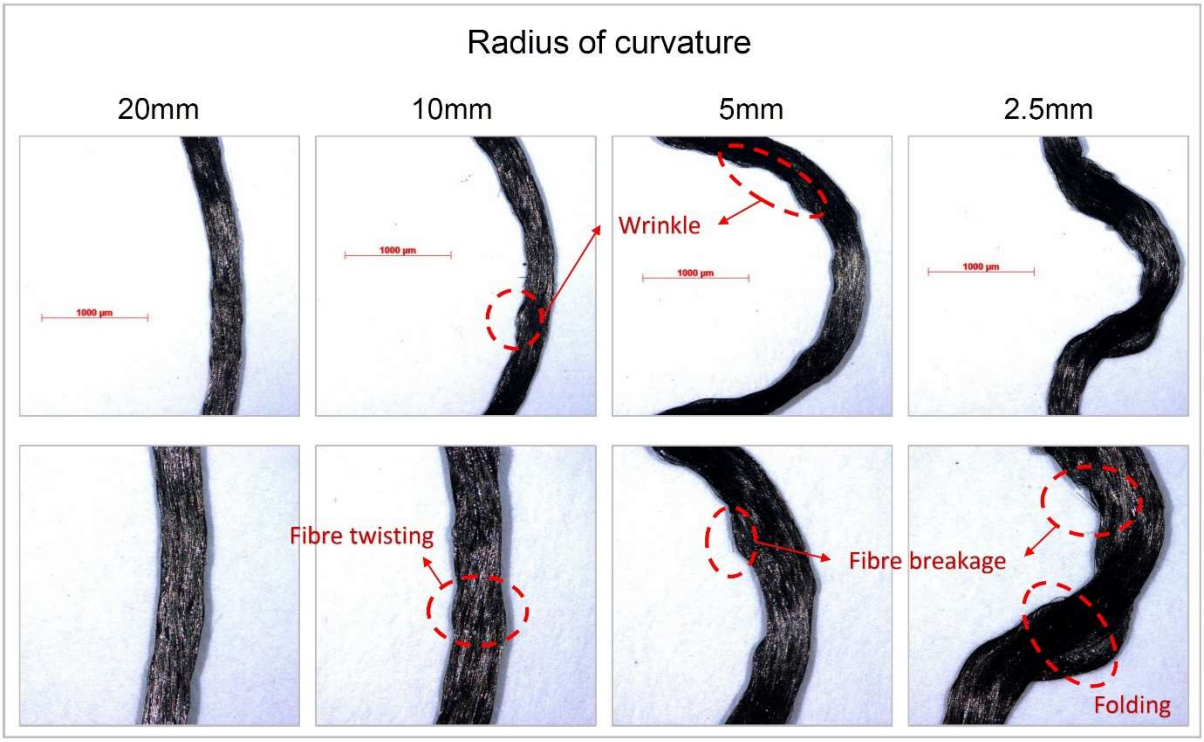

Figure 5-8 Optical microscopy images of the printed composites with various curvature radius (length of the scale bar in figure = 1000 μm)

5.5.2 FE modelling

The mechanism of 3D printing continuous fibre is further investigated by FE modelling. As shown in Figure 9, the comparison between the printed straight stripe and the printed stripe at a turning angle of 30° is presented. The distribution of three stress components is discussed. The stress in the fibre direction S11 is the component with the maximum value, which is also used to interpret the deformation of continuous fibres in the printing process. The shear stress S12 indicates the possibility of fibre breakage (although no fibre breakage can be observed in this simulation because only elastic properties of fibre tape are considered). As the tape has

much higher strengths in the fibre direction, fibre breakages are more likely caused by the shear stress in our studied process. The distribution of pressure reflects the force received from the nozzle and print bed, which determines the mechanical response of fibre tape in the printing process.

To better view stress distributions in the fibre tape, the rigid nozzle is hidden from visualisation. As shown in Figure 5-9, the two stress components (S11 and S12) are not evenly distributed in the cross-section transverse to the printing direction, which is likely the reason for the fibre misalignment as well as the gaps between the tape and printer bed (as shown in Figure 5-5). The contact pressure on the fibre tape is studied further, including compressive force received from the nozzle and cohesive force received from the print bed (red circle 1 and 2, respectively). As can be seen, the front edge (black dashed line) of the cohesive area is not perpendicular to the printing direction, due to the circular outlet of the nozzle which also results in the printing defects such as void rich area at the edges of the stripe (as shown in Figure 5-7 from CT images). When the fibre tape is printed at an angle, the concentration of S11 and S12 is aggravated in the curved section, indicating the more severe deformation and potential fibre breakage. Meanwhile, the absolute value of cohesive force received from the printer bed increases significantly and concentrates on the outer edge of the curved section, which indicates the trend of de-bonding in this area with a high absolute value of the cohesive force. However, the compressive pressure received from the printer nozzle increases slightly in the case with a turning angle. Since we focus more on the bonding between the bed and tapes rather than the compressive force from the nozzle (fibres would not be damaged by pressure in our printing), the pressure shown in the following discussion will be the absolute value of the cohesive force received from the print bed.

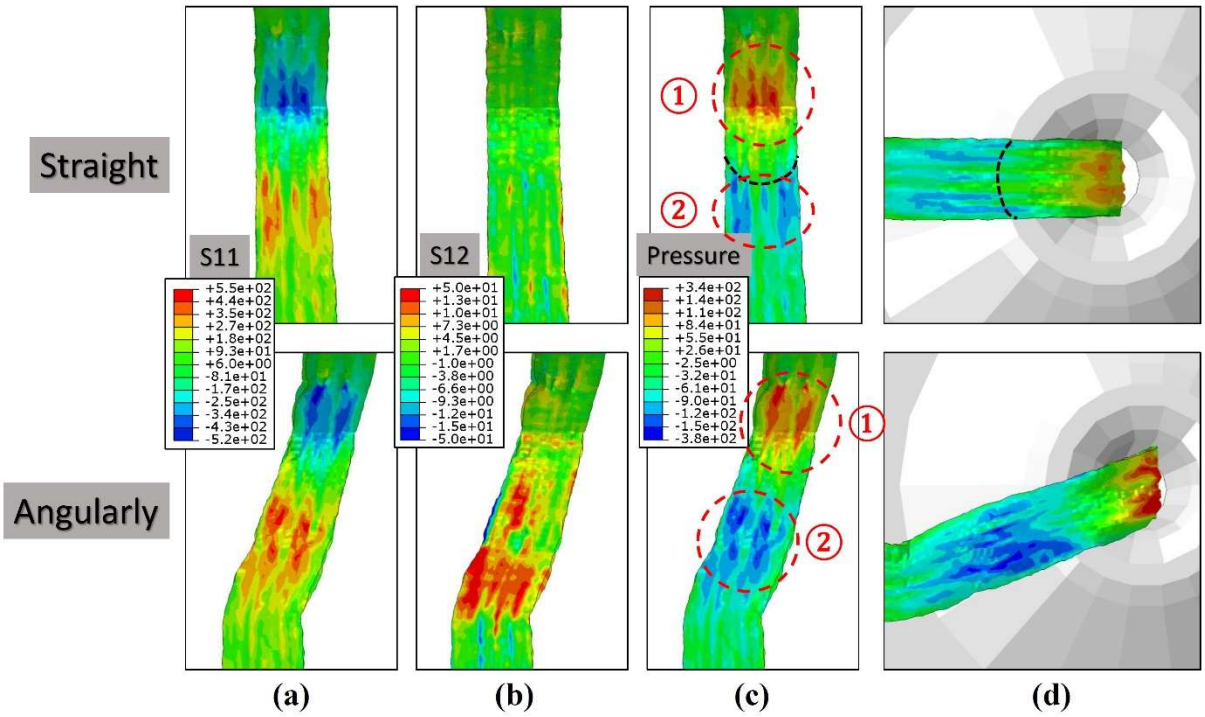

Figure 5-9 Mechanism analysis of 3D printing continuous fibre tape straight and angularly (30°): (a) S11, (b) S12, (c) contact pressure and (d) bottom view.

Figure 5-10 presents FE modelling results for the distribution of S11 in printed continuous fibres tape at various turning angles. From 15º to 75º, stress concentration exists at the curved section and the maximum value gradually increases as the turning angle becomes larger. With small turning angles such as 15º and 30º, the tape can be printed entirely on the bed with a more-or-less constant width and the location of maximum stress is close to the outer edge of the curved section, which is consistent with the μCT scanning result in Figure 5-6 (a). With a relatively larger turning angles 45º-75º, the location of maximum stress gradually shifts to the inner edge of the curved section, while the outer edge of the tape lifts and no longer sticks on the bed (the black circle in Figure 5-10). Also, the values of three stress components have a sharp rise from the turning angle 45º. This is in good agreement μCT scans in Figure 5-6 (b), showing fibre twisting and folding. It is revealed that the folding occurs because of the de-

bonding between the tape and the printer bed and the excessive tensile force from the nozzle. When turning angle increases to 90º, the width of printed tape in the simulation is enlarged because of the excessive tensile force, but the 'swap' of the inner and outer edges observed in experiments cannot be simulated. Since the filament is simplified as a tape with a rectangular cross-section in our FE model and shell elements are used to simulate the tape, only the initiation of folding phenomenon can be captured. Similar results occur in the modelling cases with a turning angle larger than 90º, thus these results are not shown in this discussion section. The S11 (macro) stress obtained from the simulation can be compared with the recalculated fibre tensile strength based on the fibre volume fraction (3530 * 20% = 706 MPa), in order to evaluate the possibility of fibre breakage. The maximum value of S11 rises sharply and exceeds the recalculated strength in the cases with turning angle 60º and 75º, and it decreases to 552 MPa in the case with 90º truing angle due to the tape model used in the simulation, which all indicates a strong possibility of fibre breakage. Compared with the experimental result from μCT-scan, it also reveals that the fibre misalignment in the fused filament and the unmatched diameter do protect continuous fibres from breakage, although they cause some defeats such as the inaccuracy of the paths.

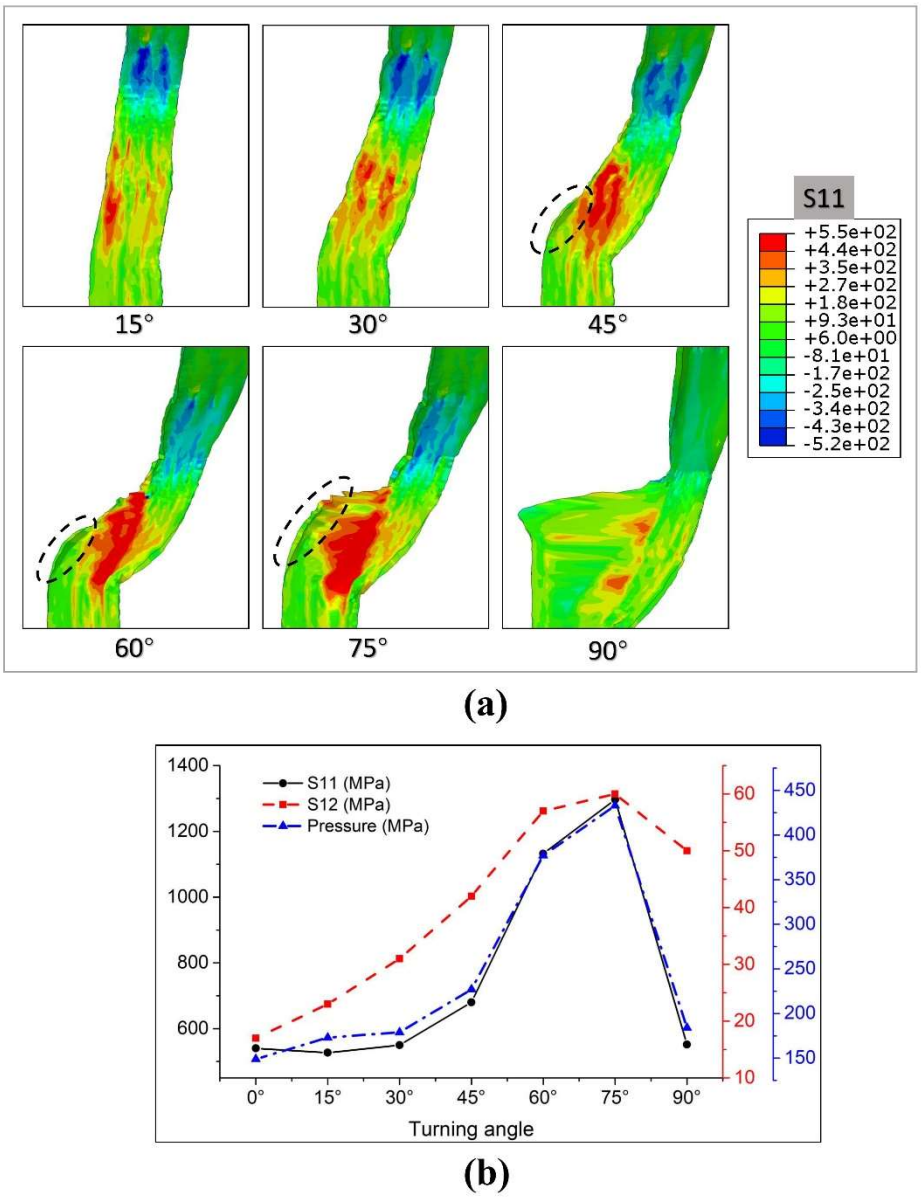

Figure 5-10 Stress distributions in printed tapes at various turning angles (from 15° to 90°): (a) Distribution of S11 (b) Maximum values of three stress components

Figure 5-11 presents the distribution of shear stress S12 in printed tapes at various curvatures. With the decrease of curvature radius from 20 mm to 2.5 mm, the area with a high value of shear stress extends gradually. As mentioned before, the increase of maximum values of shear stress indicates a greater possibility of fibre breakage. It is also consistent with the result from

optical microscopy in Figure 5-8, wherein the fibre breakage was captured in the cases with curvature radius 5 mm and 2.5 mm. Since the curvature radiuses used in the modelling cases are larger than the minimum curvature radius calculated by the typical elastic assumptions, the fibre breakages are more likely to be caused by the shear stress rather than the axial stress in the fibre direction. When the curvature radius comes to 10 mm, 5 mm and 2.5 mm, the wrinkling of the tape appears in the inner periphery (black circles in Figure 5-11), also with a higher frequency as the curvature radius decreases, which is in good agreement with the experimental result in Figure 5-8.

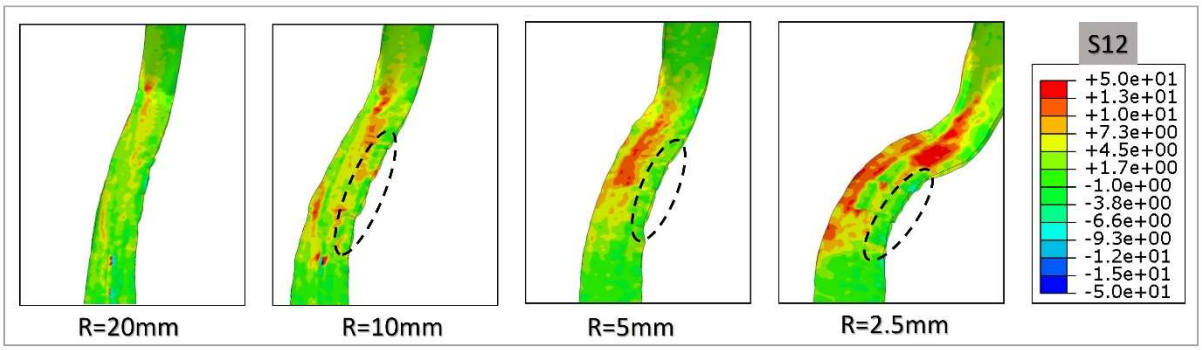

(a)

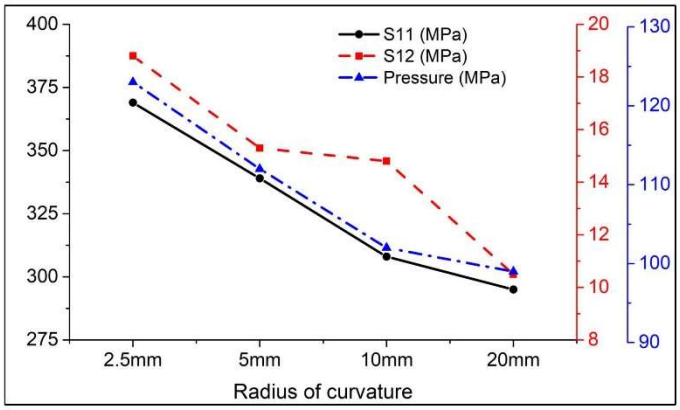

(b)

Figure 5-11 Stress distributions in printed tapes at various curvature (Radius of curvature from 20 mm to 2.5 mm): (a) Distribution of S12 (b) Maximum values of three stress components

5.5.3 Parametric studies of tape width and fibre volume fraction

The first parametric study is the influence of the fibre bundle size on the printing process. In the real 3D printing process, the width of the printed tape is determined by the fibre bundle size and the off-distance between print bed and nozzle. Printing experiments of 1 mm, 2 mm and 3 mm tapes are simulated with 30° turning angle and 0.1 mm off-distance (the diameter of the nozzle outlet is scaled up accordingly). As shown in Figure 5-12, the increase of width to 2 mm or 3 mm enlarges the area with a high value of S12. This indicates that fibre misalignment and breakage are more likely to be induced when using a larger fibre bundle size. The maximum values of three stress components increase approximately linearly, but the deformation of the curved section in these three cases are very similar.

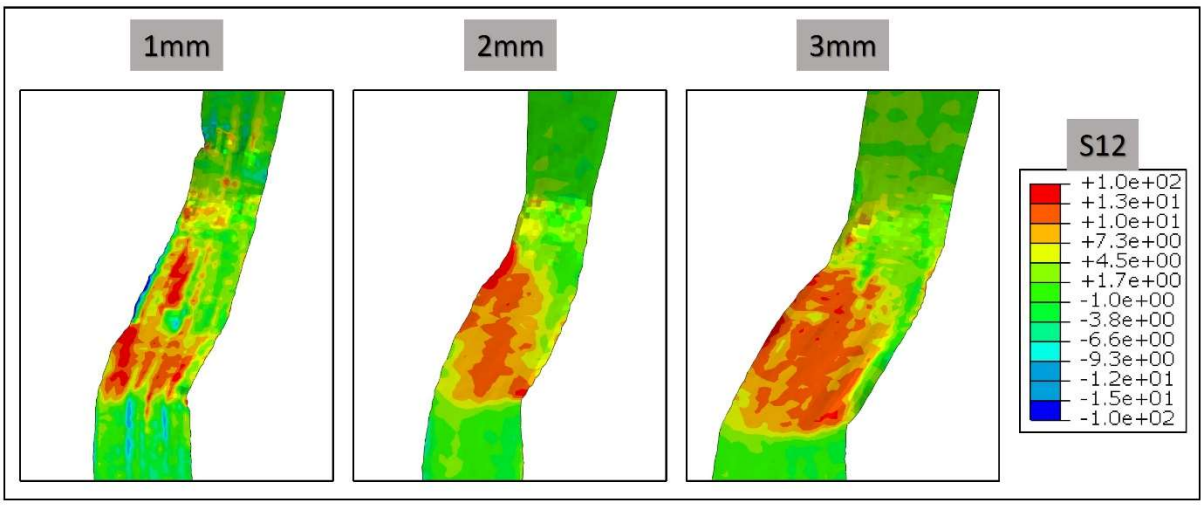

(a)

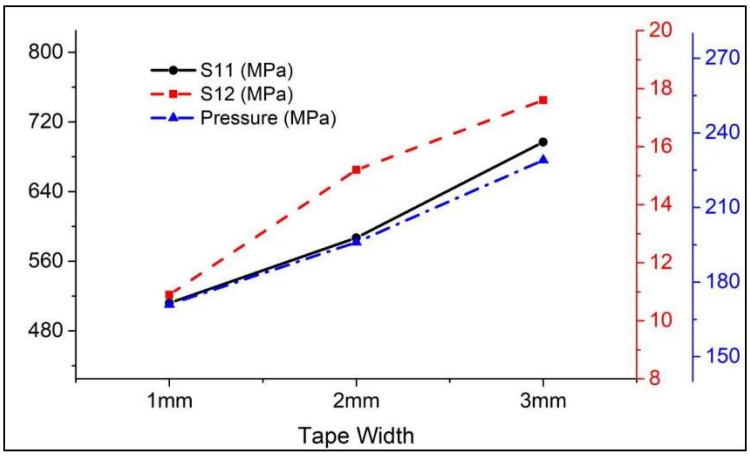

(b)

Figure 5-12 Comparison of FE modelling results at 30° turning angle between different tape widths: (a) Distribution of S12 (b) Maximum values of three stress components

Another investigated parameter is the fibre volume fraction of filament. Since the filament is heated to 250°C to melt the PA6 thermoplastic matrix in the printing process, the fibre volume fraction mainly affects the elastic modulus in fibre direction (E1). In this parametric study, 0.5-, 1- and 1.5-times elastic modulus are used, representing equivalent fibre volume fraction V_f of 15%, 25% and 40% approximately (The V_f of commercial filaments with 1K continuous carbon fibres is usually between 20% to 30%). As shown in Figure 5-13, the three stress

components increase significantly as a higher fibre fraction is used. With 1.5-times elastic modulus, the widening of the curved section is similar to that in the cases with large turning angles (> 90º), which means the increase of fibre volume fraction has a great influence on the defect formation. The sharp increase of S11 stress to 2001 MPa also indicates the fibre breakage. It is therefore suggested that when printing composite filaments with high fibre volume fractions, the printing defects including shape inaccuracy, fibre folding and breakage, would happen at a relatively small turning angle, even using a small fibre bundle size.

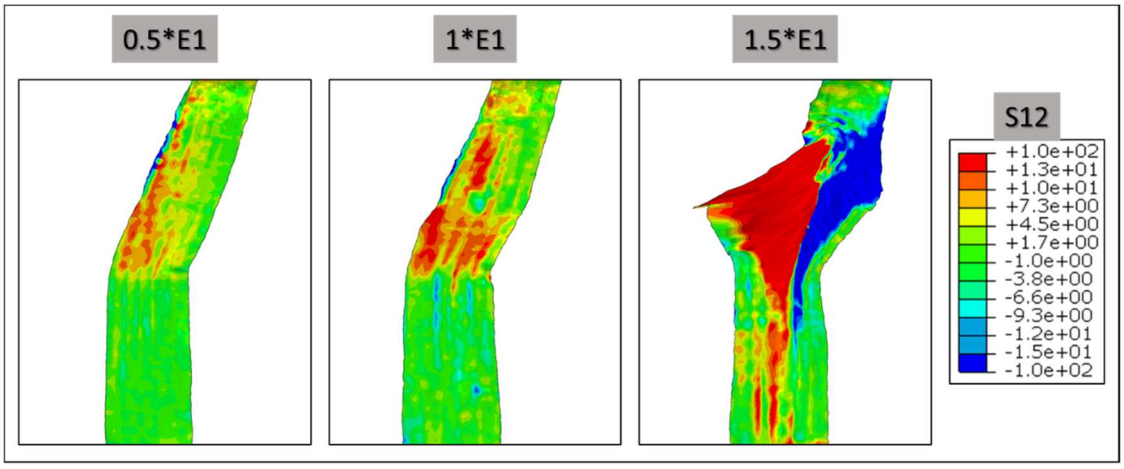

(a)

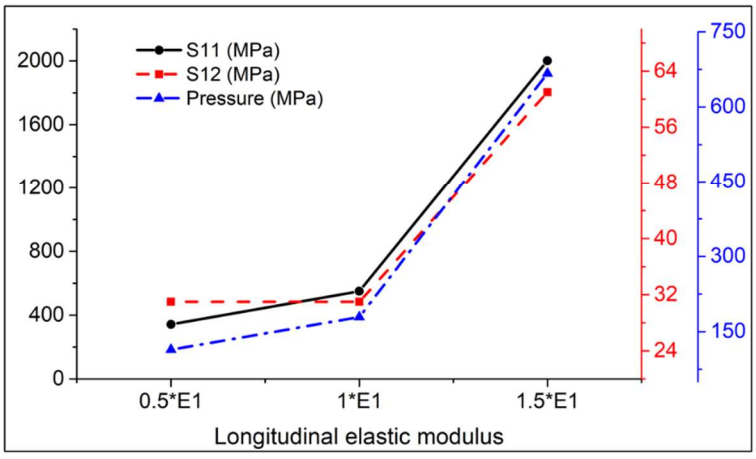

(b)

Figure 5-13 FE Modelling results at 30° turning angle with different elastic modulus in fibre direction: (a) Distribution of S12 (b) Maximum values of three stress components

5.6 Conclusions

This chapter investigates the mechanism of 3D printing continuous carbon fibre filament from both experiments and numerical simulations. In the straight-printed stripe, high porosity and fibre misalignment are observed, which is caused by the weak interface of materials and the uneven pressure from the tip of the nozzle. When fibre tapes are printed with a small turning angle or curvature, filaments can be flattened on the bed with nearly constant width and fibre paths. As the turning angle and curvature increases, multiple printing defects occur and aggravate, including path error, fibre twisting, folding and misalignment, caused by the excessive tensile force from the nozzle, de-bonding with the print bed and the inconsistent diameter of nozzle outlet and fibre filament.

In the samples with angles >120° and curvature radius < 5mm, fibre breakage and the significant change of thickness can be seen, which means such turning angles and curvatures should be avoided in the paths design of the continuous fibre printing. The good agreement between experimental and numerical results also indicates the FE model could offer a useful tool for analysing the printing process of continuous fibre filament. Further parametric studies show that the increase of fibre bundle size would aggravate the printing defects including fibre misalignment and breakage. The deformations of printed stripes are approximately the same in the cases with 30° turning angle. The increase of fibre volume fraction has a great influence on the defect formation. Some printing defects observed only in the cases with large turning angles, such as shape inaccuracy and fibre folding, would appear in the cases with higher fibre volume fractions when printing at a relatively small turning angle and fibre bundle size.

Other printing parameters worth studying, such as nozzle speed and off-distance, would also influence the quality of finished CCFRP composites. Part of printing defects, for example, filament folding and fibre breakage, can not be observed directly in the current model, since

only elastic properties and shell elements are used to simulate the simplified tape. Therefore, the FE model should be improved to better investigate the alignment and breakage of fibres in the printing process. Future research is still required to address those issues and inform the design of 3D printing process for continuous fibre reinforced composites.

Chapter 6 Hybrid manufacturing of curved continuous carbon fibre reinforced dual-polymer composites [*]

Abstract

A hybrid technique was developed to manufacture curved continuous carbon fibre reinforced composites based on 3D printing, vacuum bagging and oven curing. Composite preforms were first manufactured by fused filament fabrication (FFF) 3D printing of continuous carbon fibre reinforced thermoplastic polyamide-6 (PA-6) filaments. Powder thermoset epoxy was added to the preforms to fill up the gaps, remove air voids and enhance the interfacial bonding through a traditional vacuum bagging and oven curing process. Uniaxial tensile tests showed that the stiffness and strength of the printed composites were increased by 29.3% and 22.1%, respectively, compared to the thermoplastic-only composite specimens. The hybrid manufacturing technique was also adopted to investigate the performance of 3D-printed curved continuous fibres in a notched specimen under uniaxial tension. It was shown that the placement of continuous carbon fibres along the principal stress trajectories increased the failure strength and the fracture toughness of the composites by 81% and 157%, respectively, compared to the unidirectional and the concentric placement methods.

Keywords

Fused filament fabrication; 3D printing; vacuum-bag-only (VBO) dual polymer composites; principal stress trajectory, thermoplastics, thermosets.

[*] This chapter was submitted to Composites Part B in July 2021.

6.1 Introduction

3D printing of composites has seen fast development in the past decades, as it offers the benefits to manufacture complex composite products at low cost for fixtures, tools, moulds as well as load-bearing structures [1]. One of the most attractive printing techniques is the fused filament fabrication (FFF) of continuous carbon fibre reinforced thermoplastic (cCFRTP) composites, where the filament is melted and deposited layer by layer to form a 3D composite part [131]. As the printing path can be customised, FFF 3D printing has the potential to manufacture highly complex composite structures that can hardly be manufactured by conventional manufacturing techniques [43, 116].

One of the challenging issues for FFF 3D printing of cCFRTP composites, however, is the weak fibre/matrix interface, as well as the high viscosity of the plastic matrix which can induce substantial air voids [3, 6]. This usually results in the printed composites having less competitive strength and stiffness than traditionally manufactured cCFRTP by press or autoclave moulding. For example, the commercial 3D printer Mark Two from Markforged® is capable of printing continuous CF/PA6 filament, but the uniaxial tensile strength of the printed composites is 30% lower than traditionally manufactured cCFRTP with the same polymer matrix and fibre volume fraction [19, 20]. Post-printing techniques have been reported to compact the printed composites and thus improve their mechanical properties, *e.g*. hot-press [58, 59]. Other *in situ* consolidation techniques have also been reported, *e.g*. micro-screw [56], microwave enhanced consolidation [15], roller compaction [53], *etc*.

Research has also been carried out to optimise the printing paths in order to maximise the reinforcement of the continuous carbon fibres. For example, placement of fibres along principal stress trajectories [43], and optimisation of the fibre orientation together with optimisation of the structural topology [51] have been demonstrated. When such printing paths are customised,

there are gaps between the printing paths at some locations [14]. An infill technique therefore needs to be adopted to bridge the gaps between the printed fibre tows and to ensure the structural integrity of the printed composites. The aforementioned hot-press technique is less attractive, as it would require a mould as well as additional thermoplastic materials that have a low melting temperature thermoplastic matrix in the printed composite preform, in order that the fibres can be stabilised during the press-moulding step.

In this study, we present a low-cost hybrid manufacturing technique to address this issue. Instead of using thermoplastic fillers and a hot press process, a low viscosity powder epoxy is used to fill up the gaps and to enhance the composite properties after consolidation by vacuum bagging and oven curing. The solid state powder epoxy is easy to store (without the need of refrigeration as with liquid epoxy resins) and its low viscosity and lower melt and curing temperature [132] allows the printed fibres to be stabilised on their designed printing paths.

This chapter is organised as follows. Section 2 introduces the manufacturing processes of 3D printing of CF/PA-6 preforms and the post-processing with powder epoxy. Section 3 presents the set-up of uniaxial tensile tests and the design of cases, including the UD 0˚ samples and the single-edge notched samples. The result and discussion section first compares the mechanical performance of the UD 0˚ samples before and after the post-processing. Characterisation of the cross-sections and fracture profiles is carried out via scanning electron microscopy (SEM). The experimental results for the tests of single-edge notched plates are then shown, including the strength, fracture toughness and strain distribution obtained from the digital image correlation (DIC), in order to evaluate the improvement brought from the optimised fibre placement.

6.2 Hybrid manufacturing

6.2.1 3D printing of CF/PA-6 preforms

A Prusa i3 MK3s printer was used in this study and the schematic diagram of 3D printing

CF/PA-6 composite preforms is shown in Figure 6-1(a). The printing material, 0.375mm-diameter 1K carbon fibre (CF) filament, was sourced from Markforged® (Massachusetts, USA). Previous authors had evidenced that polyamide 6-I (PA6-I) was the polymer matrix for CF filaments and the polymer coating was a polyamide 6 (PA6) [7]. The cross-section of the filament is shown in Figure 6-1(b), in which noticeable air bubble and voids trapped around the carbon fibres were observed. The volume fraction of carbon fibres V_f was measured as 21.34% [25]. In the FFF 3D printing process, the CF filaments were heated to the temperature of 245°C and the off-distance between the nozzle tip and the print bed was set to 0.1 mm, which is the same as the printing setting of Markforged system for this type of CF filament (the melting point of PA-6 is about 215°C). The speed of nozzle movement was consistent with the 10mm/s feed rate of the filament, which means the free end of the CF filament is slightly under tension due to the twine of the spool, but the feeding of filament is not affected. Samples were printed onto an unheated Garolite print plate which was coated in a layer of PVA, to ensure adequate adhesion during printing. Since the filaments used in this study contain continuous fibres and the toolpath cannot be started and stopped during the printing, the continuous toolpath (G-code) was necessary. It was generated via MATLAB and then transferred to the printer.

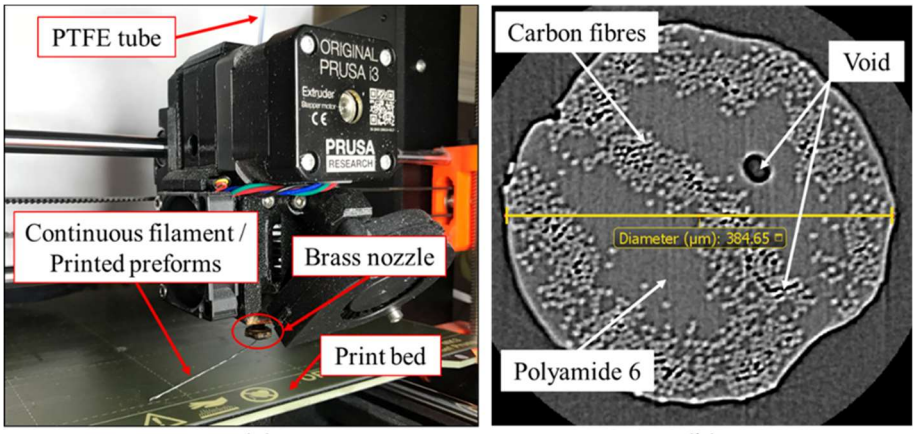

Figure 6-1 (a) Schematic diagram for 3D printing of composites CF/PA-6 preforms (b) the

cross-section of the CF filament

6.2.2 Post processing of thermoplastic-thermosetting dual matrix composites

The thermosetting epoxy powder (PE6405, density 1.22 g/cm3) has been engineered by Swiss CMT (Siebnen, Switzerland) and then produced by FreiLacke (Bräunlingen, Germany). As shown by Differential Scanning Calorimetry (DSC) characterisation in Figure 6-2(a), the epoxy sinters and melts at around 45-60 °C. The low melt viscosity (minimum of 1.26 Pa·s at 120°C) and low rate of cure below 120 °C allow more time to fully infuse the CF/PA-6 preforms [132]. Then the curing is carried out through a heat activated catalytic process, where the curing agent requires a temperature of at least 150 °C for reaction initiation [133, 134].

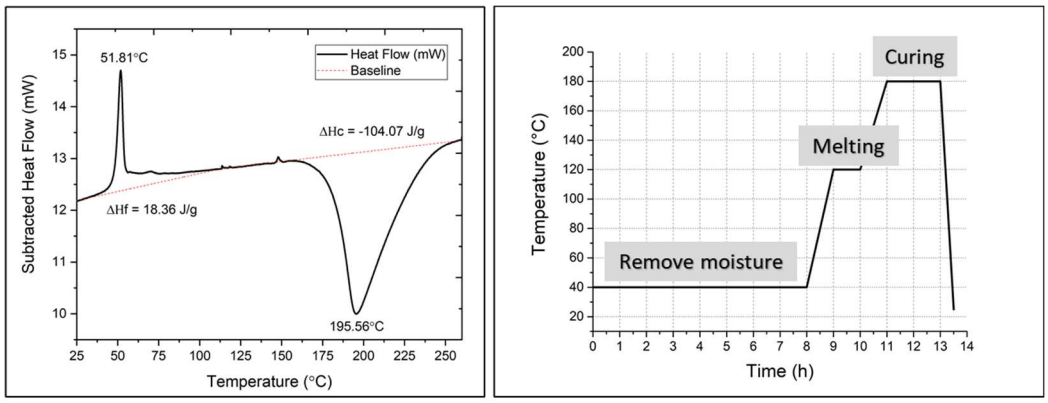

Figure 6-2 (a) DSC characterisation of the PE6405 epoxy powder [132] (b) the heat cycling of the post-processing

As shown in Figure 6-3(a), the aluminium-made plate with a polytetrafluoroethylene (PTFE) non-stick ply was used as the bottom mould. The powder-epoxy was sprinkled manually, only on top of the printed CF/PA-6 preforms, allowing to fill the voids due to a very low viscosity of melted epoxy [133] since the preforms in our study were thin. For the samples with larger

thickness (that were composed of more than two CF/PA-6 preforms), powder was sprinkled between the preforms to enhance the adhesion. The peel ply and breather fabric allowed to remove melted powder epoxy excess. As shown in Figure 6-3(b), the 3D-printed CF/PA-6 preforms with sprinkled powders were vacuum-bagged and then put into an oven for heating. Since the melting/sintering temperature of PE6405 epoxy is considerably lower than the curing temperatures, a three-stage heating profile was typically used as presented in Figure 6-2(b). The pre-curing cycle was set at 40 °C for 8 hours to remove all possible moisture from the powder. The temperature was then ramped to 120 °C for 1 hour, melting the powder. Following this, the plate was cured at 180 °C for 2 hours.

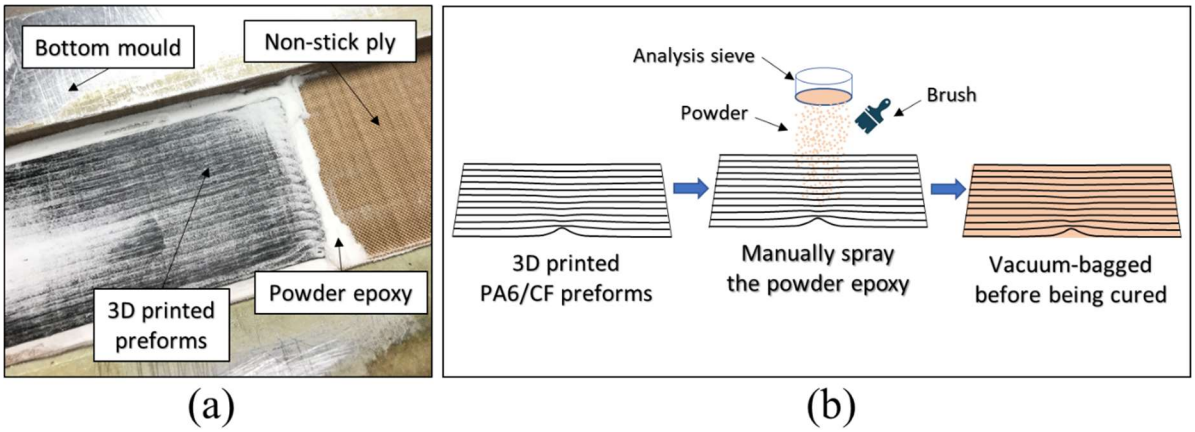

Figure 6-3 (a) Bottom mould and printed CF/PA-6 preforms with sprinkled powders (b) the schematic diagram of the post-processing treatment

6.3 Mechanical testing

6.3.1 Instruments and 2D-DIC set-up

The mechanical tests were performed using an MTS Criterion® Model 45 (C45.305) with a 300 kN load cell. A crosshead speed of 0.5 mm/min was used for all tests and the samples were clamped in hydraulic grips with a clamping pressure of approx. 80 bar. In each type of test,

three specimens were tested. A speckle pattern was applied to the surface of each specimen for the digital image correlation (DIC). All the data obtained from the 2D video extensometer were processed through a MATLAB script to measure full-field displacement and strains [135].

6.3.2 Uniaxial tensile tests

The uniaxial tensile tests of the Unidirectional (UD) 0˚ samples were carried out according to ASTM D3039 (Standard Test Method for Tensile Properties of Polymer Matrix Composite) to study the tensile strength and stiffness of samples before and after post-processing. The length, width and thickness of the samples were 200mm, 15mm and 1mm, respectively. End tabs with a length of 50mm were used when testing these unidirectional materials. Since the thickness of the printing layer is 0.15mm approximately, eight layers with 0° unidirectional fibres were printed for each sample. The tensile strength and stiffness will be calculated based on the measured dimensions of each sample.

Uniaxial tensile tests of single-edge notched plates were also conducted as another case study. The performance of optimised fibre placement along principal stress trajectories, including the strength and fracture toughness, was investigated and compared with the unidirectional and the concentric placement methods. The dimensions of the single-edge notched samples are 200mm-length, 36mm-width and 1mm-thickness. A single-edge notch is designed in the horizontal centreline of the plate with the 4mm-length and 4mm-width. The fibre placement of these three kinds of single-edge notched samples are shown in Figure 6-4. Concentric placement (Figure 6-4b) is the most popular method for the FFF 3D printing of thermoplastic materials, in order to achieve a better surface and the densest infill for the 3D-printed composites with complex geometries. It was also used in the Eiger system for Markforged 3D printing of continuous fibres [72]. For the unidirectional placement in Figure 6-4(a), the 4*4 mm notch would be milled mechanically by a wet saw. As for the optimised placement method

(in Figure 6-4c), the principal stress trajectories were generated through finite element analysis (FEA) and used as the guidance of the fibre paths, which was demonstrated the stiffness would be improved and the stress concentration would be eased [43].

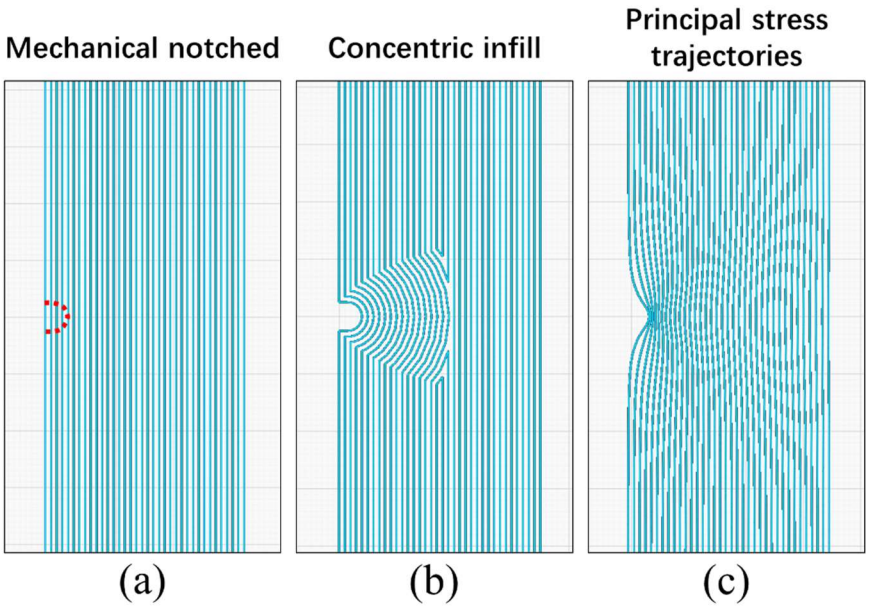

Figure 6-4 Fibre placement of three kinds of single-edge notched samples: (a) Mechanical notched (b) Concentric infill (c) Principal stress trajectories

6.4 Results and discussion

In this section, the thermal properties of dual-polymer composites are first presented. Then the SEM characterisation for the cross-section of UD 0˚ samples is presented to reveal the porosity and bonding condition before and after the post-processing. For the results of the mechanical tests, the tensile properties and the fracture profiles of the standard UD 0˚ samples are first presented for comparison purpose (before and after post-processing). Then the notched samples after post-processing are demonstrated to discuss the effect of different fibre placement methods.

6.4.1 Material characterisation

6.4.1.1 Thermal and microstructure characterisation

The results of Dynamic Mechanical Analysis (DMA) for the CF/PA-6 printed preforms and the dual-polymer composites are shown in Figure 6-5. The dual cantilever mode was conducted using a PerkinElmer® DMA 8000, with the temperature ramp of 2 °C/min from 50 °C to 160 °C. For the CF/PA-6 printed preforms, the onset of the rubbery state was about 80 °C and reached to its glass transition point T_g (first peak of the tan delta) at 102.3 °C. Then the material transited to the viscous state quickly, with the viscous flow temperature (second peak of the tan delta) of 128.0 °C. The uneven surface of samples after DMA (in Figure 6-5a) also indicated the plastic deformation of the material during the viscous state. This thermal-mechanical behaviour of CF/PA-6 preforms subsequently allowed for a better consolidation and void removal during the melting phase of powder epoxy at 120 °C. After post-processing with epoxy, the glass transition temperature was improved to 128.7 °C and no viscous state was found. It indicated a better thermal-mechanical behaviour of the dual-polymer composites in this study and is assumed to be caused by the hardness of cured epoxy as well as the reaction between nylon-6 and epoxy. The main reaction is the nucleophilic attack on the oxirane ring by the amide nitrogen of the nylon [136], as shown in Figure 6-6a. It follows an alternate ring-opening copolymerization mechanism that leads to polyester and polyether networks [137], which is a typical reaction for the curing of epoxy resin with an amine hardener.

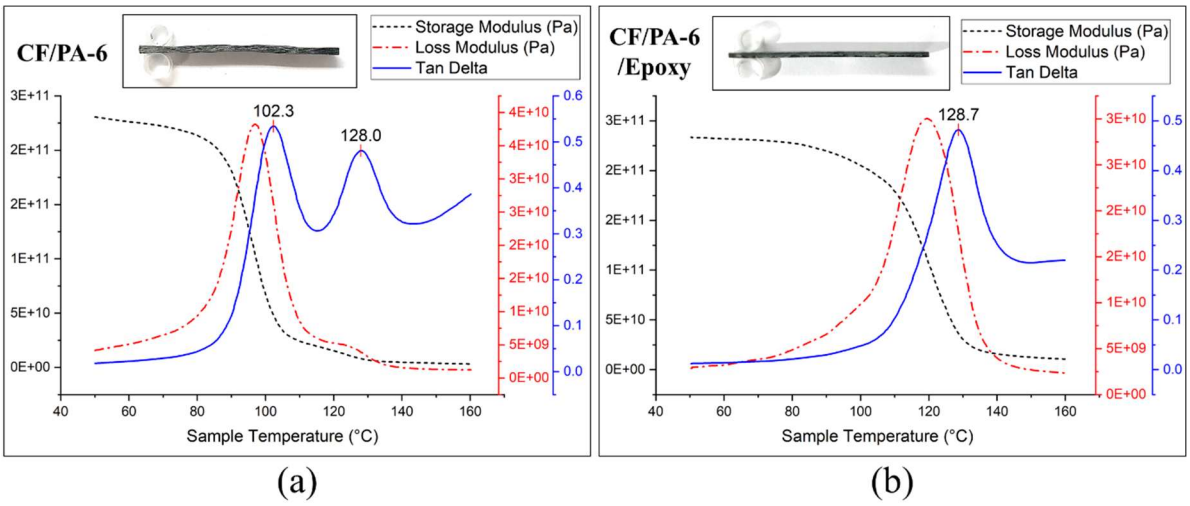

Figure 6-5 DMA traces of (a) CF/PA-6 and (b) CF/PA-6/Epoxy.

The thermal properties were also evaluated using DSC, with the temperature ramp of 20 °C/min from 30 °C to 300 °C. T_g was only defined via DMA, however, since it is more sensitive to the glass transition point than DSC. As shown in Figure 6-6b, only one glass transition peak was observed for the CF/PA-6 preforms. The melting peak was found to be absent even when the samples were exposed to 300 °C. Previous authors have highlighted that the shape and size of the melting peaks observed in DSC are dependent on the thermal history of the nylon polymer [98]. Since the curing temperature used is lower than the melting point of PA6, the alignment of straight/curved continuous fibres can be generally maintained during the consolidation.

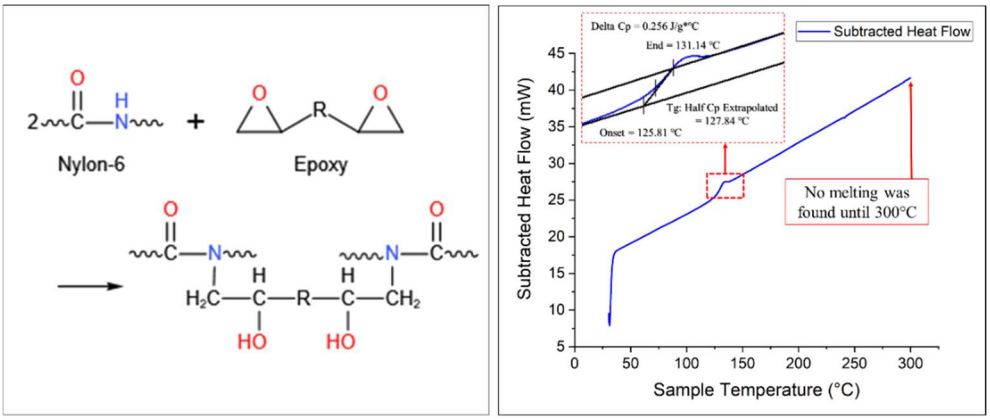

Figure 6-6 (a) Reaction mechanism of PA-6/epoxy [136] (b) DSC characterisation of the 3D-printed CF/PA-6 preforms.

The comparison of the cross-sections is shown in Figure 6-7. The UD 0˚ specimens (before testing) was cut into 5 pieces and embedded in epoxy. Then these samples were polished using a Saphir® 520 polishing machine, with the sandpapers from P400, P800 to P1200 grit and the diamond suspension from 9, 3 to 1 µm. The cross sections were observed using a HITACHI® TM400 Tabletop Microscope. As shown in Figure 6-7a, two kinds of voids were observed in the 3D-printed CF/PA-6 preforms, including the voids between layers and the gaps between the fibre paths. On the contrary, no apparent voids can be found in the dual-polymer composites after the post-processing, also the melted epoxy can be observed to infiltrate to the composites from the gaps between the fibre paths, as shown in Figure 6-7b. The weight and dimensions before and after post-processing were measured, wherein the weight was increased by 4.88% after post-processing (thus the weight fraction of the infilled epoxy was 4.67%). Additionally, the thickness of the samples was reduced by 3.8% with a relatively consistent width. The decrease in thickness mainly resulted from the vacuum pressure acting on the CF/PA-6 preforms with a rubbery/viscous state (at the post-processing temperature of 120°C).

Detailed SEM characterisations of the cross-section are shown in Figure 6-8 to further evaluate

the microstructures, in which the observed position of the CF/PA-6 preforms located at the area without those large pores as shown in Figure 6-7a. 15 pictures were taken for samples before and after post-processing, respectively, to measure the volume fraction of fibre and void. The calculation was performed on Avizo software with two filters to differentiate the matrix, fibres and void. In the printed CF/PA-6 preforms, before post-processing with epoxy, the fibre volume fraction was improved from 21.3% (in the CF filament) to 31.7% due to the pressure provided from the nozzle during printing process. The porosity in these specimens was measured as 2.69%, and matrix-rich area and significant pores were found, as shown in Figure 6-8a. Besides that, apparent cracks were observed to propagate along the interface between printing layers. It was assumed to be caused by the temperature difference between the printing layer and printed layer below it during the printing process. On the contrary, almost no voids were found in the cross-section of the dual-polymer specimens. The infill epoxy and the vacuum pressure slightly improved the fibre volume fraction to 34.6% and significantly reduced the porosity to 0.06%. However, matrix-rich areas still existed since the matrix of CF/PA-6 filament stayed solid under the curing temperature. A few micro-cracks can be found but they were relatively small compared with those in the samples before post-processing.

Table 6-1 Fibre and void volume fraction before and after post-processing

	Fibre volume fraction	Void volume fraction
Original filament	21.3% [25]	-
Printed preforms before post-processing (CF/PA-6)	31.7%	2.69%
Dual-polymer composites (CF/PA-6/Epoxy)	34.6%	0.06%

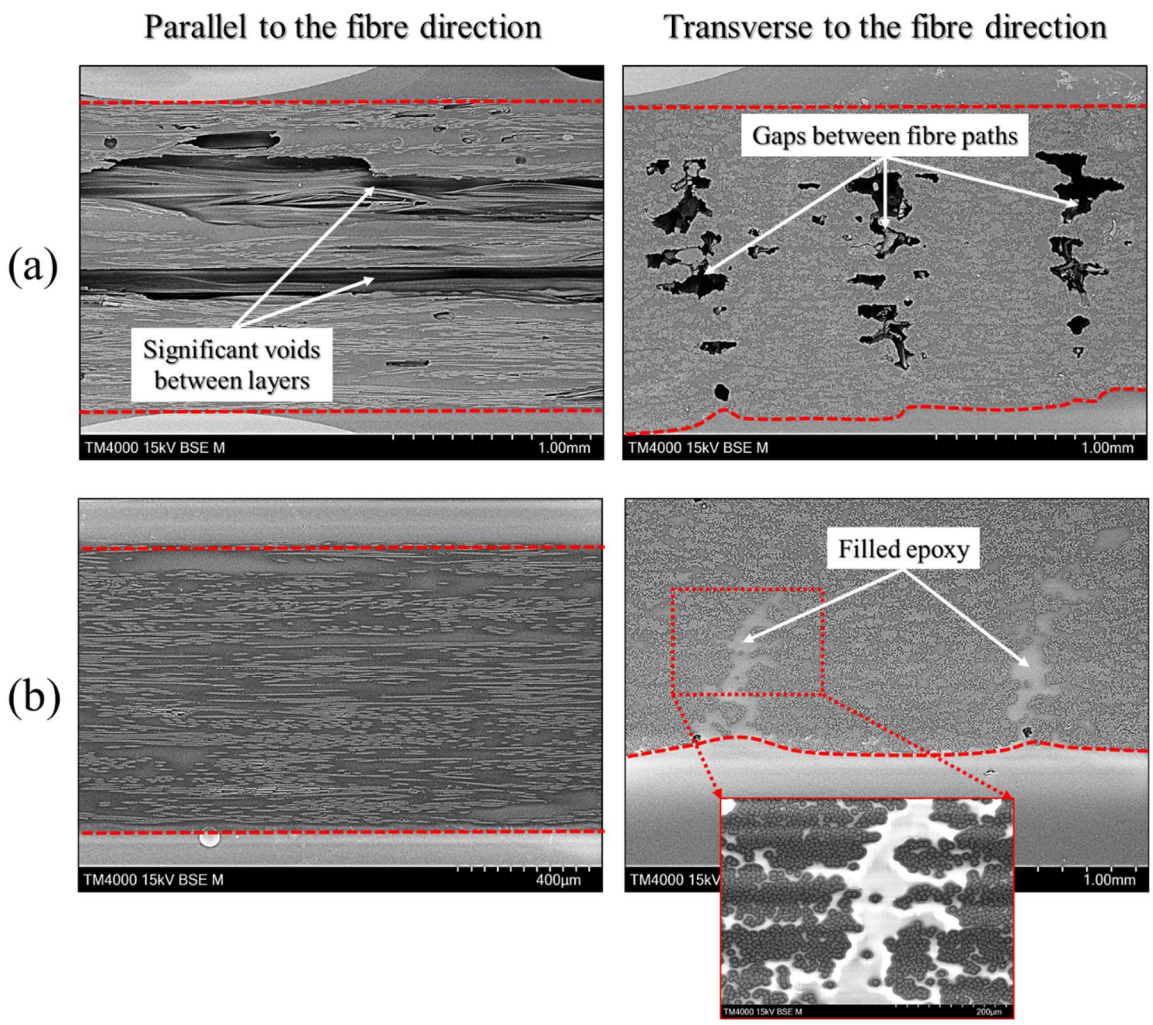

Figure 6-7 Comparison of the cross-sections: (a) 3D-printed CF/PA-6 preforms and (b) dual-polymer composites after the post-processing (The areas between two dotted red lines are the samples.)

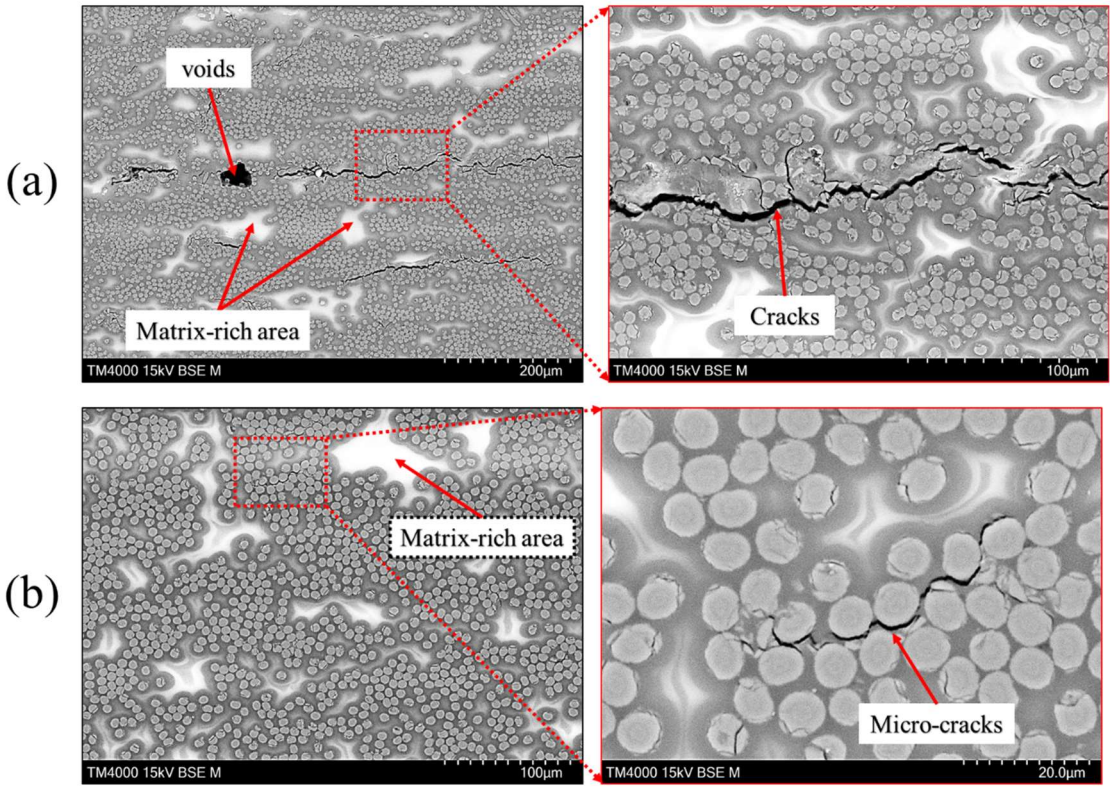

Figure 6-8 Detailed SEM characterisation for (a) 3D-printed CF/PA-6 preforms and (b) dual-polymer composites after the post-processing

6.4.1.2 Mechanical behaviour

The comparison of the mechanical performance of the UD 0˚ samples are shown in Figure 6-9. The tensile properties of the samples before post processing with the powder epoxy are consistent with the result provided from the Markforged material data sheet [138] (strength of 800 MPa and stiffness of 60 GPa). The tensile stiffness and strength of the printed composites were increased by 29.3% and 22.1%, respectively (according to ASTM D3039 Standard Test Method for Tensile Properties of Polymer Matrix Composite). The failure strain was slight decreased due to the brittleness of the added epoxy.

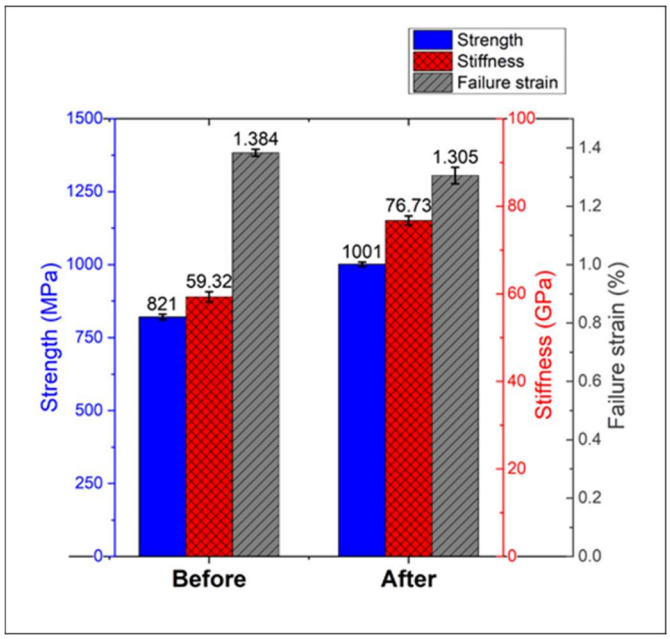

Figure 6-9 Mechanical performance in test direction of the UD 0˚ CF/PA-6 samples before and after post processing with powder epoxy

6.4.1.3 Fractographic behaviour

Further analysis was conducted by the SEM for the fracture profile, as shown in Figure 6-10. For the fracture profiles parallel to the fibre direction, it can be seen that the melted epoxy infiltrated the printed composites and infilled the voids between layers, which should effectively reduce the delamination during the loading process. In addition, more fibre breakages were found in the fracture profile of the CF/PA-6 samples after post processing with epoxy. It meant the treatment with powder epoxy enhanced the bonding between these unidirectional fibre paths and eased the fibre split and crack propagation along fibre direction.

Figure 6-10 c & d compares the fracture profiles transverse to the fibre direction. The samples before post-processing exhibited a plastic behaviour, in which the voids and cracks led to an inhomogeneous profile with localised stress concentration and then resulted in the yielding of large fibre bundles. Multiple micro-cracks between fibres and matrix were also observed,

indicating weak interfacial properties and increased crack propagation. In contrast, the dual-polymer composites after post-processing exhibited a relatively brittle behaviour, with the failure in matrix-rich areas first. Since the adhesion between fibres and matrix was good and no apparent voids occurred in the composites, a homogeneous stress profile was obtained and the sample finally failed with only a few fibres pulled out, resulting from the micro-cracks shown in Figure 6-8b.

In summary, the melted epoxy infiltrated the CF/PA-6 preforms from the gaps between the print paths and then infilled the apparent voids and interlayer cracks during the curing process. The PA-6 was further consolidated due to the vacuum pressure and its rubbery/viscous state at the melting stage of the curing process. However, the epoxy did not get into the micro-cracks/voids between the PA-6 matrix and single carbon fibres, since the PA-6 matrix remained relatively solid to maintain the fibre alignment during the heating cycling.

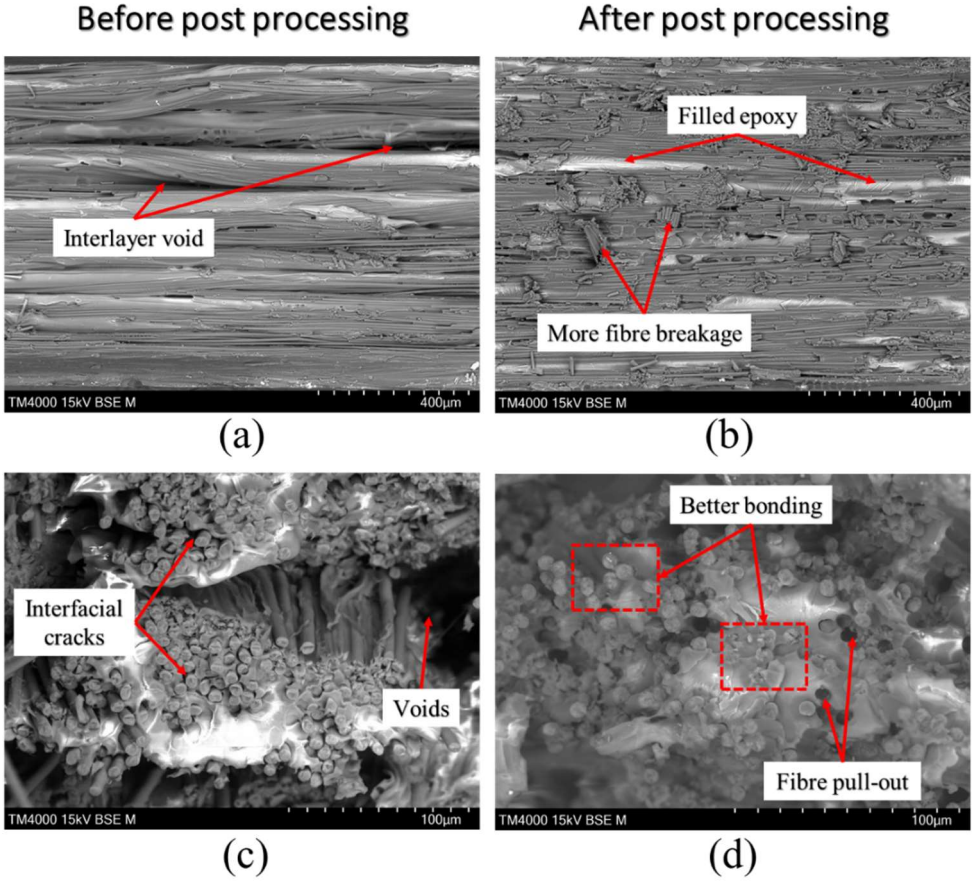

Figure 6-10 SEM fracture profiles (a) & (b): parallel to; (c) & (d) transverse to the fibre direction

6.4.2 3D-printed single edge notched plate

The dual-polymer technique allows the manufacturing of composites with low-porosity and customised curved fibre paths. All of the specimens in this section were made via the hybrid manufacturing technique, in order to eliminate the influence of voids and then better investigate the effect of fibre placement. The strength and fracture toughness of three different fibre placement methods for the single edge notched plate are first presented. The load-displacement curves and the failure pattern are then discussed, also with the distribution of maximum principal strain obtained from the DIC analysis. The ultimate strength is defined as the maximum force carried by the test specimen prior to failure, divided by the gross cross-sectional area (disregarding the notch). The notch stress intensity factor (mode I) K at the crack tip under a uniaxial stress for the edge crack in a plate is calculated as Eq (17) - (19) [139, 140]:

$$K = f(a/w) \cdot \sigma \cdot \sqrt{\pi a} \tag{17}$$

$$f(a/w) = 1.122 - 0.231\left(\frac{a}{w}\right) + 10.55\left(\frac{a}{w}\right)^2 - 21.71\left(\frac{a}{w}\right)^3 + 30.382\left(\frac{a}{w}\right)^4 \tag{18}$$

$$K_C = f(a/w) \cdot \sigma_{peak} \cdot \sqrt{\pi a} \tag{19}$$

where a is the crack length, w is the width of the plate, $f(a/w)$ is the geometry factor and σ is the remote tensile stress. The notch fracture toughness (mode I), K_C, is the highest value of stress intensity that the plate can withstand without fracture [141]. σ_{peak} is defined as the peak stress without the crack initiation in each case. The data for the calculation of fracture toughness are shown in Table 6-2.

Table 6-2 Data of three kinds of single-edge notched samples

	Notch depth a (mm)	a/w	Geometry factor	σ_{peak} (MPa)
Mechanical notched	4.14	0.1118	1.2025	282.49
Concentric infill	3.88	0.1048	1.1924	214.85
Principal stress trajectories	3.52	0.0951	1.1793	888.80

As shown in Figure 6-11, the strength and fracture toughness of the samples with stress-lines placement were increased by 81.3% and 157.5%, compared to the mechanical notched samples. The improvement of the properties resulted from the stress re-distribution brought from the optimised fibre paths as well as the prevention of the defects caused by the mechanical manufacturing process. As shown in Figure 6-12, no cracks occurred before the ultimate load of the samples with stress-lines placement. The samples finally failed in a brittle mode, accompanied by symmetrical crack propagation along the angular direction. In contrast, cracks initiated at the tip of the notch during the loading process of the mechanical notched sample. They immediately propagated along the fibre direction when the load came to 58% of the maximum force. The manufactured defect and premature cracks significantly reduced the fracture toughness of this sample. Subsequent fibre breakage in the transverse direction resulted in the eventual failure of the sample.

Although no manufactured defeat was introduced to the samples with concentric placement, the strength and fracture toughness were reduced by 31.0% and 33.0% compared to the mechanical notched samples. As shown in Figure 6-12, cracks initiated near the notch and at the centre of the samples at 60% of the ultimate load, with the former being caused by the stress concentration and the latter resulting from the different mechanical response between the left (curved) and right (straight) parts of the fibres. The final failure exhibited mainly fibre splitting on the left, and only tensile breakage on the right. It revealed that the concentric fibre placement

method of composites with complex geometries was inappropriate. The difference between the curved and straight fibres (inevitable in such concentric placement) divided the samples into two parts, which lowered the mechanical properties, even compared with the samples processed by mechanical cutting or drilling.

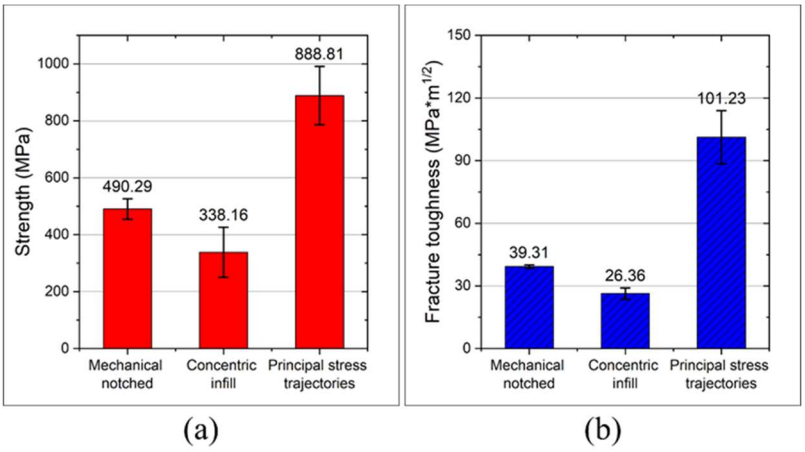

Figure 6-11 (a) Ultimate strength and (b) fracture toughness of the single-edge notched samples

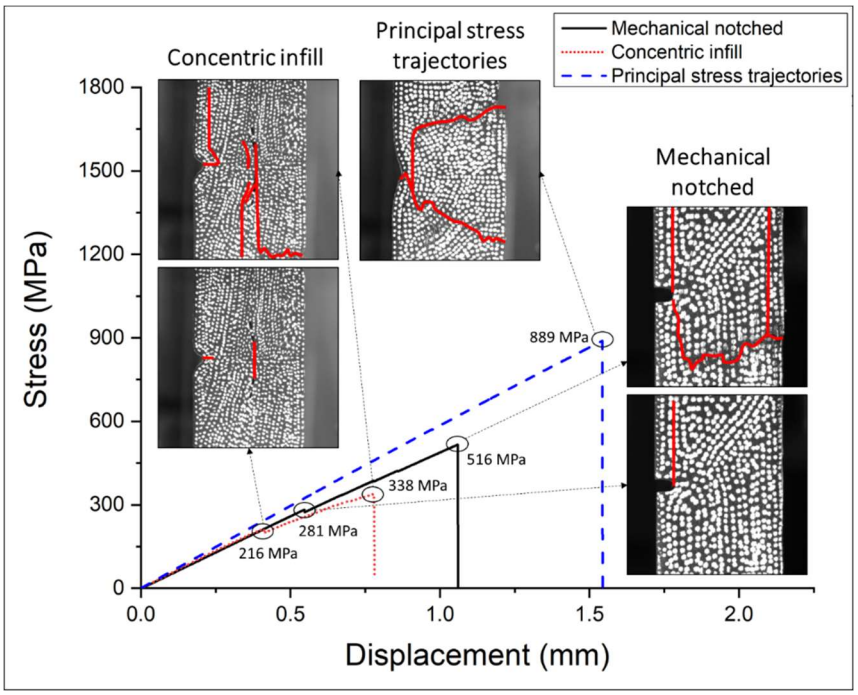

Figure 6-12 Stress-displacement curves and crack propagation in samples

The distributions of maximum principal strain (prior to failure) are shown in Figure 6-13, in which (b) & (d) are the states before the ultimate load for the samples with mechanical notched and concentric placement, respectively. A uniform interval type of distribution was adopted for all contour plot legends, in which the contour limit was set as the maximum value of each individual sample to better identify the concentration in the images. Obvious strain concentrations are seen in (b) & (d) due to the cracks, so Figure 6-13(a) & (c) & (e) are more suitable for evaluating the effect of fibre placement on the stress/strain distribution. For the mechanical notched samples (a) and (b), the highest values of strain are concentrated in a small area around the tip of the notch. For the samples with concentric placement (c) and (d), the highest strain concentrations are also located at the tip of the notch, but are extended angularly to the vertical centreline of the samples. Although the manufactured defects were avoided, the semi-circular fibre placement around the notch could not transfer the tensile load properly. For the samples with principal stress-lines placement (e), the strain distribution was quite even and very limited comparatively, since almost the entire domain exhibited in the red colour. The maximum value of this case was 44.0% lower than that of the concentric case, also 27.3% lower than that of the mechanical notched case. This indicated that the fibre placement along principal stress trajectories distributed the loads from the notch to the whole structure, reducing the localised strain. This improved strain distribution delayed the failure until the applied stress reached 89% of the value required for the fracture of the unnotched specimen (ultimate strength of 1001 MPa for the UD 0° samples).

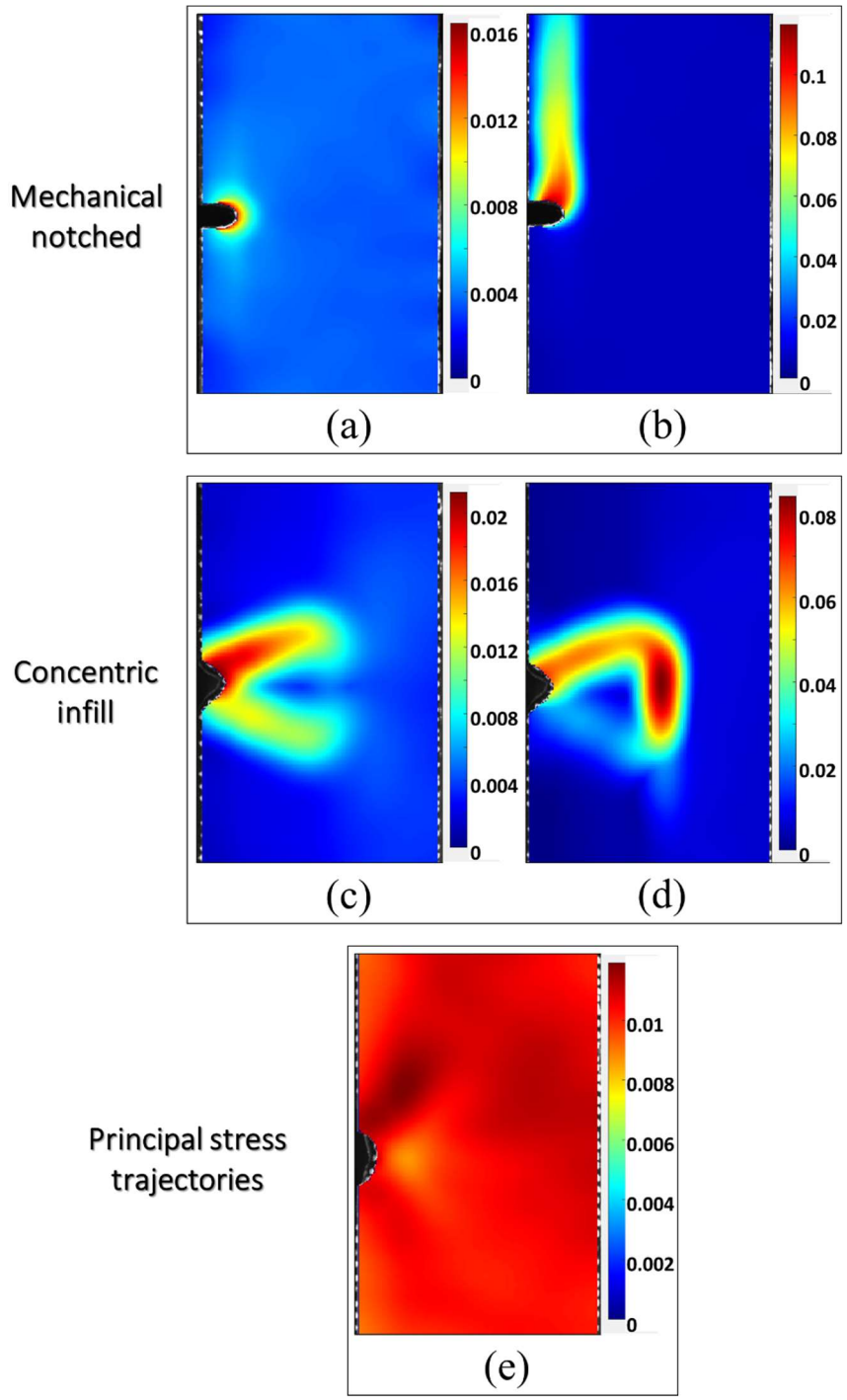

Figure 6-13 Distribution of maximum principal strain obtained from DIC measurement prior to failure: (a) before yielding and (b) ultimate load of the mechanical notched sample; (c) before yielding and (d) ultimate load of the concentric infill sample (e) before failure of the stress-lines sample (different legend scales were used to better identify the strain concentration in each case)

6.5 Conclusions

In this chapter, a low-cost hybrid manufacturing technique was presented, in which 3D-printed thermoplastic composite preforms were infiltrated and cured with a thermosetting powder epoxy, in order to manufacture composites with low-porosity and designed curved fibre paths. The epoxy mainly infiltrated from the gaps between the print paths and significantly reduced the porosity of dual-polymer composites from 2.69% to 0.06%. The original PA-6 matrix was further consolidated but remained relatively solid to maintain the fibre alignment during the heating and post-processing cycle. DMA and DSC investigations demonstrated that the PA-6 and epoxy polymers are compatible. The tensile stiffness and strength of the carbon fibre reinforced PA-6 composites were improved by 29.3% and 22.1%, respectively, after the post-processing treatment with epoxy powder. Uniaxial tensile tests of three types of single-edge notched plates were conducted to evaluate the effect of different fibre placement methods. Compared with the mechanical notched samples, optimised fibre placement along the principal stress trajectories increased the strength and fracture toughness by 81.3% and 157.5%, respectively. It was also revealed that the general concentric placement method was inappropriate for the fused filament fabrication 3D printing of continuous carbon fibre reinforced thermoplastic composites with complex geometries.

Although the epoxy powders were manually sprinkled onto the printed composites, this hybrid manufacturing technique could potentially be automated in the future by *in situ* spraying epoxy powder or resin ink. Other high performance thermoplastic composite filaments with high fibre volume fractions could also be used in the future, e.g. carbon fibre reinforced polyether ether ketone, to enable the application of printed composites to meet high temperature requirements in aerospace and other industrial sectors.

Chapter 7 Effectiveness of fibre placement in 3D-printed open-hole composites under uniaxial tension [*]

Abstract

This chapter presents a hybrid manufacturing technology that enables the fabrication of 3D-printed dual-polymer composites with low porosity and customised continuous carbon fibre reinforcement. The thermoplastic composites preform was first manufactured via fused filament fabrication (FFF) 3D printing and then consolidated with the thermoset powder epoxy in the oven. After that, the effect of fibre placement on the mechanical performance of open-hole composites under uniaxial tension was comprehensively studied. A concept of placing continuous fibres along the higher in-plane principal stress trajectories was adopted and found to improve the strength of the composites and postpone the crack initiation, compared with the drilled samples. Additional fibres, along the lower in-plane principal stress trajectories and around the hole, were found to significantly alter the failure mode and mechanical performance of the samples. Together with the digital image correlation measurement, a FE model was also built based on the actual printing paths to understand the stress distributions due to different fibre placement methods. The study offers a very useful tool for the customised design of 3D-printed composites with complex shapes and/or geometric singularities.

Keywords

3D printing; curved fibre paths; open-hole composites; CFRP; principal stress trajectories.

[*] This chapter was submitted to Composites Science and Technology in June 2021.

7.1 Introduction

Continuous carbon fibre reinforced polymer (CCFRP) composites are commonly used in aerospace and automotive industries due to their high strength and high stiffness-to-weight ratios [87]. Traditional manufacturing techniques of CCFRP, such as compression moulding and vacuum bagging, usually face challenges to fabricate composite structures with complex geometries [116]. Other processes like automated tape laying (ATL) and automated fibre placement (AFP) use computer-guided robotics to lay fibre tapes/tows onto a mould [111, 115], allowing for more complex layup geometries. However, they inevitably cost more on infrastructure and defects would happen during the tow steering due to their wide fibre tows, for example the out-of-plane wrinkling. Recently, additive manufacturing (also called 3D printing) is being developed for the fabrication of composites with highly complex shapes and fast processing. Among them, Fused Filament Fabrication (FFF) 3D printing melts and deposits thermoplastic filament layer by layer to create three-dimensional parts without the resort to a mould [131]. Since 2014, Markforged® has released series of desktop 3D printers, *e.g.* Mark One/Two, which can print composites with 1K continuous fibre reinforcement [2]. The advantages of low cost and convenience make 3D printing a potential manufacturing method for continuous fibre reinforced composites.

Despite the advantages and capabilities, 3D printing also comes with its own limitations. One challenging issue is the significant voids content in the finished parts [6]. It has been demonstrated that three types of voids are generated in 3D-printed CFRP composites. The first type of voids are the entrapped air voids, which are mainly generated during the extrusion of thermoplastic filament [142]. Also, the mixed short or continuous fibres would aggravate this problem since the fibres reduce the fluidity of the melted thermoplastic. The second type of voids are the intrinsic gaps between adjacent printing beads in a single layer [14] due to the inadequate bonding [3]. Another void type is the physical gap at the layer/layer interfaces,

generated by the temperature difference between different layers during the printing process. Previous studies have attempted to reduce the porosity in 3D-printed composites by introducing a compaction stage, for example, *in situ* consolidation techniques such as ultrasonic vibrations [55, 143] and vibrational stamping with a hot-compaction roller [53]. Modification of nozzle geometry has also been investigated and it was observed that the inter-bead voids were reduced to about 3% by using a nozzle with a square-like cross-section in the 3D printing of thermoplastic [13]. On the other hand, low-viscosity materials have been used in inkjet-based 3D printing to reduce the voids [144, 145]. As mentioned before, when mixed in the polymer continuous carbon fibres reduce the fluidity of the matrix significantly and aggravate the formation of voids, which have not been effectively addressed.

One of the advantages of the 3D printing of CCFRP composites is the opportunity and flexibility to control the deposition paths of materials, which could better utilise the superior mechanical properties of continuous fibres. For the composites with geometric singularity such as a hole/notch, FFF 3D printing can steer the fibre paths around the hole/notch rather than printing an intact sample with all straight fibre paths followed by traditional drilling. A few optimisation methods for continuous fibre placement were introduced so far. Our previous research presented a new concept to place curved continuous fibres along principal stress trajectories in order to improve the strength and stiffness [43]. Also, Li *et al*., proposed an ingenious path-designed 3D printing approach that considers the load transmission path and anisotropic property of the continuous carbon fibre reinforced filament [50]. However, this would cause gaps between the printed beads of continuous fibres when steering the fibres [33, 35]. Although some printing systems tried to deposit thermoplastic in those gaps, they could not be completely filled and some gaps are usually too small to accommodate a single printing path [6]. This would eventually lead to high void content and consequently results in much lower stiffness and strength than expected [20, 70, 120], not even close to those of traditionally

manufactured CCFRP composites, which limits the application of FFF 3D-printed CCFRP composites in real industry.

In this study, FFF 3D printing was combined with low-cost post-processing treatments to demonstrate the fabrication of 3D-printed composites with low porosity and customised curved continuous fibres reinforcement. First, composite preforms of continuous carbon fibre-reinforced thermoplastic were 3D-printed by the FFF technique. Then post-processing (oven curing with vacuum bagging) was conducted, wherein thermosetting epoxy powders were sprayed onto the preforms to fill the gaps. Case studies of open-hole composites were performed, in which continuous carbon fibres were placed along the principal stress trajectories generated from finite element analysis (FEA) of a neat polymer material. Three customised fibre placement methods around the hole were investigated and compared with drilled samples as well as samples printed from Markforged® commercial printer Mark Two. Finally, uniaxial tensile tests together with FEA of 3D-printed curved fibre reinforced composites were conducted to understand the mechanisms behind various fibre placement methods around the hole.

7.2 Methodology

The current study adopted a hybrid manufacturing technology that consists of 3D printing of CCFRP composite preforms and post-processing with powder epoxy. Uniaxial tensile tests of 3D-printed open-hole composites were performed, in which six cases with different material placement methods and/or manufacturing techniques were investigated.

7.2.1 Hybrid manufacturing

A Prusa® i3 mk3 printer was used to print the CCFRP composite preforms, as shown in Figure 7-1a. The printing filaments were sourced from Markforged®, which consists of 1K continuous carbon fibres and polyamide 6 (PA6) [7]. A brass nozzle with an M6 screw was also sourced

from Markforged® and used for the printing of continuous fibres. A printing temperature of 245°C and a printing speed of 10 mm/s were adopted. Considering the diameter of the filament is around 0.375 mm, an off-distance of 0.1 mm between the bed and nozzle tip was found to provide good pressure on the printed filament for adhesion without noticeable fibre breakage, resulting in an average width of a single printed stripe to be 1-1.5 mm. The feeding mechanism was not activated, so the end of the filament was slightly under tension during the printing process and the feed rate of the filament was consistent with the printing speed. As shown in Figure 7-1a, a polytetrafluoroethylene (PTFE) tube was inserted into the print-head to guide the filaments and the composites were printed to the bed coated with a layer of PVA glue, ensuring sufficient adhesion for the first printed layer. The print bed was not heated as no warping occurred during the printing of composite preforms with such continuous fibres. Since the filaments used in this study contain continuous fibres and the toolpath do not have to be started and stopped during printing, the continuous toolpath (G-code) was necessary. G-code was generated via MATLAB and then transferred to the printer. A printed open-hole composite preform is shown in Figure 7-1b, with a length of 200 mm and a width of 36 mm in accordance with Configuration B in ASTM D5766 (Standard test method for open-hole tensile strength of composite laminates).

Then post-processing of composites preforms was conducted to reduce the voids and enhance the mechanical performance. The powder epoxy PE6405 used in this study was engineered by Swiss CMT and provided by FreiLacke. Previous research [132] revealed that the powder epoxy melted around 45-60°C and a temperature of more than 150°C was required for the initiation of curing. The temperature gap between melting and curing as well as the low viscosity of the resin (minimum of 1.26 Pa·s at 120°C [132]) would enable void filling in the composites preforms. To cure the epoxy powders in the open-hole composite preform, an aluminium-made mould was used and a cylinder pin was attached to it to leave a hole in the

finished samples, as shown in Figure 7-2a. PTFE non-stick ply and release agent were also used for subsequent demoulding. Epoxy powders were manually sprayed on the printed preform before vacuum bagging (shown in Figure 7-2b), followed by a three-stages curing cycle in the oven based on its thermal properties. The temperature was set to 40°C for 8 hours to remove the moisture and then ramped to 120°C for 1 hour to melt the powders. After that, the system was consolidated at 180°C for 2 hours.

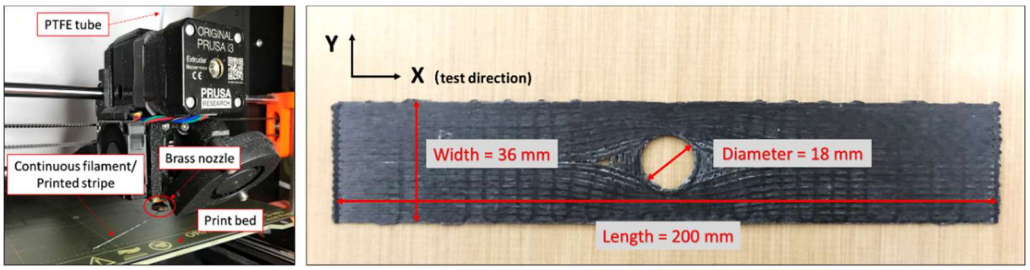

(a) (b)

Figure 7-1 3D printing of continuous CF filament, and (b) a printed open-hole composite preform.

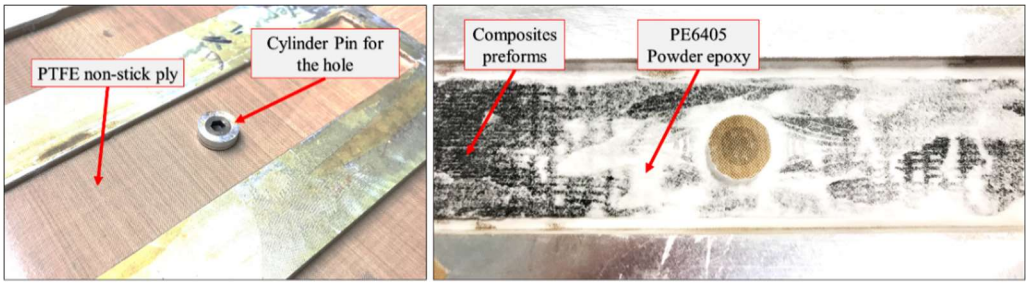

(a) (b)

Figure 7-2 (a) The aluminium mould, and (b) the open-hole preform with sprayed powder epoxy

7.2.2 Case study

The diameter of the hole in the printed composite preforms was set to 18 mm (w/D ratio = 2),

in order to better investigate the influence of fibre placement on the mechanical performance. The enlargement of the hole was also adopted in previous researches [43, 146]. A 35mm-long end tab was used at each end to prevent gripping damage, since only four-layers CF preforms (0.6-0.8 mm thickness approximately) were printed for each sample in these cases.

As mentioned above, six cases with different fibre placement methods and manufacturing techniques were performed and compared. In the traditional method, continuous fibres are laid straight and the hole is made by drilling. In this study, the 'drilled' samples were produced via a hybrid process, in which continuous fibres were placed along the longitudinal direction of the sample by 3D printing and then a hole was drilled on the consolidated plate with the designed dimensions. Different to the 'drilled' samples, a new concept was adopted to place continuous curved fibres for the open-hole CCFRP composites, which was demonstrated to reduce the stress concentration and improve the stiffness [43]. In this fibre placement method, principal stress trajectories were generated from finite element analysis (FEA) of the neat polymer matrix based on the tensile loading condition and used as the guidance for the path design of continuous carbon fibres, as described in detail in our previous work [43]. Three cases with customised curved fibre were studied in this chapter, as shown in Figure 7-3 (a-c). In curved fibre case 1, continuous fibres were aligned with maximum stress trajectories in each layer of the composites. Since no fibres were deposited on the left and right sides of the hole in this case (see Figure 7-3a), resin-rich areas occurred and led to substantial defects which could intrigue unexpected early crack initiation due to lack of structural integrity. Alternatively, additional neat PA material was printed, placed in these interspaces and post-processed together with the composite preforms to make a complete hole (as called 'case1-complete', see Figure 7-6). In case 2, fibres were placed along with maximum and minimum stress trajectories alternately layer by layer, which is similar to the traditional [90°/0°] cross-ply laminates. This placement method was also proposed by Anisoprint® as a weight-saving design [147]. As the

stacking sequence is balanced and symmetric, so it could potentially provide the maximum bending stiffness and have no membrane–bending coupling effects [148]. In case 3, continuous fibres were placed along maximum stress trajectories and additional fibres were printed on top of the trajectory-based fibres around the hole with an intention to better maintain the hole integrity and delay the initiation of failure. The 3D-printed preforms of these three curved fibre cases were treated via oven curing with powder epoxy as mentioned above. For the comparisons of different manufacturing techniques, open-hole specimens without any post-processing treatments were also printed by the commercial Mark Two printer. In the default setting of the Eiger system provided by Markforged®, continuous fibres could not be used in the top and bottom four layers, hence 12-layers composites were printed in the manufacturing of Markforged sample (the cross-section can be seen in the SEM characterisation in Figure 7-7b), in which four layers of PA6 were printed on both top and bottom. The continuous fibres in the middle four layers were placed along 0°/+45°/90°/-45° alternately and two rings of fibres were printed around the hole using a default concentric approach, as shown in Figure 7-3d. In the Eiger slicing software, “wall” and “infill” PA6 were also printed in the fibre layers, for better surface finishing and lower porosity, respectively. The average thickness and fibre volume of these six cases are shown in Table 7-1.

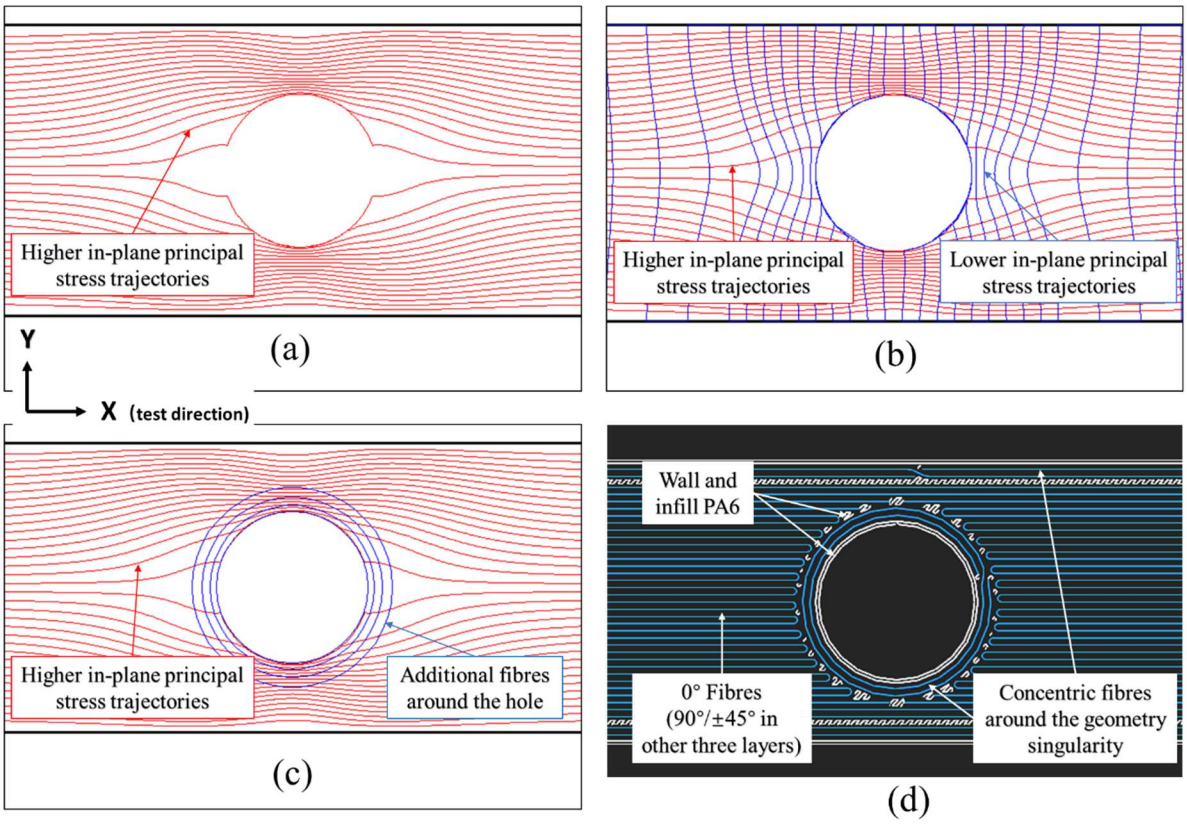

Figure 7-3 Placement methods: (a) case 1 (b) case 2 (c) case 3 (d) Markforged sample

Table 7-1 Datasheet of six cases for open-hole tension

	Case 1	Case 1 (complete)	Case 2	Case 3	Drilled	Markforged
Materials	PA6/CF + epoxy powder					PA6/CF
Consolidation	Yes	Yes	Yes	Yes	Yes	No
Thickness (mm)	0.63	0.63	0.80	0.63	0.60	1.48
Fibre volume (cm^3)	3.336	3.336	4.104	3.427	3.179	2.930

7.3 Mechanical testing and finite element modelling

7.3.1 Mechanical tests of open-hole samples

The open-hole tensile tests were performed using an MTS Criterion® Model 45 (C45.305) with a 300 kN load cell, as shown in Figure 7-4. A crosshead speed of 0.5 mm/min was used for all

tests and the samples were clamped in hydraulic grips with a clamping pressure of approx. 100 bar. In each type of test, three specimens were tested. A speckle pattern was applied to the surface of each specimen and 2D strains were measured with digital image correlation (DIC). All the DIC data were processed through a MATLAB script to obtain the full-field displacements and strains.

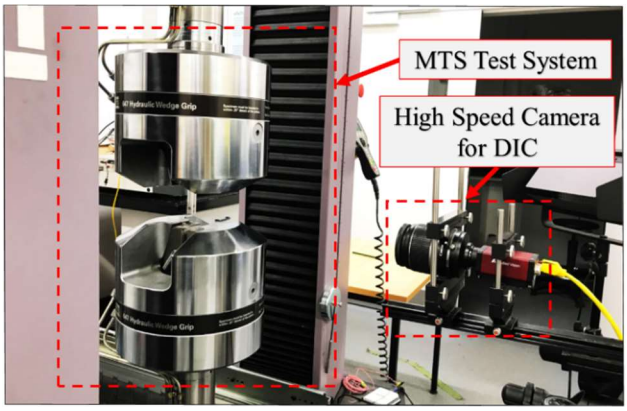

Figure 7-4 MTS test system with digital image correlation

7.3.2 Finite element modelling

In this chapter, finite element models were built to numerically investigate the effect of different fibre placement methods and correlate with the experimental measurements. The dimensions and the boundary conditions of the domain are shown in Figure 7-5a, in which only half of the specimen was analysed with sliding supports because of the symmetry. Since the fibres would be embedded into the domain in the following step, the radius of the central hole was reduced to 8 mm to make sure all the nodes of embedded part (composite preform) stay within the host part (epoxy matrix). Because the composites specimen in the open-hole tensile test can be considered as a plate, the thickness of the domain was set as the thickness of single printed stripe (*i.e.* 0.11 mm) to reduce the computational cost. As such the degree of freedom in vertical displacement along the thickness direction was constrained. The left end of the

model was fixed and a displacement along longitudinal direction was applied to the right end of the plate. It should be noted that the embedded composite preform was built based on actual printing paths. First, the printing paths (*i.e.* coordinates of the nodes) were imported into Texgen software to obtain the fibre parts of the model, wherein the dimension of cross-section (1.0 mm by 0.11 mm) was defined by X-ray computed micro-tomography (μCT) characterisation in our previous paper [25]. In Texgen software, the material direction of each element (fibre longitudinal direction) was defined as the tangent direction of the point on the printing path. As shown in Figure 7-5b, the composite preforms in four different cases were meshed by C3D8R elements with an approximate global seed size of 0.33 in Texgen and then imported to Abaqus to embed into a matrix part as reinforcement. Previous research also demonstrated that the embedded element technique worked effectively in prediction of the elastic properties in meso-FE modelling of fibre reinforced composites [149].

As shown in Figure 7-5b, only four cases obtained from the hybrid manufacturing technique were simulated, because the detailed printing paths could not be extracted from the closed Eiger software. Also, as revealed from the previous research [6] and the following SEM characterisation, the weak interface between layers and the voids trapped in the Markforged samples would significantly influence the prediction of their mechanical performance, which is exactly the reason why the hybrid manufacturing was adopted in this study. The material properties used in the finite element models are shown in Table 7-2. The longitudinal modulus of the printed carbon fibre stripe was provided by Markforged® [138] and other properties of the Markforged® CF were calculated using the rule of mixture based on a volume fraction of 34.5% of the AS4 carbon fibre in the stripe [150, 151]. Since the constitutive law (in particular the plastic behaviour) of the printed stripe was very challenging to establish and the interface between printed stripe and infill epoxy was difficult to calibrate, only elastic behaviour of Markforged® CF and PE6405 epoxy were concerned in the finite element modelling as our first

step. Therefore, the finite element modelling in this chapter will mainly investigate the stress distributions and mechanisms on how curved fibres transfer the loading from the periphery of the hole to other areas.

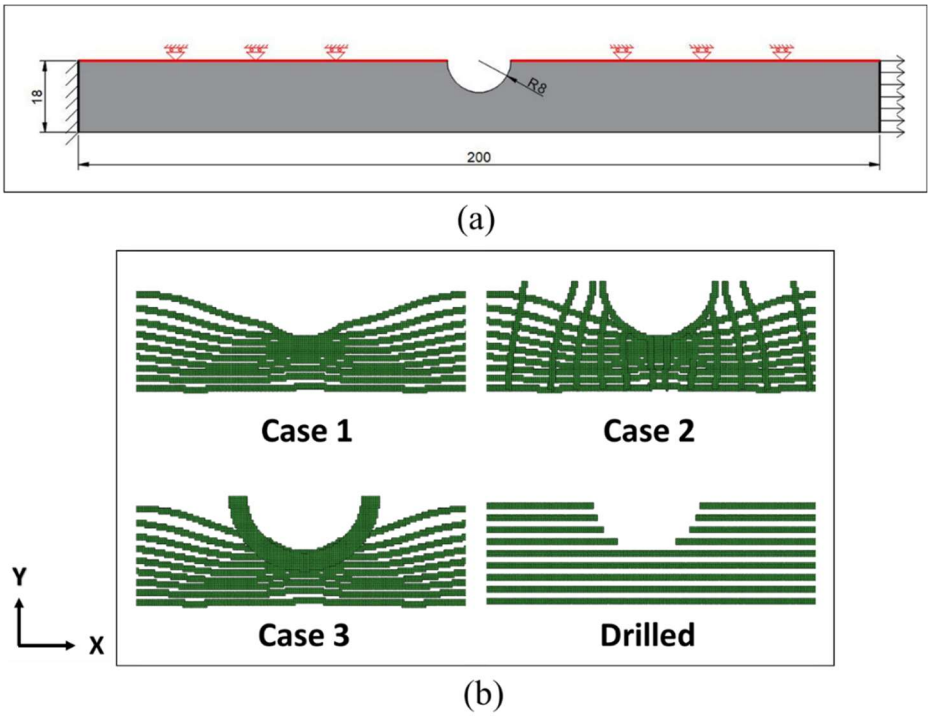

Figure 7-5 (a) Dimensions and boundary conditions of the FE model (unit: mm), and (b) FE model of the printed preform in four different cases (epoxy matrix is hidden)

Table 7-2 Elastic properties of printed stripe and epoxy in the FE models [150, 152]

Material properties	Markforged® CF	PE6405 epoxy
Longitudinal Modulus E_1 (MPa)	54000	3000
Transverse E-Modulus E_2 & E_3 (MPa)	7728	3000
In-plane Poisson's Ratio v_{12} & v_{13}	0.104	0.37
Transverse Poisson's Ratio v_{23}	0.121	0.37
In-plane shear Modulus G_{12} & G_{13} (MPa)	7625	-
Transverse Shear Modulus G_{23} (MPa)	2864	-

7.4 Results and discussion

In this section, the manufacturing quality of the finished samples obtained from two different

techniques were first presented, including the surface profiles and SEM characterisation of the cross-sections. Then the experimental results of open-hole tension were shown, including the crack propagation, tensile properties and the hole integrity prior to failure. After that, the numerical results from FE models were demonstrated and compared with those obtained from mechanical tests, including the stiffness and strain distribution. Finally, the stress distribution on fibres and the matrix are shown to discuss the load transferring mechanisms of fibre placements and their further response on the matrix behaviour, respectively.

7.4.1 Manufacturing quality

Optical images of the samples for the six cases are shown in Figure 7-6 and the thickness of samples after post-processing are shown in Table 7-1, in which the values of curved case 1, case 3 and the drilled samples were nearly the same (about 0.6 mm) and the thickness of curved case 2 was increased to 0.8 mm because of the additional fibres printed in the transverse direction. The thickness of samples printed from Markforged® system was 1.5 mm due to the additional top and bottom layers of PA6, but only four layers of continuous fibres were printed in each sample. It was assumed that those additional PA6 layers would not contribute significantly to the tensile strength and stiffness of the printed composites, therefore, the thickness of Markforged® samples was still considered as 0.6 mm, approximately the thickness of the fibre layers, in the following calculations and analysis. Comparing the cross-section images in Figure 7-7a with the surface image of case 1 in Figure 7-6, the melted epoxy powders were more effective in filling the microscale voids in the composite preforms than filling the relatively larger geometric gaps between fibre paths. In the finished samples of curved fibre case 1, there was no material formed at the top and bottom peripheries of the hole due to the low viscosity of epoxy during the consolidation process, but a relatively complete hole was achieved in the ‘case1-complete’ with additional PA6 infills and case 2 & 3 with adequate fibres being placed around the hole during the printing process to avoid large gaps for forming

resin-rich areas in the subsequent oven curing process.

The SEM characterisation in Figure 7-7 reveals the microstructure of finished samples from the hybrid manufacturing and Markforged® Mark Two printer. The samples were placed in a slow-cure epoxy resin and then the observed surfaces were polished. The areas between two solid red lines are the cross-sections of the samples. As shown in Figure 7-7a, there were no noticeable voids and good fibre/matrix adhesion can be found in the sample from hybrid manufacturing. For the Markforged® sample in Figure 7-7b, a sandwich-like structure can be seen, wherein the continuous fibres were placed between the additional PA6 layers. Two kinds of voids were found in the Markforged® sample, *i.e.*, voids trapped in the fibre layers and those between fibre and PA6 layers. The former would accelerate the initiation and propagation of the cracks while the latter would result in the delamination between layers during the loading process. These microstructure defects and porosity could substantially influence the mechanical performance, which will be further discussed with the experimental test data.

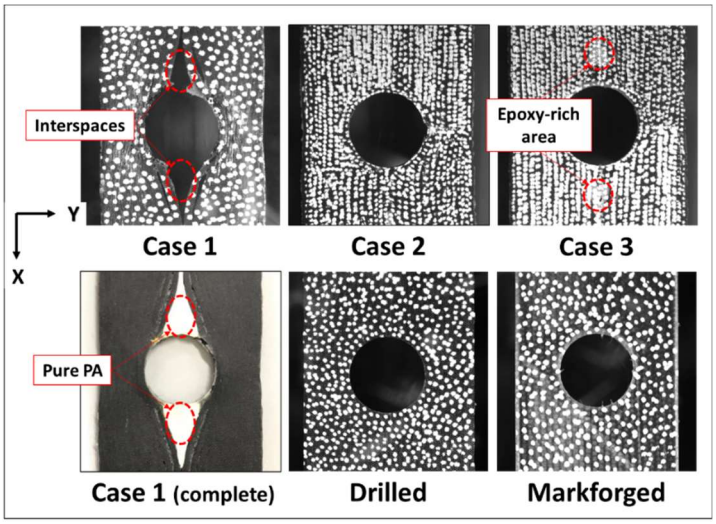

Figure 7-6 Surface images of finished samples (white dots for DIC measurement).

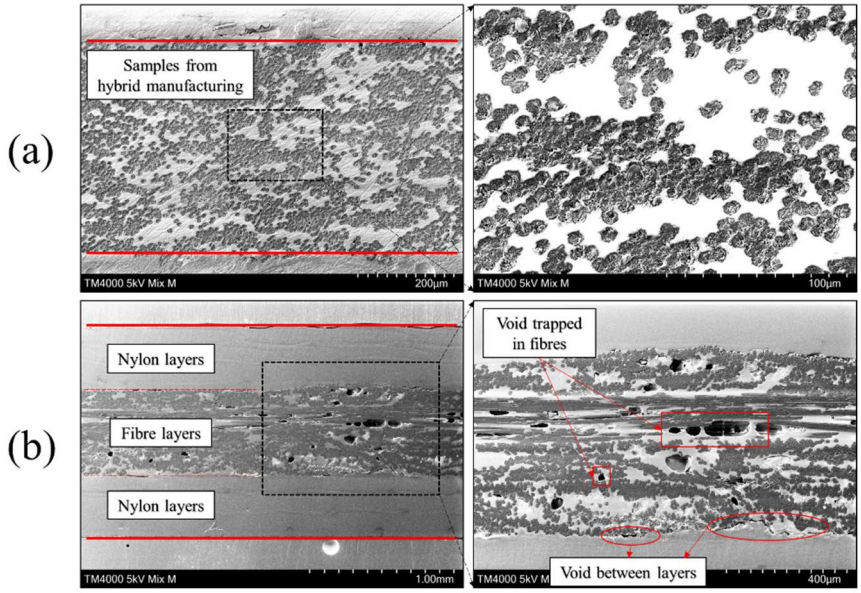

Figure 7-7 SEM of cross-sections: (a) hybrid manufactured samples, and (b) Markforged® printed samples.

7.4.2 Mechanical performance

7.4.2.1 Load-displacement response and damage evolution

The load-displacement curves and cracks propagation from the open-hole tensile tests are shown in Figure 7-8. For the drilled samples, the yielding point (the first drop of the load) appeared much earlier than the point of ultimate failure. The average ultimate tensile load of the drilled samples was 6.4 kN, and the average yielding point of these three samples was 3.26 kN (with a small standard deviation of 0.15 kN). The crack initiated at the one edge of the hole at the yielding point and then propagated quickly throughout the sample along the longitudinal direction, as shown in Figure 7-8a. The premature damage was reasonably assumed to be caused by the defects resulted from the drilling process. The subsequent crack propagation led to a substantial drop of loading until the crack was arrested at a substantial distance to the hole (almost to the end-tabs). After that, similar cracks appeared on the other side of the hole and finally the sample was damaged with the tensile breakage of fibres.

For the curved fibre case 1, no yielding and crack initiation can be found before it came to the point of ultimate tensile load. Comparing the samples with and without a complete hole, the ultimate load of case1-complete was improved from 7.2 kN to 8.8 kN due to the additional PA material placed in the interspaces. Those PA materials were also damaged at the point of ultimate load. Therefore, similar failure patterns were captured for these two types of samples. As shown in Figure 7-8b, two kinds of cracks were observed at the same time, including fibre splitting (with the cracks approximately along the longitudinal direction) and fibre breakage caused by the tensile loading. The former resulted from the failure of the matrix between fibres because continuous fibres were only placed along the longitudinal direction in this case, and the latter was more likely caused by the excessive tension. These cracks were not located at the left and right edges of the hole as in the drilled samples. The fibre breakage occurred at the outer edge of the sample and located away from the transverse centreline of the hole. A relatively brittle failure pattern was presented in the curved fibre case 1, mostly attributed to the used thermoset epoxy, and two kinds of cracks appeared and propagated simultaneously.

In the curved fibre case 2, samples failed in tension but the cracks located far away from the central area of the sample, as shown in Figure 7-8c. The fibres placed along lower in-plane principal stress trajectories improved the stiffness of samples in the transverse direction and also prevented the fibre splitting. In this case, the fibre placement effectively enhanced the sample and eliminated the effect of the hole. The change in the crack locations indicated the opportunities for customising the failure modes in future 3D printing with designed curved fibre paths. Curved fibre case 3 with fibres placed around the hole in addition to the principal stress trajectories also exhibited a brittle failure mode. Although the epoxy matrix in the interspaces was damaged during the loading process (see Figure 7-8c), no fibre breakage occurred before the point of ultimate load. The breakage of fibres initiated above the hole and propagated through the samples around the circumference of the hole. Comparing with case 1,

the change of the failure mode was apparently caused by the fibres placed around the hole, which prevented the edges of the hole from the crack initiation and also partly enhanced the sample in the transverse direction. The failure modes of these three curved fibre cases were all brittle but exhibited different initiation and propagation of the cracks. It revealed that the fibre placement along higher in-plane principal stress trajectories would make a relatively even stress distribution and the additional fibres (in the case 2 & 3) also changed the failure pattern significantly. The effect of the interaction between fibre placements in different layers will be further analysed in the following finite element modelling. Finally, the Markforged® samples, as the state-of-the-art commercial 3D printing technology, were used to compare the hybrid manufacturing technology in this study. As shown in Figure 7-8a, the ultimate tensile load of Markforged® sample was quite low compared with all other cases, which was partly due to the default, quasi-isotropic fibre placement in its Eiger slicing software. The percentage of continuous fibres placed end-to-end was lower than 30% even in the 0° ply (as shown in Figure 7-3d), and other plies with 90°/±45° fibres contributed less to the tensile load carrying capacity. In the loading process, the cracks initiated from the outer edge of the samples, approximately along the centreline of the hole. Then, they propagated around the circumference of the hole like those in case 3, which also resulted from the additional loops of fibres placed around the hole.

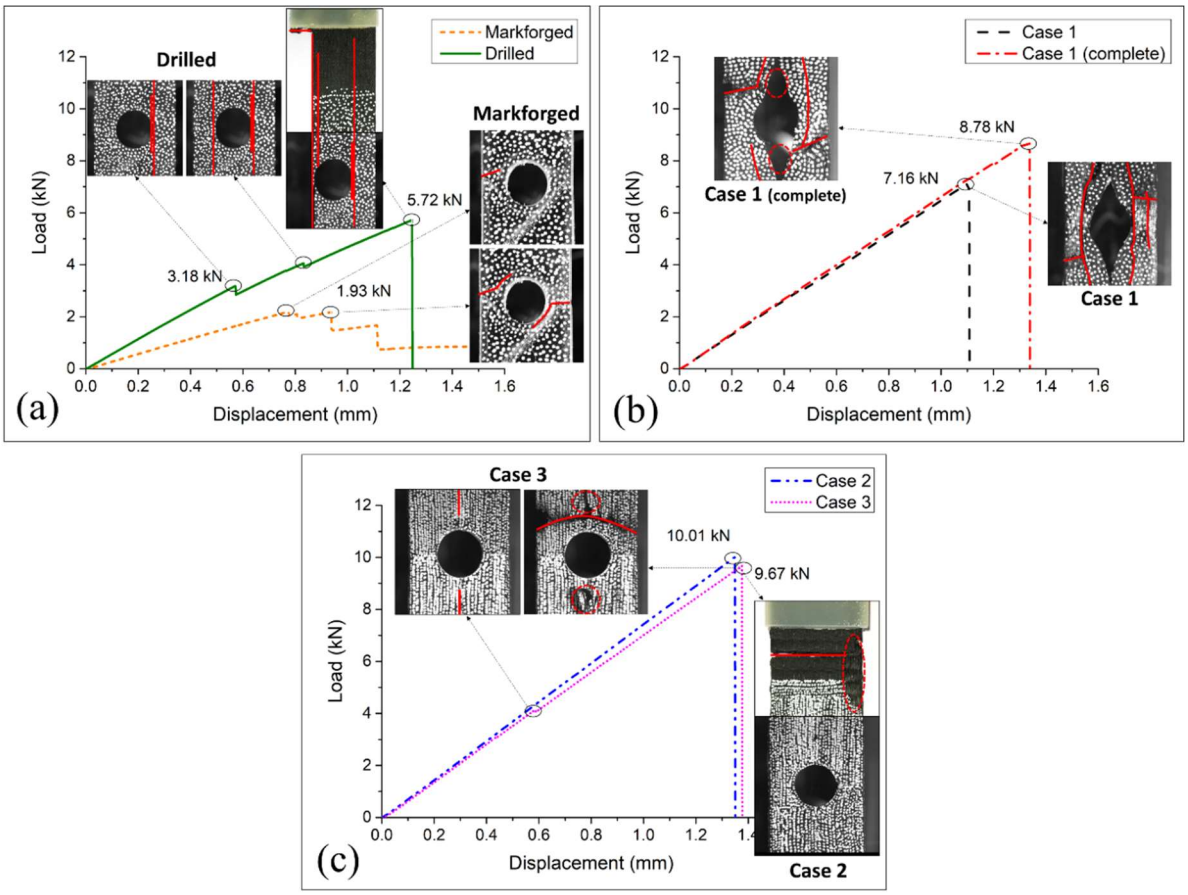

Figure 7-8 Load-displacement curves and crack propagation of samples: (a) Drilled and Markforged, (b) Curved fibre Case 1, and (c) Case 2 and 3.

7.4.2.2 Strength and stiffness

The strength and stiffness of six different cases were calculated as Eq. (20) – (22):

$$F_x^{OHT} = P^{max}/A \tag{20}$$

$$\varepsilon_x = s/L \tag{21}$$

$$E_x = F_x^{OHTu}/\varepsilon_x \tag{22}$$

where F_x^{OHT} is the ultimate tensile strength in the test direction, P^{max} is the maximum force carried by test specimen prior to failure, A is the gross cross-sectional area (disregarding the hole), ε_x is the strain in the test direction, s is the displacement in the loading direction, L is the

length of the sample, and E_x is the stiffness in the test direction.

As shown in Figure 7-9, both the yielding strength and the ultimate tensile strength were calculated for the drilled samples. As mentioned above, the former is only 50.9% of the latter. Considering the apparent cracks at the yielding point, the yielding strength can better indicate the actual bearing capacity of the open-hole composite. The strength of case1-complete was improved by 21.0% compared with the case 1 sample without materials placed at the interspaces, but the stiffness of these two samples were almost the same. Comparing with drilled samples, the customised fibre placement in case1-complete improved the strength and the stiffness by 166% and 5%, respectively. The initiation of the crack was significantly postponed by the customised fibre paths, with only 5% increased usage of fibres. Although the stiffness was slightly improved, the increase of strength was apparent because of the better load transfer and the avoidance of fibre cut-off during the drilling process. The results of case 2 & 3 were compared with those of case1-complete in the following discussion to better evaluate the influence of the additional fibres. For the curved fibre case 2, the strength and stiffness were decreased by 12.0% and 10.2%, respectively, even though the usage of fibres in the composite preforms was increased by 23.02%. The decreases in the strength and stiffness values could be partly due to the larger thickness of case 2 (from 0.6 to 0.8 mm). For the case 3, the tensile strength was increased by 11.4% and the stiffness was improved by 6.6% (compared with the case1-complete) with the additional fibre placed around the hole, about a 2.7% increment of fibre usage. It revealed that the additional fibre placed around the hole could effectively improve the strength and postpone the crack initiation, which can be seen in the samples of case 3 and Markforged®. However, considering the increased fibre usage, those continuous fibres placed in the transverse direction (such as those along the lower in-plane principal stress trajectories) had little effect on the strength and stiffness in the loading direction, especially for such uniaxial tension.

The Markforged® Mark Two printer combines continuous fibres and thermoplastic (usually PA6) for better manufacturability during printing. It became the most popular system for continuous fibre 3D printing for commercial uses as well as academic research. In this study, the uniaxial tensile strength of the open-hole composites printed by Mark Two was 95.6 MPa, only 23.8% of the value of curved fibre case 1. Their stiffness was only 45.7% of the case 1. As mentioned before, the lower strength and stiffness was attributed to the default fibre placement in Eiger system, which was less effective for an open-hole composite under uniaxial tension. The voids in the finished samples fairly reduced the mechanical performance, as shown in Figure 7-7b. It should be noted that the PA6 thermoplastic used in Mark Two is a relatively weak matrix as compared to the thermosetting matrix such as the epoxy used in our study.

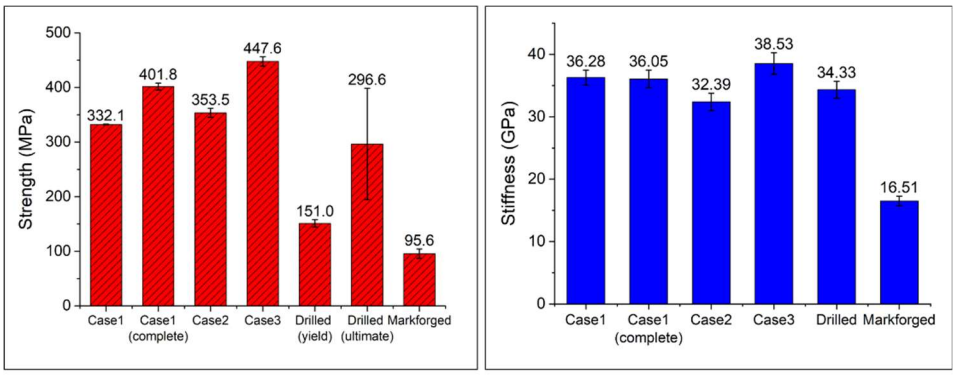

Figure 7-9 (a) Stiffness and (b) strength of open-hole composites under uniaxial tension.

7.4.2.3 Hole integrity prior to failure

The elongation and eccentricity of the hole prior to failure are calculated as Eq. (23) – (25):

$$\delta_x = (D_x - D)/D \tag{23}$$

$$\delta_y = (D_y - D)/D \tag{24}$$

$$e = \sqrt{1 - (\frac{D_y}{D_x})^2} \tag{25}$$

where δ_x is the hole elongation in transverse direction, δ_y is the hole elongation in longitudinal direction, e is the eccentricity of deformed hole, D_x is the diameter in the transverse direction, D_y is the diameter in the longitudinal direction, and D is the original diameter of the hole.

The elongation and eccentricity of the deformed hole prior to failure are shown in Table 7-3, wherein the deformed holes are more similar to a circle when the eccentricity is close to 0. For the Markforged and drilled samples (prior to yielding), though small eccentricity was obtained, their strengths were relatively low (100-150 MPa) at that moment. Therefore, only the data of curved fibre cases (with the strength higher than 300 MPa) will be discussed. Figure 7-10 shows an intuitional picture for the hole integrity prior to failure. Due to the lack of continuous fibre placed along the transverse direction, the elongation and eccentricity prior to failure of case 1 were relatively high. The fibres placed around the hole in case 3 also effectively reduced the elongation in the transverse direction, considering the small increase in fibre usage, but only the additional fibres along lower in-plane principal stress trajectories in case 2 could reduce the elongation in the longitudinal direction. It is assumed that the curved fibres inclining toward the circumference provided compensation for the longitudinal deformation of the hole during the loading process. The open-hole in this case was maintained with a circular profile prior to failure (with the smallest eccentricity).

Table 7-3 Experimental data for the deformation of the hole prior to failure

	Case 1 (complete)	Case 2	Case 3	Drilled (before yielding)	Markforged
δ_x	-11.29%	-1.05%	-1.93%	-1.69%	-2.36%
δ_y	4.60%	1.92%	4.15%	1.31%	2.04%
e	0.530	0.240	0.337	0.242	0.290

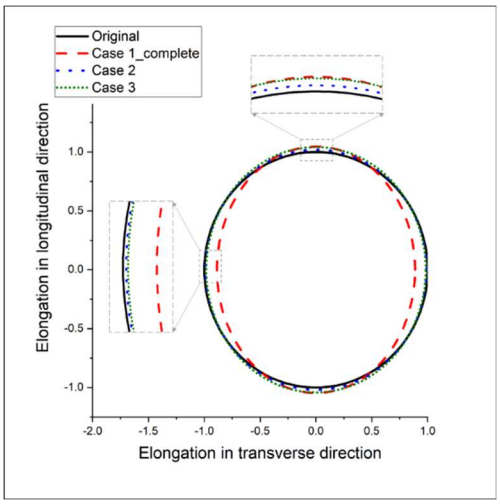

Figure 7-10 The hole integrity prior to failure.

7.4.3 Mechanism and effectiveness of fibre placement

In this section, the stress/strain distributions from both experiment and modelling will be discussed to analyse the mechanism of fibre placement in each case. The result of maximum principal strain is first presented to evaluate the mechanical response of the composites and also to validate the FE model. Then the distributions of maximum principal stress in composite preforms and von Mises stress in the epoxy matrix are shown, which effectively reveals the load transfer of continuous fibres and the potential matrix failure, respectively. A uniform interval type of distribution was adopted for all contour plot legends, in which the contour limit was set as the maximum value of each individual sample to better identify the concentration in the images.

7.4.3.1 Unidirectional fibre placement (drilled)

For the drilled samples, the maxi-principal strain highly concentrated at the edge of the hole but offset from the centreline. As shown in Figure 7-11 a & b, the maximum values located in the very small area (circled in black). Also, good agreement of the distribution can be seen, thus the following stress analysis based on the modelling result are relatively reliable. In Figure

7-11c, only the continuous fibres nearest to the hole (circled in black) were under the tensile stress with a high value. The cut-off fibres above and below the hole and those far away from the hole (all framed in black) had little effect on the load bearing. Figure 7-11d exhibited the stress concentrations in the matrix between the unidirectional fibres. They started from the left/right edge of the hole and extended along the test direction (circled in black). Since the cut-off unidirectional fibres could not effectively transfer the loading across the hole, the stress concentrations in the matrix led to the shear and/or tensile damage of the matrix, followed by longitudinal splitting of continuous fibres prior to final failure.

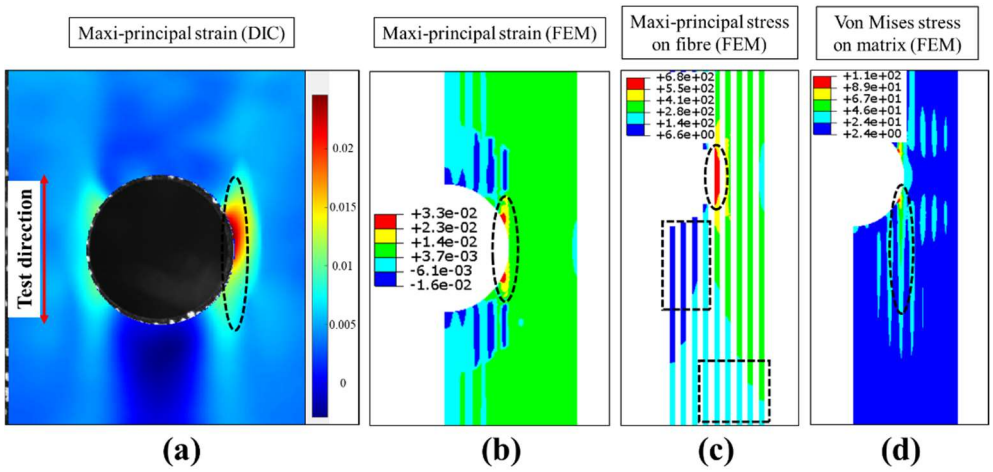

Figure 7-11 Strain and stress (unit: MPa) distributions in drilled samples

7.4.3.2 Higher in-plane principal stress trajectories (case 1)

Good agreement between experiments and modelling was also obtained for the maximum principal strain in case 1. As shown in Figure 7-12 a & b, the strain concentration at the edge of the hole (circled in black) still existed, but the maximum values were shifted from the edge to the angular area far away from the hole (framed in black). Compared with the drilled sample, an even distribution of strain was observed in case 1 (most of the areas were in yellow and red colour). In Figure 7-12c, the distribution of maximum principal stress on the fibre preform

explained the mechanism behind, wherein the maximum value located at the peripheries of the hole was reduced by 17.6% and those fibres far away from the hole (framed in black) still contributed to withstand of the tensile loading. Therefore, the stress concentration in the matrix was eliminated from the left and right edges of the hole. However, the potential failure of the matrix still occurred at those slim areas between fibres (black dotted line in Figure 7-12d). In addition, the concentration located on the top and bottom sides of the hole resulted in the damage of the pure PA area (circled in black) in the experiments.

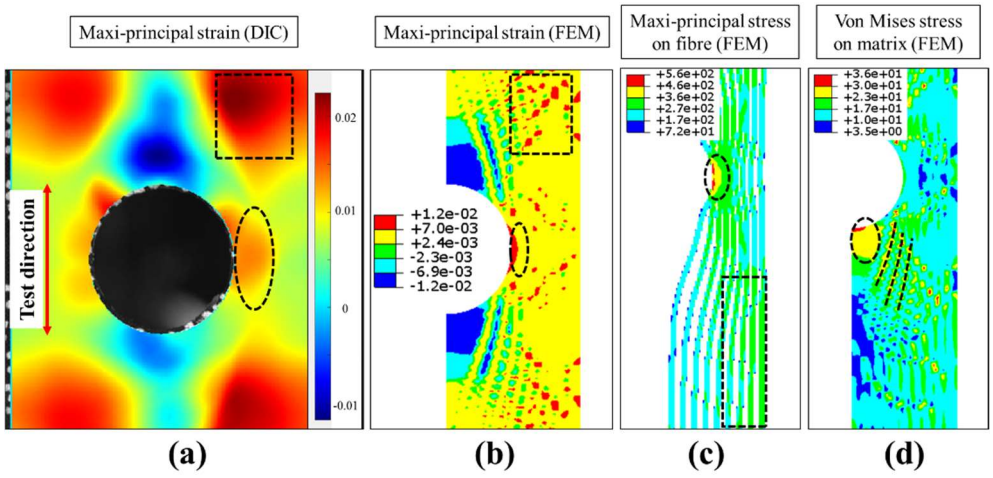

Figure 7-12 Strain and stress (unit: MPa) distributions in case 1

7.4.3.3 Principal stress trajectories with additional fibres (cases 2 & 3)

For case 2, the distribution of maximum principal strain exhibited similar features between the experiments and modelling, in which almost the whole composite plate was under tension. The strains with relatively high values were located at the peripheries of the hole and angular areas away from the hole. As shown in Figure 7-13c, the stress concentration in the fibre preforms occurred at the edge of the hole, with a similar maximum value as in case 1. The continuous fibres near the longitudinal centreline of the samples also contributed more to the load-bearing (most of the fibres were in green colour). For the stress distribution in the matrix, due to the

reinforcement of the additional fibres placed along the lower in-plane principal trajectories, almost no concentration was observed. The result indicated the customised fibre placement in case 2 nearly made a perfect re-distribution of the stress in the matrix and hence prevented the matrix from early damages.

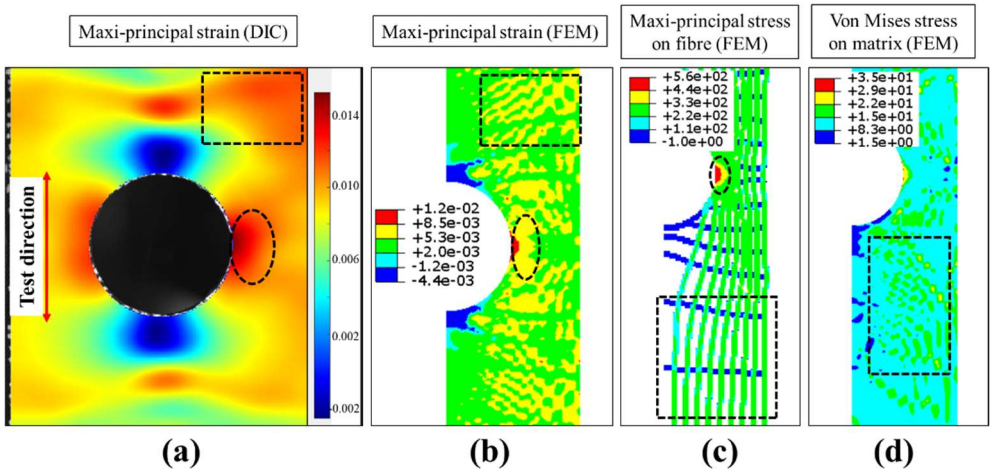

Figure 7-13 Strain and stress (unit: MPa) distributions in case 2

For case 3, the framed concentration of maxi-principal strain (in Figure 7-14a) occurred in the matrix-rich area. Due to the additional fibres placed around the hole, the strain concentration at the edge of the hole extended along the circumference of the hole, which can be seen in both experimental and modelling results (circled in black in Figure 7-14a & b). Also, the maximum stress on fibres was reduced by 19.6% (circled in black in Figure 7-14c) compared with case 1, indicating the additional fibres could eliminate or postpone the fibre breakage at the edge of the hole. As shown in Figure 7-14c & d, the stress concentrations were shifted to the outside of the additional fibres (framed in black), in both fibres and matrix, which also corresponded to the area where the crack propagated in the experiment.

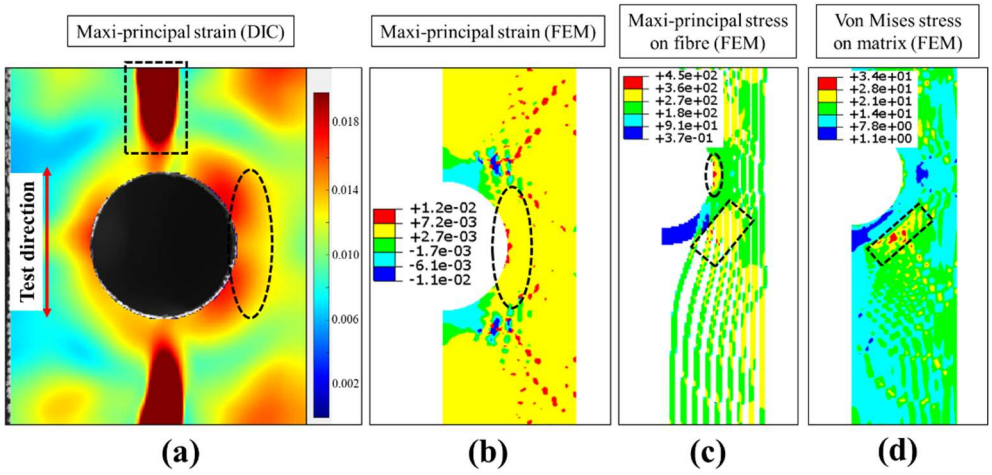

Figure 7-14 Strain and stress (unit: MPa) distributions in case 3

7.4.3.4 Concentric fibre placement (Markforged)

The modelling-based analysis would not be conducted for the Markforged® samples, since it was hard to obtain the fibre paths from the closed Eiger system. The voids would cause additional damages during the loading process, such as the delamination and fibre splitting, which made the printing path-based FE analysis for this case less meaningful. The distribution of maximum principal strain from DIC is shown in Figure 7-15. It can be seen the fibres placed around the hole also altered the strain distribution. The region with the concentration was expanded slightly and moved offset from the centreline but the strain was still highly concentrated around the hole (most of the rest areas were in blue colour). It means the continuous fibres in this case could not transfer the load to the whole structure effectively.

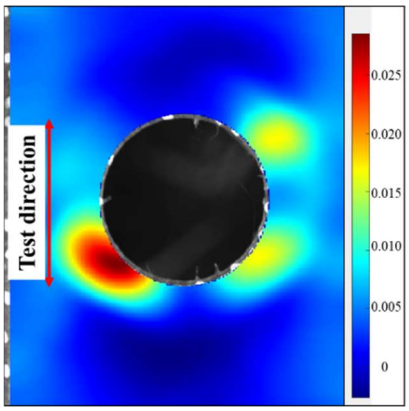

Figure 7-15 Distribution of maxi-principal strain in Markforged samples.

7.5 Conclusions

This chapter presents a comprehensive study for the effectiveness of fibre placement on 3D-printed open-hole composites. The tensile properties, crack propagation, hole integrity prior to failure as well as the mechanism of the load transfer were discussed. The results can be used as the guidance for the future customised design of 3D-printed CCFRP composites with complex shapes and geometric singularities. Main conclusions are drawn as below:

(1) The predominant damage of the drilled sample with unidirectional fibre placement is fibre splitting. The manufactured defects and stress concentration around the hole significantly reduced the strength of the samples.

(2) The fibre placement along higher in-plane principal stress trajectories optimised the stress distribution. The tensile properties were improved and the fibre breakage was shifted away from the periphery of the hole. However, fibre splitting still occurred and the hole was severely deformed prior to failure.

(3) First type of the additional fibres, placed along lower in-plane principal stress trajectories, made a perfect distribution for the stress in both fibres and matrix. The damage was located far away from the central area of the sample. Also, better hole

integrity was kept during the loading process.

(4) Second type of the additional fibres, placed around the hole, performed the best to further improve the tensile properties and postpone the crack propagation, considering a small increment of fibre usage.

(5) The fibre placement method and the manufacturing technique of Markforged system were found to be less effective for uniform distribution of stress/strain in this open-hole composite.

In real engineering applications, the mechanical performance, structural integrity and crack propagation of the printed composites should be considered simultaneously and balanced. The FE model and mechanism presented in this chapter can be considered as a starting point for the further complicated design of 3D-printed multiple layers CCFRP composites. It is worth mentioning that the FE model in this chapter is based on elastic analysis and failure criteria and constitutive models for composites need to be evaluated and implemented in future FE models to enable the failure predictions of such printed curved CCFRP composites. Also the overlap of fibres occurred during the printing process, thus manufacturing constraints also need to be taken into account to inform the fibre placement.

Chapter 8 Fibre orientation and topology optimisation for 3D printing of continuous carbon fibre reinforced polymer composites [*]

Abstract

This study presents a sequentially coupled optimisation of structural topology and fibre orientation for 3D printing of continuous carbon fibre reinforced polymer composites. Topology optimisation was first carried out to obtain the geometry of the structure under a specific load, and then the continuous carbon fibres were placed along the identified principal stress trajectories. Composite performs were 3D-printed by Fused Filament Fabrication (FFF) followed by a post-process of oven curing (with vacuum bagging) using epoxy powders to fill up the gaps. Case study of Messerschmitt-Bolkow-Blohm (MBB) beam under three-point bending was performed, wherein different materials (polylactic acid and short fibre reinforced nylon-6) and printing systems (Markforged® with continuous fibres) were used to evaluate the mechanical performance of the 3D-printed composites. MBB test results showed that the 3D-printed composites with optimised fibre orientation achieved 305% and 256% higher strength and stiffness than Markforged® printed composites. The printed composites also achieved the comparably high stiffness-to-weight ratio as the traditionally manufactured composites by using only 20% continuous carbon fibres.

Keyword

Topology optimisation; 3D printing; fibre orientation; stress trajectory; continuous carbon fibre.

[*] This chapter was submitted to Composites Science and Technology in July 2021.

8.1 Introduction

Continuous carbon fibre reinforced polymer (CCFRP) composite is an exceedingly high strength and stiffness but low weight composite material [116], which is widely used to meet the requirement of high strength-stiffness-to-weight ratios in aerospace, automotive, renewable energy and infrastructure sectors [15, 87, 88]. In some practical situations, where lighter but even stiffer structures are desired, not every single part of the composite is actually needed, meaning that materials in some regions do not contribute much to the structure's stiffness. Thus, the removal of material in those regions may remarkably reduce the structure's weight without much negatively changing its stiffness. This usually is best achieved by topology optimisation [153]. Over the past few decades, topology optimisation has been utilised to design structures made of isotropic materials such as steel and thermoplastic, with numerous methods having been developed, including Solid Isotropic Material with Penalization (SIMP) [154, 155], level-set method [156, 157], Evolutionary Structural Optimisation (ESO) [158, 159] and other feature-mapping methods [160, 161]. CCFRP laminates are usually made of transversely isotropic unidirectional (UD) or orthotropic woven lamina therefore more challenging to implement topology optimisation. According to the research conducted by Lee et al. [162], the topology optimised structure made of UD lamina performs badly when Tsai-Wu failure theory is considered. Quasi-isotropic (QI) laminates have been optimised by using the SIMP or SIMP-like approaches, for instance, Dai et al. conducted topology optimisation for QI laminated composite plates with design-dependent load [163], but the challenge of manufacturing was not taken into consideration. A battery-hanging structure composed of QI laminates and metal was optimised by Chen et al. [164], in which the layout of each layer was smoothed and thus the structure was simplified for the convenience of manufacturing. However, this consequently made the whole layout different from the original output of topology optimisation to a large extent.

In the traditional manufacturing, the CCFRP structures with topology-optimised geometry have to be machined by mechanical processes such as cutting or drilling, in which the carbon fibres in the structure are cut off, leading to the potential risk of residual damage and defects [165]. In addition, as the fibre direction in the UD and woven lamina are pre-defined and not confront to the topology-optimised geometry, the reinforcing performance of the continuous fibre are not maximised. As an alternative, additive manufacturing technology has the potential to fabricate composites with highly complex geometries. Among them, the thermoplastic materials in Fused Filament Fabrication (FFF) 3D printing can be mixed with short and continuous fibres, and then deposited layer by layer to produce the three-dimensional composites at a faster production time [43]. In 2014, Markforged® released the first commercial printer that enabled the 3D printing of composites with 1K continuous fibre reinforcement [2]. Other researchers also developed in-house printers for CCFRP composites [28, 59], which were generally achieved by impregnating the fibres with a thermoplastic matrix prior to extruding or within the printer nozzle. Compared with traditional manufacturing methods, 3D printing of CCFRP offers more design freedom [115], because of the layer by layer deposition of smaller fibre tows (1-2 mm). The opportunities arise from 3D printing CCFRP for controlling fibre placement and reducing material waste can be combined with the topology optimisation of composites.

Alongside the development of 3D printing techniques for CCFRP, new optimisation methods have been developed for both topology and local material orientation [166, 167]. The most popular methods include Continuous Fibre Angle Optimisation (CFAO), Discrete Material optimisation (DMO) [49] and stress-based method [168]. In the CFAO method, every element in the finite element analysis (FEA) equips two variables, *i.e.*, pseudo density which is used to determine whether the material exists or not, and an angle to determine the local orientation of the fibres. Jiang et al. used CFAO to optimise the MBB beams and performed bending tests

[169]. The average stiffness of the sample was increased by 12.4% and 29.9%, respectively, compared to the counterparts with horizontal and vertical material orientation. However, the experimental specimens were manufactured only with the reinforcement of chopped and discontinuous fibres. In addition, local optimum usually occurred in the CFAO method, which was mainly caused by the transform tensor that contains periodically changing functions. Nomura et al. then developed a simultaneous optimisation method based on CFAO to address this issue [170]. However, it did not work very well in the circumstances when the load was applied to a single point or a small region, compared to the methods in which the optimisation of topology and orientation were conducted sequentially. Different from CFAO, DMO is not likely to encounter the local optima problem. However, the orientation outputs of DMO method were constituted by a set of discrete and manually given values, which significantly reduced the design freedom. It was also very challenging to be directly implemented in engineering applications as the fibre orientations are highly discretised [171].

As another common approach the stress-based method assumes that highest stiffness would be achieved once fibre paths are in line with the principal stress trajectories. It can be conducted with high computational efficiency without encountering local optima problems. It has also been proven that the stress-based method improves the structure's stiffness and leads to better stress distributions the orthotropic materials [43, 168]. However, very few experimental tests have been reported to validate this method due to the challenge of controlling continuous fibre paths and the limitations of current 3D printing techniques for CCFRP, in particular the high voids content remained in the printed parts [6]. The entrapped air voids and physical gaps at layer-layer interfaces result in much lower stiffness and strength than expected [20, 70, 120]. Therefore, there is still lack of understanding about the mechanical response and failure process of printed composites with optimised topology and fibre orientation.

In this study, topology optimisation and fibre orientation optimisation were sequentially

coupled, and integrated with the FFF 3D printing process for CCFRP composites. The classical case of a MBB beam under three-points bending was investigated, wherein the topology optimisation based on SIMP was carried out and streamlines of principal stress were obtained for the continuous fibre placement secondly. Then composite preforms of continuous carbon fibre-reinforced thermoplastic were 3D-printed by FFF technique based on the optimised fibre paths. After that, a post-processing treatment (oven curing with vacuum bagging) was adopted, in which thermosetting epoxy powders were sprinkled to achieve void-free composites for experimental validations. To compare the mechanical response, samples with the same geometry were 3D-printed using polylactic acid (PLA) material and short carbon fibre reinforced nylon-6 (SCF/PA-6) composites. Other benchmark samples with concentric fibre placement were also printed using commercial printer Mark Two from Markforged®. Mechanical tests were performed and Digital Image Correlation (DIC) was used to characterise strain distribution prior to failure. Furthermore, finite element models were developed to compare the stiffness-to-weight ratio of the 3D-printed samples with that of traditionally manufactured composites using different stacking sequences.

8.2 Sequential coupling of topology optimisation and fibre orientation optimisation

In this study, a sequential optimisation strategy for both topology and fibre orientation was adopted. The structure of neat, isotropic polymer matrix material (such as epoxy in this study) was topologically optimised first using the SIMP method. The streamlines of higher and lower in-plane principal stress of the topologically optimised structure under the specific loading condition were generated and used as the guidance to place the fibres to reinforce the structure.

8.2.1 Topology optimisation

The key objective of topology optimisation in this research is to maximise the global stiffness while removing material that does not contribute much to the stiffness of the composite

structure. To represent whether material should exist or not, the whole design domain Ω is first discretised into finite elements, and the pseudo density ρ can be given:

$$\rho(x) = \begin{cases} 0 & if\ x \in \Omega \setminus \Omega_s \\ 1 & if\ x \in \Omega_s \end{cases} \tag{26}$$

where Ω_s stands for the area that is constructed by solid material, x stands for a position in the design domain Ω.

Discrete values (between 0 and 1) are then replaced by continuous variables and the SIMP is introduced:

$$E_e(\rho_e) = E_{min} + \rho_e^p(E_0 - E_{min}),\ \rho_e \in [0,1] \tag{27}$$

where ρ_e is the continuous design variable in the interval of $[0,1]$, E_{min} is a very small stiffness of voids which is necessary to prevent singularity of stiffness matrix, and p is the penalisation parameter ($p = 3$ in this case).

In such a condition, the optimisation problem can be defined as:

$$\min_{\rho}: c(\rho) = U^T K U = \sum_{e=1}^{N} E_e(\rho_e) u_e^T k_0 u_e\ , \rho \in [0,1] \tag{28}$$

$$subject\ to: \qquad \sum_{e=1}^{N} v_e(\rho_e)\ / V_0 = f \tag{29}$$

$$KU = F \tag{30}$$

where c is the compliance, U is the global displacement vector, K is the global stiffness matrix, F is the vector of forces applied on the nodes, k_0 is the element stiffness matrix of elements with unit Young's modulus, u_e is the displacement vector of element. v_e is the volume of element, f is the prescribed volume fraction, and N is a set of indices of the elements.

It is worth noting that directly implementing the above steps would possibly result in the

structure similar to a checkerboard consisting of alternating solid and void elements, and consequently such a structure will be extremely difficult to manufacture. In addition, the optimised structures are usually mesh dependent, which means that once the meshing changes, the outcome structure would become different.

In order to prevent these problems filter techniques were developed, including sensitivity filtering [172], density filtering [173], *etc*. Among them the filter based on a Helmholtz-type PDE developed by Lazarov and Sigmund developed [174] have proven to successfully resolve the above issues. It can be described as:

$$-R^2\nabla^2\tilde{\rho} + \tilde{\rho} = \rho \tag{31}$$

where $\tilde{\rho}$ denotes the filtered density field and R denotes the radius of the filter. Unlike sensitivity filter and density filter, it does not require information about neighbouring elements but only mesh information, thus more computationally efficient. By using filtered density $\tilde{\rho}$ instead of ρ, the mesh dependency and checkerboard issues can be avoided.

However, when the value of $\tilde{\rho}$ is an intermediate value between ρ_{min} and 1, the phenomenon of grey scale would occur, which makes the status of material fuzzy. This is undesirable in topology optimisation especially when manufacturability is considered. In order to address this, Heaviside function developed by Wang et al. [175] is introduced in this research:

$$\overline{\tilde{\rho}} = \frac{tan\ (\beta\eta) + tanh\left(\beta(\tilde{\rho} - \eta)\right)}{tanh(\beta\eta) + tanh\left(\beta(1-\eta)\right)} \tag{32}$$

where η is the threshold for density, and β is a parameter that controls the slope of the projection process. In this way, filtered density value $\tilde{\rho}$ which is larger than η would be projected to 1, and similarly, those smaller than η would be projected to 0, which makes it possible for a result of crisp black and white design with little grey scales.

In order to update material density, sensitivity analysis is proposed:

$$\frac{\partial c}{\partial \rho} = \frac{\partial c}{\partial \overline{\widetilde{\rho}}} \frac{\partial \overline{\widetilde{\rho}}}{\partial \widetilde{\rho}} \frac{\partial \widetilde{\rho}}{\partial \rho} \tag{33}$$

And the method of moving asymptotes (MMA) [176] is utilised to acquire the optimal solution of the problem due to its effectiveness.

8.2.2 Fibre placement based on principal stress trajectories

Since the mechanical properties of carbon fibres are superior in the fibre direction, continuous carbon fibres should be preferably placed along the direction of maximum tensile and compressive stresses. In other words, the optimised fibre paths align with the stress trajectories which are streamlines based on the orientation of the higher and lower in-plane principal stress.

To demonstrate the above approach for fibre placement, the classical MBB beam with a length of 210 mm and a height of 35mm (length/height ratio = 6:1) was performed. Only half of the structure with sliding supports was analysed due to symmetry. Figure 8-1(a) shows the dimension of the structure and the position of the external load. The material used in the topology optimisation was epoxy with Young's modulus $E = 3.0\ GPa$ and Poisson's ratio $v = 0.37$. The geometry of topology-optimised result is shown in Figure 8-1(b) and the higher and lower in-plane principal stress trajectories of the optimised cases are shown in Figure 8-2(c), together with other printing paths of 3D-printed samples. More details of the printer paths were presented in Section 3.

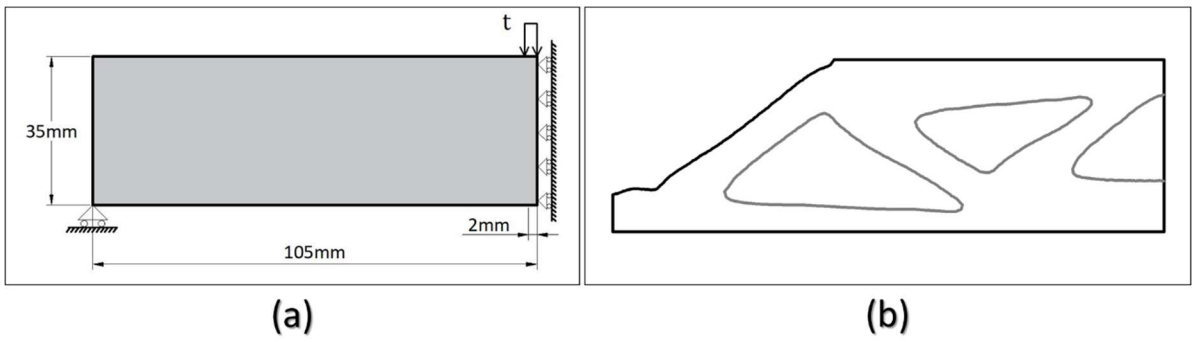

Figure 8-1 (a) The domain of MBB beam and (b) the geometry of optimised beam

8.3 Manufacturing

In this section, the manufacturing process of the experimental samples was presented, including the FFF 3D printing and the post-processing of the 3D-printed preforms with optimised fibre paths. The short carbon fibre reinforced nylon-6 (SCF/PA-6) was first used, since it was demonstrated that mixed SCF could significantly improve the flexural properties of composites, compared with the pure thermoplastic materials [138]. The manufacturing of the pure PA-6 sample was also attempted, but the sample was not adopted as the severe warpage always led to the beforehand instability/tilt during the bending tests. As a result, a PLA sample was printed, which is also the most widely-used material in FFF 3D printing. After that, a sample with continuous fibres was printed for comparison, using the commercial Markforged® printing system using its default fibre placement method. Finally, the target sample with optimised fibre paths was prepared via the hybrid manufacturing, including the printing of CCF/PA-6 preforms and the post-processing with thermosetting epoxy powder. Each type of sample consisted three specimens for the later bending testing.

8.3.1 FFF 3D printing

A Prusa i3 MK3s printer was used in this study for the printing of PLA and SCF/PA-6 samples and a Mark Two printer was used for the Markforged sample (continuous carbon fibre reinforced PA-6). The printing parameters and materials sources are shown in Table 8-1. CCF/PA-6 composite preforms were first printed using Prusa i3 MK3s printer (with a brass nozzle from Markforged®) in order to achieve customised fibre paths. The printing CF filament (with a diameter of 0.375 mm) was also sourced from Markforged® and consists of a fibre bundle (approximately 1000 continuous 7 μm diameter carbon fibres) and an impregnated polymer (polyamide 6-I) [7]. Since the CF filament contains continuous fibres and there was no filament cutter on the Prusa printer, the toolpaths cannot stop and start as they would during

thermoplastic printing. Necessary continuous toolpaths (G-code) were generated through a MATLAB script and transferred to the printer. All the samples were printed onto an unheated Garolite print plate which was coated with a layer of PVA, ensuring adequate adhesion during printing.

Table 8-1 Printing parameters for the MBB samples with different materials

	Print temp (°C)	Bed temp (°C)	Printing speed (mm/min)	Nozzle diameter (mm)	Material sources
PLA	210	60	60	0.4	Prusa® PLA Galaxy Silver
SCF/PA-6	275	90	60	0.4	Markforged® Onyx
Markforged	270	room temp	10	1.3	Markforged® CCF and PA-6
CCF/PA-6 preforms	245	room temp	10	1.3	Markforged® CCF

The detailed printing paths of the MBB samples are shown in Figure 8-2. For the PLA and SCF/PA-6 samples, the walls with 0.8 mm width were first printed around the geometry singularity to achieve a better outer surface, and then a pattern of ±45° lines infill (100% infill) was used to enhance the structure and reduce the voids. As shown in Figure 8-2b, the default material placement method in Markforged® Eiger system was adopted. Two paths of PA-6 and two paths of concentric continuous fibres were printed first as the wall around the geometry singularity and then the CF filaments were printed in a sequence of 0°/+45°/-45°/90° as the primary infill. After that, PA-6 was printed at the interspaces in each layer to fill the remaining gaps. As can be seen, some relatively large resin-rich areas were generated from the Eiger system, even when a placement method with maximum fibre usage was chosen. The volume fraction of carbon fibres was calculated as 17.34% in the printed composite part, since a 34.5% of fibre volume fraction was declared by Mrakforged® for the CF filament. For the CCF/PA-

6 preforms with optimised fibre paths, the CF filaments were printed first along the outline of the structure and then the higher and lower in-plane principal stress trajectories in each layer, as shown in Figure 8-2c. A printed single-layer CCF/PA-6 preform was shown in Figure 8-3. Since the rest areas would be infilled by powder epoxy, the fibre volume fraction of the final composite was calculated as 20.60%. As can be seen in Figure 8-2, an excess length of 10 mm was printed on both the left and right ends for all samples so that they can stand on the support properly during the bending test.

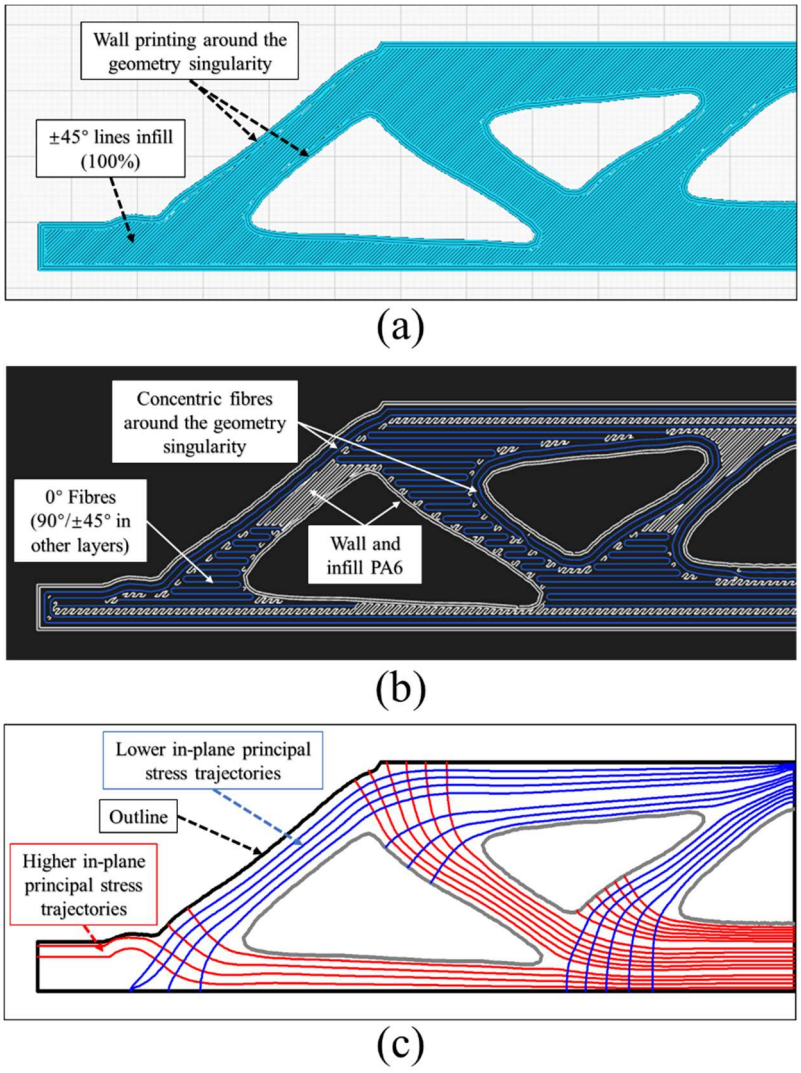

Figure 8-2 The printing paths for samples: (a) PLA and SCF/PA-6 (b) Markforged and (c) CCF/PA-6 preforms (with optimised fibre paths)

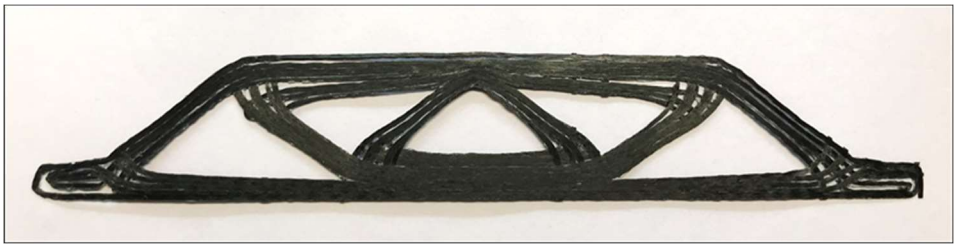

Figure 8-3 The printed single-layer CCF/PA-6 preform with optimised fibre paths along principal stress trajectories

8.3.2 Post processing of 3D-printed CCF/PA-6 preforms

Considering the gaps between print paths and the weak adhesion between layers, post-processing treatment was needed for the fabrication of a complete three-dimensional sample, in which melted matrix should infiltrate the CCF/PA-6 preforms and the fibre alignment was maintained during the post-processing. Thus, the continuous fibres could act as the reinforcement of the composites to evaluate the effect of fibre placement method.

In this study, an aluminium-made mould was designed for the post-processing, as shown in Figure 8-4a. The 3D-printed CCF/PA-6 preforms were placed in the male mould and the powder epoxy was sprinkled above and between layers. Then the female mould was placed on top of them. In addition, polytetrafluoroethylene (PTFE) non-stick ply and the release agent were applied on the moulds for the demoulding purpose. The system was put into an oven for heating, with vacuum bagging, in which the female mould would provide even pressure on the sample. The thermosetting epoxy powder (PE6405, density 1.22 g/cm3) used in this study was engineered by Swiss CMT and then produced by FreiLacke. The epoxy sinters and melts at around 45-60 °C, reaching a minimum viscosity for infiltration around 120°C [132]. Curing was carried out through a heat activated catalytic process where the curing agent required a temperature of at least 150 °C for reaction initiation [133, 134]. For this reason, a three-stage

heating profile was used as presented in Figure 8-4b. The curing was first set at 40 °C for 8 hours to remove all form of moisture from the powder. The temperature then ramped to 120 °C for 2 hours, melting the powder and consolidating the system. Following this, the system was cured at 180 °C for 2 hours. The low melt viscosity (minimum of 1.26 Pa·s at 120 °C), the low curing temperature (compared with the melting point of PA-6, 215 °C) and the even vacuum pressure aimed to achieve a CCF/PA-6/Epoxy composites sample with low-porosity and customised fibre paths.

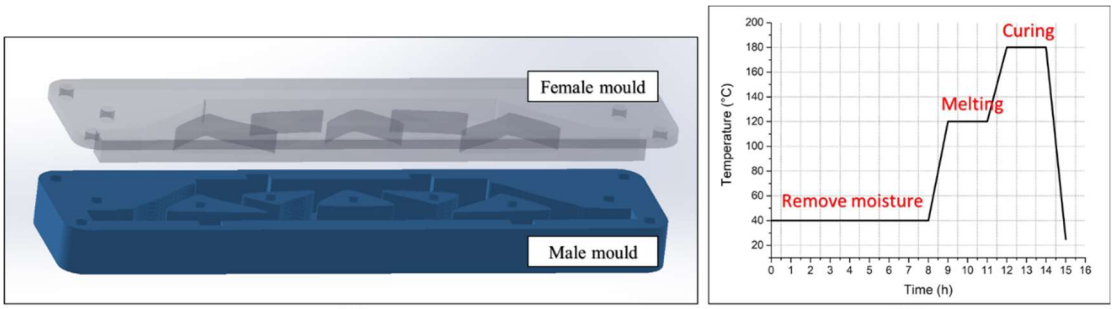

Figure 8-4 (a) The mould design for the post-processing of CCF/PA-6 preforms (b) The three-stage heating profile of post-processing

8.4 Three-point bending tests of 3D-printed MBB beams

8.4.1 Mechanical tests

The experimental set-up is shown in Figure 8-5. The three-point bending tests were performed on an Instron 3360 testing system with a 50 kN load cell, in which the diameter of the loading nose and the support was 5 mm. The span was set to 210 mm and 3D-printed fixtures were used to hold the MBB samples. A crosshead speed of 2 mm/min was applied for all tests, while a pre-load 1 mm/min was used to remove slack in the specimen (no data was captured during preload). To measure the 2D strains using digital image correlation (DIC), a speckle pattern was applied to the surface of each specimen. After the tests, all the DIC data were processed

through a MATLAB script to obtain the full-field displacements and strains.

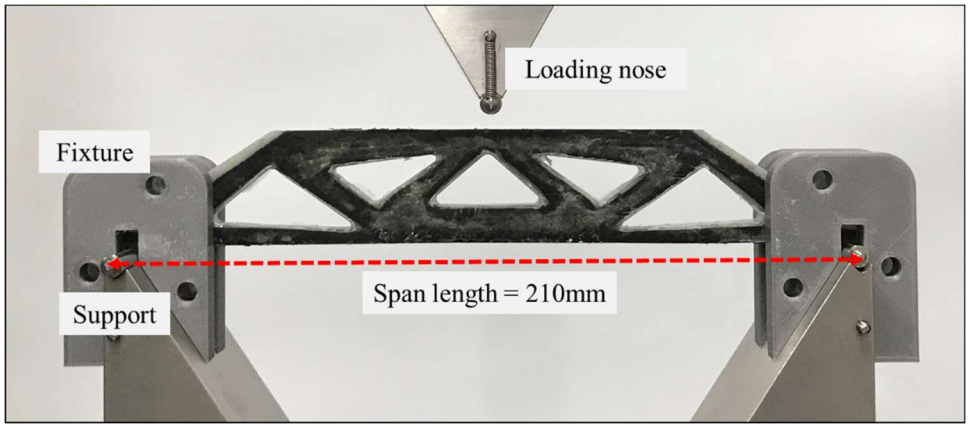

Figure 8-5 The set-up of three-point bending test of MBB beam

To avoid the out-of-plane failure such as distortion and instability, all the experimental specimens were manufactured with the thickness more than 7 mm, *i.e.*, thickness-to-height ratio is higher than 1:5. As shown in Figure 8-6a, the PLA sample experienced a stage of noticeable plastic deformation without decrease in carrying capacity at the peak load before the damage. It finally failed in a balanced and symmetry pattern with distributed cracks in the structure. For the SCF/PA-6 sample, the yielding happened at the early stage of the loading process with the decrease of flexural stiffness, since the PA6 matrix is more ductile than the PLA. Delamination became the predominant damage of the SCF/PA-6 sample before it reached to the peak load. This was assumed to be caused by the mixed short carbon fibres, which introduced more voids in the composites and reduced the adhesion between the adjacent layers [121].

The loading process of the samples with continuous carbon fibres reinforcement are shown in Figure 8-7. For the Markforged sample, less plastic deformation occurred but same delamination problem was observed. The delamination due to the weak layer-to-layer adhesion (especially between the layers with and without the continuous fibres) has also been reported

in previous research [2]. After the delamination beneath the loading nose (a stage can be seen in the load-displacement curve), the specimen exhibited out of plane distortion leading to a clear drop of carrying capacity.

The response of the CCF/PA-6/Epoxy sample with optimised fibre paths is shown in Figure 8-7b. The failure was quite brittle with the crack initiating from the right support and propagating along the edge of the structure. Rather than the fall-into-pieces failure in the PLA sample, the optimised fibres tended to prevent the central area of the structure from early failure. In addition, the consolidation of the powder epoxy during the post-processing enhanced the strength between layers, thus no noticeable delamination was seen in the area beneath the loading nose for the CFF/PA-6/Epoxy sample.

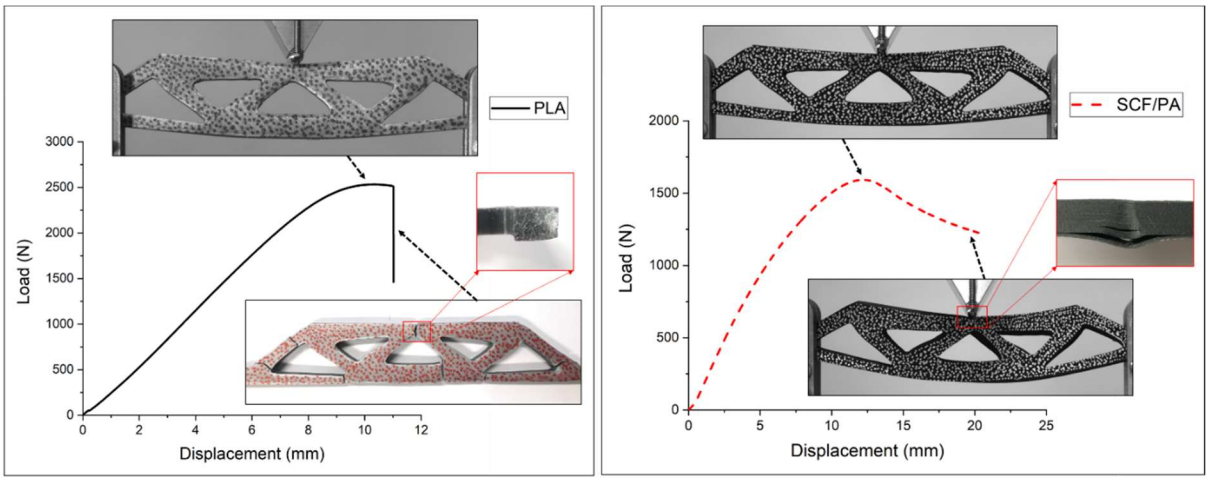

Figure 8-6 Load-displacement curves and crack propagation: (a) PLA and (b) SCF/PA-6

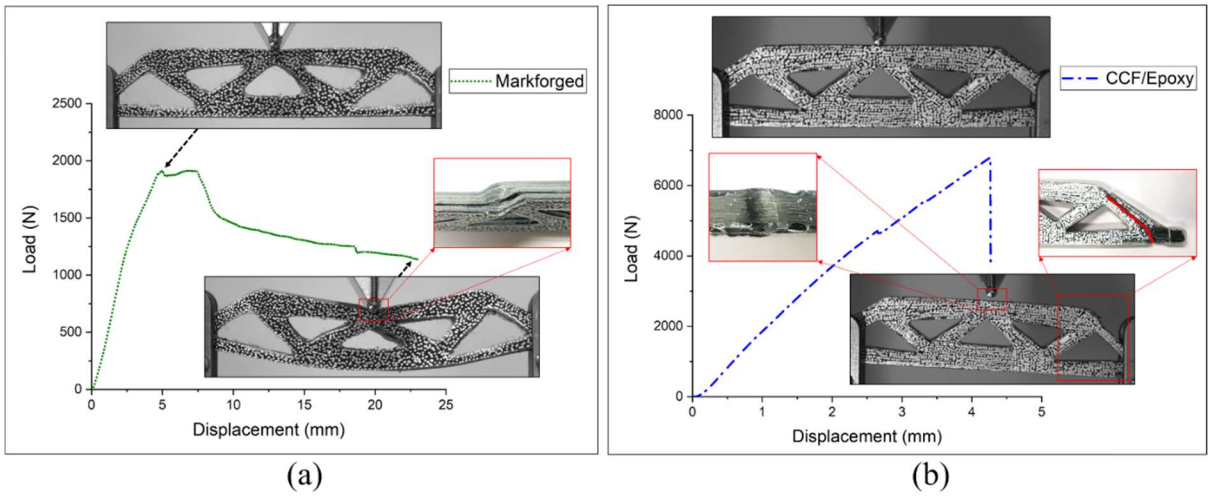

Figure 8-7 Load-displacement curves and crack propagation: (a) Markforged and (b) CCF/PA-6/Epoxy

The flexural strength, flexural strain, flexural modulus and stiffness-to-weight ratio were calculated as Eq. (34) – (37):

$$\sigma = \frac{3PL}{2bh^2} \tag{34}$$

$$\varepsilon = \frac{6\delta h}{L^2} \tag{35}$$

$$E_B = \frac{L^3 m}{4bh^3} \tag{36}$$

$$\nu = \frac{E_B}{\rho} \tag{37}$$

where σ is the flexural stress, ε is the flexural strain, E_B is the flexural modulus of elasticity in bending, P is the force, ν is stiffness-to-weight ratio (also called specific stiffness), L is the support span, b is the thickness of samples, h in the height of samples, δ is the maximum deflection of the centre of samples, m is the slope of the tangent to the initial straight-line portion of the load-deflection curve and ρ is the gross density of the structure (disregarding the topology-optimised area).

As shown in Figure 8-8, the mechanical properties of these four types of 3D-printed MBB samples are presented. The comparison of the samples without continuous fibres reinforcement was first discussed. It can be seen the SCF/PA-6 sample exhibited a lower flexural strength, modulus and specific stiffness than the PLA sample. As mentioned above, this was due to the ductile PA6 matrix and the delamination-dominated failure. For the Markforged sample, the flexural modulus and specific stiffness were significantly increased by 2-3 times because of the reinforcement of continuous carbon fibres. However, the strength was even slightly decreased because of the delamination. This was also revealed in a previous study about topology optimisation and continuous fibres using a Markforged printer [177]. In contrast, the CCF/PA-6/Epoxy sample with optimised fibre paths in this study exhibited superior mechanical properties. Compared with the Markforged printed sample, the flexural strength, modulus and stiffness-to-weight ratio of the printed CCF/PA-6/Epoxy sample were increased by 305%, 256% and 229%, respectively. The volume fraction of the included fibre was improved slightly from 17.34% to 20.60%, thus the superior mechanical properties of the CCF/PA-6/Epoxy sample apparently resulted from the optimisation of the fibre placement as well as the less void content after the post-processing.

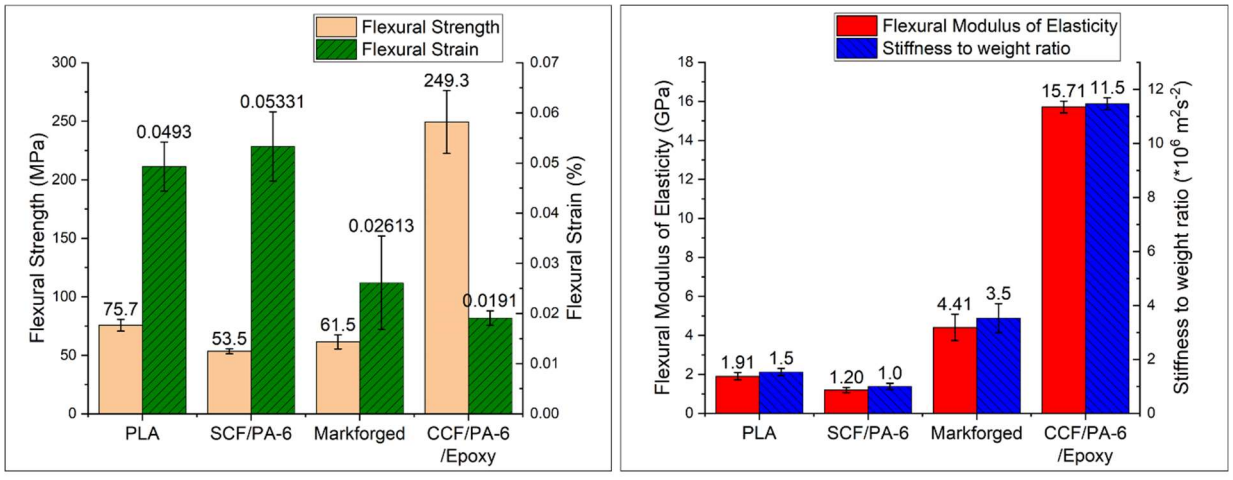

Figure 8-8 Mechanical properties of MBB samples: (a) Flexural strength and stiffness (b)

Flexural modulus and stiffness-to-weight ratio

The distribution of maximum principal (maxi-principal) strain at the peak load was shown in Figure 8-9. The highest strain values of the PLA and SCF/PA-6 samples both located at the bottom of the structure where the material is under largest tension due to bending. For the Markforged sample in Figure 8-9c, high strain concentrated on both sides of the loading position, which was due to the early delamination. For the CCF/PA-6/Epoxy sample, the optimised fibre placement enhanced the structure and shifted the high strains from the central area to the upper-left and upper-right corners of the specimen. The value of the maxi-principal strain in this case was significantly reduced by 80%, which indicated an even distribution.

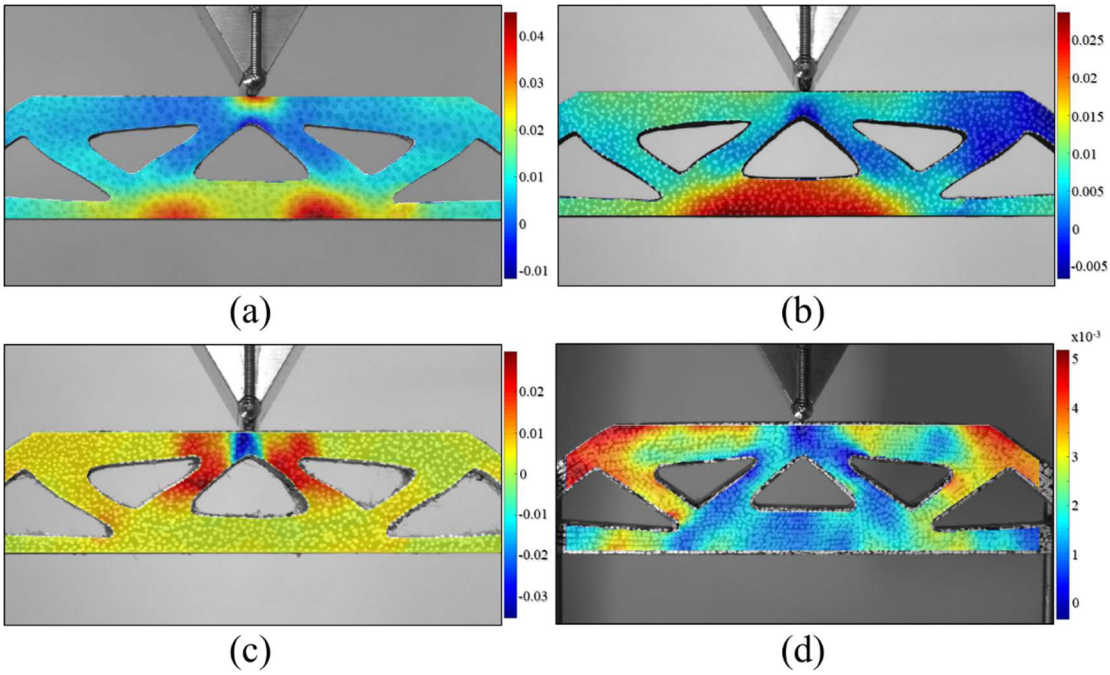

Figure 8-9 The distribution of maxi-principal strain at the peak load: (a) PLA (b) SCF/PA-6 (c) Markforged (d) CCF/PA-6/Epoxy (different legends were used to better identify the strain concentration in each case)

8.4.2 Failure analysis of CCF/PA-6/Epoxy sample

To further investigate the microstructure of the unique CFF/PA-6/Epoxy sample, SEM characterisation of the cross-sections and fracture profiles are presented. As shown in Figure 8-10(b), no apparent voids and pores can be seen in the middle-bottom part of the specimen even after the bending test, confirming that the low porosity and good fibre/matrix bonding was achieved via the hybrid manufacturing. However, the localised matrix-rich area in Figure 8-10(a) indicated an uneven fibre distribution for the microstructure of composites, which was mainly caused by the original fibre distribution in the Markforged® CF filament [25]. Since the PA-6 matrix had to stay solid during the post-processing to maintain the fibre alignment, the excess PA-6 matrix could not be removed and also a relatively low fibre fraction remained.

The fracture profiles of CFF/PA-6/Epoxy sample after the bending test are shown in Figure 8-11. It can be seen the failure of the specimen began from the location close to the support, in which the printed fibre paths along higher and lower in-plane principal stress trajectories intersected. As shown in Figure 8-11 b & c, the shear failure of the matrix happened between the print paths along minimum stress trajectories, while the fibres along maximum stress trajectories were broken by the shear/tensile stress here. Then the cracks extended to the edge of the specimen, as shown in Figure 8-11 d & f. Splitting occurred and propagated along the longitudinal direction of fibres in this area, followed by the fibre/matrix de-bonding. Finally, the crack was arrested by the crossover fibres at the top-right corner (as shown in Figure 8-11a), leading to the final failure of the specimen. In summary, the optimised fibre paths re-distributed the stresses and avoided the central part of the specimen from the bending failure, which can be evidenced from the microstructure image after test in Figure 8-10. In addition, no delamination and micro-cracks were not found in these areas. Therefore, the vulnerable position was shifted close to the supports and the specimen was mainly damaged by the shear failure of matrix and the fibre/matrix de-bonding.

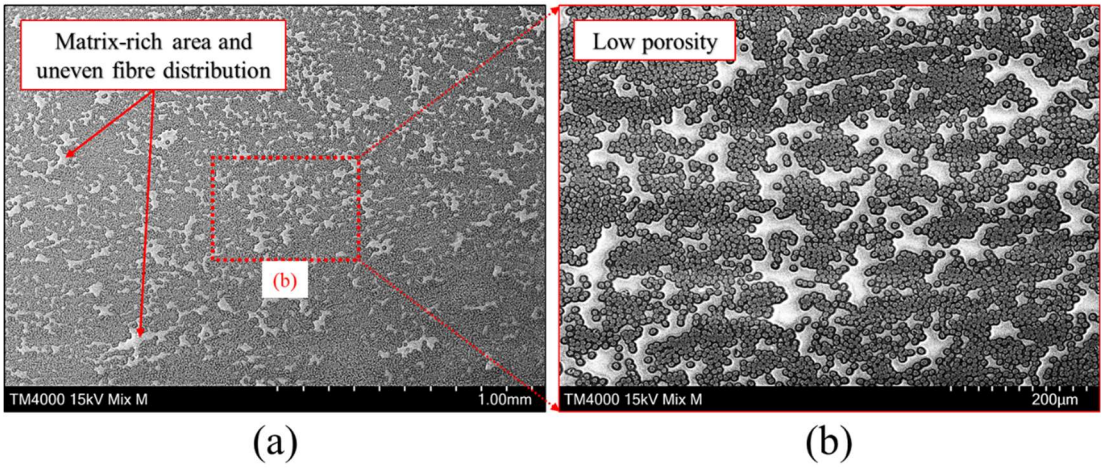

Figure 8-10 Cross-section of the middle-bottom part of the CCF/PA-6/Epoxy specimen

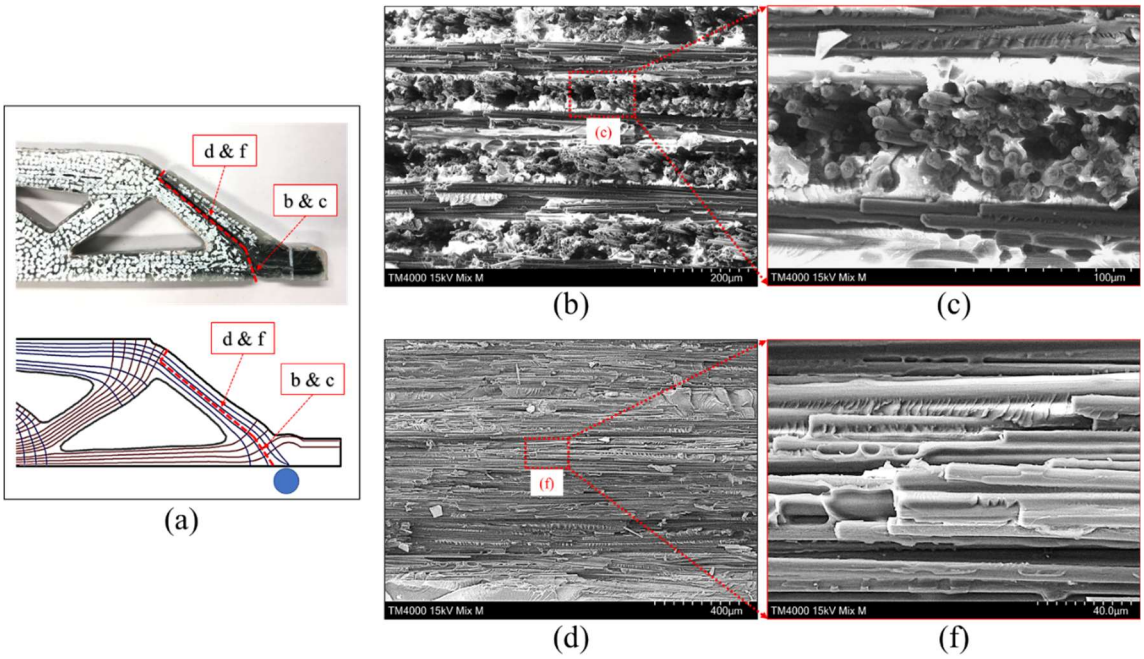

Figure 8-11 Fracture profile of the CCF/PA-6/Epoxy specimen: (a) & (b) shear failure at the directly-loaded area (c) & (d) fibre/matrix de-bonding

8.5 Comparison with traditionally manufactured composites

In order to assess the lightweight performance of 3D-printed CCF/PA-6/Epoxy with optimised fibre placement, finite element analysis of the traditionally manufactured composite beams was

carried out for comparisons. As shown in Table 8-2, only the elastic properties were used in the FE models to evaluate the stiffness-to-weight ratios. The properties were obtained based on the rule of mixture of T300 Carbon Fibre and PE6405 Epoxy, in which CFRP composites with two different volume fractions were performs, 20.6% (the same as the experimental CFF/PA-6/Epoxy sample) and 50% (approximately the highest value of the general traditionally manufactured composites), respectively.

As shown in Figure 8-12, two geometries of the domain were investigated in finite element analysis. The 'Topology' case used the same topology-optimised geometry as for the 3D-printed samples whilst the 'Beam' case has an intact 230*35 mm domain before the topology optimisation. Three different stacking sequences were adopted in each case, including 'UD 0°' [0°], 'Cross-ply' $[0°/90°]_s$ and 'QI' $[0°/45°/-45°/90°]_s$. In the finite element modelling, S4R conventional shell elements were used and the 'Composites Layup' module in Abaqus software was applied to define the stacking sequence and properties of the elements. The two supports were fixed and a displacement was applied to the loading nose along vertical direction. The out-of-plane displacement at all nodes was constrained. The interaction between the loading nose and the composite beam was defined as 'Hard contact' to only allow normal compression with a penalty in the tangential direction (coefficient of friction = 0.3). The reaction force of the loading nose was captured to calculate the stiffness-to-weight ratio.

Table 8-2 The elastic properties of the materials used in the FE modelling

	Density (g/cm^3)	Ex (GPa)	Ey (GPa)	G (GPa)	v12	v21
T300 Carbon Fibre	1.76	230	-	-	0.2	-
PE6405 Epoxy	1.22	3	-	-	0.37	-
20.6% CFRP	1.37	49.762	4.507	1.647	0.335	0.03
50% CFRP	1.54	116.5	8.699	3.188	0.285	0.021

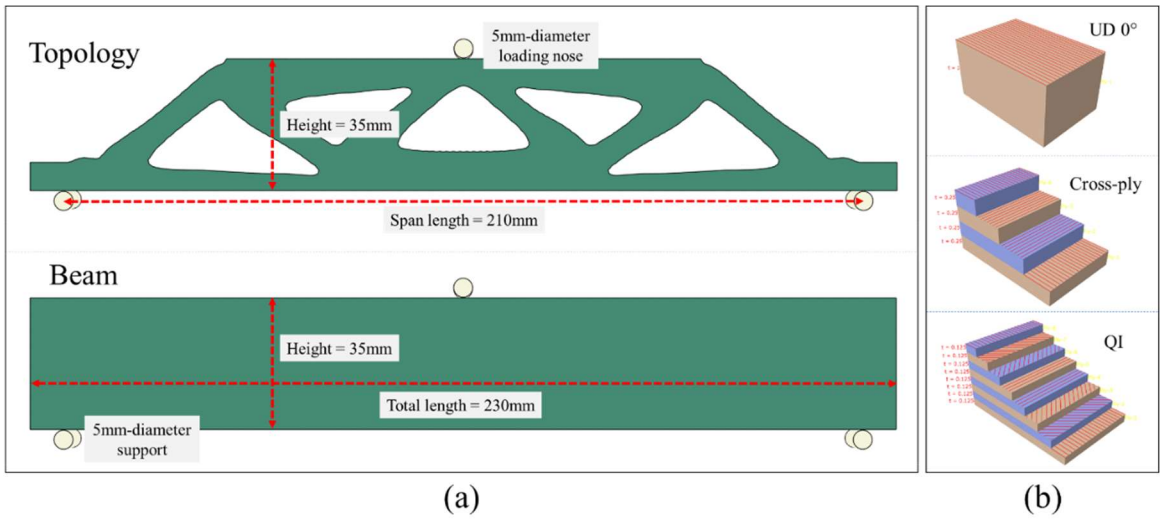

Figure 8-12 (a) Set-up of the FE models (b) Three traditional stacking sequences

As shown in Figure 13, the flexural modulus and gross density of all the cases with continuous fibre reinforcement were presented and compared. The modulus of Markforged sample was the smallest among them, which means the state-of-the-art commercial printing system (with the embedded Eiger slicing software) was barely useful for the lightweight design with topology optimisation and the continuous fibres were not properly used to increase the load bearing capacity. For the beam without any topology optimisation under the three-point bending, the order of the modulus from high to low was: UD > QI > Cross-ply, which was also revealed in the previous research about the bending performance of the CFRP composites [178]. For the traditionally manufactured composites with a topology-optimised geometry, the QI sample exhibited higher modulus than those with other two stacking sequences. This was because part of the +45˚/-45° fibres coincidentally aligned with the 'rods' in the central area of the topology-optimised geometry, therefore, they had a similar effect of the optimised fibre paths along stress trajectories. In contrast, for the samples with stacking sequences UD and Cross-ply, more fibres were cut off and became discontinuous, which significantly lowered down the stiffness of the samples. Compared with the values of traditionally manufactured composites with topology-

optimised geometry, optimised paths improved the flexural modulus by more than 25%. The flexural modulus of CCF/PA-6/Epoxy experimental sample also reached 86.5% of the value of 'Beam' case with the same fibre volume fraction.

Figure 8-14 compared the stiffness-to-weight ratio of the composite structures. The increase of the specific stiffness reasonably followed with the increase of fibre volume fraction, since the carbon fibres have significantly higher stiffness but just slightly higher density than the matrix (such as the epoxy in this study). For the traditional manufacturing, only the specific stiffness of the sample with QI stacking sequence was apparently improved by the topology optimisation, because the rod-similar geometries in the central area were partly enhanced by the +45˚/-45° fibres. In contrast, other traditionally manufactured composites exhibited similar values before and after the topology optimisation. For the sample with optimised fibre paths, the stiffness-to-weight ratio was higher than all the values of the traditionally manufactured composites with the same fibre volume fraction (V_f = 20.6%). Same trend was observed in the samples with the higher fibre fraction (V_f = 50%). However, unlike the FFF 3D printing, samples from traditional manufacturing had to be machined by drilling and/or cutting to achieve a topologically optimised geometry, which would inevitably cause material waste and manufacturing defects. In view of this, the usage of carbon fibre per 1 mm thickness during the manufacturing process was also calculated and presented. It can be seen the sample with optimised fibre placement achieved the comparably high stiffness-to-weight ratio as the traditional composites but using only about 20% continuous carbon fibres.

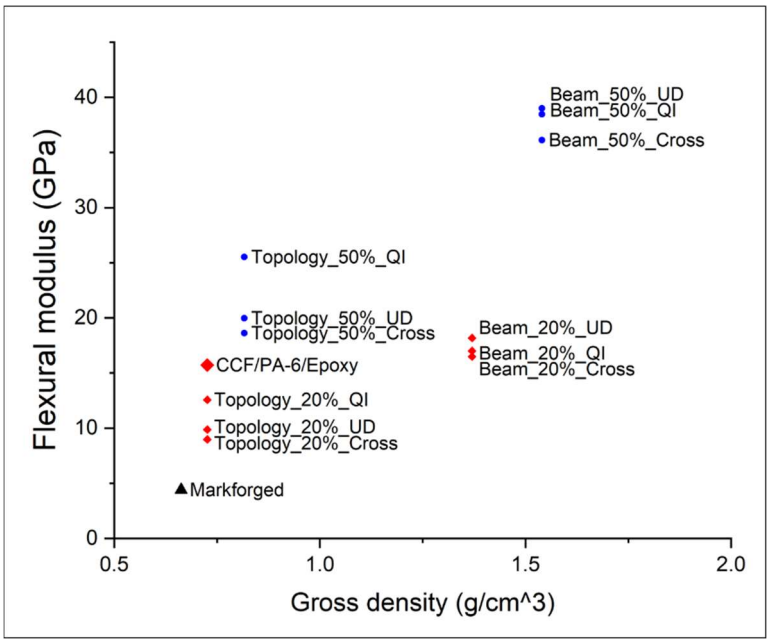

Figure 8-13 The flexural modulus and gross density of the MBB samples with continuous fibres

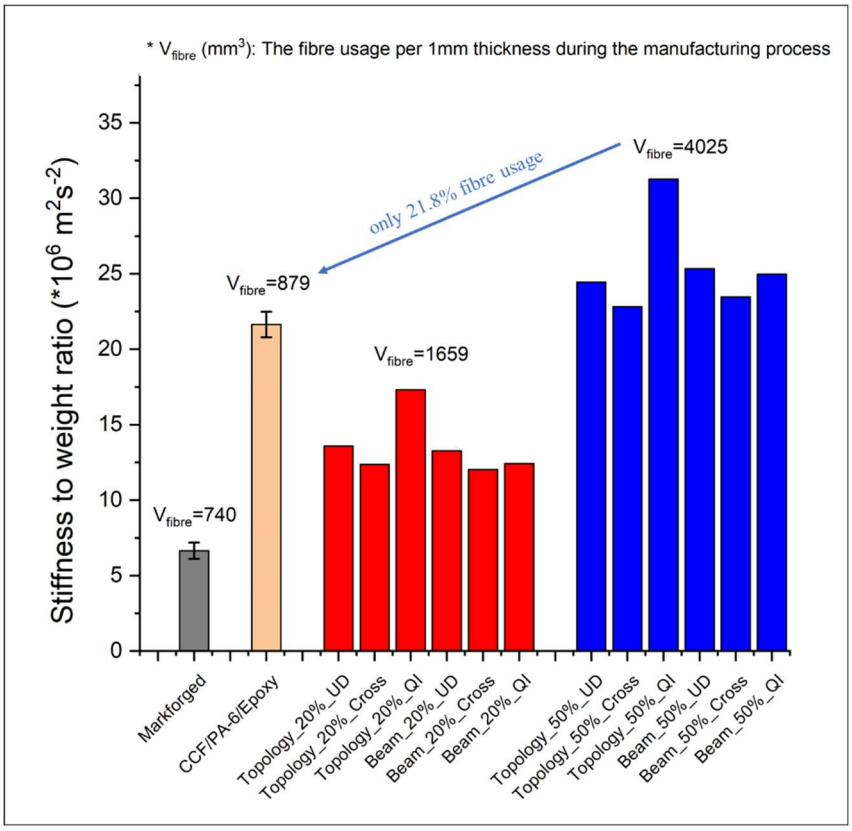

Figure 8-14 The stiffness-to-weight ratios of the MBB samples with continuous fibres

8.6 Conclusions

This chapter presented a sequential optimisation strategy for both topology and fibre orientation, in which continuous carbon fibres were placed along the higher and lower in-plane principal stress trajectories in the topology-optimised MBB structure. Three-point bending tests of MBB beams were carried out to investigate the failure pattern and mechanical properties of 3D-printed topology-optimised MBB structure. FE models were also built to compare the lightweight performance with traditionally manufactured composites. Main conclusions are drawn as below:

(1) CCF/PA-6/Epoxy composites with low-porosity and customised fibre paths were manufactured via the hybrid manufacturing technique combining the FFF 3D printing and post-processing using powder epoxy.

(2) Compared with Markforged printed CCF/PA-6, the strength and stiffness of the hybrid manufactured CCF/PA-6/Epoxy for a MBB structure under three-point bending were increased by 305% and 256%, respectively.

(3) The optimised fibre placement method achieved an even stress/strain distribution in the MBB structure and the post-processing technique prevented the sample from delamination failure.

(4) With the same fibre volume fraction and topology-optimised geometry, the optimised fibre paths led to a flexural modulus 25% higher than all traditionally manufactured composites with common stacking sequences.

(5) The proposed sequential optimisation of both topology and fibre orientation can achieve a comparably high stiffness-to-weight ratio as the traditional composites but using only 20% of continuous carbon fibres.

This study demonstrated the potential of manufacturing ultra-lightweight composite structures

via 3D printing such that the structural topology optimisation and continuous fibre orientation are integrated. Future research is needed to address the overlap issue of fibre paths and to develop the mould-free post-posting technique. More importantly the fibre volume fraction of the 3D-printed composites needs to be substantially increased, *e.g*. to 50%, to maximise the fibre reinforcement performance.

Chapter 9 Conclusions and future work

9.1 Main conclusions

In this thesis, FFF 3D printing of continuous curved carbon fibre reinforced polymer composite is investigated via simulations and experiments. For broader the industrial applications, the mechanical performance of 3D-printed CFRP composites, including the strength, stiffness, failure mode and the lightweight performance, are expected to be improved by optimising the localised anisotropic design.

A design concept, placing continuous curved fibres along the principal stress trajectories, was developed for the 3D-printed composites with geometric singularity. It could be also combined with the topology optimisation to achieve better lightweight performance. The comprehensive study of this curved fibre placement method was conducted both numerically and experimentally. As for the manufacturing of the designed specimens, the mechanism of the printing process was studied to reduce the defects and the post-processing technique was developed to reduce the porosity. Thus, the improvement for mechanical response of the curved fibre placement design could be accurately assessed. Main findings are summarised as follow:

(1) Fibre placement methods for geometric singularity:

- The fibre placement method was developed to customise continuous fibre paths along the principal stress trajectories based on specific loading conditions. Then it was achieved in the printing experiment by a modified desktop printer with the continuous toolpaths, in which the fibre paths were steered around the geometric singularities (open-hole or single-edge notch) to create the samples with complex geometries.
- Compared with the traditional unidirectional fibre placement with drilling or cutting processes, the tensile strength of the samples with fibre paths along higher in-plane

principal stress trajectories were improved 166% in open-hole tensile tests and 81.3% in single-edge notch tensile tests. The improvement of the strength and postpone of the crack initiation were mainly contributed by the avoidance of fibre cut-off and the material enhancement around the geometric singularity.

- The improvement of the mechanical response was also contributed by the stress re-distribution, wherein the stress/strain concentration near to the singularity was decreased and more fibres were included for the load-carrying even they were far away from the geometric singularity. The stiffness was only increased slightly (5-10%) under the uniaxial tension due to the material overlap around the geometric singularity.
- Additional reinforcement methods were adopted on the basis of the above maximum stress lines. For example, the fibres along lower in-plane principal stress trajectories enhanced the structure transverse to the loading direction and reduced the prior-to-failure deformation rate of the geometric singularity from 11% to 1%. An even stress-distribution was obtained in both fibre and matrix regions, thus shear failure in the matrix-rich areas between print paths was prevented from the samples. Another type of the additional fibres, placed around the hole, performed the best to further improve the tensile properties, considering a small increment of fibre usage.

(2) 3D printing process of continuous carbon fibres:

- The single printed stripe of continuous carbon fibre filament was characterised using X-ray μCT scanning and optical microscopy. The void content and slight fibre misalignment were observed even when printing straight, which was caused by the weak interface between fibre and matrix and the uneven pressure from the tip of the nozzle.
- When fibres were printed with a small curvature (angles <30° and curvature radius > 20mm), filaments could be flattened on the bed with nearly constant width and fibre

paths. As the turning angle and curvature increased, the twisting of fibres occurred and then evolved to the folding in the curved section, which was caused by the excessive tensile force from the nozzle and the de-bonding with the print bed. The inaccuracy of the print paths also aggravated as the curvature increased due to the mismatched diameters of nozzle outlet and fibre filament.

- In the printed stripes with angles >120° and curvature radius < 5mm, fibre breakage and the significant change of thickness in the curved section were observed, which meant such turning angles and curvatures should be avoided in the path design of the continuous fibre printing.
- Further parametric studies in the simulation showed that the increase of fibre bundle size would not aggravate the printing defects in the cases with a small turning angle. However, the increase of fibre volume fraction had a huge impact on the defect formation. Some printing defects observed only in the cases with large turning angles, such as shape inaccuracy and fibre folding, would appear in the case with higher fibre volume fraction when printing at a relatively small turning angle and fibre bundle size.

(3) Post-processing technique with powder epoxy:

- A hybrid technique was developed to manufacture curved continuous carbon fibre reinforced composites. Composite preforms were first manufactured by FFF 3D printing of continuous CCF/PA-6 filaments. Powder thermoset epoxy was then added to the preforms to fill up the gaps, remove air voids and enhance the interfacial bonding through a traditional vacuum bagging and oven curing process.
- The melted epoxy mainly infiltrates through the gaps between the print paths and significantly reduced the porosity to 0.06%. During the heating and post-processing cycle, the original PA-6 matrix is further consolidated but it remains relatively solid to maintain the fibre alignment.

- The tensile stiffness and strength (per ASTM D3039) of the carbon fibre reinforced PA-6 composites are improved by 29.3% and 22.1%, respectively, after the post-processing treatment with epoxy powder. Also, the CCF/PA-6/Epoxy composites with low-porosity and customised fibre paths could be achieved via the hybrid manufacturing technique combining the FFF 3D printing and post-processing using powder epoxy.

(4) 3D-printed composites with optimisation of topology and fibre orientation:

- A sequentially coupled optimisation of structural topology and fibre orientation was adopted and the case study of MBB beam under three-point bending was performed. Topology optimisation was first carried out to obtain the geometry of the structure under a specific load, and then the continuous carbon fibres were placed along the identified principal stress trajectories. The samples with customised fibre paths and topology-optimised geometry were made via the hybrid manufacturing technique for the experimental tests.
- The optimised fibre placement method achieved an even stress/strain distribution in the MBB structure and the post-processing technique prevented the sample from delamination failure. Compared with Markforged printed CCF/PA-6, the strength and stiffness of the hybrid manufactured CCF/PA-6/Epoxy for a MBB structure under three-point bending were increased by 305% and 256%, respectively.
- With the same fibre volume fraction and topology-optimised geometry, the optimised fibre paths led to a flexural modulus 25% higher than all traditionally manufactured composites with common stacking sequences. The proposed sequential optimisation also achieved a comparably high stiffness-to-weight ratio as the traditional composites but using only 20% of continuous carbon fibres.

Few studies work on the 3D-printed composite structures with curved continuous fibres as well

as the optimisation for both topology and fibre orientation. Due to the manufacturing for customised curved fibre paths, only several studies have performed their experiments, and there is no standard test method for the 3D-printed composite structures with curved fibres and their lightweight performance. Therefore, a detailed discussion will be presented in the following to compare the work in this study with the state-of-the-art industrial printing system and academic research about the lightweight 3D-printed composite structures.

Compared with the state-of-the-art industrial printing system: For the lightweight structure with the same topology-optimised geometry, the strength and stiffness of the sample in this study are increased by 305% and 256%, compared with the specimens from Markforged®. The stiffness-to-weight ratio, also called specific stiffness, is increased by 3.25 times. The major defects of the Markforged® printing system are the high porosity and the concentric fibre placement. The former results in the beforehand damage such as crack initiation and delamination, while the latter is more like a quasi-isotropic design and do not contribute on the load carrying under their targeted loading conditions. In addition, Marforged® used only one matrix material for the whole printing system, PA-6, to achieve better wetting between fibre/matrix. However, the conflict between the brittleness of carbon fibres and the flexibility of PA-6 indeed decreases the stiffness of its printed part.

Compared with the state-of-the-art research that conducted the manufacturing of specimens and mechanically tested 3D-printed composite structures with the topology-optimised geometry [52]: This research group combined their fibre strengthening placement paths with the topology optimisation, but they did not have their own printing system for the customised fibre paths. Therefore, the compromise has to be made and they used the Markforged printing machine for the experimental specimens. Due to the closure of the slice software, their fibre strengthening placement paths had not been achieved as designed, also the manufactured defects were inevitable, including the high porosity and the delamination. Thus, the mechanical

performance could not be evaluated accurately and they finally compared their sample only with those without continuous fibre reinforcement.

9.2 Recommendations for future work

The work carried out in this thesis demonstrated that 3D printing has the potential to produce lightweight and high-performance composites, by integrating customised fibre placement, voids-removing techniques and topology optimisation. However, the full potential and advantages are still yet fully explored and more work needs to be done in the future. Main bullet points are drawn as below:

(1) Fabrication of continuous fibre filament with higher fibre fraction and better fibre/matrix wetting

Besides the void content, another challenging issue for 3D printing of cCFRP composites is the low fibre fraction (normally about 20-30%), as compared with the traditionally-manufactured composites (about 50-60%). Considering the improvement of mechanical performance brought from the optimised fibre paths, the continuous fibre filaments with higher fibre fraction will further enable more widely-used of 3D-printed composites as structural parts. One of the main difficulties of the fabrication of CF filament with high fibre fraction is the inadequate wetting between fibre and matrix. When the fibre fraction increases, the fibre tow could not be surrounded by the matrix material, causing the filament splitting and weak adhesion between layers as well as adjacent paths during the printing. Some researchers adopted low-viscosity matrix (for example thermosetting material) and the pre-treatment of fibres for the better wetting between fibre and matrix. In addition, the printing filament can be made as a thin fibre tape, thus more pressure and heating can be provided during the printing process for better adhesion.

(2) Design of printing nozzle for better path accuracy and less manufactured-defects

As mentioned in the chapter 5, although the reasons for path inaccuracy and manufactured-defects are identified, a new modified printing nozzle should be developed to achieve better path accuracy and less manufacturing defects, in particular when printing shape corners and large curvatures. For example, the nozzle should be designed with a rectangle outlet, so a consistent and even pressure can be applied on the heated filament, reducing the defects while printing straight. Also, the dimension of the outlet is consistent with the required printed width and the rotation of the print-head should be available while printing with curvatures and turning angles. Therefore, the CF filament would not swing inside the nozzle and the inaccuracy of the printed paths as well as others defects, such as twisting and wrinkling, would be reduced.

(3) Dual-nozzle printing for the better infill of the gaps between fibre paths

The post-processing technique with powder epoxy works well for eliminating the micro voids/cracks, but the gaps between fibre paths could not be infilled perfectly due to the low viscosity of the melted epoxy. Therefore, a dual-nozzle printing system needs to be developed to enable the deposition of thermoplastic in the relatively large gaps between fibre paths. Unlike the printing of pure thermoplastic material, the mechanical performance of 3D-printed cCFRP composites depends more on the placement of continuous fibre, also there is a minimum length of the deposited CF filament in each time due to the use of feeding and cutting devices. Thus, a path generation method of continuous fibre for complex geometries should be developed to satisfy the mechanical requirement and achieve composite structures with high value of the inclusion of continuous fibre. In addition, another extruder head should be available for the printing of pure thermoplastic material, in order to fill the gaps which are too small to be printed with continuous fibre filaments, such as the tapered or striped gaps with a width smaller than 1 mm or a length smaller than 10 mm.

(4) Mould-free post-processing treatment

Although the post-processing technique used in this thesis can effectively produce the low-porosity composites with customised fibre paths, moulds still have to be used for the highly complex geometries, for example the structures after topology optimisation. The thermosetting powder used in Chapter 6 enabled the infill of the micro-voids because of its low melted viscosity, but such low-viscosity melted epoxy could not be trapped in those large gaps between the print paths. Thus, a mould was needed for a full infusion and better surface finish when the post-processing was adopted for the composite structures with such complex geometry. Therefore, the mould-free post-processing technique should be developed to preserve the low cost and rapid prototyping advantages of additive manufacturing. The ideal way is the printing of the dual-polymer composites, in which the thermoplastic material with higher melting temperature can be used for the infill of larger gap and the maintaining of geometry as well as paths accuracy, while the thermosetting material will be melted to fill the micro-voids in the 3D-printed composites during the post-processing, so a mould-free post-processing treatment can be developed to reduce the porosity of the 3D-printed composites.

(5) Modelling of multi-layers 3D-printed composites with curved fibre reinforcement

As presented in chapter 7, the combination of different fibre placements in multi-layers has the potential to customise the mechanical properties and even the failure mode of the printed composites, but it can only be investigated via the trial-and-error tests at the current stage. Most of the researches, which worked on the 3D-printed composites with continuous reinforcement, performed only the standard tests for the 3D-printed composite materials with unidirectional fibre placement. Experimental tests and numerical simulations for the 3D-printed composite structures remain low, especially for those with curved fibre placement and inconsistent localised fibre fraction. In addition, most of the modelling approaches are limited to the elastic performance of the 3D-printed composites. The failure criteria of the traditional FRP composites cannot be used for the 3D-printed composites anymore. Besides the inconsistent

localised fibre fraction and orientation, the different porosity and interfacial properties also make the 3D-printed composites irrational to be assumed as a homogenous domain. Thus, the modelling theory and method of 3D-printed composites with curved fibres are worth being developed, and more precise analysis and predictions of damage propagation should be achieved in the future.

Publications from the thesis

Zhang H, Yang D, Sheng Y. Performance-driven 3D printing of continuous curved carbon fibre reinforced polymer composites: A preliminary numerical study. **Composites Part B: Engineering**. 2018;151:256-64.

Zhang H, Dickson AN, Sheng Y, McGrail T, Dowling DP, Wang C, Neville A, Yang D. Failure analysis of 3D printed woven composite plates with holes under tensile and shear loading. **Composites Part B: Engineering**. 2020;186:107835.

Zhang H, Chen J, Yang D. Fibre misalignment and breakage in 3D printing of continuous carbon fibre reinforced thermoplastic composites. **Additive Manufacturing**. 2021;38:101775.

Zhang H, Wu J, Robert C, Ó Brádaigh CM, Yang D. Hybrid manufacturing of curved continuous carbon fibre reinforced dual-polymer composites. (Submitted to **Composites Part B: Engineering**)

Zhang H, Li A, Wu J, Sun B, Wang C, Yang D. Effectiveness of fibre placement in 3D-printed open-hole composites under uniaxial tension. (Submitted to **Composites Science and Technology**)

Zhang H, Wang S, Zhang K, Wu J, Li A, Liu J, Yang D. Fibre orientation and topology optimisation for 3D printing of continuous carbon fibre reinforced polymer composites. (Submitted to **Composites Science and Technology**)

Additional publications during the period of doctoral studies

Yang D, **Zhang H**, Wu J, McCarthy ED. Fibre flow and void formation in 3D printing of short fibre reinforced thermoplastic composites: An experimental benchmark exercise. **Additive Manufacturing**. 2021;37:101686.

Zhang H, Zhang L, **Zhang H**, Wu J, An X, Yang D. Fibre Bridging and Nozzle Clogging in 3D Printing of Discontinuous Carbon Fibre Reinforced Polymer Composites: Coupled CFD-DEM Modelling. (Submitted to **The International Journal of Advanced Manufacturing Technology**)

Reference

[1] Wang X, Jiang M, Zhou Z, Gou J, Hui D. 3D printing of polymer matrix composites: A review and prospective. Composites Part B: Engineering. 2017;110:442-58.
[2] Kabir SMF, Mathur K, Seyam A-FM. A critical review on 3D printed continuous fiber-reinforced composites: History, mechanism, materials and properties. Composite Structures. 2020;232.
[3] N. Turner B, Strong R, A. Gold S. A review of melt extrusion additive manufacturing processes: I. Process design and modeling. Rapid Prototyping Journal. 2014;20(3):192-204.
[4] Zhuo P, Li S, Ashcroft IA, Jones AI. Material extrusion additive manufacturing of continuous fibre reinforced polymer matrix composites: A review and outlook. Composites Part B: Engineering. 2021.
[5] Ning F, Cong W, Hu Z, Huang K. Additive manufacturing of thermoplastic matrix composites using fused deposition modeling: A comparison of two reinforcements. Journal of Composite Materials. 2017:002199831769265.
[6] Blok LG, Longana ML, Yu H, Woods BKS. An investigation into 3D printing of fibre reinforced thermoplastic composites. Additive Manufacturing. 2018;22:176-86.
[7] Chabaud G, Castro M, Denoual C, Le Duigou A. Hygromechanical properties of 3D printed continuous carbon and glass fibre reinforced polyamide composite for outdoor structural applications. Additive Manufacturing. 2019;26:94-105.
[8] Papon EA, Haque A, Mulani SB. Process optimization and stochastic modeling of void contents and mechanical properties in additively manufactured composites. Composites Part B: Engineering. 2019;177.
[9] Kumar N, Jain PK, Tandon P, Pandey PM. The effect of process parameters on tensile behavior of 3D printed flexible parts of ethylene vinyl acetate (EVA). Journal of Manufacturing Processes. 2018;35:317-26.
[10] Schirmeister CG, Hees T, Licht EH, Mülhaupt R. 3D printing of high density polyethylene by fused filament fabrication. Additive Manufacturing. 2019;28:152-9.
[11] Wang JY, Xu DD, Sun W, Du SM, Guo JJ, Xu GJ. Effects of nozzle-bed distance on the surface quality and mechanical properties of fused filament fabrication parts. IOP Conference Series: Materials Science and Engineering. 2019;479.
[12] Heller BP, Smith DE, Jack DA. Effects of extrudate swell and nozzle geometry on fiber orientation in Fused Filament Fabrication nozzle flow. Additive Manufacturing. 2016;12:252-64.
[13] Papon MEA, Haque A, Sharif MAR. Effect of Nozzle Geometry on Melt Flow Simulation and Structural Property of Thermoplastic Nanocomposites in Fused Deposition Modeling. In: Proceedings of American Society for Composites 2017. Conference, Conference 2017.
[14] Rodriguez JF, Thomas JP, Renaud JE. Characterization of the mesostructure of fused-deposition acrylonitrile-butadiene-styrene materials. Rapid Prototyping Journal. 2000;6(3):175-86.
[15] Li N, Link G, Jelonnek J. 3D microwave printing temperature control of continuous carbon fiber reinforced composites. Composites Science and Technology. 2020;187.
[16] Li N, Link G, Jelonnek J, Morais MVC, Henning F. Microwave additive manufacturing of continuous carbon fibers reinforced thermoplastic composites: Characterization, analysis, and properties. Additive Manufacturing. 2021;44.
[17] Dickson AN, Barry JN, McDonnell KA, Dowling DP. Fabrication of continuous carbon, glass and Kevlar fibre reinforced polymer composites using additive manufacturing. Additive Manufacturing. 2017;16:146-52.
[18] Pascual-González C, Iragi M, Fernández A, Fernández-Blázquez JP, Aretxabaleta L, Lopes CS. An approach to analyse the factors behind the micromechanical response of 3D-printed

composites. Composites Part B: Engineering. 2020;186.
[19] Goh GD, Dikshit V, Nagalingam AP, Goh GL, Agarwala S, Sing SL, et al. Characterization of mechanical properties and fracture mode of additively manufactured carbon fiber and glass fiber reinforced thermoplastics. Materials & Design. 2018;137:79-89.
[20] Justo J, Távara L, García-Guzmán L, París F. Characterization of 3D printed long fibre reinforced composites. Composite Structures. 2017.
[21] Dickson AN, Dowling DP. Enhancing the bearing strength of woven carbon fibre thermoplastic composites through additive manufacturing. Composite Structures. 2019;212:381-8.
[22] Imeri A, Fidan I, Allen M, Wilson D, Canfield SJTIJoAMT. Fatigue analysis of the fiber reinforced additively manufactured objects. 2018;98(9):2717-24.
[23] Araya-Calvo M, López-Gómez I, Chamberlain-Simon N, León-Salazar JL, Guillén-Girón T, Corrales-Cordero JS, et al. Evaluation of compressive and flexural properties of continuous fiber fabrication additive manufacturing technology. 2018;22:157-64.
[24] Pyl L, Kalteremidou K-A, Van Hemelrijck D. Exploration of specimen geometry and tab configuration for tensile testing exploiting the potential of 3D printing freeform shape continuous carbon fibre-reinforced nylon matrix composites. Polymer Testing. 2018;71:318-28.
[25] Zhang H, Chen J, Yang D. Fibre misalignment and breakage in 3D printing of continuous carbon fibre reinforced thermoplastic composites. Additive Manufacturing. 2021;38.
[26] Matsuzaki R, Ueda M, Namiki M, Jeong TK, Asahara H, Horiguchi K, et al. Three-dimensional printing of continuous-fiber composites by in-nozzle impregnation. Sci Rep. 2016;6:23058.
[27] Nakagawa Y, Mori K-i, Maeno T. 3D printing of carbon fibre-reinforced plastic parts. The International Journal of Advanced Manufacturing Technology. 2017;91(5-8):2811-7.
[28] Tian X, Liu T, Yang C, Wang Q, Li D. Interface and performance of 3D printed continuous carbon fiber reinforced PLA composites. Composites Part A: Applied Science and Manufacturing. 2016;88:198-205.
[29] Li N, Li Y, Liu S. Rapid prototyping of continuous carbon fiber reinforced polylactic acid composites by 3D printing. Journal of Materials Processing Technology. 2016;238:218-25.
[30] Baumann F, Scholz J, Fleischer J. Investigation of a New Approach for Additively Manufactured Continuous Fiber-reinforced Polymers. Procedia CIRP. 2017;66:323-8.
[31] Saari M, Cox B, Richer E, Krueger PS, Cohen AL. Fiber Encapsulation Additive Manufacturing: An Enabling Technology for 3D Printing of Electromechanical Devices and Robotic Components. 3D Printing and Additive Manufacturing. 2015;2(1):32-9.
[32] Pappas JM, Thakur AR, Leu MC, Dong X. A parametric study and characterization of additively manufactured continuous carbon fiber reinforced composites for high-speed 3D printing. The International Journal of Advanced Manufacturing Technology. 2021;113(7-8):2137-51.
[33] Shiratori H, Todoroki A, Ueda M, Matsuzaki R, Hirano Y. Mechanism of folding a fiber bundle in the curved section of 3D printed carbon fiber reinforced plastics. Advanced Composite Materials. 2019:1-11.
[34] Borowski A, Vogel C, Behnisch T, Geske V, Gude M, Modler N. Additive Manufacturing-Based In Situ Consolidation of Continuous Carbon Fibre-Reinforced Polycarbonate. Materials (Basel). 2021;14(9).
[35] Matsuzaki R, Nakamura T, Sugiyama K, Ueda M, Todoroki A, Hirano Y, et al. Effects of Set Curvature and Fiber Bundle Size on the Printed Radius of Curvature by a Continuous Carbon Fiber Composite 3D Printer. Additive Manufacturing. 2018;24:93-102.
[36] Ishii K, Todoroki A, Mizutani Y, Suzuki Y, Koga Y, Matsuzaki R, et al. Bending fracture rule for 3D-printed curved continuous-fiber composite. Advanced Composite Materials.

2018;28(4):383-95.
[37] Liu B, T. Haftka R, A. Akgün M, Todoroki A. Permutation genetic algorithm for stacking sequence design of composite laminates. Computer Methods in Applied Mechanics and Engineering. 2000;186(2):357-72.
[38] Todoroki A, Haftka RT. Stacking sequence optimization by a genetic algorithm with a new recessive gene like repair strategy. Composites Part B: Engineering. 1998;29(3):277-85.
[39] Setoodeh S, Abdalla MM, Gürdal Z. Design of variable–stiffness laminates using lamination parameters. Composites Part B: Engineering. 2006;37(4-5):301-9.
[40] Passos AG, Luersen MA, Steeves CA. Optimal curved fibre orientations of a composite panel with cutout for improved buckling load using the Efficient Global Optimization algorithm. Engineering Optimization. 2016;49(8):1354-72.
[41] Khan S, Fayazbakhsh K, Fawaz Z, Arian Nik M. Curvilinear variable stiffness 3D printing technology for improved open-hole tensile strength. Additive Manufacturing. 2018;24:378-85.
[42] Yamanaka Y, Todoroki A, Ueda M, Hirano Y, Matsuzaki R. Fiber Line Optimization in Single Ply for 3D Printed Composites. Open Journal of Composite Materials. 2016;06(04):121-31.
[43] Zhang H, Yang D, Sheng Y. Performance-driven 3D printing of continuous curved carbon fibre reinforced polymer composites: A preliminary numerical study. Composites Part B: Engineering. 2018;151:256-64.
[44] Sugiyama K, Matsuzaki R, Malakhov AV, Polilov AN, Ueda M, Todoroki A, et al. 3D printing of optimized composites with variable fiber volume fraction and stiffness using continuous fiber. Composites Science and Technology. 2020;186.
[45] Hou Z, Tian X, Zhang J, Zheng Z, Zhe L, Li D, et al. Optimization design and 3D printing of curvilinear fiber reinforced variable stiffness composites. Composites Science and Technology. 2021;201.
[46] Malakhov AV, Polilov AN. Design of composite structures reinforced curvilinear fibres using FEM. Composites Part A: Applied Science and Manufacturing. 2016;87:23-8.
[47] Fernandes RR, van de Werken N, Koirala P, Yap T, Tamijani AY, Tehrani M. Experimental investigation of additively manufactured continuous fiber reinforced composite parts with optimized topology and fiber paths. Additive Manufacturing. 2021;44.
[48] Jiang D, Hoglund R, Smith D. Continuous Fiber Angle Topology Optimization for Polymer Composite Deposition Additive Manufacturing Applications. Fibers. 2019;7(2).
[49] Stegmann J, Lund E. Discrete material optimization of general composite shell structures. International Journal for Numerical Methods in Engineering. 2005;62(14):2009-27.
[50] Li N, Link G, Wang T, Ramopoulos V, Neumaier D, Hofele J, et al. Path-designed 3D printing for topological optimized continuous carbon fibre reinforced composite structures. Composites Part B: Engineering. 2020;182.
[51] Nomura T, Kawamoto A, Kondoh T, Dede EM, Lee J, Song Y, et al. Inverse design of structure and fiber orientation by means of topology optimization with tensor field variables. Composites Part B: Engineering. 2019;176.
[52] Chen Y, Ye L. Topological design for 3D-printing of carbon fibre reinforced composite structural parts. Composites Science and Technology. 2021;204.
[53] Ueda M, Kishimoto S, Yamawaki M, Matsuzaki R, Todoroki A, Hirano Y, et al. 3D compaction printing of a continuous carbon fiber reinforced thermoplastic. Composites Part A: Applied Science and Manufacturing. 2020;137.
[54] Zhang J, Zhou Z, Zhang F, Tan Y, Tu Y, Yang B. Performance of 3D-Printed Continuous-Carbon-Fiber-Reinforced Plastics with Pressure. Materials (Basel). 2020;13(2).
[55] Qiao J, Li Y, Li L. Ultrasound-assisted 3D printing of continuous fiber-reinforced thermoplastic (FRTP) composites. Additive Manufacturing. 2019;30.
[56] Liu T, Tian X, Zhang Y, Cao Y, Li D. High-pressure interfacial impregnation by micro-

screw in-situ extrusion for 3D printed continuous carbon fiber reinforced nylon composites. Composites Part A: Applied Science and Manufacturing. 2020;130.
[57] O'Connor HJ, Dowling DP. Low-pressure additive manufacturing of continuous fiber-reinforced polymer composites. Polymer Composites. 2019;40(11):4329-39.
[58] Mei H, Ali Z, Yan Y, Ali I, Cheng L. Influence of mixed isotropic fiber angles and hot press on the mechanical properties of 3D printed composites. Additive Manufacturing. 2019;27:150-8.
[59] Yamawaki M, Kouno Y. Fabrication and mechanical characterization of continuous carbon fiber-reinforced thermoplastic using a preform by three-dimensional printing and via hot-press molding. Advanced Composite Materials. 2017:1-11.
[60] Pascual-González C, San Martín P, Lizarralde I, Fernández A, León A, Lopes CS, et al. Post-processing effects on microstructure, interlaminar and thermal properties of 3D printed continuous carbon fibre composites. Composites Part B: Engineering. 2021;210.
[61] Hou Z, Tian X, Zheng Z, Zhang J, Zhe L, Li D, et al. A constitutive model for 3D printed continuous fiber reinforced composite structures with variable fiber content. Composites Part B: Engineering. 2020;189.
[62] Ichihara N, Ueda M, Urushiyama Y, Todoroki A, Matsuzaki R, Hirano H. Progressive damage simulation for a 3D-printed curvilinear continuous carbon fiber-reinforced thermoplastic based on continuum damage mechanics. Advanced Composite Materials. 2020;29(5):459-74.
[63] van de Werken N, Hurley J, Khanbolouki P, Sarvestani AN, Tamijani AY, Tehrani M. Design considerations and modeling of fiber reinforced 3D printed parts. Composites Part B: Engineering. 2019;160:684-92.
[64] Malakhov AV, Polilov AN, Zhang J, Hou Z, Tian X. A Modeling Method of Continuous Fiber Paths for Additive Manufacturing (3D Printing) of Variable Stiffness Composite Structures. Applied Composite Materials. 2020;27(3):185-208.
[65] Sanei SHR, Arndt A, Doles R. Open hole tensile testing of 3D printed continuous carbon fiber reinforced composites. Journal of Composite Materials. 2020;54(20):2687-95.
[66] Pyl L, Kalteremidou K-A, Van Hemelrijck D. Exploration of the design freedom of 3D printed continuous fibre-reinforced polymers in open-hole tensile strength tests. Composites Science and Technology. 2019;171:135-51.
[67] Mack J, McGregor O, Mitschang P. Prepreg Lay-up Technology for Manufacturing of Lattice Structure Fuselage Sections. InProceeding of the 16th European Conference on Composite Materials2014. p. 22-6.
[68] Hoa SV. Factors affecting the properties of composites made by 4D printing (moldless composites manufacturing). Advanced Manufacturing: Polymer & Composites Science. 2017;3(3):101-9.
[69] Dudek P. FDM 3D Printing Technology in Manufacturing Composite Elements. Archives of Metallurgy and Materials. 2013;58(4).
[70] Hao W, Liu Y, Zhou H, Chen H, Fang D. Preparation and characterization of 3D printed continuous carbon fiber reinforced thermosetting composites. Polymer Testing. 2018;65:29-34.
[71] Vaneker THJ. Material Extrusion of Continuous Fiber Reinforced Plastics Using Commingled Yarn. Procedia CIRP. 2017;66:317-22.
[72] Der Klift FV, Koga Y, Todoroki A, Ueda M, Hirano Y, Matsuzaki R. 3D Printing of Continuous Carbon Fibre Reinforced Thermo-Plastic (CFRTP) Tensile Test Specimens. Open Journal of Composite Materials. 2016;06(01):18-27.
[73] Mori K-i, Maeno T, Nakagawa Y. Dieless Forming of Carbon Fibre Reinforced Plastic Parts Using 3D Printer. Procedia Engineering. 2014;81:1595-600.
[74] Türk D-A, Kussmaul R, Zogg M, Klahn C, Leutenecker-Twelsiek B, Meboldt M. Composites Part Production with Additive Manufacturing Technologies. Procedia CIRP.

2017;66:306-11.
[75] Daniel IM, Rowlands RE, Whiteside JB. Effects of material and stacking sequence on behavior of composite plates with holes. Experimental Mechanics. 1974;14(1):1-9.
[76] Lucking WM, Hoa SV, Sankar TS. The Effect of Geometry on Interlaminar Stresses of [0/90]s Composite Laminates with Circular Holes. Journal of Composite Materials. 1984;18(2):188-98.
[77] Pagano NJ, Pipes RB. The Influence of Stacking Sequence on Laminate Strength. Journal of Composite Materials. 1971;5(1):50-7.
[78] Srinivasa Rao B, Rudramoorthy R, Srinivas S, Nageswara Rao B. Effect of drilling induced damage on notched tensile and pin bearing strengths of woven GFR-epoxy composites. Materials Science and Engineering: A. 2008;472(1-2):347-52.
[79] Kim S-Y, Koo J-M, Kim D, Seok C-S. Prediction of the static fracture strength of hole notched plain weave CFRP composites. Composites Science and Technology. 2011;71(14):1671-6.
[80] Green BG, Wisnom MR, Hallett SR. An experimental investigation into the tensile strength scaling of notched composites. Composites Part A: Applied Science and Manufacturing. 2007;38(3):867-78.
[81] Shyha IS, Aspinwall DK, Soo SL, Bradley S. Drill geometry and operating effects when cutting small diameter holes in CFRP. International Journal of Machine Tools and Manufacture. 2009;49(12-13):1008-14.
[82] Huang J, Haftka RT. Optimization of fiber orientations near a hole for increased load-carrying capacity of composite laminates. Structural and Multidisciplinary Optimization. 2005;30(5):335-41.
[83] Breault S. Improving load distributions in cellular materials using stress trajectory topologies: University of Rhode Island; 2012.
[84] Mendoza Jasso AJ, Goodsell JE, Ritchey AJ, Byron Pipes R, Koslowski M. A parametric study of fiber volume fraction distribution on the failure initiation location in open hole off-axis tensile specimen. Composites Science and Technology. 2011;71(16):1819-25.
[85] Zhan X, Meng Y, Zhou J, Qi C, Zhang C, Gu D. Quantitative research on microstructure and thermal physical mechanism in laser melting deposition for Invar alloy. Journal of Manufacturing Processes. 2018;31:221-31.
[86] Li J, Su M, Wang X, Liu Q, Liu K. Laser deposition-additive manufacturing of ceramics/nanocrystalline intermetallics reinforced microlaminates. Optics & Laser Technology. 2019;117:158-64.
[87] Parandoush P, Lin D. A review on additive manufacturing of polymer-fiber composites. Composite Structures. 2017;182:36-53.
[88] Jenett B, Calisch S, Cellucci D, Cramer N, Gershenfeld N, Swei S, et al. Digital Morphing Wing: Active Wing Shaping Concept Using Composite Lattice-Based Cellular Structures. Soft Robot. 2017;4(1):33-48.
[89] Esposito Corcione C, Gervaso F, Scalera F, Montagna F, Sannino A, Maffezzoli A. The feasibility of printing polylactic acid-nanohydroxyapatite composites using a low-cost fused deposition modeling 3D printer. Journal of Applied Polymer Science. 2017;134(13).
[90] Khashaba UA, Sebaey TA, Selmy AI. Experimental verification of a progressive damage model for composite pinned-joints with different clearances. International Journal of Mechanical Sciences. 2019;152:481-91.
[91] Caminero M, Chacón J, García-Moreno I, Reverte J. Interlaminar bonding performance of 3D printed continuous fibre reinforced thermoplastic composites using fused deposition modelling. Polymer Testing. 2018;68:415-23.
[92] Caminero M, Chacón J, García-Moreno I, Rodríguez G. Impact damage resistance of 3D printed continuous fibre reinforced thermoplastic composites using fused deposition modelling.

Composites Part B: Engineering. 2018;148:93-103.
[93] Al Abadi H, Thai H-T, Paton-Cole V, Patel VI. Elastic properties of 3D printed fibre-reinforced structures. Composite Structures. 2018;193:8-18.
[94] Koricho EG, Khomenko A, Fristedt T, Haq M. Innovative tailored fiber placement technique for enhanced damage resistance in notched composite laminate. Composite Structures. 2015;120:378-85.
[95] Uhlig K, Tosch M, Bittrich L, Leipprand A, Dey S, Spickenheuer A, et al. Meso-scaled finite element analysis of fiber reinforced plastics made by Tailored Fiber Placement. Composite Structures. 2016;143:53-62.
[96] Crothers P, Drechsler K, Feltin D, Herszberg I, Kruckenberg T. Tailored fibre placement to minimise stress concentrations. Composites Part A: Applied Science and Manufacturing. 1997;28(7):619-25.
[97] Dickson AN, Ross K-A, Dowling DP. Additive manufacturing of woven carbon fibre polymer composites. Composite Structures. 2018;206:637-43.
[98] Mei Z, Chung D. Thermal history of carbon-fiber polymer-matrix composite, evaluated by electrical resistance measurement. Thermochimica acta. 2001;369(1-2):87-93.
[99] Hashin Z, Rotem A. A Fatigue Failure Criterion for Fiber Reinforced Materials. Journal of Composite Materials. 1973;7(4):448-64.
[100] Hashin ZJJoam. Failure criteria for unidirectional fiber composites. 1980;47(2):329-34.
[101] Nunes F, Silvestre N, Correia JR. Structural behaviour of hybrid FRP pultruded columns. Part 2: Numerical study. Composite Structures. 2016;139:304-19.
[102] Duarte A, Sáez AD, Silvestre N. Comparative study between XFEM and Hashin damage criterion applied to failure of composites. Thin-Walled Structures. 2017;115:277-88.
[103] R. Koloor SS, Khosravani MR, Hamzah RIR, Tamin MN. FE model-based construction and progressive damage processes of FRP composite laminates with different manufacturing processes. International Journal of Mechanical Sciences. 2018;141:223-35.
[104] Markforged I. Markforged materials datasheet. 2016.
[105] Jin N, Wang F, Wang Y, Zhang B, Cheng H, Zhang H. Failure and energy absorption characteristics of four lattice structures under dynamic loading. Materials & Design. 2019;169.
[106] Pinho ST, Robinson P, Iannucci L. Fracture toughness of the tensile and compressive fibre failure modes in laminated composites. Composites science and technology. 2006;66(13):2069-79.
[107] Xu J, Li C, Mi S, An Q, Chen M. Study of drilling-induced defects for CFRP composites using new criteria. Composite Structures. 2018;201:1076-87.
[108] Hashin Z. Failure criteria for unidirectional fiber composites. 1980.
[109] Li S, Sitnikova E. A critical review on the rationality of popular failure criteria for composites. Composites Communications. 2018;8:7-13.
[110] Li S, Wang M, Jeanmeure L, Sitnikova E, Yu F, Pan Q, et al. Damage related material constants in continuum damage mechanics for unidirectional composites with matrix cracks. International Journal of Damage Mechanics. 2018;28(5):690-707.
[111] Bakhshi N, Hojjati M. An experimental and simulative study on the defects appeared during tow steering in automated fiber placement. Composites Part A: Applied Science and Manufacturing. 2018;113:122-31.
[112] Eneyew ED, Ramulu M. Experimental study of surface quality and damage when drilling unidirectional CFRP composites. Journal of Materials Research Technology. 2014;3(4):354-62.
[113] KozaczuK K. Automated fiber placement systems overview. Prace Instytutu Lotnictwa. 2016.
[114] Kim BC, Weaver PM, Potter K. Manufacturing characteristics of the continuous tow shearing method for manufacturing of variable angle tow composites. Composites Part A: Applied Science and Manufacturing. 2014;61:141-51.

[115] Frketic J, Dickens T, Ramakrishnan S. Automated manufacturing and processing of fiber-reinforced polymer (FRP) composites: An additive review of contemporary and modern techniques for advanced materials manufacturing. Additive Manufacturing. 2017;14:69-86.
[116] Zhang H, Dickson AN, Sheng Y, McGrail T, Dowling DP, Wang C, et al. Failure analysis of 3D printed woven composite plates with holes under tensile and shear loading. Composites Part B: Engineering. 2020;186.
[117] Todoroki A, Oasada T, Mizutani Y, Suzuki Y, Ueda M, Matsuzaki R, et al. Tensile property evaluations of 3D printed continuous carbon fiber reinforced thermoplastic composites. Advanced Composite Materials. 2020;29(2):147-62.
[118] Mei H, Ali Z, Ali I, Cheng L. Tailoring strength and modulus by 3D printing different continuous fibers and filled structures into composites. Advanced Composites and Hybrid Materials. 2019;2(2):312-9.
[119] Shang J, Tian X, Luo M, Zhu W, Li D, Qin Y, et al. Controllable inter-line bonding performance and fracture patterns of continuous fiber reinforced composites by sinusoidal-path 3D printing. Composites Science and Technology. 2020;192.
[120] Pei E, Lanzotti A, Grasso M, Staiano G, Martorelli M. The impact of process parameters on mechanical properties of parts fabricated in PLA with an open-source 3-D printer. Rapid Prototyping Journal. 2015.
[121] Yang D, Zhang H, Wu J, McCarthy ED. Fibre flow and void formation in 3D printing of short-fibre reinforced thermoplastic composites: An experimental benchmark exercise. Additive Manufacturing. 2020.
[122] Khan S, Lee D-H. An adaptive dynamically weighted median filter for impulse noise removal. EURASIP Journal on Advances in Signal Processing. 2017;2017(1).
[123] Dijkstra DJ. Guidelines for rheological characterization of polyamide melts (IUPAC Technical Report). Pure and Applied Chemistry. 2009;81(2):339-49.
[124] Beakou A, Cano M, Le Cam J-B, Verney V. Modelling slit tape buckling during automated prepreg manufacturing: A local approach. Composite structures. 2011;93(10):2628-35.
[125] Wohl C, Palmieri FL, Forghani A, Hickmott C, Bedayat H, Coxon B, et al. Tack measurements of prepreg tape at variable temperature and humidity. In: Proceedings of Composites and Advanced Materials Expo (CAMX 2017). Conference, Conference 2017.
[126] Iragi M, Pascual-González C, Esnaola A, Lopes CS, Aretxabaleta L. Ply and interlaminar behaviours of 3D printed continuous carbon fibre-reinforced thermoplastic laminates; effects of processing conditions and microstructure. Additive Manufacturing. 2019;30.
[127] El-Dessouky HM, Lawrence CA. Ultra-lightweight carbon fibre/thermoplastic composite material using spread tow technology. Composites Part B: Engineering. 2013;50:91-7.
[128] Ma Y, Ueda M, Yokozeki T, Sugahara T, Yang Y, Hamada H. A comparative study of the mechanical properties and failure behavior of carbon fiber/epoxy and carbon fiber/polyamide 6 unidirectional composites. Composite Structures. 2017;160:89-99.
[129] Leopold C, Schutt M, Liebig WV, Philipkowski T, Kurten J, Schulte K, et al. Compression Fracture of CFRP Laminates Containing Stress Intensifications. Materials (Basel). 2017;10(9).
[130] Poulios K, Niordson CF. Micro-buckling of periodically layered composites in regions of stress concentration. Composite Structures. 2016;157:424-35.
[131] Brenken B, Barocio E, Favaloro A, Kunc V, Pipes RB. Fused filament fabrication of fiber-reinforced polymers: A review. Additive Manufacturing. 2018;21:1-16.
[132] Robert C, Pecur T, Maguire JM, Lafferty AD, McCarthy ED, Ó Brádaigh CM. A novel powder-epoxy towpregging line for wind and tidal turbine blades. Composites Part B: Engineering. 2020;203.

[133] Maguire JM, Nayak K, Brádaigh CMÓ. Characterisation of epoxy powders for processing thick-section composite structures. Materials & Design. 2018;139:112-21.
[134] Mamalis D, Flanagan T, Brádaigh CMÓ. Effect of fibre straightness and sizing in carbon fibre reinforced powder epoxy composites. Composites Part A: Applied Science and Manufacturing. 2018;110:93-105.
[135] Blaber J, Adair B, Antoniou A. Ncorr: open-source 2D digital image correlation matlab software. Experimental Mechanics. 2015;55(6):1105-22.
[136] Kim K-W, Kim D-K, Kim B-S, An K-H, Park S-J, Rhee KY, et al. Cure behaviors and mechanical properties of carbon fiber-reinforced nylon6/epoxy blended matrix composites. Composites Part B: Engineering. 2017;112:15-21.
[137] Zhu W, Yan C, Shi Y, Wen S, Liu J, Wei Q, et al. A novel method based on selective laser sintering for preparing high-performance carbon fibres/polyamide12/epoxy ternary composites. Sci Rep. 2016;6:33780.
[138] Markforged.com. Composites-data-sheet. 2020. p. http://static.markforged.com/downloads/composites-data-sheet.pdf.
[139] Liu M, Gan Y, Hanaor DAH, Liu B, Chen C. An improved semi-analytical solution for stress at round-tip notches. Engineering Fracture Mechanics. 2015;149:134-43.
[140] Radaj D. State-of-the-art review on extended stress intensity factor concepts. Fatigue & Fracture of Engineering Materials & Structures. 2014;37(1):1-28.
[141] Kaman MO. Effect of fiber orientation on fracture toughness of laminated composite plates [0°/θ°]s. Engineering Fracture Mechanics. 2011;78(13):2521-34.
[142] Ning F, Cong W, Qiu J, Wei J, Wang S. Additive manufacturing of carbon fiber reinforced thermoplastic composites using fused deposition modeling. Composites Part B: Engineering. 2015;80:369-78.
[143] Gunduz I, McClain M, Cattani P, Chiu G-C, Rhoads J, Son S. 3D printing of extremely viscous materials using ultrasonic vibrations. Additive Manufacturing. 2018;22:98-103.
[144] Chen Z, Li J, Liu C, Liu Y, Zhu J, Lao C. Preparation of high solid loading and low viscosity ceramic slurries for photopolymerization-based 3D printing. Ceramics International. 2019;45(9):11549-57.
[145] Zheng S, Zlatin M, Selvaganapathy PR, Brook MA. Multiple modulus silicone elastomers using 3D extrusion printing of low viscosity inks. Additive Manufacturing. 2018;24:86-92.
[146] Khan S, Fayazbakhsh K, Fawaz Z, Nik MA. Curvilinear variable stiffness 3D printing technology for improved open-hole tensile strength. Additive Manufacturing. 2018;24:378-85.
[147] Anisoprint. PARTS WITH THE HOLES (KIRSCH PROBLEM) 2020.
[148] Vasiliev VV, Morozov EV. Chapter 3 - Mechanics of Laminates. In: Vasiliev VV, Morozov EV, editors. Advanced Mechanics of Composite Materials and Structures (Fourth Edition): Elsevier; 2018. p. 191-242.
[149] Tabatabaei SA, Lomov SV, Verpoest I. Assessment of embedded element technique in meso-FE modelling of fibre reinforced composites. Composite Structures. 2014;107:436-46.
[150] Ghebretinsae F, Mikkelsen O, Akessa A. Strength analysis of 3D printed carbon fibre reinforced thermoplastic using experimental and numerical methods. IOP Conference Series: Materials Science and Engineering: IOP Publishing; 2019. p. 012024.
[151] Meddad A, Azaiez J, Ait-Kadi A, Guenette R. Micromechanical modeling of tensile behavior of short fiber composites. Journal of composite materials. 2002;36(4):423-41.
[152] Mamalis D, Murray JJ, McClements J, Tsikritsis D, Koutsos V, McCarthy ED, et al. Novel carbon-fibre powder-epoxy composites: Interface phenomena and interlaminar fracture behaviour. Composites Part B: Engineering. 2019;174:107012.
[153] Bendsoe MP, Kikuchi N. Generating optimal topologies in structural design using a homogenization method. 1988.

[154] Bendsøe MP. Optimal shape design as a material distribution problem. Structural optimization. 1989;1(4):193-202.
[155] Bendsoe MP, Sigmund O. Topology optimization: theory, methods, and applications: Springer Science & Business Media; 2013.
[156] Wang MY, Wang X, Guo D. A level set method for structural topology optimization. Computer methods in applied mechanics and engineering. 2003;192(1-2):227-46.
[157] Challis VJ. A discrete level-set topology optimization code written in Matlab. Structural and multidisciplinary optimization. 2010;41(3):453-64.
[158] Chu DN, Xie Y, Hira A, Steven G. Evolutionary structural optimization for problems with stiffness constraints. Finite Elements in Analysis and Design. 1996;21(4):239-51.
[159] Huang X, Xie M. Evolutionary topology optimization of continuum structures: methods and applications: John Wiley & Sons; 2010.
[160] Guo X, Zhang W, Zhong W. Doing topology optimization explicitly and geometrically—a new moving morphable components based framework. Journal of Applied Mechanics. 2014;81(8).
[161] Norato J, Bell B, Tortorelli DA. A geometry projection method for continuum-based topology optimization with discrete elements. Computer Methods in Applied Mechanics and Engineering. 2015;293:306-27.
[162] Lee JW, Kim JJ, Yoon GH. Stress constraint topology optimization using layerwise theory for composite laminates. Composite Structures. 2019;226:111184.
[163] Dai Y, Feng M, Zhao M. Topology optimization of laminated composite structures with design-dependent loads. Composite Structures. 2017;167:251-61.
[164] Chen J, Xu Y, Gao Y. Topology Optimization of Metal and Carbon Fiber Reinforced Plastic (CFRP) Laminated Battery-Hanging Structure. Polymers. 2020;12(11):2495.
[165] Davim JP, Reis P. Study of delamination in drilling carbon fiber reinforced plastics (CFRP) using design experiments. Composite structures. 2003;59(4):481-7.
[166] Gao T, Zhang W, Duysinx P. A bi-value coding parameterization scheme for the discrete optimal orientation design of the composite laminate. International Journal for Numerical Methods in Engineering. 2012;91(1):98-114.
[167] Zhou K, Li X. Topology optimization for minimum compliance under multiple loads based on continuous distribution of members. Structural and Multidisciplinary Optimization. 2008;37(1):49-56.
[168] Gea H, Luo J. On the stress-based and strain-based methods for predicting optimal orientation of orthotropic materials. Structural and Multidisciplinary Optimization. 2004;26(3-4):229-34.
[169] Jiang D, Hoglund R, Smith DE. Continuous fiber angle topology optimization for polymer composite deposition additive manufacturing applications. Fibers. 2019;7(2):14.
[170] Nomura T, Dede EM, Lee J, Yamasaki S, Matsumori T, Kawamoto A, et al. General topology optimization method with continuous and discrete orientation design using isoparametric projection. International Journal for Numerical Methods in Engineering. 2015;101(8):571-605.
[171] Nik MA, Fayazbakhsh K, Pasini D, Lessard L. Surrogate-based multi-objective optimization of a composite laminate with curvilinear fibers. Composite Structures. 2012;94(8):2306-13.
[172] Sigmund O, Petersson J. Numerical instabilities in topology optimization: a survey on procedures dealing with checkerboards, mesh-dependencies and local minima. Structural optimization. 1998;16(1):68-75.
[173] Bruns TE, Tortorelli DA. Topology optimization of non-linear elastic structures and compliant mechanisms. Computer methods in applied mechanics and engineering. 2001;190(26-27):3443-59.

[174] Lazarov BS, Sigmund O. Filters in topology optimization based on Helmholtz-type differential equations. International Journal for Numerical Methods in Engineering. 2011;86(6):765-81.
[175] Wang F, Lazarov BS, Sigmund O. On projection methods, convergence and robust formulations in topology optimization. Structural and Multidisciplinary Optimization. 2011;43(6):767-84.
[176] Svanberg K. The method of moving asymptotes—a new method for structural optimization. International journal for numerical methods in engineering. 1987;24(2):359-73.
[177] Chen Y, Ye LJCS, Technology. Topological design for 3D-printing of carbon fibre reinforced composite structural parts. 2021;204:108644.
[178] Sideridis E, Papadopoulos G. Short-beam and three-point-bending tests for the study of shear and flexural properties in unidirectional-fiber-reinforced epoxy composites. Journal of Applied Polymer Science. 2004;93(1):63-74.